UNIVERSIDAD COMPLUTENSE DE MADRID
FACULTAD DE CIENCIAS QUÍMICAS

TESIS DOCTORAL

Cinética de la cristalización

MEMORIA PARA OPTAR AL GRADO DE DOCTOR

PRESENTADA POR

Pablo Montero de Hijes

Directores

Carlos Vega de las Heras
Eduardo Santiago Sanz García

Madrid

© Pablo Montero de Hijes, 2021

Universidad Complutense de Madrid

Facultad de ciencias químicas

Tesis doctoral

Cinética de la cristalización

Memoria para optar al grado de doctor

presentada por

Pablo Montero de Hijes

directores

Carlos Vega de las Heras

Eduardo Santiago Sanz García

Universidad Complutense de Madrid
Facultad de Ciencias Químicas
Departamento de Química Física

Cinética de la cristalización

Memoria para optar
al grado de Doctor en Ciencias Químicas
realizada por

Pablo Montero de Hijes

Directores:
Prof. Carlos Vega de las Heras
Prof. Eduardo Santiago Sanz García
Dpto. Química-Física

Madrid, 2021

In memoriam

A Gorki.

Dedicatoria

A mis padres, por todo.
A Isa, por estar a mi lado.

Agradecimientos

Quiero empezar mi agradecimiento con una reflexión. Si tuviese que escoger los tres elementos que más determinan la vida de una persona, creo que serían esfuerzo, aprendizaje y suerte, pero no considero las tres igual de influyentes. Quien se esfuerza pero no aprende en el proceso y quien aprende pero no se esfuerza en aplicar lo aprendido dependen de la suerte para avanzar. Pero, incluso quien se esfuerza y aprende es posible que sin oportunidades no desarrolle todo su potencial. No obstante, mientras que esfuerzo y aprendizaje dependen de uno mismo, a la suerte le damos igual. Es externa, inhomogénea, estocástica, relativa y dinámica. Es por eso que la probabilidad de ser afortunado durante toda la vida y en todos los aspectos es insignificante. De ahí que quien quiera tener la posibilidad de cumplir sus metas, se debe preparar para cuando la suerte llame a su puerta incluso sin tener garantías de que eso vaya a ocurrir.

Las decisiones son fundamentales en el aprendizaje y su valor se aprecia mejor con el tiempo. Buenas decisiones son abono para la suerte. Si he llegado hasta aquí es en parte porque he tomado buenas decisiones. Sin embargo, sería imposible que todo esto se repitiera sin la suerte. Cómo explicar sin ella que me haya dirigido la tesis Carlos, una de las mejores personas con las que alguien se puede cruzar en la vida. Suerte. No obstante, también sería imposible sin esfuerzo, pues fue gracias a estar preparado tras varios años de estudio, prácticas, viajes y sacrificios que Eduardo me diera esta oportunidad. Que alguien de su inteligencia y calidad docente e investigadora creyese en mi es un orgullo. Suerte, pero también esfuerzo. A mis directores de tesis, Eduardo y Carlos, os doy las gracias por haberme enseñado el oficio de la ciencia, por poner vuestro tiempo y conocimiento a mi disposición y también por los buenos ratos que hemos pasado, que la verdad han sido muchos y han hecho que mi etapa predoctoral haya sido muy feliz.

También quiero agradecer a quien me introdujo en la simulación molecular durante mi trabajo de fin de grado. Recuerdo escoger su proyecto porque quería aprender a programar ya que no sabía si buscaría trabajo en alguna empresa y eso me podría ser útil. Chantal, muchas gracias por el apoyo que me diste en mis inicios, hoy estoy aquí porque supiste transmitir, motivar y me diste apoyo por lo que decidí emprender la carrera investigadora. De mano de Chantal conocí a Pablo Rosales quien con gran vocación docente me dedicó todo el tiempo que necesité para aprender de programación, simulaciones y comentar cualquier cuestión científica que surgiese. Un agradecimiento especial va para Jorge, quien me ayudó mucho en mi primer año de doctorado el cual no fue fácil. Compartimos despacho y muchas risas y es para mi un ejemplo de que se puede trabajar muy duro sin estresarse un ápice. Con nosotros en el despacho, durante ese año también estuvo Victor, un genio y gran persona a quien agradezco todos los buenos momentos y su amplio conocimiento de distintas temáticas que siempre estuvo abierto a compartir. Además, durante la tesis, he podido coincidir con muchas personas, ya sea en congresos, colaboraciones o en la facultad, que siempre han aportado cosas positivas. Muchas gracias a JL, Valentino, Eva, Maria, Kaihang, Keith, Erik, Alberto, Laurent, Caupin, Mac, Paco, Anibal, Samuel, Ignacio, Cintia y Miguel. Y también gracias a toda la Red de Simulación Molecular.

A Christoph Dellago le agradezco que me aceptase para hacer una estancia en su grupo de la Universidad de Viena aunque desafortunadamente la pandemia del Covid-19 justo un mes antes de comenzar lo hiciera inviable.

En el contexto de la pandemia Covid-19, quiero agradecer muy sentidamente en esta tesis a la generación que vivió la guerra civil, la posguerra y la dictadura, que dedicó su vida a trabajar de sol a sol, ellos, y a criar y cuidar, ellas, y que desgraciadamente han tenido que pasar algo tan duro, muchos de ellos en soledad, en sus últimos años. Solía decirse que mi generación era la mejor preparada de la historia, para mi, la vuestra es la mejor y punto.

Agradecer también a los de siempre, Antonio, Mario, Rober, Sergio, Victor, gracias por estar siempre ahí para lo bueno porque con vosotros no hay nunca nada malo. Amigos, sois una de mis grandes suertes. Otra es mi familia. Agradezco inmensamente a mis abuelos y abuelas. A Tino todo, mi referente, a Teresa por su alegría, a Victoria por su fuerza y paz, y a José, que nos dejó demasiado pronto, por enseñarme a caminar con la mirada en alto. Gracias también a mis primas, primos, tíos y tías que siempre me habéis querido mucho como yo a vosotros.

Un agradecimiento muy especial va a mis padres quienes han dado lo mejor de si mismos para que yo hoy tenga una buena vida y espero con este trabajo honrar su esfuerzo. Se que están muy orgullosos, pero yo lo estoy aún más de ellos. Gracias papá por cultivar mi mente. Por llevarme al cine, al museo, a exposiciones, al teatro, a conciertos, a la libreria Antonio Machado, al círculo de Bellas Artes... Es posible que en su momento no te lo agradeciese demasiado, ya sabes que yo prefería el fútbol, pero como padre hiciste bien en no darme siempre lo que quería sino lo que era mejor. A día de hoy disfruto aún más de tu conversación mi sabio padre. Gracias mamá por absolutamente todo. No puedo describir cada cosa que has hecho por mi porque necesitaría escribir un libro solo para hablar de ti. Eres mi mayor suerte. También le doy las gracias al camarada Ramón, tu compañero, que ha estado estos años a tu lado y te quiere y te cuida.

Muy especialmente, quiero agradecer a Isa por estar a mi lado en estos cuatro años de tesis en los que hemos vivido tantas cosas juntos. Me has dado el equilibrio necesario para poder llevar a cabo esta tarea y te doy también las gracias por tu apoyo para continuar juntos en la nueva aventura que nos aguarda. Contigo han llegado grandes personas a las que también quiero agradecer el cariño que me han demostrado.

Dada mi forma de ver la vida, me cuesta limitar los agradecimientos pues acierto a imaginar en qué medida tantas circunstancias y personas han sido parte del proceso. Muchas gracias a todas ellas.

Gracias al Estado Español por financiar mi tesis con la ayuda BES-2017-080074.

Publicaciones

El apartado de resultados de esta tesis está basado en las siguientes publicaciones:

Capítulo 1
"Interfacial free energy of a liquid-solid interface: Its change with curvature", P. Montero de Hijes, J. R. Espinosa, E. Sanz, C. Vega, *J. Chem. Phys.* 151 (14), 144501, 2019.

Capítulo 2
"Interfacial Free Energy and Tolman Length of Curved Liquid–Solid Interfaces from Equilibrium Studies", P. Montero de Hijes, J. R. Espinosa, V. Bianco, E. Sanz, C. Vega, *J. Phys. Chem. C* 124 (16), 8795-8805, 2020.

Capítulo 3
"The Young–Laplace equation for a solid–liquid interface", P. Montero de Hijes, K. Shi, E. G. Noya, E. E. Santiso, K. E. Gubbins, E. Sanz, C. Vega, *J. Chem. Phys.* 153 (19), 191102, 2020.

Capítulo 4
"On the thermodynamics of curved interfaces and the nucleation of hard spheres in a finite system", P. Montero de Hijes, C. Vega, enviado, 2021.

Capítulo 5
"Equivalence between condensation and boiling in a Lennard-Jones fluid", I. Sanchez-Burgos, P. M. de Hijes, P. Rosales-Pelaez, C. Vega, E. Sanz, *Phys. Rev. E* 102 (6), 062609, 2020.

Capítulo 6
"Anomalous Behavior in the Nucleation of Ice at Negative Pressures", V. Bianco, P. Montero de Hijes, C. P. Lamas, E. Sanz, C. Vega, *Phys. Rev. Lett.* 126 (1), 015704, 2021.

Capítulo 7
"Ice growth rate: Temperature dependence and effect of heat dissipation", P. Montero de Hijes, J. R. Espinosa, C. Vega, E. Sanz, *J. Chem. Phys.* 151 (4), 044509, 2019.

Capítulo 8
"Viscosity and self-diffusion of supercooled and stretched water from molecular dynamics simulations", P. Montero de Hijes, E. Sanz, L. Joly, C. Valeriani, F. Caupin, *J. Chem. Phys.* 149 (9), 094503, 2018.

Otras publicaciones no incluidas en la tesis:

"Avalanche mediated devitrification in a glass of pseudo hard-spheres" P. Rosales-Pelaez, P. Montero de Hijes, E. Sanz, C. Valeriani, *J. Stat. Mech.: Theory and Exp.* 2016 (9), 094005, 2016.

"Brownian versus newtonian devitrification of hard-sphere glasses" P. Montero de Hijes, P. Rosales-Pelaez, C. Valeriani, P. N. Pusey, E. Sanz, *Phys. Rev. E* 96 (2), 020602, 2017.

"Homogeneous nucleation of NaCl in supersaturated solutions" C. P. Lamas, J. R. Espinosa, M. M. Conde, J. Ramirez, P. Montero de Hijes, E. G. Noya, C. Vega, E. Sanz, *en revisión en Phys. Chem. Chem. Phys.*, 2021.

Índice general

Resumen

Introducción

La cristalización de un líquido consta de varias etapas, empezando por que éste se encuentre en condiciones de metaestabilidad. Por ejemplo, un caso típico es el de un líquido que se enfría más allá de su temperatura de coexistencia. Por lo tanto, la temperatura y la presión del mismo correspondan a la región cristalina en el diagrama de fases de la sustancia por lo que el cristal es la fase más estable y por lo tanto la que cabría esperar. Sin embargo, esta no es condicion suficiente para observar la transición de forma espontánea dado que se trata de un proceso activado que puede tomar un tiempo considerable en función de las condiciones termodinámicas[1]. Este tipo de procesos se caracterizan por la transición entre estados separados por una barrera de energía. En este caso, dicha barrera se forma por la competición energética entre estabilidad termodinámica y la penalización de crear interfase sólido-líquido. La tensión interfacial es una variable clave en el proceso pues es la que se opone a la transición y da lugar a que el proceso sea activado logrando que un líquido metaestable pueda sobrevivir durante largo tiempo. Cuando la cristalización emerge en una sustancia pura el proceso se denomina nucleación homogénea mientras que en presencia de impurezas o sustratos, el proceso se denomina nucleación heterogénea. En ambos casos, son fluctuaciones de orden local las responsables del inicio de la transición pero mientras que en la nucleación homogénea ocurren en el seno del fluido, en la nucleación heterogénea ocurren también próximas a una intefase lo cual facilita la nucleación[2–4]. Una entidad física relevante aquí es el núcleo crítico que determina la cantidad mínima de la fase emergente necesaria para superar la barrera de energía por completo. Estos núcleos son esquivos teniendo tamaños del orden del nanómetro y tiempos de vida media del orden del nanosegundo ya que pasado este tiempo, o bien funden, o bien desencadenan la cristalización completa de la sustancia. Por esto, estudiar nucleación supone una ardua tarea. La simulación molecular ha demostrado ser una herramienta clave a la hora de solventar esta dificultad ya que accede a información microscópica como el tamaño y el tiempo de vida media del núcleo crítico y para lidiar con el tiempo requerido para observar nucleación se han desarrollado técnicas especiales[5]. Una vez que la barrera se ha superado, el núcleo continua creciendo en detrimento del líquido metaestable hasta que todo el sistema cristaliza en lo que se conoce como crecimiento, la última etapa del proceso.

La formación de hielo es probablemente la cristalización de mayor relevancia dado que influye en la vida de forma directa. Un ejemplo cotidiano es la formación de hielo en vías públicas que se intenta evitar mediante la adición de sales inorgánicas, típicamente NaCl, que son corrosivas para la carrocería de los vehículos y que pueden terminar en aguas subterráneas si se dan precipitaciones, alterando así la calidad de las mismas[6]. Además, numerosos accidentes aéreos están relacionados con la formación de hielo en la aeronave ya que en las nubes es común que haya gotas de agua subenfriada[7,8]. De hecho, en ciencias del clima la formación de hielo juega un papel central por lo que también lo hace en cuanto al calentamiento global ya que el hielo refleja más radiación solar que el agua líquida y su formación también influye en el intercambio de gases entre la atmósfera y el océano[9]. En un plano tecnológico, el control de la formación de hielo es clave en diferentes industrias como son farmacéuticas, de almacenamiento alimentario, criopreservación de tejidos y órganos[10–13] y en el desarrollo de materiales[14]. Todo ello sin mencionar los retos aún desconocidos a los que la humanidad se enfrentará en el futuro, ya que nuestra supervivencia siempre estará ligada al agua. Por suerte, podemos inspirarnos en la criobología donde encontramos múltiples ejemplos de cómo la vida ha logrado, en diferentes formas, adaptarse a temperaturas extremadamente bajas donde cabe esperar la formación de hielo[15–19]. Pese a su vital importancia, todavía hay muchas preguntas por responder en lo que se refiere al agua y su cristalización.

Existen también otros sistemas cuya relevancia es notable. Por ejemplo, un sistema arquetipo sobre el cual desarrollar formalismos y metodologías es la esfera dura. Este modelo se compone de esferas que interactúan únicamente de forma repulsiva. En concreto, dicha interacción actúa solo en el momento en el que impactan unas con otras sin que puedan existir solapamientos. En 1957, Alder y Wainwright demostraron mediante simulaciónes de dinámica molecular que la esfera dura presenta transición de fase fluido-sólido aún teniendo solamente interacción repulsiva[20]. Además, ciertas partículas coloidales que se pueden observar experimentalmente interactuan de forma muy próxima al modelo de esfera dura[21]. Otro modelo arquetipo pero que sí incluye interacción atractiva es el Lennard-Jones. Dicho modelo reproduce sistemas reales de gases nobles y es ampliamente utilizado también en el desarrollo de campos de fuerza de mayor complejidad. Por ejemplo, entre los mejores modelos para simular agua encontramos al TIP4P/2005 y al TIP4P/Ice los cuales utilizan en su campo de fuerza una interacción tipo Lennard-Jones entre los oxígenos de la molécula de agua. Tanto esfera dura como Lennard-Jones presentan incógnitas en cuanto a lo que su nucleación se refiere pese a haber sido estudiados durante décadas.

Esta tesis se centra en el estudio por simulación de la cinética de la cristalización, aunque también se dedica gran parte a la termodinámica ya que ésta influye sobre la cinética. En cuanto a los sistemas estudiados, consideramos principalmente el agua, dada su relevancia, así como la esfera dura al ser un modelo muy simple que permite profundizar mucho en un determinado problema. También se incluye de forma secundaria el modelo Lennard-Jones, otro modelo arquetipo. La nucleación representa una gran parte de los esfuerzos realizados. Entre las incógnitas más relevantes que tratamos de resolver encontramos, por una parte, la variación de la tensión interfacial con la curvatura del núcleo crítico la cual estudiamos tanto para el agua como para los modelos esfera dura y Lennard-Jones. Por otra parte, se investiga el efecto del colectivo de simulación en la nucleación. Aunque normalmente para la nucleación se considera el isotérmico-isobárico (NpT), en este trabajo exploramos también el colectivo canónico (NVT) donde algunos trabajos han demostrado lograr interfases curvas en equilibrio estable. Para ello se utiliza el modelo esfera dura con la intención de estudiar con ella la ecuación de Tolman y la de Young-Laplace. Puesto que el formalismo y la metodología empleados son de carácter general también lo aplicamos al caso de la nucleación de burbujas y de gotas de Lennard-Jones. Por último, se encuentra un bloque con distintos aspectos de la formación de hielo donde se estudia la nucleación a presión negativa, la variación de la velocidad de crecimiento de hielo con la temperatura y las anomalías de las propiedades dinámicas del agua subenfriada.

Objetivos

La tesis tiene los siguientes objetivos:

1. Estudiar para el agua y los modelos esfera dura y Lennard-Jones la dependencia de la tensión interfacial con la curvatura del núcleo crítico dada su relevancia en la nucleación y contextualizar los resultados en base a la ecuación de Tolman.

2. Investigar la conexión entre las interfases curvas estables que se pueden observar en el colectivo NVT y la nucleación. Contextualizar los resultados en base a la Teoría Clásica de Nucleación (CNT por sus siglas en inglés), la ecuación de Young-Laplace y el formalismo termodinámico de interfases curvas.

3. Transferir y extender la metodología empleada en la nucleación de cristales a otras transiciones de fase como la cavitación o la condensación. Estudiar el efecto de invertir la fases emergente y metaestable para el caso de la nucleación de un fluido Lennard-Jones.

4. Describir la nucleación de hielo a presiones negativas utilizando la técnica de seeding[22] para obtener el tamaño del núcleo crítico, la tensión interfacial, la barrera de energía libre y la tasa de nucleación.

5. Medir el efecto de la temperatura en la velocidad de crecimiento de hielo y acabar el debate entre simulación y experimento donde las simulaciones son puestas en duda al usar un termostato que artificialmente mantiene constante la temperatura del sistema. Demostrar que existe un máximo en la velocidad de crecimiento de hielo en función de la temperatura y explicar el resultado en un marco teórico como la ecuación de Wilson-Frenkel.

6. Caracterizar la dinámica anómala del agua metaestable y demostrar que se puede explicar con un modelo de dos estados del agua en el que dos fases líquidas diferenciadas coexisten.

Resultados

Siguiendo el orden de los objetivos, a continuación se resumen brevemente los resultados principales de la tesis:

1. De acuerdo a la ecuación de Tolman, se obtuvo una dependencia lineal de la tensión interfacial con el inverso del radio de curvatura tanto para el agua (TIP4P/Ice y mW) como para esfera dura y Lennard-Jones. Comparando con dicha ecuación se obtuvo el valor de la longitud de Tolman (parámetro que determina la desviación de la tensión interfacial frente a su valor a coexistencia debido a la curvatura). Se observó que la longitud de Tolman es prácticamente constante para la cristalización en un modelo dado, aunque su valor no es universal y varía de unos sistemas a otros[23].

2. Utilizando esferas duras, se logró estabilizar núcleos esféricos en el colectivo NVT, los cuales resultaron ser críticos al lanzar la simulación en el colectivo NpT. Extendiendo así la técnica de seeding, se estudió la nucleación mediante núcleos estables lo que a su vez permitió obtener la longitud de Tolman por su definición. Además, este procedimiento nos permitió observar que también es posible estabilizar núcleos de geometría cilíndrica y planar[24].

3. Analizando los núcleos estables de esfera dura se demostró que en la ecuación de Young-Laplace para una interfase sólido-líquido, la presión de la fase interna ha de ser aquella que corresponde a un sólido sin estrés cuyo potencial químico es igual al de la fase líquida que le rodea. De hecho, se observó que la presión real del sólido es menor que la del líquido para esfera dura lo que implica que el núcleo crítico está estresado. También se demostró que la presión promedio del sistema es igual a la de la fase externa[25].

4. A continuación se recurrió al formalismo termodinámico de interfases curvas logrando reproducir teóricamente los resultados de los núcleos estables y desarrollando así un programa que permitiera estimar tamaños de núcleos estables (y por ende críticos) en esfera dura en función de las condiciones termodinámicas del colectivo y de la variación de la tensión interfacial con las mismas previamente obtenida por simulación. Esto nos permitió hacer una descripción extensa sobre la nucleación de esferas duras además de sentar las bases para un futuro estudio en otras sustancias como el agua.

5. También se aplicó con éxito la extensión de la técnica de seeding donde es posible estabilizar núcleos a la cavitación y la condensación en un fluido Lennard-Jones. Esto nos permitió observar una similitud prácticamente exacta entre gota y burbuja de Lennard-Jones a efectos de nucleación[26].

6. En cuanto al bloque final centrado en la formación de hielo, por una parte se pudo observar una nueva anomalía del agua ya que tanto el tamaño del núcleo crítico como la tensión interfacial, la barrera de energía libre y la tasa de nucleación presentan un comportamiento no monotónico fruto de un reentrante en la curva de coexistencia a presiones negativas. Esto sugiere a su vez también un comportamiento no monotónico en la curva de nucleación homogénea. El modelo utilizado fue el TIP4P/Ice[27].

7. Por otra parte, se pudo demostrar el máximo en la velocidad de crecimiento de hielo en función de la temperatura en una simulación sin termostato (utilizando el colectivo microcanónico NVE). Para ello se utilizó el modelo TIP4P/Ice. Estos resultados se ajustaron luego a la ecuación Wilson-Frenkel que incluye términos cinéticos y termodinámicos ya que es fruto de una competición entre estos términos lo que da lugar al extremo. Con estos resultados se logró disipar las dudas sobre las simulaciones con termostato[28].

8. Finalmente, se estudiaron las propiedades de transporte del agua subenfriada con el modelo TIP4P/2005, comprobando la anomalía en la difusión del agua tanto en el coeficiente de difusión como en la viscosidad a distintas temperaturas (cubriendo cinco isotermas desde 220 a 300 K). Estos datos se ajustaron a un modelo de dos estados del agua. Además se observó el desacoplamiento entre viscosidad y coeficiente de difusión

en función de la temperatura cuando esta disminuye lo suficiente incumpliendo así la relación de Stokes-Einstein[29].

Conclusiones

En esta tesis se han cubierto distintos aspectos relacionados con la cristalización. Se han utilizado modelos arquetipo como la esfera dura y el Lennard-Jones para tratar de resolver incógnitas fundamentales y también se ha estudiado el agua, cuya relevancia es evidente. Para el agua se han utilizado los modelos TIP4P/Ice, TIP4P/2005 y mW. Gran parte de la tesis se ha centrado en la nucleación. Se ha estudiado la dependencia de la tensión interfacial con la curvatura en el contexto de la ecuación de Tolman tanto para el agua como para la esfera dura y el Lennard-Jones. Se ha observado una dependencia lineal con el inverso del radio de curvatura satisfaciendo así la ecuación de Tolman. Se ha logrado estabilizar núcleos cristalinos de esfera dura en contacto con líquido y se ha demostrado que éstos representan a su vez núcleos críticos. Por lo tanto se ha obtenido la tasa de nucleación de esferas duras mediante núcleos estables. En ocasiones los núcleos estables, fueron en realidad metaestables ya que fundieron o transitaron hacia otras geometrías formando un cilindro sólido rodeado de líquido o una interfase plana entre el sólido y el líquido. Por otra parte, dado que logramos simular núcleos estables durante largos tiempos hemos podido caracterizarlos en detalle llegando a evaluar la ecuación de Young-Laplace. También se ha desarrollado un programa teórico basado en la termodinámica de interfases curvas que reproduce los resultados de simulación de núcleos estables logrando una descripción extensa de la nucleación de esferas duras además de sentar las bases para un futuro estudio en otras sustancias como el agua. Se han extendido estos avances al estudio de la nucleación en un fluido Lennard-Jones, estudiando tanto cavitación como condensación observando una práctica equivalencia a efectos de nucleación entre una gota y una burbuja. En cuanto a la formación de hielo, se ha aplicado la técnica de seeding para estudiar el efecto en la nucleación de las presiones negativas y se ha estudiado cómo depende la velocidad de crecimiento de la temperatura. Concretamente se ha observado un máximo fruto de la competición entre el empuje de la estabilidad termodinámica y la ralentización de la cinética. Por último, para el agua metaestable, se ha podido describir su cinética anómala mediante un modelo de dos estados a partir de datos tanto del coeficiente de difusión como de la viscosidad, los cuales a su vez han servido para demostrar que el agua subenfriada deja de cumplir la relación de Stokes-Einstein a cierta temperatura.

Summary

Introduction

Liquids crystallize in three steps. First, the liquid should be metastable. A good example would be a liquid that has been supercooled beyond its temperature of coexistence. This means that its temperature and pressure should correspond to the crystalline phase in the phase diagram of the substance. Thus, the crystal would be more stable and one should expect the liquid to transform into it. However, this condition is not enough to observe the phase transition spontaneously. This is due to the fact that this is an activated process which may take long depending on the thermodynamic conditions[1]. In this kind of process there is a transition between states that are separated by a free energy barrier. In this particular case, the free energy barrier appears due to the competition between thermodynamic stability and the energy cost of creating solid-liquid interface. The interfacial free energy is a key variable in the process since it is the one that goes against the transition allowing a metastable liquid to survive long times. When crystallization originates within a pure substance, the process is known as homogeneous nucleation but, in the presence of impurities or substrates, it is known as heterogeneous nucleation. In both cases, local fluctuations are responsible for triggering the phase transition although whereas in homogeneous nucleation they occur in the bulk of the metastable liquid, in the heterogeneous case they occur also near an interface which facilitates the nucleation[2–4]. A relevant entity in this process is the critical nucleus. It determines the minimum amount of the emerging phase that is needed to overcome the free energy barrier. These clusters are elusive having sizes in the order of nanometers and lifetimes in the order of nanoseconds. After this short time they either melt or trigger the whole crystallization of the system. Therefore, studying nucleation is a difficult task. Molecular simulations have proved to be a useful tool to solve this since they can access microscopic information like the critical nucleus size or its lifetime. In order to deal with the long times needed to observe nucleation, special techniques have been developed[5]. Once the free energy barrier is overcome, the nucleus keeps growing at expense of the liquid until the whole system crystallizes in what is known as growth, the last step of crystallization.

Ice formation is probably the most relevant crystallization process as it directly affects life. An everyday example is the formation of ice in roads and sidewalks which we try to avoid with the addition of inorganic salts, typically NaCl, which can corrode the body of the vehicles. Moreover, if a rainfall occurs, salts may end up in the underground water affecting its quality[6]. Besides this, numerous aircraft accidents are related to the formation of ice over the structure of the aircraft since it is common to find supercooled water droplets within the clouds[7,8]. In fact, ice formation plays a central role in climate science and, thus, the global warming issue. Ice reflects more light than water and its formation also affects the exchange of gases between the oceans and the atmosphere[9]. From a technological point of view, controlling the appearance of ice is key in the pharmaceutical industry and also for food storage, cryopreservation of tissues and organs[10–13] as well as in material engineering[14]. Moreover, there is room for new challenges, yet unknown, that we may face in the future since our existence is linked to water. Fortunately, we can look for answers in cryobiology where we find several examples of how life has achieved, in different forms, to adapt to very low temperatures where the formation of ice is very likely[15–19]. Despite its importance, there are still several open questions in which regards to water and its crystallization.

Apart from water, there are also other systems that are relevant. For instance, hard spheres are an archetype model to develop and test formalisms and methodologies. This model is composed of spheres with just repulsive interactions. In fact, this interaction only happens when the spheres bounce on each other without the possibility of overlapping. In 1957, Alder and Wainwright showed, by means of molecular dynamics simulations, that hard spheres present fluid-solid transition even though they only have repulsive interaction[20]. Moreover, certain colloids that can be created in the laboratory interact very similar to the theoretical model of hard spheres[21]. Another archetype model is the Lennard-Jones. This model reproduces noble gases and it is widely used in the development of more complex force fields. For example, among the best water models, we find the TIP4P/2005 and the TIP4P/Ice which include a Lennard-Jones interaction for their oxygens. Both hard spheres and Lennard-Jones present open questions regarding its nucleation even though they have been studied for decades.

This thesis is focused on the study of crystallization kinetics by means of simulations. Also, thermodynamics is involved as it directly affects crystallization kinetics. The main systems considered here are water given its relevance and hard spheres as they are quite simple allowing us to deepen in a certain problem. Also, some calculations are performed for Lennard-Jones, another archetype model. Most efforts have been done in the investigation of nucleation. Among the most relevant topics that are covered, we find the variation of the interfacial free energy with the curvature of the nucleus which we study for all systems, i.e. water, hard spheres, and Lennard-Jones. Also, the effect of the simulation ensemble is investigated. Typically, nucleation is studied in the isothermal-isobaric ensemble (NpT), in this work, we also explore the possibility of using the canonical ensemble (NVT) where previous work have shown that is possible to equilibrate a curved interface. To do this, we use hard spheres and we test the Tolman and the Young-Laplace equations for a solid-liquid interface. Since the technique and formalism are general, we also apply it to the nucleation of bubbles and droplets of Lennard-Jones. Lastly, we focus on water and in particular, we study nucleation at negative pressure, the ice growth rate as a function of supercooling as well as anomalies in the transport properties of supercooled water.

Objectives

The thesis has the following objectives:

1. Studying the dependence of the interfacial free energy (which is a key variable in nucleation) with the curvature of the critical cluster in the context of Tolman's equation for water, hard spheres, and Lennard-Jones.
2. Connecting the curved interfaces in equilibrium observed in the NVT ensemble with nucleation. Applying the Classical Nucleation Theory (CNT), the Young-Laplace equation, and the formalism of curved interfaces to discuss the results.

3. Extending the methods that are developed for crystallization to other phase transitions like cavitation or condensation. Studying the effect of inverting the emergent and metastable phase in the case of nucleation in a Lennard-Jones fluid.

4. Studying ice nucleation at negative pressures via the seeding technique[22] in order to obtain the critical nucleus size, interfacial free energy, free energy barrier and nucleation rate.

5. Computing the growth rate of ice as a function of supercooling without using thermostats since simulations are in doubt due to its use. Showing that a maximum in the growth rate actually exists following the Wilson-Frenkel theory.

6. Characterizing the anomalous dynamics of supercooled water by means of a two state model of water.

Results

Below, the results of the thesis are summarized following the same order than in the objectives:

1. The dependence of the interfacial free energy with the inverse of the radius of the critical cluster was obtained for water (TIP4P/Ice and mW models) as well as for hard spheres and Lennard-Jones. A linear tendency was found in agreement with Tolman's equation. By comparing with such equation, the Tolman length was obtained finding that is almost constant for a given system in which regards to crystallization[23].

2. Spherical clusters of hard spheres were stabilized in the NVT ensemble. Such clusters were shown to be critical in the NpT ensemble. This allowed us to extend the seeding technique. We measured the Tolman length again from its definition finding good agreement with the previous approach. Moreover, these simulations showed that it is also possible to stabilize cylinders and planar slabs in the NVT ensemble[24].

3. By means of the NVT-seeding approach, we tested the Young-Laplace equation for a solid-liquid interface. These calculations were performed for hard spheres showing that in order to use the Young-Laplace equation, one needs to consider for the inner solid phase a macroscopic phase without interface at the same chemical potential than the external liquid. In fact, the actual pressure of the nucleus is smaller than the external liquid indicating that this solid is stressed. Also, we showed that the average pressure in the system equals the one of the external phase due to the mechanical equilibrium condition[25].

4. Previous results were reproduced theoretically by means of the thermodynamic formalism of curved interfaces. We could reproduce critical nuclei sizes and properties like density and pressure. This formalism allowed us to extensively describe the nucleation of hard spheres and it is a building block for future studies in other substances like water.

5. The NVT-seeding approach was also implemented to study other kinds of nucleation like cavitation and condensation of Lennard-Jones. This allowed us to show that a droplet and a bubble of Lennard-Jones are equivalent in terms of nucleation[26].

6. Regarding the series of works on water crystallization, on the one hand, it was shown a new anomaly of water. Its interfacial free energy, free energy barrier to nucleation and nucleation rate present a returning point along an isotherm at negative pressures, describing, thus a non-monotonic tendency. The model of this study was the TIP4P/Ice[27].

7. On the other hand, the maximum in the growth rate against the supercooling was measured by means of molecular dynamics simulations without using a thermostat. These simulations were performed in the microcanonical ensemble (NVE) using the TIP4P/Ice water model. These results fitted well to a Wilson-Frenkel expression which explains the maximum as the result of the competition between thermodynamic and kinetic terms. These results closed the debate were simulations were blamed for the discrepancies with experiments due to the use of thermostats[28].

8. Finally, transport properties of supercooled water were measured using the TIP4P/2005 model. In particular, self-diffusion coefficient and viscosity were computed showing the anomaly of diffusion in supercooled water. Five different isotherms were covered (between 220 and 300 K). These results were fitted to a model of two states of water. Also, the break down of the Stokes-Einstein relation could be observed[29].

Conclusions

Different topics within the crystallization process have been covered in this thesis. Two archetype models have been used, being hard spheres and Lennard-Jones, allowing us to deal with fundamental questions. Water has also been studied given its relevance. Three different water models have been used (TIP4P/Ice, TIP4P/2005, and mW). The thesis is focused in nucleation. The dependence of the interfacial free energy with curvature is studied for hard spheres, Lennard-Jones, and water. A linear tendency between the interfacial free energy and the inverse of the radius of curvature was observed following Tolman's equation. Stable hard sphere nuclei in contact with liquid have been obtained using the NVT ensemble. Then they have been shown to be critical when launched in the NpT ensemble. Therefore, nucleation rates of hard spheres were obtained from stable nuclei. In some cases, the stable clusters were in fact metastable. Some clusters melted or transformed into cylinders or planar slabs surrounded by metastable liquid. These stable clusters have allowed us to study them in detail, even testing the Young-Laplace equation. A program based on the thermodynamic formalism of curved interfaces has been developed. This program fairly reproduces the simulation results and serves as a building block for a future extension to other substances like water. These advances have been applied to the nucleation of a Lennard-Jones fluid. Both cavitation and condensation have been observed finding that they are equivalent in terms of nucleation. Regarding the ice formation, the seeding technique has been applied to study the effect of negative pressures. Also, the temperature effect over the growth rate has been studied. In particular, a maximum has been found due to the competition between the thermodynamic driving force and the slow down of kinetics with supercooling. Finally, we have described the anomalous kinetics of supercooled water by means of a two state model. Both the self-diffusion coefficient and the viscosity have been provided allowing us to test the validity of the Stokes-Einstein relation. In fact, this relation is shown to break down at certain temperature.

Bibliografía

[1] P. G. Debenedetti. *Metastable liquids: Concepts and Principles.* Princeton University Press, 1996.

[2] D. Kashchiev. *Nucleation: Basic Theory with Applications.* Butterworth-Heinemann, Oxford, 2000.

[3] K. F. Kelton and A. L. Greer. *Nucleation in Condensed Matter.* Pergamon, Elsevier, Oxford, 2010.

[4] K. F. Kelton. *Crystal Nucleation in Liquids and Glasses.* Academic, Boston, 1991.

[5] Gabriele C. Sosso, Ji Chen, Stephen J. Cox, Martin Fitzner, Philipp Pedevilla, Andrea Zen, and Angelos Michaelides. Crystal nucleation in liquids: Open questions and future challenges in molecular dynamics simulations. *Chemical Reviews*, 116(12):7078–7116, 2016.

[6] C Postigo, Daniel Emilio Martinez, Sebastian Grondona, and Karina Silvia Beatriz Miglioranza. Groundwater pollution: sources, mechanisms, and prevention. 2018.

[7] Marcia K Politovich. Aircraft icing caused by large supercooled droplets. *Journal of Applied Meteorology (1988-2005)*, pages 856–868, 1989.

[8] Stewart G Cober, George A Isaac, and J Walter Strapp. Characterizations of aircraft icing environments that include supercooled large drops. *Journal of Applied Meteorology*, 40(11):1984–2002, 2001.

[9] M Hood. Noble gases and the cryosphere. 2001.

[10] R Geidobler and G Winter. Controlled ice nucleation in the field of freeze-drying: fundamentals and technology review. *European Journal of Pharmaceutics and Biopharmaceutics*, 85(2):214–222, 2013.

[11] Guillermo Petzold and José M Aguilera. Ice morphology: fundamentals and technological applications in foods. *Food Biophysics*, 4(4):378–396, 2009.

[12] Xu Xue, Hai-Lan Jin, Zhi-Zhu He, and Jing Liu. Quantifying the growth rate and morphology of ice crystals growth in cryoprotectants via high-speed camera and cryomicroscope. *Journal of Heat Transfer*, 137(9):091020, 2015.

[13] Tadanori Sei, Takehiko Gonda, and Yoshiyasu Arima. Growth rate and morphology of ice crystals growing in a solution of trehalose and water. *Journal of crystal growth*, 240(1-2):218–229, 2002.

[14] Angelos Michaelides and Karina Morgenstern. Ice nanoclusters at hydrophobic metal surfaces. *Nature Materials*, 6:597–601, 2007.

[15] CA Knight, CC Cheng, and AL DeVries. Adsorption of alpha-helical antifreeze peptides on specific ice crystal surface planes. *Biophysical journal*, 59(2):409–418, 1991.

[16] Jun Hyuck Lee, Ae Kyung Park, Hackwon Do, Kyoung Sun Park, Sang Hyun Moh, Young Min Chi, and Hak Jun Kim. Structural basis for antifreeze activity of ice-binding protein from arctic yeast. *Journal of Biological Chemistry*, 287(14):11460–11468, 2012.

[17] Chris Sidebottom, Sarah Buckley, Paul Pudney, Sarah Twigg, Carl Jarman, Chris Holt, Julia Telford, Andrew McArthur, Dawn Worrall, Rod Hubbard, et al. Heat-stable antifreeze protein from grass. *Nature*, 406(6793):256–256, 2000.

[18] Steffen P Graether, Michael J Kuiper, Stephane M Gagne, Virginia K Walker, Zongchao Jia, Brian D Sykes, and Peter L Davies. β-helix structure and ice-binding properties of a hyperactive antifreeze protein from an insect. *Nature*, 406(6793):325–328, 2000.

[19] Christopher B Marshall, Garth L Fletcher, and Peter L Davies. Hyperactive antifreeze protein in a fish. *Nature*, 429(6988):153–153, 2004.

[20] B. J. Alder and T. E. Wainwright. Phase transition for a hard sphere system. *J. Chem. Phys.*, 27(5):1208–1209, 1957.

[21] P. N. Pusey and W. van Megen. Phase behaviour of concentrated suspensions of nearly hard colloidal spheres. *Nature*, 320(27):340, 1986.

[22] E. Sanz, C. Vega, J. R. Espinosa, R. Caballero-Bernal, J. L. F. Abascal, and C. Valeriani. Homogeneous ice nucleation at moderate supercooling from molecular simulation. *J. Am. Chem. Soc.*, 135(40):15008–15017, 2013.

[23] P Montero de Hijes, Jorge R Espinosa, Eduardo Sanz, and Carlos Vega. Interfacial free energy of a liquid-solid interface: Its change with curvature. *J. Chem. Phys.*, 151(14):144501, 2019.

[24] P Montero de Hijes, Jorge R Espinosa, Valentino Bianco, Eduardo Sanz, and Carlos Vega. Interfacial free energy and tolman length of curved solid-liquid interfaces from equilibrium studies. *J.Phys.Chem.C*, 124:8795, 2020.

[25] P Montero de Hijes, K Shi, EG Noya, EE Santiso, KE Gubbins, E Sanz, and C Vega. The young–laplace equation for a solid–liquid interface. *The Journal of Chemical Physics*, 153(19):191102, 2020.

[26] I Sanchez-Burgos, P Montero de Hijes, P Rosales-Pelaez, C Vega, and E Sanz. Equivalence between condensation and boiling in a lennard-jones fluid. *Physical Review E*, 102(6):062609, 2020.

[27] Valentino Bianco, P Montero de Hijes, Cintia P Lamas, Eduardo Sanz, and Carlos Vega. Anomalous behavior in the nucleation of ice at negative pressures. *Physical Review Letters*, 126(1):015704, 2021.

[28] P Montero de Hijes, JR Espinosa, C Vega, and E Sanz. Ice growth rate: Temperature dependence and effect of heat dissipation. *The Journal of chemical physics*, 151(4):044509, 2019.

[29] P Montero de Hijes, E Sanz, L Joly, C Valeriani, and F Caupin. Viscosity and self-diffusion of supercooled and stretched water from molecular dynamics simulations. *J. Chem. Phys.*, 149:094503, 2018.

Parte I

Discusión

Discusión Integradora

El tema central de la tesis es el estudio de la cristalización y en concreto de algunos aspectos cinéticos involucrados en la misma. Por ello, se desarrollan estudios en cada una de las etapas que dan lugar a este proceso físico: metaestabilidad, nucleación y crecimiento. No obstante, el énfasis se pone en el estudio de la nucleación homogénea. Dado que la variable clave en los estudios de nucleación, es decir, la tasa de nucleación, tiene un componente cinético y otro termodinámico, también se dedica gran parte al estudio de la termodinámica de interfases curvas. La metodología empleada es la simulación molecular y entre los sistemas estudiados encontramos dos modelos arquetipo, la esfera dura[1] y el Lennard-Jones[2] así como el agua cuya relevancia es máxima. Para modelizar agua se han empleado el modelo TIP4P/Ice[3], el TIP4P/2005[4] y el mW[5]. Una breve descripción de los modelos se encuentra en el apartado de fundamento teórico, Parte II. En dicho apartado se describe también brevemente los fundamentos necesarios para comprender la metaestabilidad de un fluido y su consecuente cristalización. Además se desarrollan algunas descripciones teóricas que sostienen las ecuaciones empleadas en algunos capítulos de resultados. Una vez que los conceptos básicos que definen la cristalización han sido descritos comienzan los capítulos de resultados.

Dado que los capítulos de resultados de esta tesis los componen artículos publicados en diferentes revistas como son *The Journal of Chemical Physics*, *Physical Review Letters*, *The Journal of Physical Chemistry C* o *Physical Review E*, este apartado pretende servir de nexo entre los capítulos remarcando así el hilo conductor de la tesis. Para ello se describe brevemente cada capítulo mencionando los hechos que motivaron la realización de las investigaciones que recogen, los hallazgos más relevantes de las mismas y su conexión con otros capítulos.

El estudio comienza con la tensión interfacial ya que ésta juega un papel principal en la nucleación. Cuando dos fases macroscópicas coexisten tienen asociadas una cierta tensión interfacial, pero ésta cambia si la interfase en lugar de ser plana tiene una cierta curvatura como es el caso de un núcleo esférico de una fase inmerso en la otra[6]. Esto es lo que se conoce como efecto de curvatura en la tensión interfacial. Pero no es el único efecto de curvatura. Al utilizar el formalismo termodinámico de Gibbs[7], se considera que las fases son macroscópicas, carentes de estrés o defectos y en equilibrio termodinámico y están separadas por una superficie divisoria que contribuye al sistema pero no tiene volumen. La localización de dicha interfase es arbitraria para un sistema curvo por lo que la tensión interfacial de un sistema debe referirse a una superficie divisoria concreta. Se puede demostrar que para una interfase curva, la tensión interfacial toma un valor que cambia en función de qué superficie divisoria se considera[8–10]. Las más importantes superficies divisorias como se verá en Parte II son la superficie de tensión y la superficie divisoria de Gibbs. El primer tratamiento teórico que trató de caracterizar todo esto fue realizado por Tolman en 1949 en el contexto de la condensación de una gota[11], seguido posteriormente por Kondo en 1956[8]. Más tarde, Rowlinson y Widom popularizaron estos trabajos con la publicación de su libro *Molecular Theory of Capillarity*[9]. En su artículo, Tolman propuso una ecuación lineal para explicar el cambio de la tensión superficial (lo que en sólido-líquido se denomina tensión interfacial) con la curvatura. Dicho cambio dependería del valor de la tensión interfacial a coexistencia y de un parámetro conocido como longitud de Tolman que vendría dado por el límite a coexistencia de la diferencia entre las superficies divisorias de Gibbs y de tensión. En el Capítulo 1 se pone a prueba dicha ecuación en resultados de nucleación obtenidos por la técnica de Seeding para dos modelos diferentes de agua, mW[5] y TIP4P/Ice[3], así como para dos potenciales de simetría esférica, esfera dura[1] y Lennard-Jones[2]. La técnica de Seeding aprovecha el carácter crítico de la nucleación para obtener las condiciones termodinámicas y el tamaño del núcleo crítico (donde el término crítico hace referencia a que representa un máximo en la energía libre del sistema cuando se representa en función de un parámetro de orden que no debe confundirse con el término crítico referido a la existencia de correlaciones de alcance infinito en una transición de fase). En particular, se analiza la evolución temporal de una serie de semillas inmersas en fluido que son lanzadas independientemente. Aquella semilla (núcleo) que pasado un tiempo característico y dadas unas ciertas condiciones termodinámicas, la mitad de las veces crece y la mitad de las veces se deshace, se denomina núcleo crítico. Después se utiliza la Teoría Clásica de Nucleación (CNT por sus siglas en inglés)[12,13] para hallar variables como la tensión interfacial, la barrera de energía libre de Gibbs o finalmente la tasa de nucleación, la cual es una variable observable en experimentos. La deducción de Tolman se realizó para procesos isotérmicos pero en este trabajo estudiamos el efecto de la curvatura tanto en cambios isotérmicos como isobáricos. En todos los casos se observa una tendencia lineal con el inverso del radio de curvatura de acuerdo a la ecuación de Tolman. Además se observa, que para la cristalización de un modelo dado, la longitud de Tolman apenas varía por lo que suponerla constante es una aproximación razonable (entre sistemas sí cambia). De este modo, uno puede utilizar la técnica de Seeding para una isóbara o isoterma dada y posteriormente estimar otras suponiendo la longitud de Tolman constante siempre y cuando se conozca el valor de la tensión interfacial a coexistencia. Este protocolo fue puesto a prueba en el caso del Lennard-Jones. En los Capítulos siguientes (2, 3 y 4) nos ceñimos a la esfera dura para poder ahondar en la física del núcleo crítico con la intención de sentar las bases que en el futuro permitan aplicar lo aprendido a otros sistemas.

En el Capítulo 2 se recoge la extensión de la técnica de Seeding, denominada NVT-Seeding[14], aplicada a la cristalización. Dicha técnica se inició como parte de la tesis doctoral de otro integrante del grupo con aplicación en cavitación[14] y en esta tesis de forma paralela se desarrolló para cristalización comprobando que en ambos casos la metolodogía funciona de forma análoga. Como se ha mencionado anteriormente, el Seeding se basa en aprovechar que un núcleo crítico es inestable cristalizando la mitad de las veces y fundiendo la otra mitad. Esto se debe a que el tamaño del núcleo crítico viene determinado por el potencial químico de la fase metaestable el cual es constante en el Seeding ya que se utiliza el colectivo isotérmico-isobárico (NpT). Una vez que el núcleo supera cierto tamaño crítico, dado un cierto potencial químico en la fase metaestable, entonces éste continua creciendo al haber superado la barrera de energía libre (y convertirse en supercrítico). A la inversa, es decir, teniendo un tamaño menor al crítico, ocurriría lo contrario ya que el cluster sería subcrítico al no superar la barrera de energía libre. En cambio, algunos estudios revelaban que era posible tener una interfase curva en equilibrio si se utilizaba el colectivo canónico (NVT)[10,15,16]. En dicho colectivo el potencial químico de la fase metaestable no es constante durante la formación del núcleo crítico. Por ello decidimos insertar semillas como en la técnica de Seeding pero simularlas en el colectivo NVT buscando su estabilización. Finalmente, logramos estabilizar diez núcleos de esfera dura[17]. Ciertamente, los cristales esféricos no fueron estables de forma indefinida sino que en alguna ocasión fundieron o se transformaron en cilindro o en interfase plana como era de esperar en base a los estudios de Binder y colaboradores quienes han estudiado interfases curvas en equilibrio en el colectivo NVT durante los últimos años[10,15,16]. Después, estás configuraciones estables con núcleos esféricos fueron lanzadas en el colectivo NpT demostrando ser críticas. Es decir, se pudo lograr un equilibrio estable por parte del núcleo crítico. Esto se debe a que, aunque la temperatura del líquido es constante, ante variaciones en el tamaño del cluster sólido, el potencial químico del líquido sí cambia debido a los cambios en la presión de la fase líquida fruto de la diferencia de densidades entre las fases sólida y líquida y la necesidad de mantener N y V constantes en este colectivo[18,19]. Otro colectivo al que sería posible extender la técnica de Seeding es el isobárico-isoentálpico (NpH)[20] y previsiblemente el microcanónico (NVE) donde el potencial químico tampoco es constante. Los resultados de este trabajo comparan muy bien con los obtenidos previamente por la técnica de Seeding tradicional pero con la ventaja de poder estudiar en detalle el núcleo crítico al ser éste estable durante un tiempo considerable. En concreto, utilizamos ésta ventaja para medir con suficiente estadística el radio del núcleo en sus respectivas superficies divisorias (de tensión y de Gibbs). Esto nos permitió verificar la definición de la longitud de Tolman[21], ya que obtuvimos la diferencia entre estas superficies en función de la curvatura y extrapolamos al caso de la interfase plana. El valor obtenido por este procemiento encaja a la perfección con el obtenido en el Capítulo 1 al ajustar nuestros datos a una recta y comparar con la ecuación de Tolman. Este trabajo abre la posibilidad de estudiar un núcleo crítico cristalino en detalle. En el siguiente capítulo vemos otro ejemplo de ello.

Otra ecuación fundamental donde la tensión interfacial es protagonista y que la técnica de Seeding extendida permite comprobar es la ecuación de Young-Laplace. En ella, la tensión interfacial se relaciona con el cambio de presión entre dos fases separadas por una interfase curva de un determinado radio. Dicha ecuación se cumple en los núcleos críticos, los cuales pueden ser estables en determinadas condiciones como pudo verse en el Capítulo 2. Pese al renombre de esta ecuación, y de haber sido comprobada para interfases esféricas entre dos fases fluidas, su aplicación a la interfase esférica entre un sólido y un líquido no había sido estudiada en detalle. En el Capítulo 3 analizamos detalladamente tres de los núcleos estables de esfera dura del Capítulo 2. Para cada uno de los núcleos lanzamos nuevas trayectorias almacenando una gran cantidad de configuraciones las cuales nos permitieron medir el tensor de presiones desde el centro del núcleo. De esta manera obtuvimos una descripción microscópica de la distribución de la presión en el sistema. En concreto pudimos demostrar que, dado que tenemos equilibrio[22], la presión promedio del sistema es igual a la de la fase externa, pero la observación más importante fue que la presión del núcleo de esfera dura es menor que la del líquido que lo rodea. Esto se había observado muy recienmente en el caso del Lennard-Jones[23]. En el contexto de la ecuación de Young-Laplace esto es contraintuitivo ya que indicaría una tensión interfacial negativa lo cual impediría la formación de una barrera de energía libre de acuerdo a la CNT. Realmente lo que ocurre es que en sólidos, la diferencia de presiones viene dada por el estrés y no por la tensión interfacial. El estrés sí puede ser negativo pero la tensión interfacial no. ¿Cómo aplicar entonces la ecuación de Young-Laplace a un sistema microscópico? Tolman en su trabajo sobre la tensión superficial en la condensación de una gota[11] ya nos dio una pista al indicar que para gotas muy pequeñas había que utilizar las propiedades correspondientes a una fase macroscópica sin estrés ni defectos con el mismo potencial químico que la fase externa debido a que Gibbs desarrolló su formalismo suponiendo en su modelo que las propiedades de la fase interna (el sólido en nuestro caso) eran las mismas que las de una fase macroscopica sin interfase ni estrés. Posteriormente, Mullins completó la descripción de forma teórica[24]. En el caso de la cristalización de esfera dura este tratamiento es necesario. Dado que el líquido no está expuesto a estrés, podemos considerarlo fase macroscópica y hallar su potencial químico. Conocido éste y dada la condición de igualdad de potenciales químicos (que debe satisfacerse en un sistema que está en equilibrio) podemos hallar la presión del núcleo de acuerdo a una fase virtual macroscópica sin estrés ni interfase que esta vez sí resulta superior a la del líquido y conduce a la tensión interfacial mediante la ecuación de Young-Laplace. Esta presión suele denominarse “termodinámica”. Una consecuencia importante de este estudio es la siguiente. Puesto que el núcleo es estable, su potencial químico también es igual al de la fase fluida. Dado que su presión real, también llamada “mecánica”, no corresponde a la que tendría un sólido macroscópico sin interfase ni estrés cuyo potencial químico fuera idéntico al de la fase fluida externa, la estructura interna del nucleo crítico debe presentar diferencias estructurales con respecto a la de la fase macroscópica utilizada en la descripcion teórica.

Resulta evidente llegados a este punto que la técnica de Seeding (especialmente en su versión NVT) puede resultar tremendamente útil para estudiar en detalle los núcleos críticos. Sin embargo, los núcleos estabilizados se obtuvieron mediante prueba y error. En el Capítulo 4 se aplica la termodinámica de interfases curvas[9] para describir el cambio en la energía libre del sistema como consecuencia del crecimiento de un sólido.

Aunque este formalismo es, en principio, sólo válido para núcleos en equilibrio termodinámico (estables o inestables/críticos), decidimos utilizarlo de forma aproximada para describir el sistema, de forma teórica, también cuando no hay equilibrio termodinámico. Programando este formalismo alimentado con algunos cálculos de simulación en lo referido a las ecuaciones de estado y los efectos de curvatura, pudimos reproducir los resultados de simulación para los sistemas del Capítulo 2 incluyendo no sólo núcleos esféricos sino también cilíndricos e interfases planas. Mediante este formalismo aproximado pudimos describir cualitativamente el cambio en la energía libre del sistema, observando diferentes mínimos locales correspondiendo al líquido homogéneo o esfera, cilindro o interfase plana en contacto con líquido. En estos mínimos de energía los potenciales químicos de las dos fases (sólido y fluido) se igualan de acuerdo a la condición de equilibrio[22]. Después de validar nuestro programa lo utilizamos para visualizar cómo cada variable del sistema afecta a la estabilidad de los núcleos críticos y para encontrar bajo qué condiciones una determinada configuración (líquido homogéneo o esfera/cilindro/plano en contacto con líquido) es la más estable en el sistema. Pudimos observar que para lograr esferas eran necesarios sistemas muy grandes. Este trabajo predice que bajo ciertas condiciones es posible tener un núcleo crítico estable durante tiempos indefinidos en ausencia de fuerzas externas. También, que es posible tener un líquido subenfriado como configuración más estable debido al tamaño finito en lo que se conoce como “superestabilización”[25,26]. Con este trabajo se concluye la etapa enfocada a profundizar en el núcleo crítico utilizando el modelo de esfera dura. Se ha extendido la técnica de Seeding para estabilizar núcleos cristalinos que equivalen a núcleos críticos sobre los cuales se han verificado la ecuación de Tolman y la de Young-Laplace. Posteriormente se ha desarrollado un formalismo aproximado basado en la termodinámica de interfases curvas para describir teóricamente todo lo anterior. Este conjunto de trabajos sienta las bases para su aplicación al agua.

Con el Cápitulo 4 queda concluido el estudio la de nucleación en esferas duras. No obstante, a lo largo de dicho estudio se ha podido desarrollar técnicas y profundizar en los formalismos que trascienden a la cristalización. En el siguiente capítulo de resultados, Capítulo 5, se aplica lo aprendido hasta el momento a la condensación de gotas y además se compara con la cavitación de burbujas[27], cuya investigación se desarrolló de forma paralela como parte de otra tesis doctoral dirigida en el grupo[14]. En este trabajo se estabilizaron gotas de distinto tamaño en el colectivo NVT y se demostró que eran críticas en el colectivo NpT. Se obtuvieron distintas variables como tensión superficial, barrera de energía libre y tasa de nucleación incluyendo un par de estados obtenidos por la técnica de Umbrella Sampling. También se puso a prueba la ecuación de Tolman y se comprobó que la presión promedio del sistema coincidía con la de la fase externa y que en general la presión del núcleo era prácticamente la misma si se obtenía con un procecimiento termodinámico o mecánico, demostrando que en fluidos, por lo general, la tensión (proporcional a la diferencia de presiones entre fases donde la presión interna es la de tipo termodinámico) y el estrés (proporcional a la diferencia entre presiones de ambas fases donde la presión interna es la real del sistema o mecánica) son la misma magnitud (a diferencia de la interfase sólido-liquido). Todos estos resultados, se obtuvieron también para las burbujas y sorprendentemente se pudo comprobar que gota y burbuja son equivalentes a efectos de nucleación. Para una temperatura concreta y un radio concreto, gota y burbuja son indistinguibles desde el punto de vista de la nucleación pese a que la presión y densidad de las mismas difieran. Solamente, en la tasa de nucleación observamos una pequeña discrepancia fruto de un componente cinético que las hace ligeramente diferentes. Luego, invertir las fases fluidas emergente y metaestable, al menos, para el caso del Lennard-Jones tiene un efecto insignificante.

En el Capítulo 6 se trata el último caso de la nucleación a la vez que se comienza una serie de estudios dedicados exclusivamente al agua. En concreto, investigamos la nucleación de hielo a partir de agua subenfriada a presiones negativas. Dado que el segundo punto crítico del agua ha captado gran parte de los recursos científicos dedicados al estudio de la cristalización del agua y éste ocurre a relativa alta presión, el regimen de presiones negativas había recibido menos atención[28,29]. Por ello, otra anomalía del agua había pasado desapercibida hasta este trabajo[30]. Aquí mostramos que la nucleación de hielo a presión negativa implica comportamientos no monótonos en distintas variables. Para ello utilizamos la técnica de Seeding[31,32] lo que nos permite obtener variables claves para describir la nucleación como son la tensión interfacial, la barrera de energía libre y la tasa de nucleación, las cuales, a lo largo de tres isotermas presentan un reentrante a presiones negativas. Este fenómeno estaría relacionado con el reentrante que también obtenemos en la curva de coexistencia. El papel de la presión es clave en la nucleación. Un reciente estudio demostró que las altas presiones dificultan el proceso de nucleación debido a un aumento considerable de la tensión interfacial[6]. Este trabajo sugiere que no es posible acelerar la nucleación indefinidamente siguiendo el procedimiento inverso ya que a presiones negativas hay un punto de retorno en la tensión interfacial (entre otras variables). De hecho, sería posible utilizar "altas" presiones negativas para ralentizar la nucleación aunque con menor impacto del que lo hacen las altas presiones.

A continuación, en el Capítulo 7, nos centramos en la última etapa del proceso de cristalización. Concretamente, se estudia la velocidad de crecimiento de hielo en función del subenfriamiento del agua. Este estudio es relevante porque la comunidad se debatía fruto de una discrepancia en la velocidad de crecimiento del hielo entre algunos experimentales y simuladores como se recoge en Ref.[33]. Mientras que los simuladores observaban un máximo en la velocidad de crecimiento en función del subenfriamiento, algunos resultados experimentales no eran concluyentes y otros mostraban una tendencia monótona creciente. En simulación es habitual utilizar un termostato. Es decir, usar un algoritmo que mantiene la temperatura del sistema constante mediante un ajuste de la velocidad de las moléculas del sistema. El uso de este tipo de algoritmos era, según parte de la comunidad científica, responsable de las discrepancias. Por ello, decidimos medir la velocidad de crecimiento de hielo sin termostato ni barostato[34]. No obstante, necesitabamos mantener las condiciones termodinámicas lo más estables posible para poder determinar en que condiciones estábamos midiendo. Por eso, preparamos un gran baño de agua en contacto con un bloque de hielo y medimos su velocidad de crecimiento en el colectivo microcanónico (NVE). De esta manera obtuvimos resultados muy similares a los de simulaciones con termostato. Además pudimos contextualizar estos resultados con una expresión teórica conocida como la ecuación de Wilson-Frenkel. Según esta teoría la velocidad de crecimiento del hielo resulta de la competición entre la tendencia a la formación del hielo (el driving force en inglés) dado por la diferencia de potenciales químicos entre ambas fases, que aumenta al subenfriar, y del otro lado la difusión de moléculas de agua hacia la superficie del hielo, que disminuye al bajar la temperatura. Fruto de estas dos tendencias antagónicas en el subenfriamento surge la aparición del máximo en la velocidad de crecimiento del hielo. Paralelamente a esta investigación, surgieron unos resultados experimentales que concordaban con los obtenidos por simulación[35], zanjando así en conjunto el debate sobre el máximo en la velocidad de crecimiento del hielo.

El último capítulo de resultados lo protagoniza el agua subenfriada (Capítulo 8), fase a partir de la cual emerge la nucleación de hielo. El agua presenta numerosas peculiaridades que la convierten en un líquido anómalo pero si además se encuentra a bajas temperaturas el número de anomalías aumenta[36]. A fin de explicar estas propiedades se especuló en el pasado sobre la existencia de dos fases líquidas diferentes en el agua, una más densa que la otra, las cuales pueden tener una coexistencia entre si que acaba en un punto crítico[37–44]. En este trabajo[45], utilizamos un modelo que recoge esta descripción de dos estados. Dicho modelo lo ajustamos a datos de simulación que previamente obtenemos. Concretamente nos enfocamos en las propiedades dinámicas del agua. Normalmente, los líquidos sometidos a presión tienden a disminuir su difusión. En el caso del agua, a temperatura T constante, hay un intervalo de presiones comprendidas entre un mínimo y un máximo en el coeficiente de difusión D donde ocurre el fenómeno opuesto. Aunque esta anomalía había sido descrita previamente para el coeficiente de difusión[46,47], en este trabajo por simulación se describe sobre un gran intervalo de presiones y temperaturas a la vez que se incluye el estudio a otra propiedad dinámica, la viscosidad η, la cual había recibido menos atención, probablemente por lo costoso de su medición. En el caso de la viscosidad, se observa que hay un intervalo de presiones comprendidas entre un máximo y un mínimo en la viscosidad donde ésta disminuye con la presión. Conocer la viscosidad y el coeficiente de difusión nos permite a su vez evaluar la ecuación de Stokes-Einstein que relaciona la velocidad a la que las moléculas difunden con el tamaño de las mismas. Esta expresión predice que la cantidad $D\eta/T$ es constante pero en este trabajo demostramos que D y η se desacoplan al bajar la temperatura lo suficiente invalidando la relación de Stokes-Einstein para el agua subenfriada a partir de una cierta temperatura. El modelo propuesto, basado en la hipótesis de la existencia de dos estados para describir el agua, pudo ajustarse a dichos datos de propiedades dinámicas. Posteriormente a esta publicación, la comunidad científica siguió avanzando en esta idea hasta el punto de que se ha podido demostrar la existencia de un punto crítico líquido-líquido tanto por simulación de modelos realistas (TIP4P/Ice y TIP4P/2005)[48] como experimentalmente[49], confirmando así la existencia de las dos fases de agua líquida que en este trabajo pudimos modelizar[45].

Tras recorrer esta serie de capítulos, se encuentra un apartado con conclusiones, Parte IV, donde se hace una retrospectiva y se enumeran los mayores hitos de la tesis.

Bibliografía

[1] J Jover, AJ Haslam, A Galindo, G Jackson, and EA Müller. Pseudo hard-sphere potential for use in continuous molecular-dynamics simulation of spherical and chain molecules. *The Journal of chemical physics*, 137(14):144505, 2012.

[2] Brian B. Laird, Ruslan L. Davidchack, Yang Yang, and Mark Asta. Determination of the solid-liquid interfacial free energy along a coexistence line by Gibbs-Cahn integration. *J. Chem. Phys.*, 131(11):114110, 2009.

[3] J. L. F. Abascal, Eduardo Sanz, Ramon Garcia Fernandez, and Carlos Vega. A potential model for the study of ices and amorphous water: TIP4P/Ice. 122:234511, 2005.

[4] J. L. F. Abascal and C. Vega. A general purpose model for the condensed phases of water: TIP4P/2005. 123:234505, 2005.

[5] V. Molinero, and E. B. Moore. Water modeled as an intermediate element between carbon and silicon. *The Journal of Physical Chemistry B*, 113(13):4008–4016, 2009.

[6] Jorge R. Espinosa, Alberto Zaragoza, Pablo Rosales-Pelaez, Caridad N avarro, Chantal Valeriani, Carlos Vega, and Eduardo Sanz. Interfacial free energy as the key to the pressure-induced deceleration o f ice nucleation. *Phys. Rev. Lett.*, 117:135702, 2016.

[7] JW Gibbs. The collected works, volume i, 1928.

[8] S. Kondo. Thermodynamical fundamental equation for spherical interface. *J.Chem.Phys.*, 25:662, 1956.

[9] John Shipley Rowlinson and Benjamin Widom. *Molecular theory of capillarity.* Oxford University Press, 1982.

[10] A Tröster, M Oettel, B Block, P Virnau, and K Binder. Numerical approaches to determine the interface tension of curved interfaces from free energy calculations. *J. Chem. Phys.*, 136(6):064709, 2012.

[11] Richard C Tolman. The effect of droplet size on surface tension. *The journal of chemical physics*, 17(3):333–337, 1949.

[12] Martin Volmer and A Weber. Keimbildung in übersättigten gebilden. *Zeitschrift für physikalische Chemie*, 119(1):277–301, 1926.

[13] Richard Becker and Werner Döring. Kinetische behandlung der keimbildung in übersättigten dämpfen. *Annalen der Physik*, 416(8):719–752, 1935.

[14] P Rosales-Pelaez, I Sanchez-Burgos, C Valeriani, C Vega, and E Sanz. Seeding approach to nucleation in the nvt ensemble: the case of bubble cavitation in overstretched Lennard-Jones fluids. *Phys. Rev. E*, 101:022611, 2020.

[15] Benjamin J Block, Subir K Das, Martin Oettel, Peter Virnau, and Kurt Binder. Curvature dependence of surface free energy of liquid drops and bubbles: A simulation study. *The Journal of chemical physics*, 133(15):154702, 2010.

[16] P. Koss, A. Statt, P. Virnau, and K. Binder. The phase coexistence method to obtain surface free energies and nucleation barriers: a brief review. *Mol.Phys.*, 116:2977, 2018.

[17] P Montero de Hijes, Jorge R Espinosa, Valentino Bianco, Eduardo Sanz, and Carlos Vega. Interfacial free energy and tolman length of curved solid-liquid interfaces from equilibrium studies. *J.Phys.Chem.C*, 124:8795, 2020.

[18] Arthur Jing-Min Yang. The thermodynamical stability of the heterogeneous system with a spherical interface. *The Journal of chemical physics*, 82(4):2082–2085, 1985.

[19] Anatoly I Rusanov. The thermodynamics of processes of new-phase formation. *Russ. Chem. Rev.*, 33:385–399, 1964.

[20] LA Zepeda-Ruiz, B Sadigh, AA Chernov, T Haxhimali, A Samanta, T Oppelstrup, S Hamel, LX Benedict, and JL Belof. Extraction of effective solid-liquid interfacial free energies for full 3d solid crystallites from equilibrium md simulations. *The Journal of chemical physics*, 147(19):194704, 2017.

[21] Edgar M Blokhuis and Joris Kuipers. Thermodynamic expressions for the tolman length. *J. Chem. Phys.*, 124(7):074701, 2006.

[22] J. S. Rowlinson. Thermodynamics of inhomogeneous systems. *Pure Appl. Chem.*, 65:873, 1993.

[23] KGSH Gunawardana and Xueyu Song. Theoretical prediction of crystallization kinetics of a supercooled Lennard-Jones fluid. *J. Chem. Phys.*, 148(20):204506, 2018.

[24] WW Mullins. Thermodynamic equilibrium of a crystalline sphere in a fluid. *The Journal of chemical physics*, 81(3):1436–1442, 1984.

[25] Øivind Wilhelmsen, Dick Bedeaux, Signe Kjelstrup, and David Reguera. Communication: Superstabilization of fluids in nanocontainers. *The Journal of chemical physics*, 141(7):071103, 2014.

[26] Thomas Philippe. Nucleation and superstabilization in small systems. *Physical Review E*, 96(3):032802, 2017.

[27] I Sanchez-Burgos, P Montero de Hijes, P Rosales-Pelaez, C Vega, and E Sanz. Equivalence between condensation and boiling in a lennard-jones fluid. *Physical Review E*, 102(6):062609, 2020.

[28] Claudia Marcolli. Ice nucleation triggered by negative pressure. *Scientific reports*, 7(1):1–8, 2017.

[29] Edwin Roedder. Metastable superheated ice in liquid-water inclusions under high negative pressure. *Science*, 155(3768):1413–1417, 1967.

[30] Valentino Bianco, P Montero de Hijes, Cintia P Lamas, Eduardo Sanz, and Carlos Vega. Anomalous behavior in the nucleation of ice at negative pressures. *Physical Review Letters*, 126(1):015704, 2021.

[31] Jorge R. Espinosa, Carlos Vega, Chantal Valeriani, and Eduardo Sanz. Seeding approach to crystal nucleation. *J. Chem. Phys.*, 144:034501, 2016.

[32] E. Sanz, C. Vega, J. R. Espinosa, R. Caballero-Bernal, J. L. F. Abascal, and C. Valeriani. Homogeneous ice nucleation at moderate supercooling from molecular simulation. *J. Am. Chem. Soc.*, 135(40):15008–15017, 2013.

[33] Tillmann Buttersack and Sigurd Bauerecker. Critical radius of supercooled water droplets: On the transition toward dendritic freezing. *The Journal of Physical Chemistry B*, 120(3):504–512, 2016.

[34] P Montero de Hijes, JR Espinosa, C Vega, and E Sanz. Ice growth rate: Temperature dependence and effect of heat dissipation. *The Journal of chemical physics*, 151(4):044509, 2019.

[35] Yuntao Xu, Nikolay G Petrik, R Scott Smith, Bruce D Kay, and Greg A Kimmel. Growth rate of crystalline ice and the diffusivity of supercooled water from 126 to 262 k. *Proceedings of the National Academy of Sciences*, 113(52):14921–14925, 2016.

[36] Rui Shi and Hajime Tanaka. The anomalies and criticality of liquid water. *Proceedings of the National Academy of Sciences*, 117(43):26591–26599, 2020.

[37] Wilhelm Conrad Röntgen. Ueber die constitution des flüssigen wassers. *Annalen der Physik*, 281(1):91–97, 1892.

[38] Peter H Poole, Francesco Sciortino, Ulrich Essmann, and H Eugene Stanley. Phase behaviour of metastable water. *Nature*, 360(6402):324–328, 1992.

[39] Osamu Mishima and H Eugene Stanley. The relationship between liquid, supercooled and glassy water. *Nature*, 396(6709):329–335, 1998.

[40] Jeremy C Palmer, Fausto Martelli, Yang Liu, Roberto Car, Athanassios Z Panagiotopoulos, and Pablo G Debenedetti. Metastable liquid–liquid transition in a molecular model of water. *Nature*, 510(7505):385–388, 2014.

[41] Hajime Tanaka. Simple physical explanation of the unusual thermodynamic behavior of liquid water. *Physical review letters*, 80(26):5750, 1998.

[42] Hajime Tanaka. Simple physical model of liquid water. *The Journal of Chemical Physics*, 112(2):799–809, 2000.

[43] Lokendra P Singh, Bruno Issenmann, and Frédéric Caupin. Pressure dependence of viscosity in supercooled water and a unified approach for thermodynamic and dynamic anomalies of water. *Proceedings of the National Academy of Sciences*, 114(17):4312–4317, 2017.

[44] Hajime Tanaka. A new scenario of the apparent fragile-to-strong transition in tetrahedral liquids: Water as an example. *Journal of Physics: Condensed Matter*, 15(45):L703, 2003.

[45] P Montero de Hijes, E Sanz, L Joly, C Valeriani, and F Caupin. Viscosity and self-diffusion of supercooled and stretched water from molecular dynamics simulations. *J. Chem. Phys.*, 149:094503, 2018.

[46] FX Prielmeier, EW Lang, RJ Speedy, and H-D Lüdemann. Diffusion in supercooled water to 300 mpa. *Physical review letters*, 59(10):1128, 1987.

[47] Manish Agarwal, Mohammad Parvez Alam, and Charusita Chakravarty. Thermodynamic, diffusional, and structural anomalies in rigid-body water models. *The Journal of Physical Chemistry B*, 115(21):6935–6945, 2011.

[48] Pablo G Debenedetti, Francesco Sciortino, and Gül H Zerze. Second critical point in two realistic models of water. *Science*, 369(6501):289–292, 2020.

[49] Kyung Hwan Kim, Katrin Amann-Winkel, Nicolas Giovambattista, Alexander Späh, Fivos Perakis, Harshad Pathak, Marjorie Ladd Parada, Cheolhee Yang, Daniel Mariedahl, Tobias Eklund, et al. Experimental observation of the liquid-liquid transition in bulk supercooled water under pressure. *Science*, 370(6519):978–982, 2020.

Parte II

Fundamentos

Capítulo 1

Fundamento Teórico

Este apartado sirve de introducción teórica para la tesis ya que se resumen algunos conceptos de interés como el diagrama de fases del agua, el cálculo de propiedades dinámicas, los fundamentos de la termodinámica de interfases curvas y su relación con la Teoría Clásica de Nucleación así como las expresiones de los potenciales de interacción de los modelos utilizados.

1.1. Agua subenfriada

Un líquido es metaestable cuando se encuentra en condiciones termodinamicas (por ejemplo, presión y temperatura) donde otra fase es más estable que él. Un ejemplo es el agua subenfriada donde encontramos la fase líquida durante tiempos largos (pero no infinitos) a temperaturas por debajo de la temperatura de fusión del hielo a la presión considerada. Una forma de ver esto es con un diagrama de fases donde gráficamente quedan delimitadas las zonas donde se muestra la fase estable (aquella con menor potencial químico) para cada valor de las variables intensivas presión p y temperatura T. A continuación se muestra el diagrama de fases experimental y acorde al modelo TIP4P/2005[1]. Como se puede ver en Fig. 1.1, a cada temperatura y presión existe una única fase que es la fase de equilibrio. Además, en el caso del hielo hay distintos polimorfos los cuales tienen sus respectivas zonas de equilibrio. Si el agua líquida se enfría más allá de la curva que la separa, por ejemplo, del hielo I_h, entonces será agua subenfriada en tanto que no cristalice. Dicha cristalización puede desencadenarse mediante un evento de nucleación.

1.2. Propiedades de transporte

En esta sección se describen las ecuaciones clave y la metodología para calcular el coeficiente de difusión D y la viscosidad η en una simulación molecular. En primer lugar, D tiene una expresión sencilla y su coste computacional es menor. Para hallarlo es necesario calcular el desplazamiento cuadrático medio en el sistema $\langle(\mathbf{r}(t)-\mathbf{r}(0))^2\rangle$ ya que se cumple la siguiente ecuación

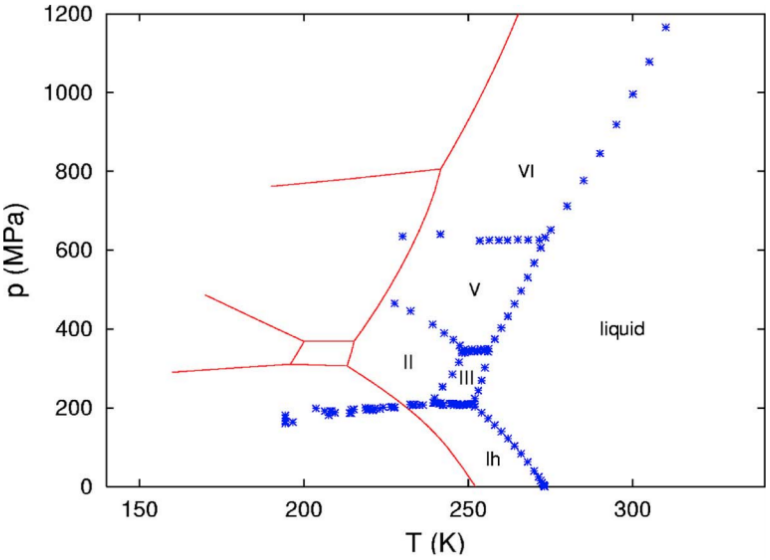

Figura 1.1: Diagrama de fases del agua. Resultados experimentales en azul y por simulacion del modelo TIP4P/2005 en rojo. Esta figura está tomada de Ref.[1].

$$\langle(\mathbf{r}(t)-\mathbf{r}(0))^2\rangle = 6Dt \tag{1.1}$$

donde t es el tiempo. Por lo tanto, calculando el desplazamiento cuadrático medio en la simulación y ajustando los resultados a una recta es posible obtener D dividiendo la pendiente por seis. Es importante notar que a tiempos cortos el sistema puede no comportarse de forma difusiva. De hecho, realmente D se define así

$$D = \lim_{t\to\infty} \frac{1}{6tN} \sum_{i=1}^{N} |\mathbf{r}(t)-\mathbf{r}(0)|^2 \tag{1.2}$$

pero dado que no podemos simular un tiempo infinito debemos asegurarnos que el sistema alcanza un régimen difusivo y que el tiempo de simulación en dicho régimen es suficiente para tener buena estadística. Una forma de ver si se ha llegado al régimen difusivo es tomar logaritmos y ajustar a una recta

$$log[\langle(\mathbf{r}(t)-\mathbf{r}(0)^2\rangle] = log(t) + c_1 \tag{1.3}$$

donde $c_1 = log(6D)$. Si se obtiene pendiente igual a uno, entonces el régimen es difusivo y se puede hallar D. No obstante, D sufre de un ligero efecto de tamaño finito en las simulaciones que usan condiciones periódicas de contorno. Se ha comprobado teóricamente y mediante simulaciones[2,3], que se puede corregir este valor para obtener el de un líquido infinito con la siguiente expresión

$$D = D_{PBC} + 2.837\frac{kT}{6\pi\eta L_{box}} \tag{1.4}$$

donde D_{PBC} es el coeficiente de difusión para el sistema finito, D para el infinito, k es la constante de Boltzmann, T la temperatura, η la viscosidad y L_{box} la longitud de la caja de simulación. Como puede comprobarse, para corregir el coeficiente de difusión es necesaria otra propiedad dinámica, la cual no sufre de efectos de tamaño finito, esta es la viscosidad. El cálculo de la misma tiene una mayor complejidad y coste computacional. Para obtener η se puede usar la fórmula Green-Kubo que relaciona la viscosidad con la función de autocorrelación de los términos no diagonales del tensor de presiones $\mathbf{p}$[4]. Es decir,

$$\eta = \frac{V}{kT}\int_0^\infty \langle p_{ij}(t_0)p_{ij}(t_0+t)\rangle dt \tag{1.5}$$

donde V es el volumen del sistema y p_{ij} representa un elemento no diagonal del tensor de presiones. Dado que el sistema, en principio, es isotrópico, p_{xy}, p_{xz} y p_{zy} son equivalentes. Así mismo, debido a la invarianza rotacional los términos $(p_{xx} - p_{yy})/2$, $(p_{yy} - p_{zz})/2$, $(p_{xx} - p_{zz})/2$, $p_{xx} - (p_{xx} + p_{yy} + p_{zz})/3$, $p_{xx} - (p_{xx} + p_{yy} + p_{zz})/3$ y $p_{xx} - (p_{xx} + p_{yy} + p_{zz})/3$ también son equivalentes por lo que la viscosidad se puede promediar sobre estos nueve términos lo que permite lograr mayor exactitud en el resultado final[5].

1.3. Termodinámica de interfases curvas

A continuación se presenta el formalismo de la termodinámica de interfases curvas en equilibrio desarrollado por Tolman[6], Kondo[7], Mullins[8]. Se considera el caso de una interfase curva dada por dos fases que por simplicidad y relevancia para este trabajo corresponden al caso de una esfera de fase α, rodeada de la fase β. Por simplicidad consideraremos un sistema monocomponente, además, en esta tesis no se han estudiado mezclas sino sólo sustancias puras. El sistema total se encuentra a número total de partículas N, volumen V y temperatura T constantes. Siguiendo el formalismo de Gibbs, estas fases son homogéneas hasta la interfase la cual contribuye termodinámicamente (términos de exceso) pero no tiene volumen, por lo tanto se tiene que el numero de partículas en el sistema, N, viene dado por

$$N = N_\alpha + N_\beta + N_{exc} \tag{1.6}$$

y el volumen V por

$$V = V_\alpha + V_\beta \tag{1.7}$$

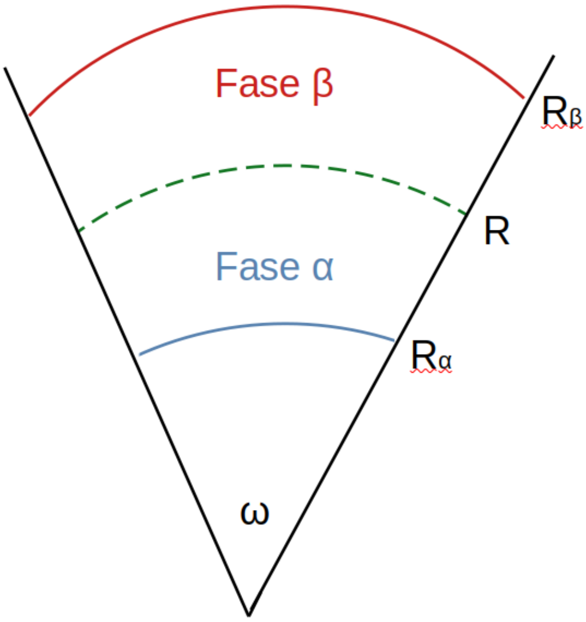

Figura 1.2: Esquema de la interfase curva desde un ángulo sólido ω. Hay dos fases α (interna) y β externa. Se contempla la arbitrariedad en la definición de la superficie divisoria determinada por R.

De acuerdo al esquema en Fig. 1.2 se describe el sistema desde el origen de la fase esférica mediante una sección cónica de ángulo sólido ω. En base a dicho esquema se tiene

$$A = \omega R^2 \tag{1.8}$$

$$V_\alpha = \frac{1}{3}\omega[R^3 - R_\alpha^3] \tag{1.9}$$

$$V_\beta = \frac{1}{3}\omega[R_\beta^3 - R^3] \tag{1.10}$$

donde A es el area interfacial, R es la localización de la interfase y R_α y R_β delimitan las fases de forma generalizada.

Siguiendo la estructura matemática del formalismo termodinámico tenemos el radio de la fase esférica R como variable extensiva. Gibbs utilizó el coeficiente denominado C para conjugar a dicha variable y no entró a describirlo explicitamente. Esta descripción fue realizada posteriormente por Kondo (quien sugiere diferenciar entre magnitud intensiva y densidad superficial aunque a efectos prácticos no parece necesario)[7]. Su descripción se detalla a continuación siguiendo el libro de Rowlinson y Widom[9]. El cambio, a temperatura constante, en la energía libre de Helmholtz para este sistema es entonces,

$$dF = -p_\alpha dV_\alpha - p_\beta dV_\beta + \gamma dA + CdR + \mu_\alpha dN_\alpha + \mu_\beta dN_\beta + \mu_{exc} dN_{exc} \tag{1.11}$$

Por otro lado, la energía libre de Helmholtz del sistema (la cual se puede obtener integrando sobre ω, a R y T constante, la ecuación 1.11) viene dada por

$$F = -p_\alpha V_\alpha - p_\beta V_\beta + \gamma A + \mu_\alpha N_\alpha + \mu_\beta N_\beta + \mu_{exc} N_{exc} \tag{1.12}$$

Puesto que este tratamiento se realiza para una interfase curva en equilibrio, es normal ver que directamente se escribe $\mu N = \mu_\alpha N_\alpha + \mu_\beta N_\beta + \mu_{exc} N_{exc}$ donde $\mu = \mu_\alpha = \mu_\beta = \mu_{exc}$ dado que una de las condiciones de equilibrio termodinámico es la homogeneidad del potencial químico. Por lo tanto, la ecuación 1.12 se puede escribir como

$$F = -p_\alpha V_\alpha - p_\beta V_\beta + \gamma A + \mu N \tag{1.13}$$

Supongamos ahora que en un sistema físico que está en equilibrio y que se puede describir con la ecuación 1.13 se modifica de manera arbitraria la localización de la interfase. Esto no es un cambio físico puesto que el sistema no se ve modificado pero, como veremos, sí tiene un efecto sobre variables físicas. Los cambios en las variables que se deben a un cambio en la localización de la interfase para un sistema dado se denominan cambios notacionales y vienen representados con corchetes. Sea X una variable que depende de la localización de la interfase, entonces un cambio notacional en X viene dado por $[dX]$. En cambio si estudiamos cómo varía X de un sistema físico a otro, entonces viene dado por dX. Sea $X = R$ donde R es el valor de la superficie divisoria, podemos estudiar cambios físicos en el tamaño de la fase α dados por dR o cambios notacionales para un sistema dado debidos a un cambio $[dR]$. Ahora bien, hay variables que sí se ven afectadas por la localización de la superficie divisoria pero hay otras que no. En un sistema físico, F, μ, p_α, p_β y N están bien definidos y no cambian en función de donde localicemos la superficie divisoria. Recordemos que en el formalismo de Gibbs, se consideran fases homogéneas y macroscópicas donde el término macroscópico hace referencia a que se considera una fase perfecta sin estrés o defectos. En este sentido, las presiones p_α y p_β no necesariamente se corresponden con las reales del sistema. Especialmente en el caso de p_α cuando se trata de un sólido es posible que la fase esférica esté sometida a estrés teniendo una presión real diferente a la definida termodinámicamente p_α. Ahora bien, si F, μ, p_α, p_β están definidas de manera única en un sistema a N, V y T constante en el equilibrio, si cambiamos la ubicación de la interfase $[R]$, entonces V_α, V_β y A se verán afectadas y la única manera de mantener constante el valor de F es que γ cambie su valor. Conclusión, en interfases curvas, el valor de γ depende de la ubicación arbitraria de la interfase. Esto no ocurre en interfases planas en equilibrio porque en este caso $p_\alpha = p_\beta$ y porque un cambio en la ubicación de la interfase no cambia A. El valor de γ es único para una interfase plana en equilibro. Entonces, un cambio en la localización de la interfase de un sistema dado solo afecta a los términos $-p_\alpha V_\alpha - p_\beta V_\beta + \gamma A$, luego se tiene que

$$[dF] = -p_\alpha[dV_\alpha] - p_\beta[dV_\beta] + \gamma[dA] + A[d\gamma] = 0 \tag{1.14}$$

Como el volumen total V no cambia, $dV_\alpha = -dV_\beta = AdR$ y $dA = (2A/R)dR$ tanto si se considera un cambio en R físico como notacional (en el sentido de localización de la superficie divisoria). Por lo tanto, se llega a

$$p_\alpha - p_\beta = \frac{2\gamma}{R} + \left[\frac{d\gamma}{dR}\right] \tag{1.15}$$

Esta es la ecuación generalizada de Young-Laplace la cual relaciona una diferencia en presión entre dos fases α y β separadas por una interfase curva (donde α tiene geometría esférica) con la tension interfacial y la curvatura. Concretamente, esta diferencia depende de la tensión interfacial γ, de la curvatura $1/R$ y del cambio en la tensión interfacial debido a la localización de la superficie divisoria para el sistema físico definido. Además, nos permite hallar el parámetro C de la ecuación 1.11, que Gibbs dejó como arbitrario, de la siguiente forma. Dado que el sistema está en equilibrio ha de ser estable (i.e $dF = 0$) para cambios arbitrarios en cualquiera de las variables de la ecuacion 1.12. Teniendo en cuenta que $dN_\beta = -dN_\alpha - dN_{exc}$ y que, como en el cambio notacional, V no cambia, podemos escribir

$$dF = -(p_\alpha - p_\beta)AdR + \frac{2\gamma}{R}AdR + CdR + (\mu_\alpha - \mu_\beta)dN_\alpha + (\mu_{exc} - \mu_\beta)dN_{exc} = 0 \tag{1.16}$$

Es decir, $dF = 0$ para cambios infinitesimales en N_α, N_{exc} o R. Para que esto sea cierto se tienen que cumplir dos cosas:

- El potencial químico ha de ser homogeneo en el sistema heterogeneo:

$$\mu_\alpha = \mu_\beta = \mu_{exc} \tag{1.17}$$

- El cambio de presiones entre las fases debe estar dado por:

$$p_\alpha - p_\beta = \frac{2\gamma}{R} + \frac{C}{A} \tag{1.18}$$

Comparando la ecuación 1.15 con la ecuación 1.18 se puede ver que

$$C = A\left[\frac{d\gamma}{dR}\right] \tag{1.19}$$

En resumen, un sistema en equilibrio tiene potencial químico homogéneo aún siendo un sistema heterogéneo y si tiene curvatura (dada por una fase esférica α inmersa en otra fase β) debe cumplir la ecuación generalizada de Young-Laplace donde se incluyen los efectos de curvatura debidos a la localización de la superficie divisoria. Además, un cambio isotérmico en la energía libre de Helmholtz de un sistema con una interfase esférica separando dos fases α y β está dado por

$$dF = -p_\alpha dV_\alpha - p_\beta dV_\beta + \gamma dA + A\left[\frac{d\gamma}{dR}\right] dR + \mu_\alpha dN_\alpha + \mu_\beta dN_\beta + \mu_{exc} dN_{exc} \quad (1.20)$$

Procedemos ahora a deducir una ecuación que recibirá el nombre de ecuación de Gibbs-Duhem interfacial. Para ello diferenciamos la ecuación 1.12,

$$\begin{aligned} dF = &-p_\alpha dV_\alpha - V_\alpha dp_\alpha - p_\beta dV_\beta - V_\beta dp_\beta + \\ &\gamma dA + A d\gamma + \mu_\alpha dN_\alpha + N_\alpha d\mu_\alpha + \mu_\beta dN_\beta + N_\beta d\mu_\beta + \mu_{exc} dN_{exc} + N_{exc} d\mu_{exc} \end{aligned} \quad (1.21)$$

La expresion anterior puede simplificarse teniendo en cuenta que las fases α y β satisfacen las ecuaciones Gibbs-Duhem, que vienen dadas por:

$$-V_\alpha dp_\alpha + N_\alpha d\mu_\alpha = 0 \quad (1.22)$$

$$-V_\beta dp_\beta + N_\beta d\mu_\beta = 0 \quad (1.23)$$

para así obtener:

$$dF = -p_\alpha dV_\alpha - p_\beta dV_\beta + \gamma dA + A d\gamma + \mu_\alpha dN_\alpha + \mu_\beta dN_\beta + \mu_{exc} dN_{exc} + N_{exc} d\mu_{exc} \quad (1.24)$$

Comparando las ecuaciones 1.20 y 1.24 es fácil deducir que tiene que cumplirse

$$N_{exc} d\mu_{exc} + A d\gamma = A\left[\frac{d\gamma}{dR}\right] dR \quad (1.25)$$

que, utilizando derivadas parciales y dividiendo por el área A, puede convertirse en

$$\Gamma \frac{\partial \mu_{exc}}{\partial R} + \frac{\partial \gamma}{\partial R} = \left[\frac{d\gamma}{dR}\right] \quad (1.26)$$

donde el parámetro $\Gamma = N_{exc}/A$ es conocido como adsorción.

Llegados a este punto, es conveniente enumerar las dos superficies divisorias más relevantes. Por una parte está la superficie de tensión R^s, la cual viene definida como aquella que hace γ mínima para un sistema dado ante cambios en la localización de la superficie divisoria. Es decir,

$$\left[\frac{d\gamma}{dR}\right]_{R=R^s} = 0 \quad (1.27)$$

Por lo tanto, tomando simplemente μ dado que estamos en equilibrio termodinámico y se cumple que el potencial químico es homogéneo y no es necesario distinguir entre fases ($\mu = \mu_{exc}$), se tiene que

$$\Gamma^s \frac{\partial \mu}{\partial R^s} = -\frac{\partial \gamma^s}{\partial R^s} \tag{1.28}$$

$$\Gamma^s \frac{\partial \mu}{\partial R^s}\frac{\partial R^s}{\partial \mu} = -\frac{\partial \gamma^s}{\partial R^s}\frac{\partial R^s}{\partial \mu} \tag{1.29}$$

y finalmente se llega a

$$\Gamma^s = -\frac{\partial \gamma^s}{\partial \mu} \tag{1.30}$$

Por otra parte, evidentemente no menos importante, esta selección de superficie divisoria conduce a la ecuación de Young-Laplace:

$$p_\alpha - p_\beta = \frac{2\gamma^s}{R^s} \tag{1.31}$$

Este formalismo se desarrolló principalmente con la idea de una gota en contacto con vapor. Sin embargo, también funciona para una fase cristalina siempre y cuando uno tenga en cuenta que un sólido tiene estrés mientras que una fase fluida no. Es decir que p_α no es igual a la presión real (también llamada mecánica), reflejando que el sólido α está deformado con respecto a la estructura perfecta que tendría un solido ideal macroscópico a esa presión mecánica. Llamaremos sólido estresado a aquel que presentar una distorsión en su geometría con respecto a una situación modelo (que en nuestro caso será un sólido sometido a presión hidrostática). En cambio, un fluido no puede tener estrés. Si es homogeneo, y conocemos su presión entonces podemos conocer su densidad y su potencial químico En un sólido, si conocemos su presión, no necesariamente conocemos su potencial químico, ni su densidad, pues puede tener deformaciones elásticas de la red cristalina y estar estresado con respecto al sólido ideal que se encuentra bajo presión hidrostática como en el formalismo de Gibbs que estamos utilizando. Por lo tanto, para poder utilizar la ecuación de Young-Laplace en la cristalización, uno debe tomar para la presión de la fase α aquella de una fase macroscópica ideal a mismo potencial químico que la fase β. Esta afirmación, fue sugerida incluso para fases fluidas por Tolman cuando se refería a gotas muy pequeñas donde la presión real del sistema podría diferir de la obtenida por el formalismo termodinámico. Para un desarrollo teórico que sostiene estas afirmaciones puede verse el trabajo de Mullins sobre cristales en equilibrio termodinámico con un fluido[8]. En esta tesis se presenta el primer resultado numérico que demuestra que este punto de vista es el correcto.

Tomando como referencia la tensión interfacial γ^s en la superficie de tensión R^s podemos hallar como varía γ para otras localizaciones de la superficie divisoria. Para ello, igualamos las ecuaciones 1.15 y 1.31 llegando a una ecuación diferencial lineal de primer orden:

$$\Delta p = \frac{2\gamma^s}{R^s} = \frac{2\gamma}{R} + \left[\frac{d\gamma}{dR}\right] \tag{1.32}$$

donde $\Delta p = p_\alpha - p_\beta$. Como puede verse, la segunda igualdad de la ecuación 1.32 es una ecuación del tipo $y' + P(x)y = Q(x)$, con $x = R$ e $y = \gamma$ que se pueden resolver primero hallando el factor de integración $I(x) = e^{\int P(x)dx}$ para llegar a la solución con la expresión

$$y = \frac{1}{I(x)}\left[\int I(x)Q(x)dx + K\right] \tag{1.33}$$

En nuestro caso, $P(x) = 2/x$, $Q(x) = 2\gamma^s/R^s$ y el factor de integración es $I(x) = x^2$, lo que traducido a nuestras variables resulta en

$$\gamma = \frac{2x\gamma^s}{3R^s} + \frac{K}{R^2} \tag{1.34}$$

Tomando el valor de γ para $R = R^s$, es decir, γ^s, podemos hallar la constante K, obteniendo $K = \gamma^s(R^s)^2/3$. Con esto se llega finalmente a la ecuación que da la variación de γ para un sistema dado en función de la localización de la superficie divisoria. Esto es

$$\gamma[R] = \gamma^s \frac{2R^3 + (R^s)^3}{3R^2R^s} \tag{1.35}$$

Ciertamente, también se podía hallar la ecuación 1.35 de una forma más sencilla si uno se da cuenta de que

$$\left[\frac{d}{dR}\right] R^2\gamma[R] = R^2\Delta p \tag{1.36}$$

e integra la expresión respecto de $[dR^2\gamma]$ en el término de la izquierda y $[dR]$ en el de la derecha, con los límites de integración definidos $(R^s)^2\gamma^s$ y R^s y los límites arbitrarios $R^2\gamma$ y R respectivamente. A continuación empleamos este procedimiento más sencillo para generalizar la ecuación 1.35 a la geometría cilíndrica o planar (donde en esta última, presumiblemente la γ no variará). Para ello, necesitamos conocer la ecuación generalizada de Young-Laplace en función de la geometría. Siguiendo los cálculos realizados hasta el momento, es posible obtener que

$$\Delta p = (n-1)\frac{\gamma}{R} + \left[\frac{d\gamma}{dR}\right] \tag{1.37}$$

donde $n = 3, 2, 1$ para esfera, cilindro o interfase plana respectivamente, aunque para $n = 1$ (interfase plana) la igualdad se cumple porque $\Delta p = \left[\frac{d\gamma}{dR}\right] = 0$. Si ahora generalizamos la expresión 1.36 para cualquier geometría n, se tiene que

$$\left[\frac{d}{dR}\right] R^{n-1}\gamma[R] = R^{n-1}\Delta p(n, \gamma, R) \tag{1.38}$$

que integrando

$$\int_{(R^s)^{n-1}\gamma^s}^{R^{n-1}\gamma} [dR^{n-1}\gamma] = \int_{R^s}^{R} R^{n-1}\Delta p(n, \gamma, R)[dR] \tag{1.39}$$

nos permite obtener la versión generalizada para cualquier n (es decir, para geometría esférica, cilíndrica o planar)

$$\gamma[R] = \gamma^s \left[\frac{(R^s)^n + (n-1)R^n}{nR^sR^{n-1}}\right] \tag{1.40}$$

Volviendo ahora por simplicidad al caso de la esfera, resulta posible obtener analíticamente la expresión para la derivada notacional de γ derivando la ecuación 1.35. Esto es,

$$\left[\frac{d\gamma}{dR}\right] = \frac{2\gamma^s}{R^s}\left(\frac{R^3 - (R^s)^3}{3R^3}\right) \tag{1.41}$$

Conocida la expresión analítica de la derivada notacional, es posible realizar como ejercicio la demostración de la consistencia de la ecuación generalizada de Young-Laplace. Sea

$$\frac{2\gamma^s}{R^s} = \frac{2\gamma}{R} + \left[\frac{d\gamma}{dR}\right] \tag{1.42}$$

teniendo en cuenta la ecuación 1.35 y la ecuación 1.41, se tiene que

$$\begin{aligned}
&\frac{2\gamma^s}{R^s} = \frac{2\gamma^s}{R^s}\left(\frac{2R^3 + (R^s)^3}{3R^2R^s}\right) + \frac{2\gamma^s}{R^s}\left(\frac{R^3 - (R^s)^3}{3R^3}\right) \\
&1 = \frac{1}{3}\left(\frac{R^s}{R}\right)^3 + \frac{2}{3} + \frac{1}{3} - \frac{1}{3}\left(\frac{R^s}{R}\right)^3 \\
&1 = 1
\end{aligned} \tag{1.43}$$

Ahora bien, no todas las superficies divisorias son igual de interesantes. Hemos visto un caso de interés, la superficie de tensión R^s. A continuación nos referimos a otro caso interesante, la superficie divisoria de Gibbs. Esta es aquella para la cual no hay partículas de exceso por lo que también se suele llamar equimolar. Es decir, cuando

$R = R^e$ entonces $N_{exc} = 0$. Esto conduce a un resultado muy interesante como puede deducirse de la ecuación Gibbs-Duhem interfacial (ecuación 1.26 para $\Gamma = 0$). Sea $R = R^e$ y $\gamma = \gamma^e$, entonces

$$\frac{\partial \gamma^e}{\partial R^e} = \left[\frac{d\gamma}{dR}\right]_{R=R^e} \tag{1.44}$$

Es decir, para un sistema dado que describimos mediante R^e el cambio en la tensión interfacial $\gamma^e(R^e)$ debido a un cambio físico en el núcleo esférico es igual al cambio en $\gamma[R]$ cuando se realiza un cambio notacional en la ubicación de la superficie divisoria para el sistema dado en el que evalúa. Esto solo se cumple si se elige la superficie divisoria de Gibbs. Además, de acuerdo a la ecuación 1.35 y a la de Young-Laplace (ecuación 1.31) se tiene que

$$\left[\frac{d\gamma}{dR}\right]_{R=R^e} = \frac{\Delta p}{3}\left[1 - \left(\frac{R^s}{R^e}\right)^3\right] \tag{1.45}$$

Tras esta descripción detallada del efecto de curvatura en la tensión interfacial debido a la arbitrariedad en la localización de la interfase para un sistema dado, damos paso al estudio del efecto de curvatura por cambios físicos en el sistema. Cada sistema de equilibrio viene determinado por unas condiciones termodinámicas. Si, manteniendo un estado de equilibrio termodinámico, estas condiciones cambiasen , entonces también cambiaría el tamaño de la fase α y la tensión interfacial. Este cambio en γ sí es físico y no notacional. El tratamiento que sigue fue desarrollado por Tolman en 1949[6] para un cambio isotérmico. Para empezar, recurrimos a la ecuación 1.30. Dado que estudiamos sistemas en equilibrio termodinámico, μ es homogéneo en el sistema. Por lo tanto, utilizando las ecuaciones 1.22 y 1.23 se obtiene

$$d\gamma^s = -\Gamma^s d\mu = -\frac{\Gamma^s}{\rho_\alpha} dp_\alpha = -\frac{\Gamma^s}{\rho_\beta} dp_\beta \tag{1.46}$$

Si se restan las ecuaciones 1.22 y 1.23 teniendo en cuenta que el potencial químico es el mismo, esto da

$$d\mu = \frac{1}{\Delta\rho} d(\Delta p) \tag{1.47}$$

donde $\Delta\rho = \rho_\alpha - \rho_\beta$. Lo que implica

$$\frac{1}{\Delta\rho} d(\Delta p) = \frac{1}{\Delta\rho} d(2\gamma^s/R^s) \tag{1.48}$$

Luego,

$$d\gamma^s = \frac{\Gamma^s}{\Delta\rho} d(\Delta p) \tag{1.49}$$

En el artículo de Tolman podemos encontrar que en una interfase curva

$$\frac{\Gamma^s}{\Delta\rho} = \delta\left(1 + \frac{\delta}{R^s} + \frac{1}{3}\frac{\delta^2}{(R^s)^2}\right) \tag{1.50}$$

con

$$\delta = R^e - R^s \tag{1.51}$$

En el mismo artículo Tolman argumenta que los términos (δ/R^s) y $(\delta/R^s)^2$ se pueden despreciar por lo que supone la diferencia δ como constante e igual al valor correspondiente a una interfase plana. Aquí hay una observación que hacer. En la interfase plana $p_\alpha = p_\beta$ y γ no tiene una variación debida a la localización de la interfase. Puesto que R^s se define como la superficie que minimiza γ, ésta es una propiedad mal definida a coexistencia. Por ello, solo podemos hablar del límite a coexistencia de $R^e - R^s$. Para no confundir, se define el parámetro $\delta_T = \text{lím}_{R^s\to\infty}(\delta) = \text{lím}_{R^s\to\infty}(R^e - R^s)$ el cual se conoce como longitud de Tolman.

De acuerdo entonces a las ecuaciones 1.49 y 1.50 e incluyendo la ecuación de Young-Laplace (ec. 1.31), se tiene

$$d\gamma^s = -\frac{2\delta_T}{R^s}\left(d\gamma^s - \frac{\gamma^s}{R^s}dR^s\right) \tag{1.52}$$

Esta ecuación diferencial tiene variables separables por lo que integrando hasta coexistencia, es decir, el límite planar donde no hay curvatura, se llega a

$$\gamma^s = \gamma_0\left(\frac{R^s}{R^s + 2\delta_T}\right) \tag{1.53}$$

Si uno expande la expresión anterior en serie de Taylor sobre δ_T en torno al valor cero y la trunca en primer orden se llega a la ecuación de Tolman

$$\gamma^s = \gamma_0\left(1 - \frac{2\delta_T}{R^s}\right) \tag{1.54}$$

donde γ_0 es la tensión interfacial a coexistencia y δ_T es la longitud de Tolman definida anteriormente como el límite a coexistencia de $\delta = R^e - R^s$. Como puede verse esta ecuación cuenta con una serie de aproximaciones. En esta tesis se pone a prueba su validez en diferentes sistemas. Con esto concluye el formalismo termodinámico de interfases curvas.

Una vez que se ha descrito el formalismo de la termodinámica de interfases curvas, se muestra su conexión con la Teoría Clásica de Nucleación (CNT).

1.4. Teoría Clásica de Nucleación

La CNT o Teoría Clásica de Nucleación trata de explicar la nucleación homogénea, esto es, la formación de una masa crítica (núcleo crítico) de fase termodinámicamente estable en el seno de otra fase metaestable. La variable clave en la nucleación es la tasa de nucleación J que se define como el número de núcleos críticos que se forman por unidad de tiempo y volumen. La CNT fue desarrollada por Volmer y Weber y también Becker y Doring[10–13] y define J como:

$$J_{CNT} = A_0 \rho_\beta \exp\left(-\frac{\Delta G_c}{kT}\right) \tag{1.55}$$

donde A_0 es un término cinético[12] y donde $\rho_\beta \exp(-\Delta G_c/kT)$ es un término termodinámico descrito normalmente con el formalismo de Gibbs. En concreto, ΔG_c es la barrera de energía libre para que se produzca la nucleación y ρ_β es la densidad de la fase externa (es decir, la que es metaestable). El término cinético de la tasa de nucleación, es decir A_0, viene dado por

$$A_0 = Zf^+ \tag{1.56}$$

donde Z es el factor de Zeldovich y f^+ es la tasa de adsorción. El factor de Zeldovich viene dado por

$$Z = \sqrt{\frac{|\Delta G(N)''|_{N_c}}{2\pi kT}} = \sqrt{\frac{p_\alpha - p_\beta}{6\pi kT \rho_\alpha N_c}} = \sqrt{\frac{p_\alpha - p_\beta}{8\pi^2 kT \rho_\alpha^2 R_c^3}} \tag{1.57}$$

donde $|\Delta G(N)''|_{N_c}$ es la curvatura de ΔG evaluada en el máximo, es decir, para $\Delta G = \Delta G_c$ siendo el número de partículas en la fase α (cuyo radio es R_c) igual a N_c donde el subíndice c hace referencia a que se trata del núcleo crítico. En cambio f^+ puede hallarse de forma rigurosa con el método de Auer y Frenkel[14]:

$$f^+ = \frac{\langle (N(t) - N(0))^2 \rangle_{N_c}}{2t} \tag{1.58}$$

es decir, midiendo la difusión de partículas en torno al núcleo crítico. Existen formas alternativas para hallar el prefactor cinético de forma aproximada. Para el caso de un núcleo cristalino en líquido[15], se puede tomar Z dado por la ecuación 1.57 pero con f^+ dado por

$$f^+ = \frac{24 D N_c^{2/3}}{\lambda^2} \tag{1.59}$$

donde λ es una longitud característica del orden del diámetro molecular correspondiente y D es el coeficiente de difusión del líquido. Para el caso de la nucleación de una gota se puede estimar f^+ con teoría cinética de gases[16], obteniendo:

$$f^+ = \sqrt{\frac{kT}{2\pi m}} \left(\frac{6\sqrt{\pi} N_c}{\rho_{liq}} \right)^{2/3} \tag{1.60}$$

donde m es la masa de las partículas y ρ_{liq} la densidad de la gota. En el caso de una burbuja, el prefactor cinético se puede estimar con el planteamiento de Blander y Katz[17]:

$$A_0 = \sqrt{\frac{(p_{vap} - p_{liq}) R_c}{\pi m}} \tag{1.61}$$

donde ρ_{vap} y ρ_{liq} son las densiades de las fases involucradas y p_{vap} y p_{liq} sus presiones.

Aunque estrictamente hablando, la CNT incluye términos cinéticos y termodinámicos, y ciertamente, J_{CNT} es una magnitud de carácter cinético, en ocasiones el término CNT se refiere solo al tratamiento teórico propuesto para obtener ΔG_c, es decir, la barrera de energía libre de Gibbs para formar un núcleo crítico. En la sección de resultados de esta tesis se muestra cómo un núcleo estable en el colectivo NVT es crítico en el NpT. Por lo tanto, debe existir una conexión entre el formalismo de interfases curvas de la sección anterior y la CNT.

A continuación se deduce el cambio en la energía libre de Gibbs cuando un núcleo esférico de la fase α se forma a presión p y temperatura T constantes en el seno de la fase β. Teniendo en cuenta que p y T son constantes, el potencial químico μ_β de la fase β también lo es pues viene determinado precisamente por esas dos variables que quedan fijas. La energía libre de Gibbs de una fase β homogénea a presión p_β está dada por:

$$G_{homogeneo} = N\mu_\beta \tag{1.62}$$

Al formarse un núcleo de fase α el sistema pasa a ser inhomogéneo. Como se verá en los resultados, el núcleo estable en el colectivo NVT es crítico en el NpT, luego podemos hallar su energía libre de Gibbs como

$$G_{inhomogeneo} = F + p_\beta V \tag{1.63}$$

donde F viene dada por la ecuación 1.13 que a continuación recordamos y sabemos que la presión del término pV que ha de sumarse a F para hallar G de acuerdo a la termodinámica ($G = F + pV$) es p_β porque la presión promedio del sistema $\langle p \rangle$ es igual a la de la fase externa cuando hay equilibrio mecánico como se verá en la sección de resultados. A continuación se muestra de nuevo la ecuación 1.13 con un matiz. De forma explícita señalizamos que la presión de la fase α es aquella que toma en ausencia de estrés o interfases cuando se encuentra al mismo potencial químico μ que la fase externa y no necesariamente debe coincidir con la presión que realmente tiene a nivel microscópico (p_α^μ). Por lo tanto

$$F = N\mu - p_\alpha^\mu V_\alpha - p_\beta V_\beta + \gamma A \tag{1.64}$$

y llegamos a

$$G_{inhomogeneo} = N\mu_\beta - p_\alpha^\mu V_\alpha - p_\beta V_\beta + \gamma A + p_\beta V \tag{1.65}$$

Conociendo las energías libres tanto de la fase metaestable homogénea como de la configuración con el núcleo crítico rodeado de fase metaestable podemos hallar la altura de la barrera de la energía libre ΔG_c, la cual determina la tasa de nucleación J_{CNT} de acuerdo a la ecuación 1.55. Esto es

$$\Delta G_c = G_{inhomogeneo} - G_{homogeneo} \tag{1.66}$$

o lo que es lo mismo

$$\Delta G_c = \gamma A - V_\alpha (p_\alpha^\mu - p_\beta) \tag{1.67}$$

La ecuación 1.67 es exacta aunque admita arbitrariedad en la localización de la superficie divisoria siempre y cuando se utilice la γ correspondiente a dicha localización. No tiene aproximaciones, solo es necesario que el núcleo crítico del colectivo NpT sea estable en el colectivo NVT. Del mismo modo que F no dependía de la localización de la superficie divisoria para un sistema dado, tampoco depende ΔG_c, ni p_α^μ, ni p_β. Por lo tanto, la localización de la superficie divisoria, que sigue siendo arbitraria al haber curvatura, de nuevo solo afecta a A, V y γ. Puesto que el núcleo crítico ocurre en el máximo del perfil de energía libre frente a un determinado parámetro de orden (típicamente una variable relacionada con el tamaño de la fase emergente α), se trata de un sistema que está en equilibrio termodinámico de tipo inestable. En cualquier caso, para el núcleo crítico se tiene que un cambio infinitesimal en la localización de la superficie divisoria $[dR]$ implica que $[d\Delta G_c] = 0$ donde los corchetes de nuevo significan un cambio notacional, es decir, el sistema físico no cambia, sólo lo hace dónde situamos la superficie divisoria entre las fases α y β. De esta manera se recupera la ecuación 1.15 obtenida en el formalismo de interfases curvas.

$$p_\alpha - p_\beta = \frac{2\gamma}{R} + \left[\frac{d\gamma}{dR}\right] \tag{1.68}$$

Si ahora consideramos R^s como superficie divisoria, entonces la ecuación 1.67 se escribiría como

$$\Delta G_c = \gamma^s (4\pi (R^s)^2) - \frac{4}{3}\pi (R^s)^3)[p_\alpha^\mu - p_\beta] \tag{1.69}$$

donde por definicion R^s es la superficie divisoria para la cual la derivada notacional de γ frente a cambios en la localización de la interfase es cero y recuperamos por tanto la ecuación de Young-Laplace

$$p_\alpha^\mu - p_\beta = \frac{2\gamma^s}{R^s} \tag{1.70}$$

Sustituyendo la ecuación 1.70 en la ecuación 1.69 se obtiene

$$\Delta G_c = \frac{1}{3}\gamma^s A^s = \frac{1}{2}V^s(p_\alpha^\mu - p_\beta) \tag{1.71}$$

donde $A^s = 4\pi(R^s)^2$ y $V^s = (4/3)\pi(R^s)^3$. La ecuación 1.71 es uno de los principales resultados de la CNT y como puede verse implica la misma condición de equilibrio (ecuación 1.15) que la termodinámica de interfases curvas cuya expresión para F (ecuación 1.13 o 1.64) hemos utilizado para conectar ambos formalismos.

Cuando se habla de CNT muchas veces se habla de la curva de energía libre y de cómo en el máximo encontramos la altura de barrera para hallar J_{CNT}. Sin embargo, la única manera de hallar la curva completa de forma rigurosa es con cálculos de energías libres con técnicas especiales como umbrella sampling[18,19], metadynamics[20], etc. De hecho, la termodinámica está planteada para sistemas en equilibrio donde, entre otras cosas, el potencial químico es homogéneo. Fuera del equilbrio, en general, se cumpliría $\mu_\alpha \neq \mu_\beta$. Aunque la termodinámica no es rigurosa fuera del equilibrio, podemos utilizar una aproximación para hallar el perfil de energía libre aunque lo realmente importante en CNT es hallar la altura del máximo y su localización con respecto a un parámetro de orden del sistema. Supongamos que γ es conocida para una determinada localización de la superficie divisoria sobre un cierto núcleo crítico. Supongamos que para las condiciones p y T del sistema, γ no cambia con el tamaño del núcleo y aproximemos el perfil de energía libre mediante estas suposiciones y la ecuación 1.67. Entonces para un radio del núcleo R el cambio en la energía libre con respecto al sistema homogéneo sería

$$\Delta G = 4\pi R^2\gamma - \frac{4}{3}\pi R^3 \Delta p^\mu \tag{1.72}$$

Tomando la derivada respecto de R e igualando a cero para hallar la condición de máximo (donde $\Delta G = \Delta G^*$), se obtiene

$$R^* = \frac{2\gamma}{\Delta p^\mu} \tag{1.73}$$

Suponiendo que γ, que es constante, es γ^s, entonces

$$R^{*s} = \frac{2\gamma^s}{\Delta p^\mu} = R^s \tag{1.74}$$

y de acuerdo a la ecuación de Young-Laplace podemos identificar que $R^{*s} = R^s$. Si sustituimos en la ecuación 1.67 los valores R^s y γ^s recuperamos ΔG_c pues tanto γ como

R están referidos a la misma superficie divisoria. Por lo tanto $R^{*s} = R^s$ y $\Delta G_c = \Delta G^{*s}$. Ahora bien, si suponemos que $\gamma = \gamma^e$, entonces

$$R^{*e} = \frac{2\gamma^e}{\Delta p^\mu} \neq R^e \neq R^s \tag{1.75}$$

como puede verse al comparar con la ecuación generalizada de Young-Laplace (ecuación 1.15). Si en la ecuación 1.67 usamos γ^e y R^e obtenemos el valor correcto de ΔG_c, sin embargo si lo que sustituimos es γ^e y R^{*e}, obtenemos un valor de ΔG en el máximo ΔG^{*e} que no coincide con la verdadera altura de la barrera ΔG_c pues γ y R no refieren la misma superficie divisoria ya que $R^e \neq R^{*e}$. Por lo tanto, la superficie divisoria correspondiente al máximo y que da un valor consistente con ΔG_c es R^s y por lo tanto la tensión interfacial de la nucleación es γ^s. Esto se explica de forma esquemática en Fig. 1.3. En ella, la curva azul describe el perfil de energía libre aproximado con $\gamma = \gamma^s$ constante y en rojo lo mismo pero con $\gamma = \gamma^e$. Como puede verse, la barrera de energía libre del sistema ΔG_c podría obtenerse tanto con $(\gamma, R) = (\gamma^s, R^s)$ como con $(\gamma, R) = (\gamma^e, R^e)$, pero cuando se supone que el valor de γ es constante y no cambia con R, si se adopta el valor de γ_s el máximo ocurre en R^s con altura ΔG_c lo cual es correcto, pero cuando se adopta el valor de γ_e el máximo ocurre en R^{*e} y su altura ΔG^{*e} es mayor que ΔG_c que es la verdadera barrera de nucleacion. Queda claro que si se supone γ constante para estimar la energia libre "fuera del equilibrio", el valor que debe tomarse es γ^s (y no γ^e).

Por lo tanto, algunas ecuaciones que describen la estabilidad de un núcleo en el colectivo NVT también describen la inestabilidad del mismo en el colectivo NpT ya que en ambos casos hay equilibrio termodinámico (aunque en el equilibrio inestable solo de manera puntual durante la nucleación). Además, se ha aclarado que cuando se utiliza la suposicion de que γ es constante durante la nucleación a p y T constantes, es γ^s el valor que debe utilizarse y que el valor de R en el máximo de ΔG es R^s. No obstante, a la hora de calcular las energías libres, cualquier superficie divisoria es válida siempre y cuando se utilice la tensión interfacial asociada a ella. Si ahora sustituimos R^s, que está dado por $R^s = (2\gamma^s)/\Delta p^\mu$, en la ecuación que da la barrera de la energía libre de nucleación de acuerdo a la CNT (ecuación 1.67), se obtiene

$$\Delta G_c = \frac{16\pi(\gamma^s)^3}{3(\Delta p^\mu)^2} \tag{1.76}$$

No obstante, está no es la expresión más común para expresar la barrera de energía libre en CNT ya que normalmente se explica con una diferencia de potencial químico entre fases dado por

$$\Delta\mu^{CNT} = \mu_\beta(p_\beta) - \mu_\alpha(p_\beta) \tag{1.77}$$

donde $\mu_\alpha(p_\beta)$ es simplemente el potencial químico de la fase α cuando ésta se encuentra a la misma presión que la fase β, es decir p_β. A continuación se deduce esa manera de

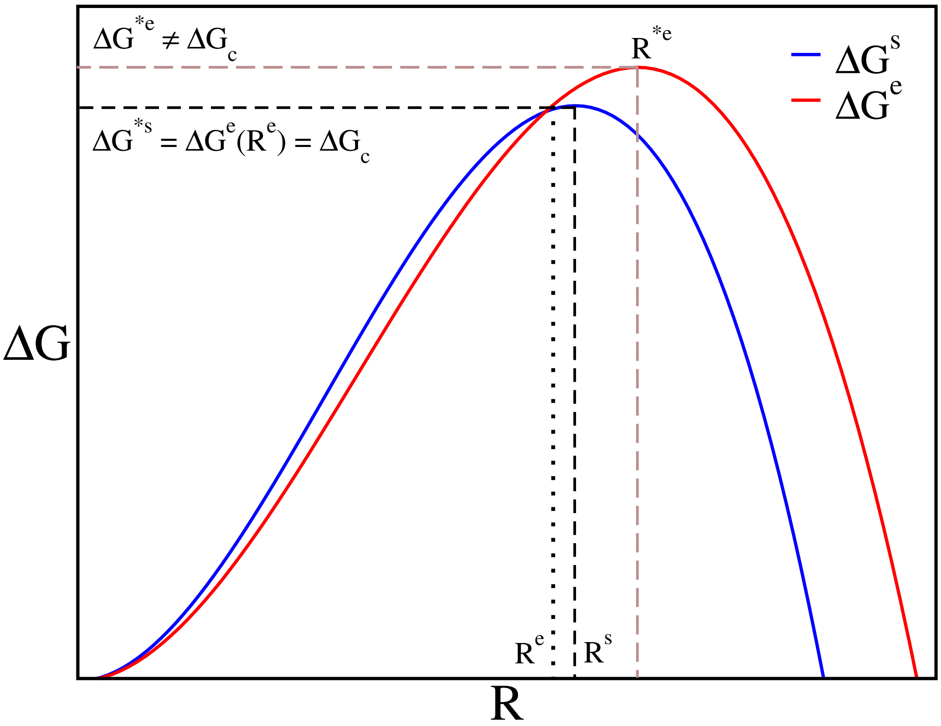

Figura 1.3: Representación esquemática de las curvas de energía libre aproximadas donde γ es constante. Cuando se considera que $\gamma = \gamma^s$ el máximo de la barrera ocurre en $R^{*s} = R^s$ y la función vale $\Delta G^{*s} = \Delta G_c$. Cuando se toma que $\gamma = \gamma^e$ el máximo de la barrera ocurre en $R^{*e} \neq R^e$ y la función vale $\Delta G^{*e} \neq \Delta G_c$. No obstante, con $\gamma = \gamma^e$, cuando $R = R^e$ entonces $\Delta G = \Delta G_c$ aunque este valor no corresponde en el máximo.

expresar la ΔG_c.

Teniendo en cuenta que la fase interna está al mismo potencial químico que la fase externa

$$\mu_\alpha(p^\mu_\alpha) = \mu_\beta(p_\beta) \tag{1.78}$$

entonces

$$\mu_\alpha(p_\beta) + \int_{p_\beta}^{p^\mu_\alpha} \nu_\alpha dp = \mu_\beta(p_\beta) \tag{1.79}$$

donde ν_α es el volumen por partícula en una fase macroscópica sin estrés ni interfase u otros defectos. Si ahora se supone que la fase α es incompresible, entonces se puede tomar ν_α como constante ante cambios en la presión, luego

$$\mu_\alpha(p_\beta) + v_\alpha \Delta p^\mu \simeq \mu_\beta(p_\beta) \tag{1.80}$$

y se llega a

$$\Delta\mu^{CNT} \simeq v_\alpha \Delta p^\mu \tag{1.81}$$

Suponiendo que se cumple de manera exacta (lo cual es una aproximación), entonces

$$\Delta\mu^{CNT} = v_\alpha \Delta p^\mu \tag{1.82}$$

o lo que es lo mismo

$$\Delta p^\mu = \rho_\alpha \Delta\mu^{CNT} \tag{1.83}$$

Si ahora sustituimos este resultado de Δp^μ en las ecuaciones 1.72 y 1.76 obtenemos las ecuaciones estándar de la CNT para expresar la barrera de energía libre:

$$\Delta G = 4\pi R^2 \gamma - \frac{4}{3}\pi R^3 \rho_\alpha \Delta\mu^{CNT} \tag{1.84}$$

$$\Delta G_c = \frac{16\pi(\gamma^s)^3}{3(\rho_\alpha \Delta\mu^{CNT})^2} \tag{1.85}$$

Aunque la ecuación 1.85 es más común cuando se habla de CNT, tal vez es preferible utilizar la ecuación 1.76 donde no se usa la aproximación de incompresibilidad. De hecho, Gibbs planteó la ecuación 1.76 para describir la altura de la barrera de energía libre[21].

Llegados a este punto es evidente que $R = R^s$ para hallar el radio donde ocurre el máximo y a la vez ser consistente con el valor de γ que nos da correctamente ΔG_c, es decir γ^s. Con esta deducción se ha demostrado la conexión entre la termodinámica de interfases curvas en equilibrio que explica la estabilización de núcleos en el colectivo NVT dados por un mínimo en la energía libre de Helmholtz, con la CNT, que explica la núcleación donde un núcleo es crítico cuando la mitad de las veces tiende a convertirse en la fase α y la otra mitad en la fase β pues se encuentra en un máximo en la energía libre de Gibbs. Es decir, en un equilibrio termodinámico inestable.

1.5. Modelos de simulación

Se comienza presentando el modelo más sencillo en cuanto a interacciones se refiere. Este es la esfera dura ya que solo tiene interacción repulsiva.

1.5.1. Esfera dura

La esfera dura es un modelo donde la interacción es puramente repulsiva y solo actúa cuando las partículas entran en contacto sin permitir que haya solapamientos. El potencial de interacción que las define es por lo tanto:

$$u_{HS}(r) = \begin{cases} \infty & r \leq \sigma \\ 0 & r > \sigma \end{cases} \tag{1.86}$$

donde σ es el diámetro de la partícula y r la distancia entre éstas. Puesto que la dinámica molecular se basa en obtener fuerzas de interacción en base a la derivada del potencial y éste potencial no es derivable, las esferas duras tienen la complicación de que necesitan algoritmos especiales que no están incorporados en paquetes de simulación optimizados de uso libre como GROMACS[22] o LAMMPS[23]. Por eso, es interesante utilizar versiones continuas que reproduzcan lo mejor posible a las esferas duras. En esta tesis se ha optado por utilizar las pseudo esferas duras[24] cuyo potencial viene dado por:

$$u_{PHS}(r) = \begin{cases} 50\left(\frac{50}{49}\right)^{49}\epsilon\left[\left(\frac{\sigma}{r}\right)^{50} - \left(\frac{\sigma}{r}\right)^{49}\right] + \epsilon & r < \left(\frac{50}{49}\right)\sigma \\ 0 & r \geq \left(\frac{50}{49}\right)\sigma \end{cases} \tag{1.87}$$

donde ϵ es la profundidad del potencial. En la esfera dura la temperatura no juega ningún papel. En la versión continua es necesario fijar una temperatura concreta para poder aproximarse a la esfera dura. En el modelo utilizado (pseudo esfera dura) esta temperatura corresponde a $T^* = T/(\epsilon/k) = 1.5$.

A pesar de ser un modelo tremendamente sencillo donde no hay interacción atractiva, las esferas duras presentan diferentes transiciones de fase incluyendo fluido-sólido[25] e incluso transción vítrea[26,27].

1.5.2. Lennard-Jones

El modelo Lennard-Jones es otro modelo arquetipo donde esta vez sí hay interacciones atractivas. Además este modelo resulta una buena aproximación para describir gases nobles de forma realista. Por otra parte, es común encontrarlo como componente de interacción en un campo de fuerzas más complejo como es el caso de los modelos TIP4P/2005 y TIP4P/Ice que se detallan a continuación. Pero primero, se muestra el potencial de interacción Lennard-Jones. Este toma distintas parametrizaciones pero aquí se considera el mismo potencial que usaron Davidchack y Laird para estudiar la tensión interfacial de un cristal en contacto con fluido en una interfase plana[28]. Por lo tanto,

$$u_{LJ}(r) = \begin{cases} 4\epsilon\left[\left(\frac{\sigma}{r}\right)^{12} - \left(\frac{\sigma}{r}\right)^{6}\right] + C_1 & r \leq 2.3\sigma \\ C_2\left(\frac{\sigma}{r}\right)^{12} + C_3\left(\frac{\sigma}{r}\right)^{6} + C_4\left(\frac{r}{\sigma}\right)^{2} + C_5 & 2.3\sigma < r < 2.5\sigma \\ 0 & 2.5\sigma \leq r \end{cases} \tag{1.88}$$

donde $C_1 = 0.016132\epsilon$, $C_2 = 3136.6\epsilon$, $C_3 = -68.069\epsilon$, $C_4 = -0.083312\epsilon$ y $C_5 = 0.74689\epsilon$.

A continuación se detallan los modelos de agua utilizados comenzando con el modelo de agua TIP4P/2005.

1.5.3. Agua TIP4P/2005

El modelo de agua TIP4P/2005[29] es un modelo rígido con cuatro sitios de interacción que consisten en tres cargas puntuales fijas y un centro Lennard-Jones. Tres de los sitios de interacción se sitúan en las posiciones del oxígeno (O) y los hidrógenos (H). El otro sitio, que se denomina sitio M, es coplanar con los sitios O y H y se sitúa en el bisector del ángulo H-O-H. La distancia O-H y el ángulo H-O-H son fijos e iguales a los valores experimentales. Es decir, 0.9572 Å y 104.52^o respectivamente. En Fig. 1.4 se muestra esquemáticamente una molécula según este modelo.

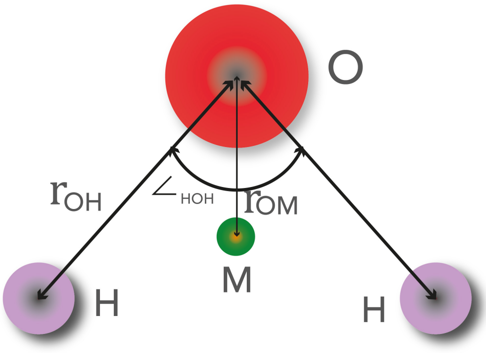

Figura 1.4: Esquema de una molécula de agua según los modelos TIP4P/2005 y TIP4P/Ice.

La energía potencial total del sistema corresponde a la suma de las interacciones entre pares de moléculas. El potencial de interacción entre éstas tiene dos contribuciones. Una de tipo Lennard-Jones y otra electroestática. En este modelo el oxígeno no porta carga pero sí contribuye al término Lennard-Jones cuya expresión viene dada por

$$u_{LJ}^{OO} = 4\epsilon\left[\left(\frac{\sigma}{r_{OO}}\right)^{12} - \left(\frac{\sigma}{r_{OO}}\right)^{6}\right] \tag{1.89}$$

donde r_{OO} es la distancia entre los oxígenos de las dos moléculas que interactúan. Por otra parte, los sitios H y M tienen carga pero no contribuyen al término Lennard-Jones. La contribución electroestática entre dos moléculas a y b viene dada por

$$u_{Coulomb} = \frac{e^2}{4\pi\varepsilon_0} \sum_{a,b} \frac{q_a q_b}{r_{ab}} \tag{1.90}$$

donde e es la carga del protón, ε_0 es la permitividad en el vacío y q_a o q_a se refieren a la carga del sitio de interacción. Por lo tanto hay cuatro parámetros que definen este potencial. Estos son la profundidad del potencial ϵ y el tamaño del centro Lennard-Jones σ, así como la carga del sitio H (o bien M pues están relacionadas como $q_H = -q_M/2$) y la distancia d_{OM} entre el oxígeno y el sitio M. Los parámetros que se encontraron como óptimos para simular fases condensadas de agua y que definen el modelo TIP4P/2005 fueron: $\epsilon/k = 93.2(\mathrm{K})$, $\sigma = 3.1589(\text{Å})$, $q_H = 0.5564(\mathrm{e})$ y $d_{OM} = 0.1546(\text{Å})$.

En Fig. 1.1 puede apreciarse su diagrama de fases el cual es cualitativamente fiel al experimental pero además está muy próximo a serlo cuantitativamente. Este modelo describe correctamente el máximo en densidad del agua que tiene lugar a 4^o Celsius, aunque su temperatura de fusión a presión ambiente es de 250 K.

1.5.4. Agua TIP4P/Ice

El modelo de agua TIP4P/Ice[30] es similar al TIP4P/2005 pero con una parametrización diferente que le otorga una mejor descripción de fases sólidas. En este modelo, las interacciones y los sitios son los mismos que en el TIP4P/2005 pero los parámetros son $\epsilon/k = 106.1(\mathrm{K})$, $\sigma = 3.1668(\text{Å})$, $q_H = 0.5897(\mathrm{e})$ y $d_{OM} = 0.1577(\text{Å})$. Su temperatura de fusión a 1 bar es 270 K, muy próxima a los 273.15 K experimentales.

1.5.5. Agua mW

Mientras que los modelos TIP4P/2005 y TIP4P/Ice, dentro de sus limitaciones, dan resultados que podrían denominarse realistas, el modelo mW es un modelo de grano grueso (*coarse grained* en inglés que indica un modelo incluso más simplificado que los modelos aproximados descritos anteriormente). No obstante, su simulación es extremadamente asequible y pese a su simplicidad describe cualitativamente muchos aspectos del agua e incluso algunos de forma cuantitativa. Este modelo de agua contiene un solo sitio de interacción pero permite formar estructuras tetrahédricas mediante interacciones de tres cuerpos. Su potencial de interacción se basa en el modelo Stillinger-Weber para el silicio. En el caso del modelo mW, el potencial de interacción viene dado por:

$$u_{mW} = \sum_i \sum_{j>1} \phi_2(r_{ij}) + \sum_i \sum_{j\neq i} \sum_{k>j} \phi_3(r_{ij}, r_{ik}, \theta_{ijk}) \tag{1.91}$$

siendo

$$\phi_2(r) = A\epsilon \left[B \left(\frac{\sigma}{r} \right)^p - \left(\frac{\sigma}{r} \right)^q \right] \exp \left(\frac{\sigma}{r - a\sigma} \right) \tag{1.92}$$

y

$$\phi_3(r, s, \theta) = \lambda\epsilon \left[cos(\theta) - cos(\theta_o) \right]^2 \exp \left(\frac{\gamma\sigma}{r - a\sigma} \right) \exp \left(\frac{\gamma\sigma}{s - a\sigma} \right) \tag{1.93}$$

donde los parámetros $A = 7.049556277$, $B = 0.6022245584$, $p = 4$, $q = 0$, y $\gamma = 1.2$ dan forma y escalan el potencial, el radio de corte reducido $a = 1.8$ asegura que todos los términos se hagan cero a una distancia $a\sigma$ y el término de la diferencia de cosenos al cuadrado con $\theta_o = 109.47^o$ favorece la estructura tetrahédrica. Por otra parte, $\lambda = 23.15$, $\epsilon = 6.189$ kcal/mol y $\sigma = 2.3925$. Este potencial tiene un coste computacional muy bajo y sirve como prototipo para posibles proyectos con agua. Uno de los mayores fallos del modelo es que predice densidades muy similares para el hielo Ih y el agua a presión ambiente y 274 K (la temperatura de fusión del modelo). Una consecuencia de esto es que la pendiente de la curva de fusión, aunque negativa (lo cual es correcto), adopta un valor enorme (lo cual es incorrecto). Este valor enorme y negativo de la pendiente es obviamente consecuencia de la ecuacion de Clausius-Clapeyron y de la enorme similitud de las densidades de hielo y agua en el modelo (en contraste con el experimento donde ambas densidades difieren en un diez por ciento aproximadamente).

A continuación comienza el apartado de resultados donde se aplican todos estos modelos.

Bibliografía

[1] J. L. F. Abascal and C. Vega. A general purpose model for the condensed phases of water: TIP4P/2005. 123:234505, 2005.

[2] In-Chul Yeh and Gerhard Hummer. System-size dependence of diffusion coefficients and viscosities from molecular dynamics simulations with periodic boundary conditions. *The Journal of Physical Chemistry B*, 108(40):15873–15879, 2004.

[3] Sami Tazi, Alexandru Boţan, Mathieu Salanne, Virginie Marry, Pierre Turq, and Benjamin Rotenberg. Diffusion coefficient and shear viscosity of rigid water models. *Journal of Physics: Condensed Matter*, 24(28):284117, 2012.

[4] Miguel Angel González and José LF Abascal. The shear viscosity of rigid water models. *The journal of chemical physics*, 132(9):096101, 2010.

[5] Ting Chen, Berend Smit, and Alexis T Bell. Are pressure fluctuation-based equilibrium methods really worse than nonequilibrium methods for calculating viscosities? *The Journal of chemical physics*, 131(24):246101, 2009.

[6] Richard C Tolman. The effect of droplet size on surface tension. *J. Chem. Phys.*, 17(3):333–337, 1949.

[7] S. Kondo. Thermodynamical fundamental equation for spherical interface. *J.Chem.Phys.*, 25:662, 1956.

[8] WW Mullins. Thermodynamic equilibrium of a crystalline sphere in a fluid. *The Journal of chemical physics*, 81(3):1436–1442, 1984.

[9] John Shipley Rowlinson and Benjamin Widom. *Molecular theory of capillarity.* Oxford University Press, 1982.

[10] M. Volmer and A. Weber. Keimbildung in ubersattigten gebilden. *Z. Phys. Chem.*, 119:277, 1926.

[11] R. Becker and W. Doring. Kinetische behandlung der keimbildung in ubersattigten dampfen. *Ann. Phys.*, 416:719–752, 1935.

[12] K. F. Kelton and A. L. Greer. *Nucleation in Condensed Matter.* Pergamon,Elsevier,Oxford, 2010.

[13] D. Kashchiev. *Nucleation: Basic Theory with Applications.* Butterworth-Heinemann, Oxford, 2000.

[14] S. Auer and D. Frenkel. Numerical prediction of absolute crystallization rates in hard-sphere colloids. 120:3015, 2004.

[15] Jorge R. Espinosa, Carlos Vega, Chantal Valeriani, and Eduardo Sanz. Seeding approach to crystal nucleation. *J. Chem. Phys.*, 144:034501, 2016.

[16] I Sanchez-Burgos, P Montero de Hijes, P Rosales-Pelaez, C Vega, and E Sanz. Equivalence between condensation and boiling in a lennard-jones fluid. *Physical Review E*, 102(6):062609, 2020.

[17] P Rosales-Pelaez, MI Garcia-Cid, C Valeriani, C Vega, and E Sanz. Seeding approach to bubble nucleation in superheated lennard-jones fluids. *Physical Review E*, 100(5):052609, 2019.

[18] S. Auer and D. Frenkel. Prediction of absolute crystal-nucleation rate in hard-sphere colloids. *Nature*, 409:1020, 2001.

[19] S. Auer and D. Frenkel. Quantitative prediction of crystal-nucleation rates for spherical colloids: A computational approach. *Annu. Rev. Phys. Chem.*, 55:333, 2004.

[20] Alessandro Barducci, Giovanni Bussi, and Michele Parrinello. Well-tempered metadynamics: A smoothly converging and tunable free-energy method. *Phys. Rev. Lett.*, 100:020603, Jan 2008.

[21] J Gibbs. *The Collected Works. Vol. 1. Thermodynamics.* Yale University Press, 1948.

[22] B. Hess, C. Kutzner, D. van der Spoel, and E. Lindahl. Algorithms for highly efficient, load-balanced, and scalable molecular sim ulation. *J. Chem. Theory Comput.*, 4:435–447, 2008.

[23] S. Plimpton. Fast parallel algorithms for short-range molecular dynamics. *J. Comput. Phys.*, 117:1, 1995.

[24] J. Jover, A. J. Haslam, A. Galindo, G. Jackson, and E. A. Muller. Pseudo hard-sphere potential for use in continuous molecular-dynamics simulation of spherical and chain molecules. *J. Chem. Phys.*, 137(14):144505, 2012.

[25] B. J. Alder and T. E. Wainwright. Phase transition for a hard sphere system. *J. Chem. Phys.*, 27(5):1208–1209, 1957.

[26] P Rosales-Pelaez, P Montero de Hijes, E Sanz, and C Valeriani. Avalanche mediated devitrification in a glass of pseudo hard-spheres. *J. Stat. Mech.: Theory Exp.*, 2016(9):094005, 2016.

[27] Pablo Montero de Hijes, Pablo Rosales-Pelaez, Chantal Valeriani, Peter N. Pusey, and Eduardo Sanz. Brownian versus newtonian devitrification of hard-sphere glasses. *Phys. Rev. E*, 96:020602, Aug 2017.

[28] Ruslan L. Davidchack and Brian B. Laird. Direct calculation of the hard-sphere crystal/melt interfacial free energy. *Phys. Rev. Lett.*, 85:4751–4754, Nov 2000.

[29] J. L. F. Abascal and C. Vega. A general purpose model for the condensed phases of water: Tip4p/2005. *The Journal of Chemical Physics*, 123(23):234505, 2005.

[30] J. L. F. Abascal, Eduardo Sanz, Ramon Garcia Fernandez, and Carlos Vega. A potential model for the study of ices and amorphous water: TIP4P/Ice. 122:234511, 2005.

Parte III

Resultados

Capítulo 1

Interfacial free energy of a liquid-solid interface: its change with curvature

P. Montero de Hijes[1], J. R. Espinosa[2,3], E. Sanz[1], and C. Vega[1]

[1]Departamento de Química Física, Facultad de Ciencias Químicas, Universidad Complutense de Madrid, 28040 Madrid, Spain

[2]Maxwell Centre, Cavendish Laboratory, Department of Physics, University of Cambridge, Cambridge CB3 0H3, United Kingdom

[3]Emmanuel College, Cambridge, CB2 3AP, United Kingdom

1.1. Abstract

We analyze the changes in the interfacial free energy between a spherical solid cluster and a fluid due to the change of the radius of the solid. Interfacial free energies from nucleation studies using the seeding technique for four different systems, being hard spheres, Lennard-Jones and two models of water (mW and TIP4P/ICE), were plotted as a function of the inverse of the radius of the solid cluster. In all cases, the interfacial free energy was a linear function of the inverse of the radius of the solid cluster and this is consistent with Tolman's equation. This linear behavior is shown not only in isotherms but also along isobars. The effect of curvature on the interfacial free energy is more pronounced in water, followed by hard spheres, and smaller for Lennard-Jones particles. We show that it is possible to estimate nucleation rates of Lennard-Jones particles at different pressures by using information from simple NpT simulations and taking into account the variation of the interfacial free energy with the radius of the solid cluster. Neglecting the effects of the radius on the interfacial free energy (capillarity approximation) leads to incorrect values of the nucleation rate. For the Lennard-Jones system the homogeneous nucleation curve is not parallel to the melting curve as was found for water in previous work. This is due to the increase of the interfacial free energy along the coexistence curve as the pressure increases. This work presents a simple and relatively straightforward way to approximately estimate nucleation rates.

1.2. Introduction

When there is an interface between two phases, there is a contribution to the free energy that can be assigned to the presence of such interface. When given per unit of area this defines the interfacial free energy γ. Strictly speaking, γ is a well and uniquely defined property, in the thermodynamic sense, when the interface between the two phases is planar so that the interfacial area is a well defined property, and when the chemical potential of the two phases is identical. Only in this way can one obtain the interfacial contribution in a non-ambiguous way. Thus, the value of γ has been extensively reported in experiments where one studies the vapor-liquid equilibrium at coexistence conditions with a planar interface[1,2]. When any of these two conditions is not satisfied (either the interface is not planar or the chemical potential of both phases in the bulk is not the same), then it is not possible to define uniquely γ and the value obtained will depend on a certain arbitrary choice[2–4]. Such choice defines where one of the phases finishes and where the other phase begins (through a dividing surface in the traditional description or through an order parameter as in more modern simulation studies). Even acknowledging this limitation, one could still recognize that it may be possible to make a specific choice that leads to a value of γ that is useful from a practical point of view. A particular area in which having a value of γ could be useful is homogeneous crystal nucleation which in turn plays a central role in a broad range of disciplines like climate science[5], food industry[6] or material science[7] to mention just a few.

In the last twenty years, molecular simulation studies have led to a huge progress in our understanding of the nucleation of solid phases. Nowadays, techniques like forward flux sampling (FFS)[8] and/or transition path sampling (TPS)[9] allow us to compute the nucleation rate J (i.e. number of critical solid clusters per unit of volume and time) in a rigorous way. Another approach to J was a combination of the traditional formalism of Volmer-Weber[10]-Becker-Doring[11] (VWBD) and computer simulations[1,12]. This pioneering route was firstly used by Auer and Frenkel[13,14] and followed by others[15–18]. Hence, the key equation leading to J is:

$$J = \rho_{liq}\sqrt{(|\Delta G''|_{N_c}/(2\pi kT))}f^{+}exp(-\Delta G_c/(kT)) \tag{1.1}$$

All that is needed in Eq. (1.1) can be obtained from computer simulations: the density of the liquid ρ_{liq}, the attachment rate f^+, the free energy barrier to nucleation ΔG_c, and the Zeldovich factor $Z = \sqrt{(|\Delta G''|_{N_c}/(2\pi kT))}$ where $|\Delta G''|_{N_c}$ is the second derivative of the Gibbs free energy of the system with respect to the size of the solid cluster (evaluated at the critical particle size N_c). Typically the values of Z and ΔG_c are obtained using the well known biasing technique umbrella sampling (US)[19] which commonly gives name to the whole procedure of Auer and Frenkel although they can also be obtained via metadynamics[20,21]. In a very important paper, Filion et al.[15] showed that US leads to values of J practically identical to those obtained from FFS. Filion et al. not only showed that the values of J agree very well with those obtained from other routes, but they also showed that the free energy barrier (and the product

Zf^+) did not depend significantly on the order parameter chosen to label the molecules as liquid or solid. A similar conclusion was recently reached by Prestipino[17] for the Lennard-Jones (LJ) and water mW[22] models. Consequently, the obtained values of J were not sensitive to the choice of the order parameter. Notice that the value of γ is not used/needed when estimating J by means of US.

As computational studies for J (either using US, FFS or TPS) are rather expensive, in the recent years we have proposed a somewhat different version of Eq. (1.1) that was denoted as seeding[23–29]. In this technique[25–28], a cluster of the solid phase is inserted into the metastable liquid and the thermodynamic conditions are varied until the cluster becomes critical (i.e. going to the liquid phase half of the times and to the solid phase the other half). Then, the value of J is estimated as:

$$J = \rho_{liq}\sqrt{\frac{|\Delta\mu|}{6\pi kTN_c}}f^+exp[(-\Delta\mu N_c)/(2kT)] \tag{1.2}$$

where $\Delta\mu$ is the difference in chemical potential between the bulk liquid and the bulk solid at the considered conditions of temperature T and pressure p. The main difference with Eq. (1.1) is that, instead of computing Z and ΔG_c rigorously, they are now estimated from the well known equations of Classical Nucleation Theory (CNT)[1,30]. While Eq. (1.1) is almost exact and leads to practically exact values of J, Eq. (1.2) is not, and hence, leads to approximate values of J. The reason why results from Eq. (1.2) are approximate is that they depend dramatically on the selection of the order parameter chosen to define the number of particles N_c in the critical cluster of radius R_c. The impact of that choice on the value of J has been discussed in detail recently by some of the authors[31]. However, we have found over the last few years that a sensible choice of the order parameter (used to label the molecules as liquid and solid) using the methodology of Lechner and Dellago[32] along with the so called mislabeling criterium[28,33,34] leads to quite reasonable estimates of J for the following systems: hard spheres, LJ, NaCl, and several water models. One can summarize the situation by saying that for a certain choice of the order parameter, the combination of the VWBD formalism and the CNT yields very good predictions of the nucleation rate J, which is an experimentally accessible property. We shall denote Eq. (1.2) as seeding which can be regarded as a combination of the VWBD formalism and Classical Nucleation Theory with input obtained from computer simulations. Besides, CNT relates the interfacial free energy and the size of the critical cluster:

$$\gamma_{CNT} = \left(\frac{3N_c\rho_{sol}^2|\Delta\mu|^3}{32\pi}\right)^{1/3} \tag{1.3}$$

where ρ_{sol} is the density of the solid. One should keep in mind that γ_{CNT} is not unique as it depends on the selection of the order parameter so it is not possible to define interfacial free energies in a unique way when the interface is not planar (and/or the chemical potentials of the two bulk phases are not identical). However, there is a certain choice of the order parameter that yields a value of γ_{CNT} that allows one to correctly estimate the free energy barrier to nucleation ΔG_c as:

$$\Delta G_c = \frac{16\pi\gamma_{CNT}^3}{3\rho_s^2|\Delta\mu|^2} \tag{1.4}$$

Notice that Eqs. (1.3) and (1.4) both assume a spherical shape for the critical cluster. We have shown in the past[28] that a judicious choice of the order parameter combined with the seeding technique leads to the values of N_c and γ_{CNT} that allows one to obtain reasonable estimates of ΔG_c and J. Thus, we can conclude that an order parameter based on the mislabeling criterion is able to produce values of γ_{CNT} that makes the CNT formalism (in combination with the VWBD kinetic formalism) a useful approach to study nucleation problems.

1.3. Interfacial free energy

In 1949, Tolman suggested that the value of γ of a spherical interface is different from that of a planar interface[35]. Still the best source to read about this issue is the classic book of Rowlinson and Widom and we refer the reader to this reference[2]. The variation of γ with the radius of the interface is given by Tolman's equation:

$$\gamma = \gamma_0 \left(1 - \frac{2\delta_{Tolman}}{R}\right) \tag{1.5}$$

Here, R is the radius of the phase forming the sphere (a solid phase in this paper), δ_{Tolman} is a constant, and γ_0 is the interfacial free energy of the planar interface at coexistence. Tolman's equation was derived to describe the variation of γ with the radius of the spherical phase while keeping the temperature constant. To derive the previous equation Tolman introduced a number of approximations that are described in the original paper (i.e. neglecting terms to evaluate an integral and performing a Taylor expansion over the final result) but more importantly it was assumed that the distance between the equimolar surface and the surface of tension (that for which Laplace's equation is valid) was constant and did not depend on the radius of the spherical phase. Thus, according to Tolman, the parameter δ_{Tolman} is just the distance between the equimolar dividing surface and the surface of tension, and for this reason it is usually denoted as the Tolman length. However, there is another simple way of looking at Eq. (1.5). For the planar interface the radius of curvature is infinite and Tolman's equation can be regarded as a simple Taylor expansion of γ in powers of $1/R$ truncated at first order. Of course, that means that second and higher order terms are neglected. Whether these terms are important or not can be tested by plotting γ as a function of $1/R$ and looking for deviations from linearity. Another important consideration is that the value of γ in Eq. (1.5) refers to that at the surface of tension and so R corresponds to such surface (thus $\gamma = \gamma_s$ and $R = R_s$). This is a convenient choice because in nucleation studies it is the surface of tension the dividing surface considered[30,36,37] and for this reason $\gamma_s \simeq \gamma_{CNT}$ and $R_s \simeq R_c$. Tolman's equation and the Tolman length have been the focus of many studies and still it is a matter of intense debate[36,38–53].

In our previous work by using the seeding technique we have obtained values of γ_{CNT} for the liquid-solid interface[28,54]. Here, we shall analyze in more detail whether the obtained values of γ_{CNT} when plotted as a function of $1/R_c$ are linear or not. There is a subtle issue though concerning the value of the interfacial free energy for the planar interface at equilibrium γ_0 (i.e. at a certain point of the coexistence curve between the liquid and the solid). Let us assume that we want to study the nucleation of a solid at a certain (T, p), at which the radius of the critical cluster is R_c. Outside the liquid-solid coexistence curve, the value of the interfacial free energy for a planar interface is not uniquely defined (i.e. it depends on an arbitrary choice of the order parameter). However, at coexistence, the interfacial free energy between two planar interfaces is well defined, unique, and can be measured in an experimental laboratory. For this reason, it is very convenient to have a simple way of mapping from γ_0 to γ as in Eq. (1.5). There are, at least, two reasonable options when one is interested in the state (T, p). The first one is the coexistence point at the same pressure. The second is the coexistence point at the same temperature (this second choice was the one adopted by Tolman). Strictly speaking there are many more as there are infinitely many curves connecting a point of the coexistence curve with the state of interest (T, p). This is illustrated in Fig. 1.1. In the panel a) the liquid-solid coexistence line of the mW model is shown[55]. In panel b) the liquid-solid[56] and vapor-liquid[57] coexistence lines of the LJ model are shown as solid lines (and their extension in the metastable region as dashed lines). As can be seen in Fig. 1.1 a) for the mW model, as the reference of the value of the interfacial free energy of the planar interface one could choose either the coexistence point at the same T or the coexistence point at the same p. It seems that for studies dealing with the liquid-solid equilibria, the choice of γ_0 at the same pressure is more convenient. For instance, for the Lennard-Jones system (see Fig. 1.1b)), for the state on the left hand side, the value of γ_0 at the same T may occur at negative pressures, and cavitation of the liquid could prevent its determination. On the other hand, for the vapor-liquid interface, the state on the right hand side, the opposite holds true. In fact, when studying the cavitation of the liquid at slightly negative pressures, γ_0 should be chosen at the same T, as the vapor pressure is always positive and there is no point of the coexistence curve at negative pressures. Therefore, we shall rewrite Eq. (1.5) as:

$$\gamma_{CNT} = \gamma_{0,T}\left(1 - \frac{2\delta_T}{R_c}\right) \tag{1.6}$$

$$\gamma_{CNT} = \gamma_{0,p}\left(1 - \frac{2\delta_p}{R_c}\right) \tag{1.7}$$

Obviously, the value of δ depends on the choice of γ_0. Hence, we shall keep the notation δ_p or δ_T to clarify this. Since all our previous studies of seeding were done at constant pressure, we shall adopt the first equation as our working expression (except for the hard sphere system where the seeding was done at constant temperature).

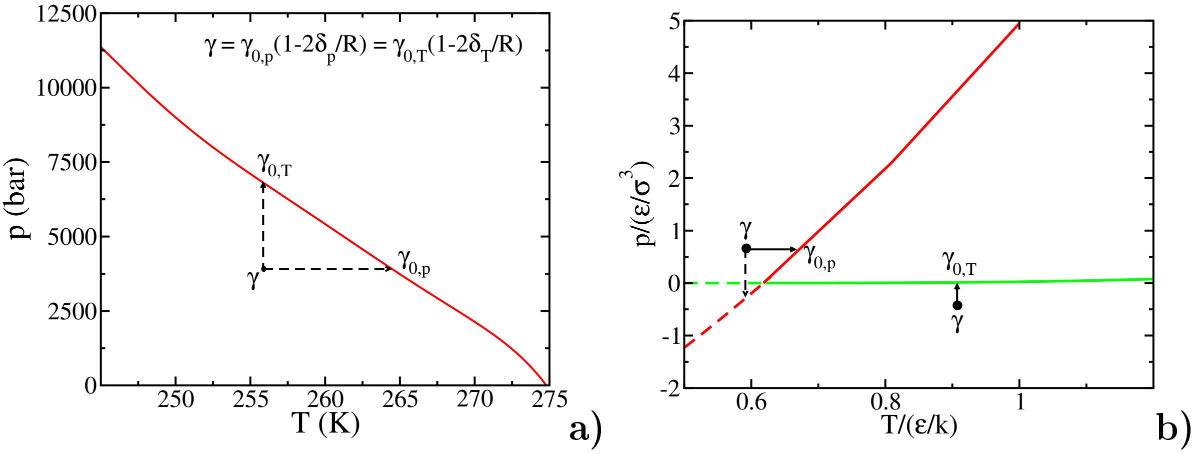

Figure 1.1: a) Schematic representation of a hypothetical γ value with respect to the melting line of the mW water model[55] and its relation with two different coexistence γ_0 values, one along the isotherm $\gamma_{0,T}$ and one along the isobar $\gamma_{0,p}$. b) Sketch of the phase diagram of the LJ model (melting[56] and vapor-liquid[57] lines in red and green respectively) suggesting that for a given problem one could be more interested in working along isobars than isotherms and vice-versa.

The main idea of this work is to plot all the values of γ_{CNT} obtained in our previous studies of seeding as a function of $1/R_c$ and to analyze the functional dependence that they describe. In particular, whether or not they appear linear. Notice that this is a post-analysis of all our previously published results as this aspect was not considered in our anterior work.

For the Lennard-Jones (LJ) system, our preceding study was done only for a pressure close to zero (i.e. $p^* = p/(\epsilon/\sigma^3) = -0.02 \simeq 0$). Since it would be useful to analyze the effect of pressure for different systems we include another seeding calculation of the LJ model under a different pressure $p^* = 4.95$. Details on the calculations are similar to those described in our previous work[28]. Notice that the LJ model considered is the truncated and shifted LJ potential in the form proposed by Broughton and Gilmer[58] and described in more detail by Laird et al.[56]. The results of the seeding calculations are presented in Table 1.1. This allows us to analyze, for LJ and the water models, if the values of δ_p are affected by pressure.

The main result of this work is shown in Fig. 1.2. Values of γ_{CNT} that are calculated by means of the seeding technique are shown as a function of $1/R_c$, which were obtained along one isotherm for the HS system (using the continuous version of Jover et al.[59]) and along several isobars for the rest of the systems. Results are presented for the HS system, for the LJ system[58] (two isobars), for the TIP4P/ICE[60] model of water (two isobars), and for the mW model[22] of water (three isobars)[28,54,61]. As can be seen, γ_{CNT} is reasonably well described (within the error estimates) by a linear fit when is plotted as a function of $1/R_c$. Systematic error sources come from the order parame-

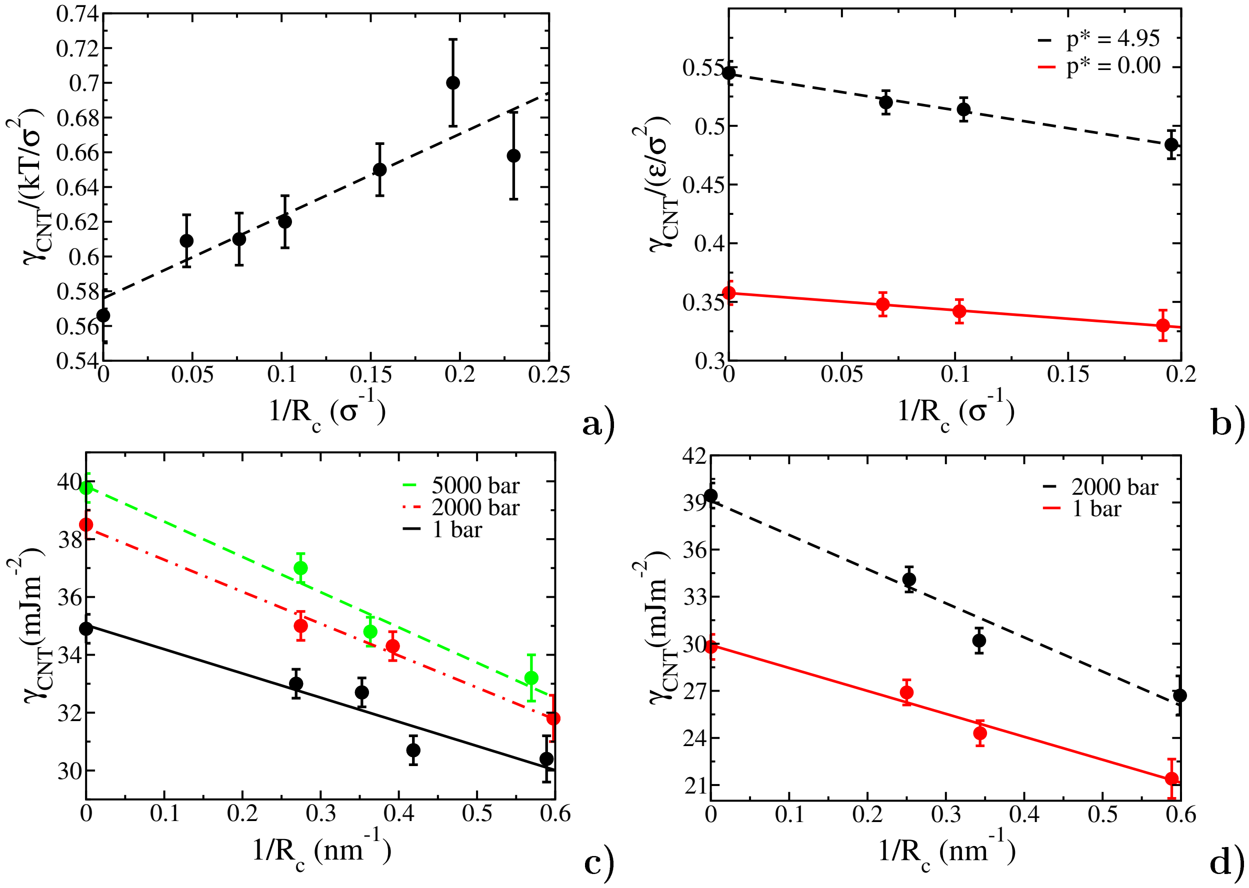

Figure 1.2: γ_{CNT} against $1/R_c$ for a) HS (one isotherm), b) LJ (two isobars), c) mW (three isobars), and d) TIP4P/ICE (two isobars). Error bars for γ_{CNT} are in the range of $3-7\%$. The parameters of the expansion analogous to the Tolman lengths are obtained from the linear fits.

N_c	N_T	$T/(\epsilon/k)$	ρ^*_{liq}	ρ^*_{sol}	$\|\Delta\mu\|/(kT)$	$\gamma_{CNT}/(\epsilon/\sigma^2)$	$f^+/(1/\tau)$	λ/σ	$\Delta G_c/(kT)$	$log_{10}(J\sigma^3\tau)$
576	31901	0.854	0.951	1.030	0.215	0.484	862.1	0.59	62	-28
3810	87665	0.915	0.940	1.019	0.114	0.514	2802.0	0.68	218	-90
12678	275758	0.945	0.934	1.015	0.075	0.520	3448.6	0.97	485	-221

Table 1.1: Results from seeding calculations for the LJ system at a reduced pressure of $p^* = p/(\epsilon/\sigma^3) = 4.95$. Number densities for the fluid and solid phase are given in reduced units (i.e. $\rho^* = (N/V)\sigma^3$). The total number of molecules of the simulation N_T and of the critical cluster N_c are given and also the reduced temperature at which the cluster is critical. We also report the chemical potential difference between the fluid and the solid $\Delta\mu$, the interfacial free energy per unit of area γ_{CNT}, the attachment rate f^+, the attachment length λ, the free energy barrier for nucleation ΔG_c and the logarithm of the nucleation rate J. τ is the unit of time in reduced units (i.e. $\tau = \sqrt{m\sigma^2/\epsilon}$).

ter choice while statistical errors may occur due to the stochasticity of the molecular dynamics trajectory. In this case, more trajectories could help minimize uncertainties. Also, for the smaller critical clusters, the error estimate increases as the preparation is more complicated and the lifetime of the seed decreases since it is more sensitive to fluctuations. In any case, the uncertainties of γ_{CNT} usually happen to be in the range $3-7\%$ being somewhat larger for the smaller clusters (i.e. low values of R_c). It should be mentioned that for the interface between a liquid and a solid the interfacial free energy of a planar interface at coexistence depends on the plane (as given by its Miller indices) of the solid in contact with the liquid[62–67]. The anisotropy is in general small (differences between planes are of about 5-8 per cent)[68]. We have also included in the fit the value of γ for $1/R_c = 0$ estimated as the average for three planes of the interfacial free energy at coexistence (at the same pressure for the LJ and water systems). The planes considered were {100},{110}, and {111} for HS and LJ systems, and basal, primary prismatic and secondary primastic for water models. The values of γ_0 obtained from rigorous calculations were taken from previous work[54,56,62,63,68–71]. Notice that for $p^* = 4.95$ we have computed, in this work, the interfacial free energy at coexistence ($T/(\epsilon/k) = 1.000$) by means of the Mold Integration technique[68] for two crystal orientations {100} and {111}. The obtained values for $\gamma_{0,p}$ were 0.56(1) and 0.51(1) respectively, in good agreement with previous estimations from Laird et al. who report values for three planes at different coexistence conditions[56]. The numerical details for the new calculations are identical as the reported for those same crystal orientations at coexistence conditions $p^* = 0.00$ and $T/(\epsilon/k) = 0.618$ in previous work[68]. As discussed in detail by Koss et al.[72,73], the fact that the crystal-fluid interfacial free energy depends on the exposed plane makes very large clusters (i.e. close to coexistence conditions) to become non-spherical and adopt a polyhedric form probably given by the Wulff construction. The surface area of such a polyhedric nucleus is larger than the surface area of a sphere with the same volume. Hence, assuming a spherical shape leads to an overestimated surface free energy. It depends on the considered system size

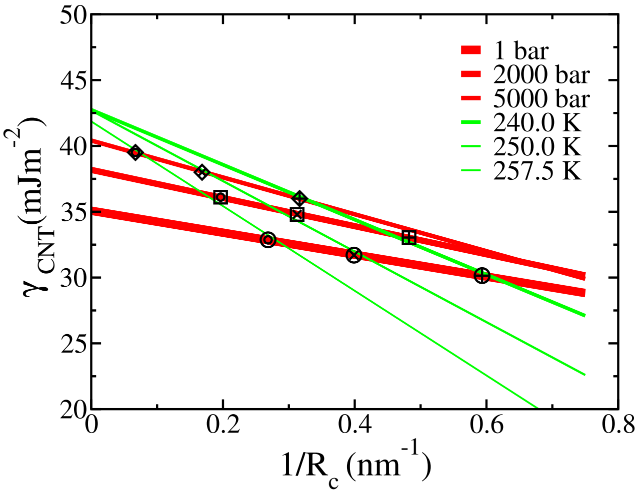

Figure 1.3: Fits of isobars (red lines) and isotherms (green lines) of γ_{CNT} versus $1/R_c$ for mW. Symbols correspond to the computed values that are fitted. There are two overlapping symbols for each value indicating which isotherm and isobar are the corresponding ones. Inner symbols imply isotherms whereas the outer symbols imply isobars. Outer: diamonds (5000 bar), squares (2000 bar), and circles (1 bar). Inner: circles (257.5 K), crosses (250.0 K), and pluses (240 K). Error bars are omitted for clarity although they are of the same order of magnitude as those of Fig. 1.2.

whether these anistropy effects can be neglected or not. Nevertheless, for the clusters considered in this work (in most cases $N_c < 18000$) we observed all of them to be spherical.

As can be seen, the results of this work for the liquid-solid interface can be described by a linear function of $1/R_c$ (although for the vapor-liquid equilibria it has been suggested that quadratic terms should be included[74,75]). The values of δ_T and $\gamma_{0,T}$ for HS as well as δ_p and $\gamma_{0,p}$ for LJ and the two models of water (mW and TIP4P/ICE) arising from the fits to Eq. (1.6) and Eq. (1.7) respectively are presented in Table 1.2 along with their corresponding errors.

For the mW our seeding results were obtained through isobars. However we were able to obtain the variation of γ with $1/R_c$ along isotherms by interpolation. As shown in Fig. 1.3, γ_{CNT} can be well described by a linear function of $1/R_c$ both through isotherms and isobars. The values of δ_T obtained are 0.24, 0.31, and 0.38 (in nm) for $T = 240, 250$, and $257, 5$ (K) respectively, whereas the values of $\gamma_{0,T}$ are 42.75, 42.69, and 41.86 (in mJ/m^2) respectively. As can be seen from the values of Table 1.2, for the mW model the values of δ_T are higher (by a factor of about two) than the values of δ_p.

In principle, δ_T and δ_{Tolman} should be identical as both correspond to isotherms and the surface to be considered in nucleation studies is that at which Tolman's equation is referred, this is the surface of tension. For this reason, δ_T in principle should correspond to the distance (difference) between the equimolar radius and the radius at the surface of tension (after assuming that it is constant along the isotherm). Part of the problem when checking this point is that although the equimolar radius is easily obtained from a density profile, the radius of tension can only be determined rigorously by determining the free energy of the system. Since free energy calculations are expensive, little or almost nothing is known about the radius of tension. This has made it difficult to obtain definitive conclusions on this issue for many years. Here, we simply show that γ_{CNT} is well described by a linear expansion over $1/R_c$, pointing out that further studies are required to establish the relation between the slope and the distance between the two surfaces. Besides, when plots are made along isobars there is no molecular theory explaining the origin of the value of δ_p (see however Ref.[49] for a recent approach). In any case, from a practical point of view, it is enough to know that the dependence of γ_{CNT} with $1/R_c$ is well described by a linear curve.

From the results of Table 1.2, it can be concluded that the values of δ_T and δ_p are smaller than a molecular diameter. In terms of the molecular diameter, they were found to be of about 1/4 for the LJ, 4/10 for the HS and the mW model of water, and of about 9/10 for TIP4P/ICE model of water (the molecular diameter of water is typically of about 0.31 nm and the first peak of the oxygen-oxygen correlation function is located around 0.28 nm). This also means that the impact of curvature effects on γ decreases in the order: water (TIP4P/ICE), water(mW), HS, and LJ.

It should be recognized that when describing the values of γ_{CNT} by using Eq. (1.6) and Eq. (1.7) both the impact of curvature and of the thermodynamic driving force are incorporated into the fit (i.e. when changing the size of the critical cluster one is also changing the value of $\Delta\mu$). We believe that this is a useful approach from a practical point of view as the value of the interfacial free energy of a planar interface cannot be defined uniquely when the system is not at the equilibrium conditions[3,4]. Attempts have been made to evaluate the impact of curvature at constant thermodynamic conditions[44]. Here, our approach is to include both effects (curvature and driving force) into the description as, in our view, the impact of curvature and thermodynamic driving force cannot be determined separately in a non-ambiguous way.

Another key issue is the sign of δ. For the HS, δ_T is negative. For the rest of the systems δ_p is positive. We also found that for the mW δ_T was positive. Further work is needed to understand the origin of this difference of sign between HS and the rest of the systems. Thus, in the case of HS the value of γ increases as the radius of the solid phase becomes smaller. That was already noticed by Auer and Frenkel[13], Filion et al.[15], and Sharma and Escobedo[76]. However, in the case of the LJ and water models, it is the opposite, the value of γ decreases as the radius of the solid phase becomes smaller. It is also obvious from the previous discussion that using the capillarity approximation (i.e. assuming that the value of the Tolman length is zero, or in other words replacing γ_{CNT} by γ_0) in nucleation studies will yield extremely poor predictions for the nucleation rate. The argument also goes the other way around. Values of γ_{CNT} obtained from fits (using expressions of CNT) to experimental measurements of the nucleation rate cannot be used to estimate the value of the interfacial free energy for the planar interface at coexistence γ_0. Notice that although determining experimentally the interfacial free

	$\gamma_{0,T}$	δ_T
HS	0.576(19)	-0.41(11)

	$\gamma_{0,p}$	δ_p
$\mathrm{LJ}_{p^*=0.00}$	0.358(3)	0.203(13)
$\mathrm{LJ}_{p^*=4.95}$	0.544(6)	0.282(33)
$\mathrm{mW}_{p=1bar}$	35.0(8)	0.12(3)
$\mathrm{mW}_{p=2000bar}$	38.4(5)	0.14(3)
$\mathrm{mW}_{p=5000bar}$	39.8(7)	0.15(3)
$\mathrm{TIP4P/ICE}_{p=1bar}$	29.9(9)	0.24(4)
$\mathrm{TIP4P/ICE}_{p=2000bar}$	39.1(1.4)	0.28(5)

Table 1.2: γ_0: Values of the interfacial free energy of the planar interface at coexistence conditions (sub T or p depending on which variable was kept constant) in units of HS (kT/σ^2), LJ (ϵ/σ^2) and water models mW and TIP4P/ICE (mJ/m^2). δ: Values of the expansion coefficient analogous to the Tolman length obtained from a linear fit of γ_{CNT} data in units of HS and LJ (σ) and water models mW and TIP4P/ICE (nm). For the LJ system the reduced pressure p^* is given in units of ϵ/σ^3. The reported uncertainties include the contribution from the standard error of the fit and the contribution due to the error bars in γ_{CNT}.

energy for a planar interface at coexistence is quite simple in the case of a vapor-liquid interface, it is extremely difficult from a technical point of view for a solid-liquid interface. For instance, the experimental values of the interfacial free energy for the ice Ih-water interface at coexistence[77–79] range from the value of 25 to 35 mJ/m^2. This explains why it has been a common approach to estimate γ_0 for the liquid-solid interface using nucleation studies combined with CNT. This work shows that this approach is wrong.

Let us now discuss the variations of $\gamma_{0,p}$ and δ_p with pressure. As can be seen in Table 1.2 the values of $\gamma_{0,p}$ increase with pressure both for the LJ system[56] and for water[54]. It remains to be explored if this is a general feature in liquid-solid interfaces. Our results suggest that δ_p increases slightly with pressure (nevertheless, the differences are only slightly larger than our statistical uncertainty). Therefore, assuming that δ_p is constant for a certain potential model seems to be a reasonable approximation. If this is the case, the knowledge of the value of δ_p for a given model allows for a relatively simple path to evaluate J over a wide range of temperatures and pressures as will be described in the next section.

1.4. A worked example: nucleation of the LJ system

The combination of Eq. (1.7) and Classical Nucleation Theory opens up a route to determine J in relatively easy way. All what is needed are values of γ_0 along the coexistence line (which must also be determined in advance), the value of δ_p for the potential model (we shall assume that is constant and does not change with pressure) and some other magnitudes that can be obtained from simple NpT simulations such as the density of the solid ρ_{sol}, the density of the liquid ρ_{liq}, and $\Delta\mu$, which can be obtained by using thermodynamic integration starting at the coexistence line. The procedure goes as follows:

- Simulations are performed to determine the coexistence line of the model. For instance, direct coexistence simulations can be useful for that purpose, although certainly other routes as free energy calculations are also possible.
- Simulations are performed (using any of the different methods proposed in the literature[4,63,65,68,71,80–83]) to determine the interfacial free energy at coexistence at the pressure of interest for the planar interface for several planes in order to estimate $\gamma_{0,p}$.
- NpT simulations are performed for the liquid and solid phase to determine the equation of state and chemical potentials (via thermodynamic integration from the coexistence point) of both phases.
- Several seeding runs are performed for a certain isobar in the region of interest to determine several values of γ_{CNT} and the value of δ_p. We shall assume that δ_p is hardly affected by pressure and therefore can be used as a constant for a certain potential model.
- At the pressure and temperature of interest, the difference in the chemical potential of both bulk phases $\Delta\mu$ is determined and the value of R_c is obtained by solving the second order equation:

$$R_c = \frac{2\gamma_{CNT}}{(\rho_{sol}\Delta\mu)} = \frac{2\gamma_{0,p}}{(\rho_{sol}\Delta\mu)}\left(1 - \frac{2\delta_p}{R_c}\right) \tag{1.8}$$

- Once the value of R_c is computed, the value of N_c is obtained as $N_c = \rho_s 4\pi R_c^3/3$, the value of ΔG_c is obtained from Eqs. (1.4) and (1.7), and Z is estimated as given by the term under the square root of Eq. (1.2) (i.e. by the expressions of CNT).
- The attachment rate f^+ is then computed from simulations or alternatively estimated (quite accurately) by using the approximate expression $f^+ = 24D(N_c)^{(2/3)}/\lambda^2$ which relates f^+ to the diffusion coefficient of the metastable liquid D and assuming that the attachment length λ is of the order of a molecular diameter σ as shown in Ref.[33]. Thus, from NpT simulations of the metastable liquid one can determine D and therefore f^+ using the approximate expression.

$p/(\epsilon/\sigma^3)$	$T_m/(\epsilon/k)$	$\gamma_0/(\epsilon/\sigma^2)$
0.00	0.618	0.358
2.29	0.809	0.445
4.95	1.000	0.544
8.74	1.250	0.685

Table 1.3: Values of γ_0 along the coexistence line of the LJ systems as reported in Ref.[56]. The values of pressure and temperature of the coexistence line are also shown.

$p/(\epsilon/\sigma^3)$	$T/(\epsilon/k)$	$log_{10}(J\sigma^3\tau)$
0.00	0.448	-7.53
2.29	0.579	-7.94
4.95	0.710	-7.84
8.74	0.890	-8.82

Table 1.4: Values of J for the LJ system alongside their thermodynamic conditions as obtained from brute force simulations.

In summary, knowing the value of δ_p of a certain system allows one to estimate values of J rather easily using information obtained from simple NpT simulations. We shall apply this protocol to the LJ model for four different pressures. The values of γ_0 come from the work of Laird et al.[56]. These values are presented (along with the values of p and T along the coexistence line of the LJ system) in Table 1.3.

Regarding δ_p, we shall use the value $\delta_p = 0.2425\sigma$ which is the average of the two values presented in Table 1.2. We shall assume that δ_p is constant and does not depend on pressure which as discussed above is a good approximation. It is certainly true that seeding runs are still needed to determine the value of δ_p for a certain pressure. However the procedure outlined here avoids performing seeding runs at other pressures allowing for a relatively fast determination of J over a wide range of temperatures and pressures. In Fig. 1.4, we show the results of J obtained from the theoretical route of this work (by using a constant value of δ_p). These are compared with results obtained from seeding[28,84] and also from brute force calculations both from this work and from that of Baidakov et al.[85]. The values of J from the brute force simulations of this work were obtained from 10 independent NpT runs of a system containing $N = 13500$ LJ particles. The value of J was determined as usual from the expression:

$$J = \frac{1}{\langle t \rangle V} \tag{1.9}$$

where $\langle t \rangle$ is the average time for crystallization of the 10 runs. Values of J from the brute force simulations are reported in Table 1.4.

As can be seen the agreement between the results of this work and the brute force

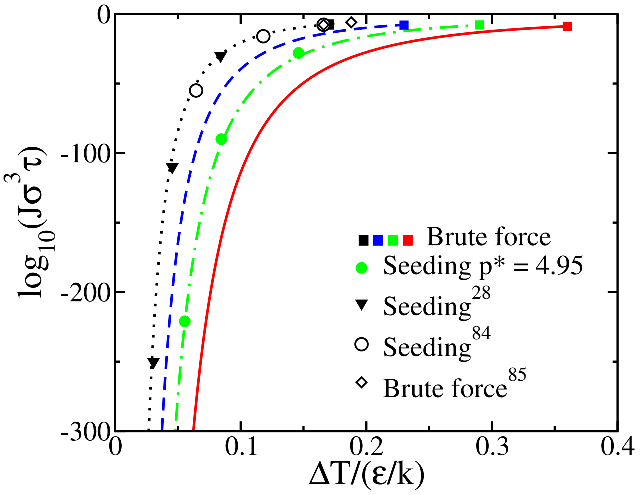

Figure 1.4: Nucleation rates J of the LJ system as estimated from the procedure described in the main text for four different isobars (lines) plotted as a function of the supercooling $\Delta T = T_m - T$. From left to right the results correspond to $p^* = 0.00, 2.29, 4.95, 8.74$. Results from brute force calculations of this work, and from seeding calculations from previous work (for $p^* = 0.00$) and from this work (for $p^* = 4.95$) are also shown.

simulations is quite good. An interesting exercise is to evaluate the effect of δ_p. In Fig. 1.5, J is presented for $p^* = 0.00$ using $\delta_p = 0.2425\sigma$ and neglecting changes in the interfacial free energy with curvature (i.e. $\delta_p = 0.0\sigma$). As can be seen when using the capillarity approximation the values of J are too low when compared to the simulation results from brute force simulations. Thus, as reported many times, one cannot use the value of $\gamma_{0,p}$ to obtain γ for nucleation studies.

Let us finish with an interesting exercise. It is relatively straightforward to determine the homogeneous nucleation line T_{HNL}. For each pressure there is a temperature below which it is not possible to have the metastable liquid because the system freezes. By connecting these temperatures, one obtains the T_{HNL} line. Since the T_{HNL} is a kinetic limit, it depends on the system size and on the typical window time available (which is quite different in simulations and in experiments). In experiments with real substances $T_{HNL,exp}$ corresponds approximately to the states at which $J = 10^{16}/(m^3 s)$ whereas in simulations of real substances the $T_{HNL,sim}$ corresponds to $J = 10^{30}/(m^3 s)$ as described in detail in previous work[33]. By using the values of $\sigma = 0.3405$ nm and $\epsilon = 0.997$ kJ/mol for argon we can estimate T_{HNL}. The results are shown in Fig. 1.6

As can be seen, the T_{HNL} is not parallel to the melting curve. The distance between the T_{HNL} and the melting line increases with pressure. The important physical conclusions of that is the following: it is more difficult to freeze a supercooled liquid at high pressure. This conclusion could already be anticipated from Fig. 1.4 where even in brute force simulations we needed further supercooling to obtain spontaneous freezing in the

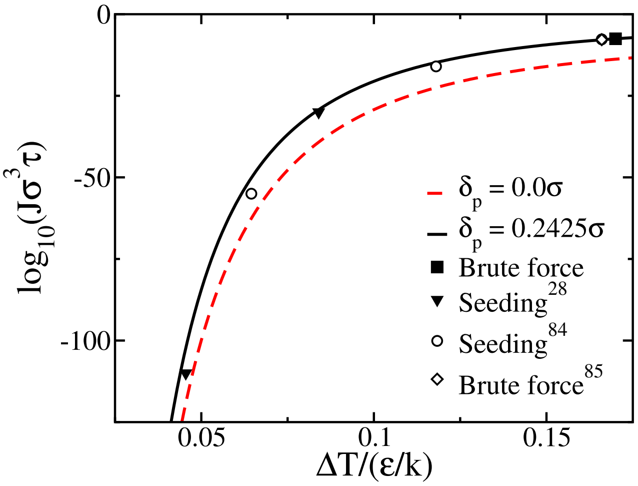

Figure 1.5: Nucleation rate J at $p^* = 0.00$ for the LJ model as a function of the supercooling ΔT computed with and without the capillarity approximation. Results are compared to results from brute force calculations and from seeding.

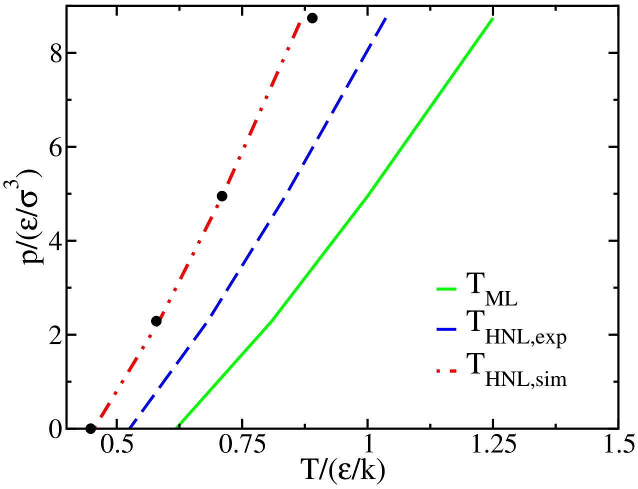

Figure 1.6: Temperature at which the homogeneous nucleation is found in experiments $T_{HNL,exp}$ (blue) and in simulations $T_{HNL,sim}$ (red). The melting line of the model (green) is also shown. Solid circles come from the brute force calculations of this work.

brute force runs. In a recent paper, a similar conclusion was obtained by analyzing the freezing of water under pressure[54]. Thus, the fact that freezing is more difficult under pressure seems to be a general conclusion. Since the value of δ_p does not change much with pressure, the reason behind this behavior is the fact that γ_0 increases with pressure along the coexistence curve both for LJ and for water. We note that the increase of γ_0 with pressure for the Lennard-Jones system is consistent with the empirical proportionality between melting temperature and γ_0 found in close-packed metals[86]. Of course, this rule does not apply to water since γ_0 also increases with pressure despite the fact that the slope of the melting line is negative. In summary, pressure slows down nucleation via an increase of γ_0 both in water and in LJ. Let us discuss now the effect of pressure on nucleation via the diffusion coefficient. In general (water being an exception), the diffusion coefficient of liquids decreases with pressure affecting the attachment rate and so lowering the nucleation rate. Nevertheless, the impact of this kinetic effect on J is rather small as compared to the impact of γ which enters to the third power in the exponential term of Eq. (1.1) through ΔG_c as reflected by Eq. (1.4).

To sum up, pressure prevents nucleation in two quite different systems: LJ and water. Although the LJ system has been studied for quite a long time, this conclusion has not been reported (as far as we know) before. Whether this is a general feature of molecular solids, whether other systems also behave in a similar way remains unexplored. Here, by using the simple approach proposed in this work, it is shown that from Ar to water, pressure prevents freezing. The key is γ_0 and now simulations are helping to determine this quantity (which is quite difficult to be obtained experimentally) and to clarify the kinetics of freezing.

1.5. Conclusions

In this paper, the values of the interfacial free energy obtained from seeding studies of nucleation are plotted as a function of $1/R_c$ (including an estimate of the value for $1/R_c = 0$). The plot is linear suggesting that γ can be expanded in series of $1/R_c$ truncated at first order. This is in line with an equation proposed by Tolman 70 years ago[35]. The value of the slope is just given by $-2\gamma_0\delta$ where δ has units of length. We notice that the value of γ_0 (i.e. the value of γ for a planar interface under coexistence) can be obtained along isotherms or isobars (or actually through other paths connecting the state of interest (T, p) with the coexistence line). This leads to two different values of δ, one when γ_0 is obtained under coexistence conditions at the same pressure δ_p and another one when γ_0 is obtained under coexistence conditions at the same temperature δ_T. For freezing studies, it seems to be easier to consider for γ_0 that of coexistence at the same pressure as the system under consideration. The values of δ_p obtained in this work are smaller than a molecular diameter and are positive for LJ, and models of water (mW and TIP4P/ICE) and negative (δ_T) for HS. Their absolute values decrease in the order: water, HS, and LJ. It is clear from this work, that the capillarity approximation (i.e. to neglect curvature effects) cannot be used in nucleation studies. Conversely, if the interfacial free energy is obtained from experimental nucleation studies the obtained value cannot be taken as an estimate of the equilibrium coexistence value for the planar interface. We have found that the value of δ_p increases slightly with pressure for the LJ and water models. The change is small and assuming that is constant and does not change with pressure seems to be a good approximation. This allows one to estimate nucleation rates within the CNT formalism (but with magnitudes estimated from computer simulations). For the LJ system we were able to obtain values of J for four isobars from simple NpT simulations. We also show evidence that the distance from the melting temperature to the homogeneous nucleation line increases with pressure for a LJ system. The same was found previously for water. Thus, pressure might make the formation of solids more difficult for systems as far apart as Ar and water. We hope the approach shown here may be useful in future studies, and we can obtain further molecular understanding on the sign and value of δ both along isotherms (as in Tolman derivation) and isobars. We have restricted our investigation to the liquid-solid interface. It remains to be studied if the conclusions of this work can or can not be generalized to the case of the vapor liquid interface. In this work we have shown that the equation proposed by Tolman in 1949 (although interpreted in a somewhat different way) allows us to understand the nucleation of a number of systems 70 years later.

1.6. Acknowledgments

This work was funded by Grant FIS2016-78117-P of the MEC and by project UCM-GR17-910570 from UCM. P. M. de H. acknowledges financial support from the FPI grant No. BES-2017-080074. J. R. E. acknowledges funding and support from the Oppenheimer Research Fellowship and from the Emmanuel College Research Fellowship.

Bibliography

[1] K. F. Kelton and A. L. Greer. *Nucleation in Condensed Matter.* Pergamon,Elsevier,Oxford, 2010.

[2] John Shipley Rowlinson and Benjamin Widom. *Molecular theory of capillarity.* Oxford University Press, 1982.

[3] B. Cheng, G. A. Tribello, and M. Ceriotti. Solid-liquid interfacial free energy out of equilibrium. *Phys.Rev.B*, 92:180102, 2015.

[4] D. Sopu, J. Rogal, and R. Drautz. Thermodynamic and kinetic solid-liquid interface properties from transition path sampling. *J.Chem.Phys.*, 145:244703, 2016.

[5] Will Cantrell and Andrew Heymsfield. Production of ice in tropospheric clouds: A review. *Bulletin of the American Meteorological Society*, 86(6):795–808, 2005.

[6] Guillermo Petzold and José M Aguilera. Ice morphology: fundamentals and technological applications in foods. *Food Biophysics*, 4(4):378–396, 2009.

[7] Angelos Michaelides and Karina Morgenstern. Ice nanoclusters at hydrophobic metal surfaces. *Nature materials*, 6(8):597, 2007.

[8] Rosalind J. Allen, Daan Frenkel, and Pieter Rein ten Wolde. Simulating rare events in equilibrium or nonequilibrium stochastic systems. *J. Chem. Phys.*, 124:024102, 2006.

[9] Peter G. Bolhuis, David Chandler, Christoph Dellago, and Phillip L. Geissler. Transition path sampling: Throwing ropes over rough mountain passes, i n the dark. *Ann. Rev. Phys. Chem.*, 53:291, 2002.

[10] M. Volmer and A. Weber. Keimbildung in ubersattigten gebilden. *Z. Phys. Chem.*, 119:277, 1926.

[11] R. Becker and W. Doring. Kinetische behandlung der keimbildung in ubersattigten dampfen. *Ann. Phys.*, 416:719–752, 1935.

[12] S. Jungblut and C. Dellago. Pathways to self-organization: Crystallization via nucleation and growth. *Eur. Phys. J. E*, 39:77, 2016.

[13] S. Auer and D. Frenkel. Prediction of absolute crystal-nucleation rate in hard-sphere colloids. *Nature*, 409:1020, 2001.

[14] S. Auer and D. Frenkel. Quantitative prediction of crystal-nucleation rates for spherical colloids: A computational approach. *Annu. Rev. Phys. Chem.*, 55:333, 2004.

[15] L. Filion, M. Hermes, R. Ni, and M. Dijkstra. Crystal nucleation of hard spheres using molecular dynamics, umbrella sampl ing, and forward flux sampling: A comparison of simulation techniques. *J. Chem. Phys.*, 133(24):244115, 2010.

[16] L. Filion, R. Ni, D. Frenkel, and M. Dijkstra. Simulation of nucleation in almost hard-sphere colloids: The discrepancy between experiment and simulation persists. *J. Chem. Phys.*, 134(13):134901, 2011.

[17] S. Prestipino. The barrier to ice nucleation in monatomic water. *J. Chem. Phys.*, 148:124505, 2018.

[18] Aleks Reinhardt and Jonathan P. K. Doye. Free energy landscapes for homogeneous nucleation of ice for a monatomic wa ter model. *J. Chem. Phys.*, 136(5):054501, 2012.

[19] Glenn M Torrie and John P Valleau. Nonphysical sampling distributions in monte carlo free-energy estimation: Umbrella sampling. *Journal of Computational Physics*, 23(2):187–199, 1977.

[20] Alessandro Laio and Michele Parrinello. Escaping free-energy minima. 99:12562, 2002.

[21] H. Niu, Y. I. Yang, and M. Parrinello. Temperature dependence of homogeneous nucleation in ice. *Phys. Rev. Lett.*, 122:245501, 2019.

[22] V. Molinero, and E. B. Moore. Water modeled as an intermediate element between carbon and silicon. *The Journal of Physical Chemistry B*, 113(13):4008–4016, 2009.

[23] Xian-Ming Bai and Mo Li. Calculation of solid-liquid interfacial free energy: A classical nucleation theory based approach. *J. Chem. Phys.*, 124(12):124707, 2006.

[24] R. G. Pereyra, I. Szleifer, and M. A. Carignano. Temperature dependence of ice critical nucleus size. *J. Chem. Phys.*, 135:034508, 2011.

[25] Brandon C. Knott, Valeria Molinero, Michael F. Doherty, and Baron Peters. Homogeneous nucleation of methane hydrates: Unrealistic under realistic conditions. *J. Am. Chem. Soc.*, 134:19544–19547, 2012.

[26] E. Sanz, C. Vega, J. R. Espinosa, R. Caballero-Bernal, J. L. F. Abascal, and C. Valeriani. Homogeneous ice nucleation at moderate supercooling from molecular simulation. *J. Am. Chem. Soc.*, 135(40):15008–15017, 2013.

[27] Jorge R. Espinosa, Carlos Vega, Chantal Valeriani, and Eduardo Sanz. The crystal-fluid interfacial free energy and nucleation rate of NaCl from different simulation methods. *J. Chem. Phys.*, 142(19):194709, 2015.

[28] Jorge R. Espinosa, Carlos Vega, Chantal Valeriani, and Eduardo Sanz. Seeding approach to crystal nucleation. *J. Chem. Phys.*, 144:034501, 2016.

[29] Y Sun, H Song, F Zhang, L Yang, Z Ye, M. I. Mendelev, C. Wang, and K. Ho. Overcoming the time limitation in molecular dynamics simulation of crystal nucleation: a persistent-embryo approach. *Phys.Rev.Lett.*, 120:085703, 2018.

[30] D. Kashchiev. *Nucleation: Basic Theory with Applications.* Butterworth-Heinemann, Oxford, 2000.

[31] Nils ER Zimmermann, Bart Vorselaars, Jorge R Espinosa, David Quigley, William R Smith, Eduardo Sanz, Carlos Vega, and Baron Peters. Nacl nucleation from brine in seeded simulations: Sources of uncertainty in rate estimates. *J. Chem. Phys.*, 148(22):222838, 2018.

[32] Wolfgang Lechner and Christoph Dellago. Accurate determination of crystal structures based on averaged local bond order parameters. *J. Chem. Phys.*, 129(11):114707, 2008.

[33] J. R. Espinosa, E. Sanz, C. Valeriani, and C. Vega. Homogeneous ice nucleation evaluated for several water models. *J. Chem. Phys.*, 141:18C529, 2014.

[34] Alberto Zaragoza, Maria M. Conde, Jorge R. Espinosa, Chantal Valeri ani, Carlos Vega, and Eduardo Sanz. Competition between ices ih and ic in homogeneous water freezing. *J. Chem. Phys.*, 143(13):134504, 2015.

[35] Richard C Tolman. The effect of droplet size on surface tension. *J. Chem. Phys.*, 17(3):333–337, 1949.

[36] A Tröster, M Oettel, B Block, P Virnau, and K Binder. Numerical approaches to determine the interface tension of curved interfaces from free energy calculations. *J. Chem. Phys.*, 136(6):064709, 2012.

[37] Antonia Statt, Peter Virnau, and Kurt Binder. Finite-size effects on liquid-solid phase coexistence and the estimation of crystal nucleation barriers. *Phys. Rev. Lett.*, 114(2):026101, 2015.

[38] Edgar M Blokhuis and Joris Kuipers. Thermodynamic expressions for the tolman length. *J. Chem. Phys.*, 124(7):074701, 2006.

[39] Benjamin J Block, Subir K Das, Martin Oettel, Peter Virnau, and Kurt Binder. Curvature dependence of surface free energy of liquid drops and bubbles: A simulation study. *J. Chem. Phys.*, 133(15):154702, 2010.

[40] J. G. Sampayo, A. Malijevsky, E. A. Muller, E. de Miguel, and G. Jackson. Evidence for the role of fluctuations in the thermodynamics of nanoscale drops and the implications in computations of the surface tension. *J. Chem. Phys.*, 132:141101, 2010.

[41] A. Malijevsky and G. Jackson. A perspective on the interfacial properties of nanoscopic liquid drops. *J. Phys. Condens. Matt.*, 24:464121, 2012.

[42] Hai Ming Lu and Qing Jiang. Size-dependent surface tension and tolman's length of droplets. *Langmuir*, 21(2):779–781, 2005.

[43] S. M. Thompson, K. E. Gubbins, J. P. R. B. Walton, R. A. R. Chantry, and J. S. Rowlinson. A molecular dynamics study of liquid drops. *J. Chem. Phys.*, 81:530, 1984.

[44] Bingqing Cheng and Michele Ceriotti. Communication: Computing the tolman length for solid-liquid interfaces. *J. Chem. Phys.*, 148(23):231102, 2018.

[45] Gabriel V Lau, Ian J Ford, Patricia A Hunt, Erich A Müller, and George Jackson. Surface thermodynamics of planar, cylindrical, and spherical vapour-liquid interfaces of water. *J. Chem. Phys.*, 142(11):114701, 2015.

[46] J. Vrabec, G. K. Kedia, G. Fuchs, and H. Hasse. Comprehensive study of the vapour-liquid coexistence of the truncated and shifted Lennard-Jones fluid including planar and spherical interface properties. *Mol. Phys.*, 104:1509, 2006.

[47] O. Wilhelmsen, D. Bedeaux, and D. Reguera. Tolman length and rigidity constants of the Lennard-Jones fluid. *J. Chem. Phys.*, 142:064706, 2015.

[48] M. N. Joswiak, R Do, M. F. Doherty, and B. Peters. Energetic and entropic components of the tolman length for mw and tip4p/2005 water nanodroplets. *J. Chem. Phys.*, 145:204703, 2016.

[49] J. W. P. Schmelzer, A. S. Abyzov, and V. G. Baidakov. Entropy and the tolman parameter in nucleation theory. *Entropy*, 21:670, 2019.

[50] David Richard and Thomas Speck. Crystallization of hard spheres revisited. ii. thermodynamic modeling, nucleation work, and the surface of tension. *J. Chem. Phys.*, 148(22):224102, 2018.

[51] KGSH Gunawardana and Xueyu Song. Theoretical prediction of crystallization kinetics of a supercooled Lennard-Jones fluid. *J. Chem. Phys.*, 148(20):204506, 2018.

[52] Azat O Tipeev. Comment on 'theoretical prediction of crystallization kinetics of a supercooled Lennard-Jones fluid [j. chem. phys. 148, 204506 (2018)]'. *J. Chem. Phys.*, 151(1):017101, 2019.

[53] KGSH Gunawardana and Xueyu Song. Response to 'comment on theoretical prediction of crystallization kinetics of a supercooled Lennard-Jones fluid [j. chem. phys. 151, 017101 (2019)]'. *J. Chem. Phys.*, 151(1):017102, 2019.

[54] Jorge R. Espinosa, Alberto Zaragoza, Pablo Rosales-Pelaez, Caridad N avarro, Chantal Valeriani, Carlos Vega, and Eduardo Sanz. Interfacial free energy as the key to the pressure-induced deceleration o f ice nucleation. *Phys. Rev. Lett.*, 117:135702, 2016.

[55] J. Russo, F. Romano, and H. Tanaka. New metastable form of ice and its role in the homogeneous crystallization of water. *Nature Materials*, 13:733, 2014.

[56] Brian B. Laird, Ruslan L. Davidchack, Yang Yang, and Mark Asta. Determination of the solid-liquid interfacial free energy along a coexistence line by Gibbs-Cahn integration. *J. Chem. Phys.*, 131(11):114110, 2009.

[57] Jeffrey R Errington. Direct calculation of liquid–vapor phase equilibria from transition matrix monte carlo simulation. *The Journal of chemical physics*, 118(22):9915–9925, 2003.

[58] J.Q. Broughton and G.H. Gilmer. Surface free energy and stress of a Lennard-Jones crystal. *Acta Metallurgica*, 31(6):845 – 851, 1983.

[59] J Jover, AJ Haslam, A Galindo, G Jackson, and EA Müller. Pseudo hard-sphere potential for use in continuous molecular-dynamics simulation of spherical and chain molecules. *The Journal of chemical physics*, 137(14):144505, 2012.

[60] J. L. F. Abascal, Eduardo Sanz, Ramon Garcia Fernandez, and Carlos Vega. A potential model for the study of ices and amorphous water: TIP4P/Ice. 122:234511, 2005.

[61] J. R. Espinosa, C. Navarro, E. Sanz, C. Valeriani, and C. Vega. On the time required to freeze water. *J. Chem. Phys.*, 145(21):211922, 2016.

[62] J. R. Espinosa, C. Vega, and E. Sanz. Ice-water interfacial free energy for the tip4p, tip4p/2005, tip4p/ice and mw models as obtained from the mold integration technique. *The Journal of Physical Chemistry C*, 120:8068–8075, 2016.

[63] Ruslan L. Davidchack, James R. Morris, and Brian B. Laird. The anisotropic hard-sphere crystal-melt interfacial free energy from fluctuations. *J. Chem. Phys.*, 125:094710, 2006.

[64] James R. Morris and Xueyu Song. The anisotropic free energy of the Lennard-Jones crystal-melt interface. *J. Chem. Phys.*, 119(7):3920–3925, 2003.

[65] J. J. Hoyt, Mark Asta, and Alain Karma. Method for computing the anisotropy of the solid-liquid interfacial free energy. *Phys. Rev. Lett.*, 86:5530–5533, Jun 2001.

[66] Richard Handel, Ruslan L. Davidchack, Jamshed Anwar, and Andrey Brukhno. Direct calculation of solid-liquid interfacial free energy for molecular systems: Tip4p ice-water interface. *Phys. Rev. Lett.*, 100:036104, Jan 2008.

[67] Ling-Kang Wu, Qiu-Lin Li, Mo Li, Ben Xu, Wei Liu, Ping Zhao, and Bing-Zhe Bai. Calculation of solid–liquid interfacial free energy and its anisotropy in undercooled system. *Rare Metals*, pages 1–11, 2018.

[68] J. R. Espinosa, C. Vega, and E. Sanz. The mold integration method for the calculation of the crystal-fluid int erfacial free energy from simulations. *J. Chem. Phys.*, 141(13):134709, 2014.

[69] Ruslan L Davidchack and Brian B Laird. Crystal structure and interaction dependence of the crystal-melt interfacial free energy. *Phys. Rev. Lett.*, 94(8):086102, 2005.

[70] Ruslan L. Davidchack. Hard spheres revisited: Accurate calculation of the solid–liquid interfaci al free energy. *J. Chem. Phys.*, 133(23):234701, 2010.

[71] E Baldi, M Ceriotti, and G. A. . Tribello. Extracting the interfacial free energy and anisotropy from a smooth fluctuating dividing surface. *J. Phys.Condens.Matter*, 29:445001, 2017.

[72] Peter Koß, Antonia Statt, Peter Virnau, and Kurt Binder. Free-energy barriers for crystal nucleation from fluid phases. *Physical Review E*, 96(4):042609, 2017.

[73] Peter Koß, Antonia Statt, Peter Virnau, and Kurt Binder. The phase coexistence method to obtain surface free energies and nucleation barriers: a brief review. *Molecular Physics*, 116(21-22):2977–2986, 2018.

[74] N Bruot and F. Caupin. Curvature dependence of the liquid-vapor surface tension beyond the tolman approximation. *Phys. Rev. Lett.*, 116:056102, 2016.

[75] S. Kim, D. Kim, J. Kim, S. An, and W. Jhe. Direct evidence for curvature-dependent surface tension in capillary condensation:kelvin equation at molecular scale. *Phys. Rev. X*, 8:041046, 2018.

[76] A. K. Sharma and F. A. Escobedo. Nucleus-size pinning for determination of nucleation free-energy barriers and nucleus geometry. *J. Chem. Phys.*, 148:184101, 2018.

[77] Laszlo Granasy, Tamas Pusztai, and Peter F. James. Interfacial properties deduced from nucleation experiments: A cahn–hilliard analysis. *J. Chem. Phys.*, 117(13):6157–6168, 2002.

[78] H. R. Pruppacher. A new look at homogeneous ice nucleation in supercooled water drops. *J. Atmosph. Sci.*, 52:1924, 1995.

[79] SC Hardy. A grain boundary groove measurement of the surface tension between ice and water. *Philosophical Magazine*, 35(2):471–484, 1977.

[80] J. Q. Broughton and G. H. Gilmer. Molecular dynamics investigation of the crystal–fluid interface. VI. Excess surface free energies of crystal–liquid systems. *J. Chem. Phys.*, 84(10):5759–5768, 1986.

[81] Stefano Angioletti-Uberti, Michele Ceriotti, Peter D. Lee, and Mike W. Finnis. Solid-liquid interface free energy through metadynamics simulations. *Phys. Rev. B*, 81:125416, Mar 2010.

[82] L. A. Fernandez, V. Martin-Mayor, B. Seoane, and P. Verrocchio. Equilibrium fluid-solid coexistence of hard spheres. *Phys. Rev. Lett.*, 108:165701, Apr 2012.

[83] Ronald Benjamin and Jurgen Horbach. Crystal-liquid interfacial free energy via thermodynamic integration. *The Journal of Chemical Physics*, 141(4):044715, 2014.

[84] Azat O Tipeev, Edgar D Zanotto, and José P Rino. Diffusivity, interfacial free energy, and crystal nucleation in a supercool ed Lennard-Jones liquid. *J. Phys. Chem. C*, 122(50):28884–28894, 2018.

[85] Vladimir G Baidakov and Azat O Tipeev. Crystal nucleation and the solid–liquid interfacial free energy. *The Journal of chemical physics*, 136(7):074510, 2012.

[86] Brian B Laird. The solid–liquid interfacial free energy of close-packed metals: Hard-spheres and the turnbull coefficient. *The Journal of Chemical Physics*, 115(7):2887–2888, 2001.

Chapter 2

Interfacial Free Energy and Tolman Length of Curved Liquid-Solid Interfaces From Equilibrium Studies

P. Montero de Hijes[1], J. R. Espinosa[2,3], V. Bianco[1], E. Sanz[1], and C. Vega[1]

[1]Departamento de Química Física, Facultad de Ciencias Químicas, Universidad Complutense de Madrid, 28040 Madrid, Spain

[2]Maxwell Centre, Cavendish Laboratory, Department of Physics, University of Cambridge, Cambridge CB3 0H3, United Kingdom

[3]Emmanuel College, Cambridge, CB2 3AP, United Kingdom

2.1. Abstract

In this work, we study by means of simulations of hard spheres the equilibrium between a spherical solid cluster and the fluid. In the NVT ensemble we observe stable/metastable clusters of the solid phase in equilibrium with the fluid, representing configurations that are global/local minima of the Helmholtz free energy. Then, we run NpT simulations of the equilibrated system at the average pressure of the NVT run and observe that the clusters are critical because they grow/shrink with a probability of 1/2. Therefore, a crystal cluster equilibrated in the NVT ensemble corresponds to a Gibbs free energy maximum where the nucleus is in unstable equilibrium with the surrounding fluid, in accordance with what has been recently shown for vapor bubbles in equilibrium with the liquid. Then, within the Seeding framework, we use Classical Nucleation Theory to obtain both the interfacial free energy γ and the nucleation rate. The latter is in very good agreement with independent estimates using techniques that do not rely on Classical Nucleation Theory when the mislabeling criterion is used to identify the molecules of the solid cluster. We therefore argue that the radius obtained from the mislabeling criterion provides a good approximation for the radius of tension,

R_s. We obtain an estimate of the Tolman length by extrapolating the difference between R_e (the Gibbs dividing surface) and R_s to infinite radius. We show that such definition of the Tolman length coincides with that obtained by fitting γ versus $1/R_s$ to a straight line as recently applied to hard spheres.

2.2. Introduction

The thermodynamics of systems having two phases with a curved interface is a fascinating topic that has been largely discussed by the scientific communities in the last decades[1–18]. A system with a fixed number of particles (N), volume (V), and temperature (T) can exhibit a stable/metastable spherical interface between the solid and liquid phase corresponding to a global/local minimum of the Helmholtz free energy (F)[2,5,15,19–30]. Thermodynamic properties of metastable states can be studied as long as there is a free energy barrier separating them from the equilibrium one, and the relaxation time of the system is shorter than the time required to overcome the free energy barrier[31–33]. According to the thermodynamic description of Rowlinson and Widom[34] for planar interfaces at equilibrium, the value of the interfacial free energy γ is unique while for curved interfaces depends on the choice of the dividing surface between the two phases[7,34]. There are two reasonable choices: the Gibbs dividing surface with radius R_e and surface free energy γ_e (where the excess number of particles is zero), and the surface of tension with radius R_s and surface free energy γ_s satisfying the Laplace equation, which for spherical interfaces reads $\Delta p = 2\gamma_s/R_s$, being Δp the pressure difference across the interface[35].

Whenever thermodynamics enters in action, one can also use Statistical Mechanics to get a microscopic insight. In fact, Kirkwood and Buff have shown that for a planar interface between fluid phases, it is possible to evaluate γ (which is unique) from a mechanical route by computing the pressure tensor[36]. This approach has been adopted in several simulation works, following the pioneering study of Chapela et al.[37]. However, there are cases where there is no rigorous mechanical route to γ, including the planar fluid-solid[38,39], curved fluid-fluid, and curved solid-fluid[7,10,34,40] interfaces. The only way to calculate γ in these cases requires the evaluation of the total Helmholtz free energy of the system F. Not surprisingly, the lack of a mechanical route to γ results in quite infrequent experimental approaches to measure γ for planar fluid-solid interfaces (ice-water interface being an excellent example of the situation[41,42]), if not entirely absent or dubiously rigorous as in the case of curved interfaces.

After this frustrating situation, several routes to γ for curved interfaces have been proposed. The first route consists in assuming that the value of γ for the curved interface is that of the planar interface. This is denoted as the capillarity approximation. The approach is simple, but there is no fundamental reason to believe that the value of γ does not depend on the curvature of the interface[13,43]. Indeed, a series of studies on nucleation phenomena have provided indirect evidences that the capillarity approximation fails, as γ changes with the curvature of the spherical phase[31,44–49].

The second route is theoretical and was initiated by Tolman. In 1949, Tolman wrote an influential paper entitled “The effect of droplet size on surface tension”[50]. He assumed that the difference δ between the curvature radii R_e and R_s of the two dividing surfaces is constant (i.e. it does not change with the radius of the spherical cluster) and that can be estimated by its value for infinitely large clusters (which defines the Tolman length δ_{Tolman}). By performing certain approximations he showed that the value of γ (along an isotherm) should change with the the inverse of R_s with an expression where the Tolman length plays a key role. The paper provides molecular evidences that γ changes with the radius of curvature of the cluster, shifting the discussion to the value of δ_{Tolman} characterizing the difference between R_e and R_s for infinitely large clusters. Determining R_e is quite simple and only requires to know the bulk densities of the two phases and the total volume (the detailed density profile is not needed). However, the absence of a rigorous mechanical method to obtain R_s (in spite of a series of attempts[7,10,34,40]) implies that it can only be determined rigorously through the cumbersome task of determining the Helmholtz free energy of the system F. Since rigorous calculations of F for systems with curved interfaces are commonly missing, R_s is not determined rigorously. This has generated an intense debate on the magnitude and sign of the Tolman length for a number of systems for more than 70 years[1–18,51].

The third route to obtain γ for curved interfaces was initiated by Turnbull and co-workers[52,53]. It uses nucleation studies to estimate values of γ for curved interfaces being this an indirect route. The idea of Turnbull was to fit the experimental values of the homogeneous nucleation rate J (i.e. number of critical clusters per unit of time and volume) using classical nucleation theory (CNT) which can be regarded as a combination of the formalism of Volmer-Weber[54]–Becker-Doring[55] and the Gibbsian formalism applied to the thermodynamics of curved interfaces[56]. This interesting approach takes advantage of experimental results for J to obtain, after a theoretical treatment, values of γ for curved interfaces[57]. This route has undergone a new revival from simulation studies in the last decade as now it is possible to estimate J for a potential model using computer simulations. Techniques like umbrella sampling[44,45] (US), forward flux sampling[46] (FFS), or transition path sampling[58] (TPS) can be used to determine J. These techniques are rigorous but rather expensive from a computational point of view. For this reason, in the last ten years, a new technique has been proposed aimed to determine J denoted as Seeding[59–65], where a solid cluster (equilibrated at a certain value of T and p) is inserted into an equilibrated liquid (at the same conditions T, p) to determine whether is critical or not. According to its time evolution in the NpT ensemble: it is critical if the probability to freeze and to melt are equal while there is no other possible result than these two options. The methodology does not allow to estimate J by itself. However, following the CNT with a “judicious” choice of the order parameter[66] used to determine the size of the critical cluster, one can reasonably estimate free energy barriers and nucleation rates getting values comparable with the ones obtained with rigorous techniques[62,67,68]. The Seeding method also provides (through the CNT formalism) values of γ for the curved interface. The Seeding scheme resembles Turnbull’s approach in the sense that it connects nucleation studies and CNT (Turnbull’s approach going from J to γ using experimental results of J, and Seeding going from γ

to J using simulation results). Interestingly, we have shown recently that the values of γ from our Seeding studies of nucleation, can be described by a "Tolman-like" expression for a number of systems including HS[49]. An interesting question (that we intend to address in this work) is whether this Tolman-like expression is also able to describe results for curved interfaces at equilibrium.

Let us now discuss the fourth route to γ for a curved interface. It simply requires to study a system that is at equilibrium and that presents a curved interface. This route has been developed for simulations studies by Binder and coworkers[2,5,19–27], showing that in a system at constant N, V, and T it is possible to have fluid-solid configurations with curved interfaces in equilibrium, corresponding to a minimum of F. Depending on the (N, V, T) conditions, the minimum of F corresponds to i) a sphere of the solid phase within the fluid; ii) an infinite cylinder of the solid phase (percolating through the periodical boundary conditions) in contact with the fluid; iii) a slab of the solid phase in contact with the fluid; iv) all the previous cases switching the roles of the fluid and solid phases. At some point, the minimum of F may correspond to an homogeneous fluid or homogeneous solid phase.

By focusing on the vapor-liquid interfaces, Binder and coworkers[2,5,21,23,27] evaluated F, and determined (for each considered system) the value of R for which γ was minimum (thus obtaining γ_s and R_s). They observed that the capillarity approximation does not work (i.e. γ_s changed with R_s) and also that the difference between R_e and R_s was not constant either. So far, these studies focused on the liquid-vapor interface are the only rigorous route so far to γ for a curved interface and can be considered as a tour de force. After all, determining F in computer simulations is possible but terribly expensive. For the fluid-solid interface, there have been simulation studies showing that a spherical cluster may be stable (or metastable)[14,15,22,24,25] although a rigorous determination of F, to the best of our knowledge, is still missing.

Let us now present the main goals of this work. In this work, we address the issue of the variation of γ with R for a curved fluid-solid interface. Aiming to provide a rationale for some fundamental aspects of this intriguing problem, we will focus on a simple and pedagogical system: hard spheres (HS). We will show that for HS it is possible to obtain stable spherical clusters of the solid phase when the system is simulated in the canonical ensemble (NVT). Our findings are consistent with a recent study of Richard et al.[14]. We then show that the clusters equilibrated in the NVT ensemble are critical when the system is run at constant NpT, being p the mean pressure of the NVT simulation. Knowing that the clusters are critical, we estimate the value of γ_s for the clusters using the CNT approximations previously used in Seeding studies[49,62]. We get consistent values with our previous Seeding work in the NpT ensemble[62]. Since, as previously shown[62], the nucleation rate estimated using CNT for the simulated clusters is consistent with that obtained from independent techniques that do not rely on CNT, we identify the cluster radius obtained in the simulations with R_s. This identification enables two different routes to estimate the Tolman length. One is to extrapolate the difference between R_e and R_s (marking the distance between the equimolar dividing surface and the surface of tension) to infinitely large clusters. The other one is to linearly fit γ_s vs $1/R_s$. We show in this paper that both definitions are consistent with each other as anticipated by Tolman.

2.3. Methods

In this work we shall not study a true HS system, but rather a pseudo hard sphere system (PHS)[69]. The main reason is that the PHS potential is continuous. An advantage of having a continuous potential is that one can use highly efficient codes as GROMACS[70] (highly optimized for parallel calculations). A good choice is represented by the truncated and shifted Mie potential with power m=50 for the repulsion and n=49 for the attraction, called also pseudo hard sphere potential[69]:

$$u_{PHS}(r) = \begin{cases} 50\left(\frac{50}{49}\right)^{49}\epsilon\left[\left(\frac{\sigma}{r}\right)^{50} - \left(\frac{\sigma}{r}\right)^{49}\right] + \epsilon & r < \left(\frac{50}{49}\right)\sigma \\ 0 & r \geq \left(\frac{50}{49}\right)\sigma \end{cases} \tag{2.1}$$

where σ represents the hard sphere diameter and ϵ is the depth of the potential. u_{PHS} reproduces almost exactly the properties of HS, like the equation of state, the diffusion coefficient, the glass transition, the phase diagram and, last but not least, the coexistence crystal-fluid interfacial free energy (which plays a major role in this work)[49,69,71–73]. The potential given by Eq.(4.18) is provided in Tabular form to GROMACS. We adopt the following parameters: $\sigma = 0.3405$ nm, $\epsilon/k = 119.87$ K (k is the Boltzmann constant), and the particle mass $m = 6.69 \cdot 10^{-26}$ kg. These parameters are taken from the standard Lennard-Jones potential used to describe Ar. Simulations are performed at $T = 179.8$ K, since the properties reproduced by u_{PHS} potential agree with the ones of HS at the reduced temperature $T^* = T/(\epsilon/k) = 1.5$. Integration time steps is fixed to 1.0 fs and the T is kept constant by using the Nose-Hoover thermostat. In the following, we convert the real units of GROMACS to reduced units: σ is the unit length; $\tau = \sigma\sqrt{m/(kT)}$ is the unit time (corresponding to 1.761ps); and kT is the unit energy. According to this, the volume is expressed as $V^* = V/\sigma^3$, the density as $\rho^* = (N/V)\sigma^3$, the pressure as $p^* = p/(kT/\sigma^3)$, and the interfacial free energy as $\gamma^* = \gamma/(kT/\sigma^2)$. Hereafter, all the quantities written with a start as superscript will refer to quantities expressed in reduced HS units. In what follows, we shall denote the PHS model, simply as HS.

Each particle of the system is labeled as fluid or solid according to the Lechner-Dellago order parameter $\bar{q_6}$[74]. The threshold value of $\bar{q_{6,t}}$ used to label each particle as liquid-like and solid-like was determined using the mislabeling criterium[61–63,68]. The mislabeling criterium states that the threshold value of the order parameter used to label particles as liquid or solid is obtained by simulating the bulk fluid and bulk solid phases and equating the small percentage of particles that are mislabeled as solid in the bulk fluid, to those that are mislabeled as liquid in the bulk solid. Particles at a distance of 1.33σ of a central one are considered neighbors. In Fig. 2.1, the mislabeling curves of HS in the fluid and solid phases are presented for the reduced pressure $p^* = p/(kT/\sigma^3) = 12.887$. From the curves, we adopt $\bar{q_{6,t}} = 0.372$ as threshold value, checking that $\bar{q_{6,t}}$ variations upon pressurization are negligible, within the pressure range explored in this work.

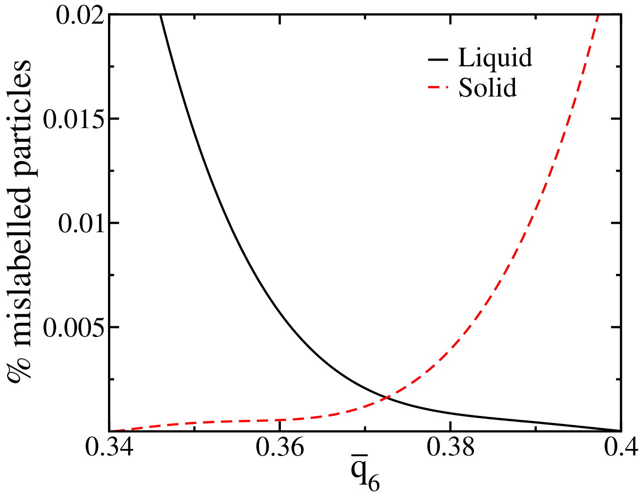

Figure 2.1: Percentage of mislabeled particles in the bulk liquid and bulk solid for PHS at $p^* = 12.887$. The crossing point determines the threshold which in this work will be of $\bar{q_{6,t}} = 0.372$. Molecules with $\bar{q}_6 > 0.372$ will be labeled as solid, whereas those with $\bar{q}_6 < 0.372$ will be labeled as liquid.

Once each particle of the system is labeled as liquid or solid we shall evaluate the size of the largest solid cluster, being N_{sol} the number of solid particles it contains.

For the adopted model, we have determined the value of the coexistence pressure[72] which is $p^* = 11.648$ (for true HS the value is of about 11.57, see Ref.[75]). Most of the simulations of this work lasted around 20ns. This timescale is (roughly) more than a thousand times the time required to diffuse a particle diameter (which for a pressure of $p^* = 12.5$ is of about 13.5ps, or $\sim 8\tau$ in reduced units of time).

2.4. Results

2.4.1. Phase Equilibrium above Coexistence: Solid Clusters Stabilized in Liquids.

We perform simulations at constant number of particles N, volume V, and temperature T. We seed a preformed spherical solid cluster of a certain size in the bulk liquid and let the system evolve towards the equilibrium. As shown in Fig. 2.2, different runs with the same values for N (total number of particles in the system) and V (volume of the simulation box), but with initial clusters differing in size, converge towards the same equilibrium state, where the solid cluster, in average, has the same size in all cases. When the initial cluster is rather small compared to the equilibrium one, it takes some time to reach the final size (green curve in Fig. 2.2). On the other hand, equilibration is much faster when the initial size is close to the equilibrium one. It should be pointed out that the size of the initial cluster cannot be chosen arbitrarily. Indeed, if the initial

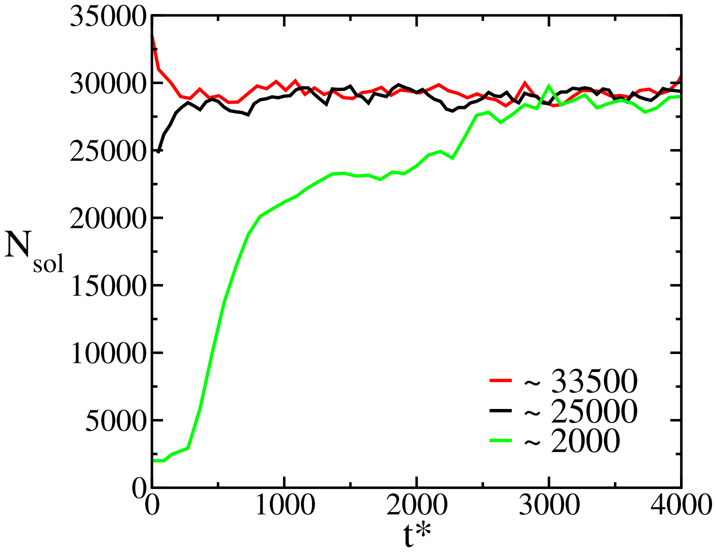

Figure 2.2: Number of particles of the largest solid cluster in the system as function of time ($t^* = t/\tau$), for $N = 105875$ and $V^* = 108265.2$. Systems only differ on the initial size of the crystal seed.

cluster is too small, it may melt; if it is too large then it may percolate through the simulation box forming a cylinder (we shall come to this point later). It should be considered also that some defects (of kinetic origin due to the fast growth) may arise when the cluster grows from a very small initial size. For this reason, it is advisable to use initial (and perfect) solid clusters close in size to the final equilibrium state. Once the equilibrium state is reached, there are thermal oscillations in the size of the solid cluster (Fig. 2.2) due to capillary waves fluctuating in the solid-fluid interface. Also, it should be noticed that it is convenient to consider the shape of the seed for technical reason albeit irrelevant in terms of stability. This is, if instead of a spherical cluster we inserted a cubic cluster, this would turn into a sphere-like cluster as soon as possible because the cubic is not even a local minimum.

We have repeated this procedure ten times, varying N and V (T is constant and for hard spheres it just scales the velocities of the particles but does not affect configurational properties), obtaining in all cases equilibrium solid clusters of spherical average shape. The results are presented in Table 2.1, where the average size of these solid equilibrium clusters (labeled as $\langle N_{sol} \rangle$) ranges from about 2000 up to 130000 particles. Notice that the size of the equilibrium cluster is uniquely determined by the values of N and V, and corresponds to a minimum in the Helmholtz free energy F. Both the values of $\langle N_{sol} \rangle$ and $\langle N_{sol} \rangle / N$ obtained for a certain value of N and V, are dictated by thermodynamics (i.e. the minimum in F) and cannot be changed at will. As can be seen in Table 2.1, we found the ratio $\langle N_{sol} \rangle / N$ to be $\in [0.1 : 0.27]$. Although not stated explicitly in the books describing the thermodynamic treatment of curved interfaces, one has the impression that it is assumed that the volume of the fluid phase is many times larger than the volume of the solid phase. At least for HS, under periodical boundary conditions this is certainly not the case.

Label	V^*	N	$\langle N_{sol} \rangle$	$\langle N_{sol} \rangle / N$	$\langle p^* \rangle$
I	10686.4	10540	1925	0.183	13.209
II	20195.5	19779	2736	0.138	13.027
III	20195.5	19829	3718	0.188	12.887
IV	49599.9	48207	5604	0.116	12.739
V	49599.9	48357	8602	0.178	12.579
VI	108265.2	104675	10498	0.100	12.517
VII	66900.1	65383	15554	0.238	12.399
VIII	108265.2	105475	23558	0.223	12.306
IX	108265.2	105875	28879	0.273	12.258
X	887000.0	853712	129926	0.152	12.011

Table 2.1: Thermodynamic variables of the closed finite systems simulated at constant temperature and volume. The pressure $\langle p^* \rangle$ is the average value obtained when the system reaches the equilibrium state. Only spherical clusters were considered. The average number of particles in the solid cluster is denoted as $\langle N_{sol} \rangle$.

In Table 2.1, we present also the values of the pressure obtained in the simulation runs during the period in which the solid cluster is stable. They fall in the range $p^* \in [12.011 : 13.209]$. Since the coexistence pressure is $p^* = 11.648$, our findings suggest that this equilibrium method applies only close to the coexistence.

By comparing the cases II and III in Table 2.1, both sharing the same volume $V^* = 20195.5$, we see that by reducing N the equilibrium solid cluster becomes smaller. The size of the equilibrium cluster is very sensitive to N. In fact, for clusters II and III, removing just 50 particles makes a change of about 1000 particles in $\langle N_{sol} \rangle$. Again, focusing on the isochoric cases VI, VIII and IX, the reduction of 1200 particles induces a change in $\langle N_{sol} \rangle$ of about 20000. As can be seen, decreasing the global density causes an increase of the volume of the phase with lower density (the fluid phase in this case) reducing the size of the solid cluster as given by $\langle N_{sol} \rangle$. Concerning the size of the equilibrium cluster we found that, while it is always possible to stabilize a cluster with a size as big as desired, the smallest equilibrium cluster we could obtain was composed by ~ 2000 particles. Below this threshold the solid clusters melted leading to the conclusion that for HS, within this method it is not possible to equilibrate solid clusters with much less than ~ 2000 particles.

In Fig. 2.3, we present the time evolution of N_{sol} for the ten systems considered in Table 2.1. Each panel contains trajectories with the same constant value of V although different constant value of N. As can be seen in Fig. (2.3)a, during a short time the initial seed grows until it reaches a stable quasi-spherical size, maintained for a significant period of time ($\tau \in [500 : 2500]$), corresponding to about ~ 250 diffusion times. At larger times, $\tau > 2500$, the system undergoes a transition to a new conformation represented by a cylindrical solid.

In Fig. (2.4) we report two snapshots of the solid cluster before and after the transition. The fact that the spherical solid clusters is stable for certain time and that

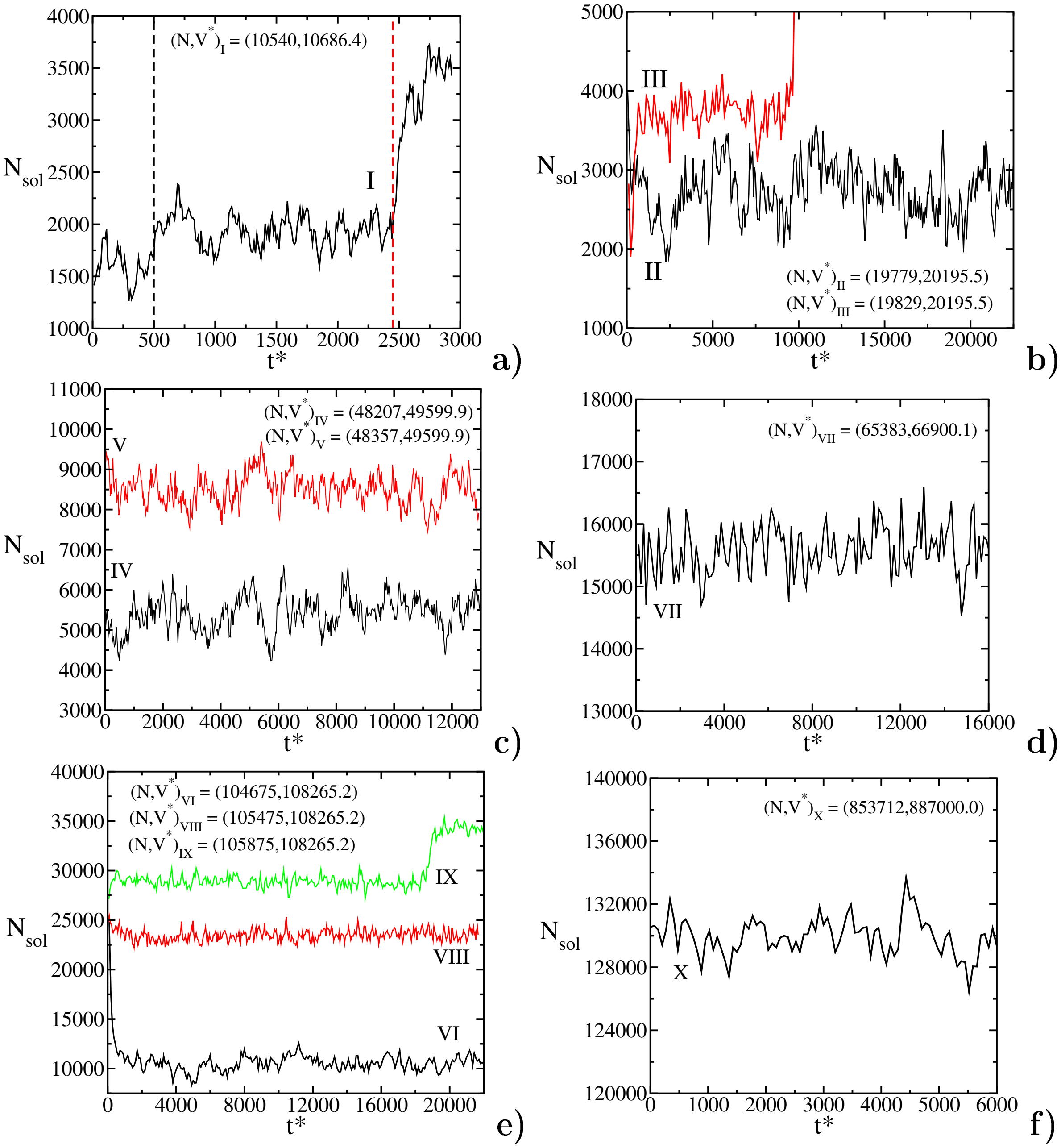

Figure 2.3: Number of particles of the largest solid cluster as a function of time in reduced units. The clusters of each panel share the same volume. Hence, the difference in cluster sizes comes from the total number of particles, in other words, the net density. Details of the runs (volume, total number of particles, number of particles in the solid cluster, and pressure of the system while the spherical cluster is stable) are given in Table 2.1. In panel a), the dashed line in the left indicates the starting point of the equilibrated coexistence of the spherical cluster within the fluid while the dashed line in the right indicates the transition to the cylindrical state.

the change to the cylindrical shape occurs rapidly indicates that there is a free energy barrier separating the spherical cluster from the cylindrical one. In this case, the spherical cluster represents a local minimum of F (a metastable configuration), while the cylinder represents a deepest (possibly global) minimum of F (we never observed the transition from a cylinder to a sphere). The same transition was observed for cases III and IX, shown in Figs. (2.3)b and (2.3)e respectively.

2.4.2. Connecting Equilibrium and Nucleation.

We shall now perform an interesting exercise. We shall perform NpT simulations at the average pressure found in the NVT run (denoted as $\langle p^* \rangle$ in Table 2.1). For the starting configuration, we shall randomly select one from the NVT run in which the cluster was stable. Then, we shall study in detail the time evolution of the solid cluster by launching up to 30 independent NpT simulations (by changing the initial velocities). These results for systems III and VII of Table 2.1 are presented in Fig. 6.2, panels a) and b) respectively. The trajectories show that around half of the times the clusters melt and the other half, they grow until crystallizing the entire system. Hence, the clusters are critical at pressure $\langle p^* \rangle$. The fact that the nucleus equilibrated in the NVT ensemble is a critical cluster in the NpT ensemble has been recently shown for bubble cavitation in the Lennard Jones system[30]. In Fig. 2.6 we show the number of particles in the solid clusters versus $\langle p^* \rangle$ at equilibrium as obtained in this work in the NVT ensemble (red dots) alongside our previous results for the size of the critical clusters obtained in the NpT ensemble (black dots)[49,62]. As can be seen there

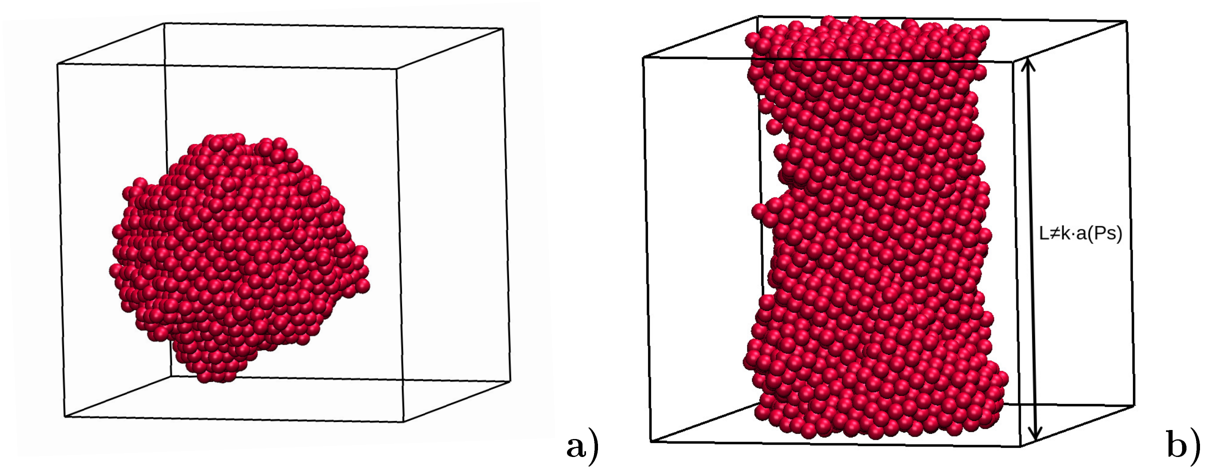

Figure 2.4: Snapshots of: a) metastable sphere and b) stable cylinder within a fluid. Only crystalline particles are shown. In b), the vertical arrowed line indicates that, in general, the size of box does not necessarily meet k times (k being an integer) the length, a, of the unit cell of the FCC hard sphere crystal at the pressure $\langle p^* \rangle$. Thus, the solid may have some stress.

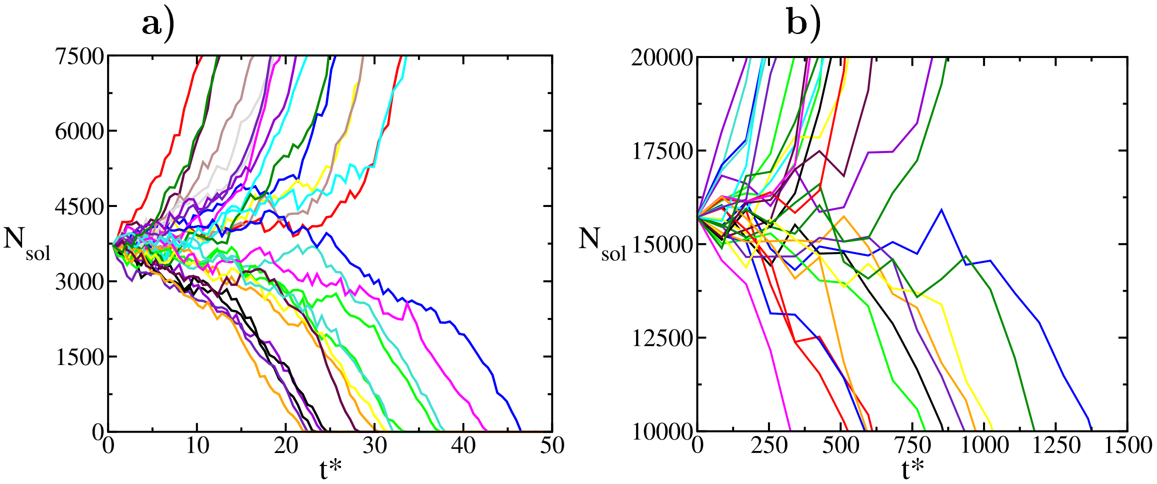

Figure 2.5: Number of particles in the largest cluster within the system in an NpT simulation at p^* equal to the average pressure during the life time of the stable sphere in the NVT run. The total number of runs is 30 in both cases. It can be seen how in $\sim 50\%$ of the trajectories the cluster either grows or disappears. The clusters correspond to cases III (left panel) and VII (right panel) of Table 2.1.

is excellent agreement between both set of results further reinforcing the connection between equilibrium and nucleation.

When the cluster is critical, it must be in the top of a Gibbs free energy (G) curve. In other words, G reaches a maximum when plotted as a function of the number of particles in the solid cluster while keeping N, p, and T constant. However, the same system was in equilibrium when it was studied at constant N, V and T. Therefore, F reaches a minimum when plotted as a function of the number of particles in the solid cluster while keeping N, V, and T constant. That indicates that changing the number of particles in the solid cluster would increase the value of the Helmholtz free energy. This is sketched in Fig. 2.7.

The consequences of the results of Fig. 6.2 and Fig. 2.7 are important. On the one hand, if a thermodynamic approach is able to describe correctly the minimum in F, it should also be able to describe the maximum in G. On the other hand, we have shown that clusters in stable/metastable equilibrium obtained in the NVT ensemble correspond with critical clusters in unstable equilibrium obtained in the NpT ensemble. As two faces of the same coin, this equivalence implies that one can infer the same information (e. g. the cluster radius, γ, or the nucleation rate) from either ensemble, as shown in the remainder of the paper. For this reason we will apply the Seeding method, previously used in the NpT ensemble (NpT-Seeding)[49,62,67], to the clusters equilibrated here in the NVT ensemble (NVT-Seeding). As discussed later on, the Seeding method uses information of the simulated clusters alongside CNT to provide estimates of γ and the nucleation rate.

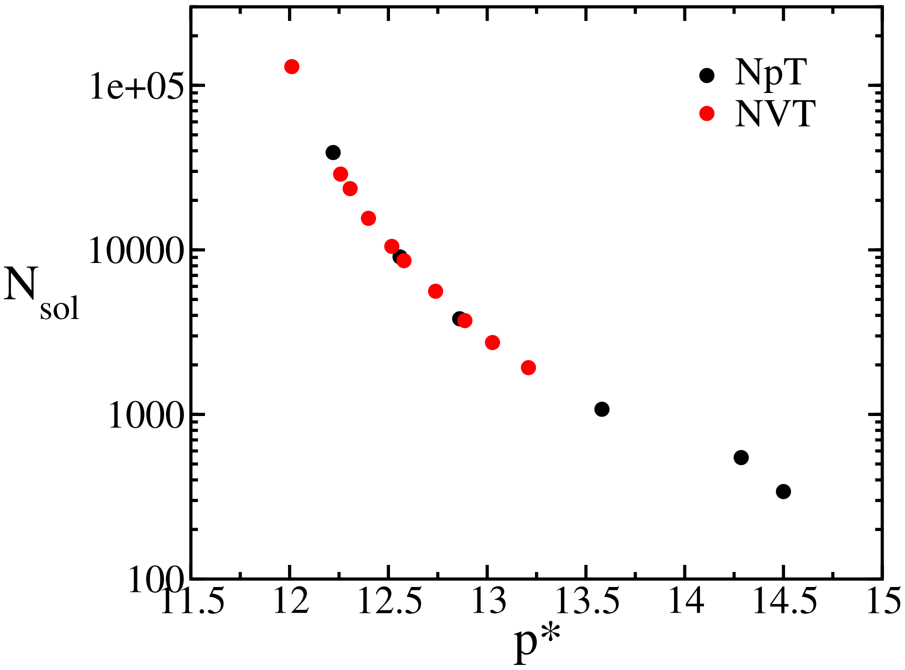

Figure 2.6: Cluster sizes against pressure. Notice that although the stable clusters from NVT simulations were tested to be critical via NpT simulations, data labeled as NpT in this figure correspond to previous work of Seeding[49,62].

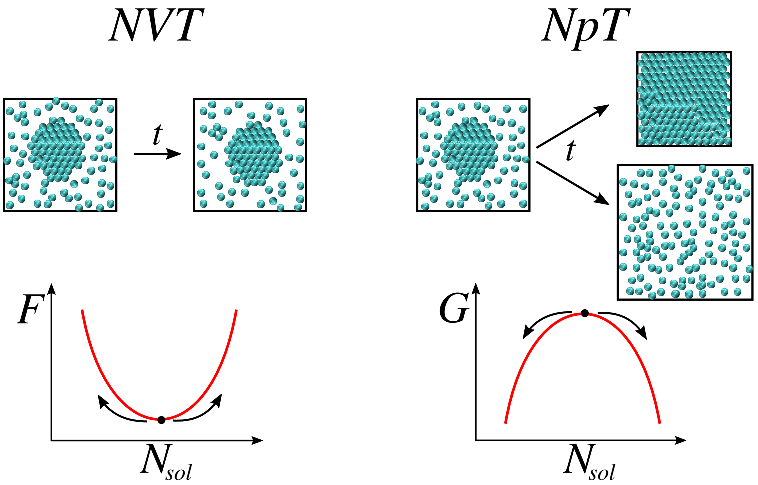

Figure 2.7: Sketch of the free energy profile for the case of a stable solid cluster composed by N_{sol} particles in the NVT ensemble (left). The system is in a free energy minimum of the Helmholtz free energy F and does not change with time (except for thermal fluctuations). By switching to the NpT ensemble, the system ends up in a maximum in the Gibbs free energy G (right) and evolves either towards to the solid phase or towards the fluid phase with the same probability. In both cases, the value of γ is the same. Equilibrium (left) and nucleation (right) can be regarded as the two faces of the same coin.

2.4.3. Estimating γ for the Clusters.

All the clusters obtained in the previous sections are in stable/metastable equilibrium in the NVT ensemble. According to the thermodynamic description presented in the book of Rowlinson and Widom[34] when the system reaches the equilibrium one obtains:

$$F = N\mu - p_{sol}V_{sol} - p_{liq}(V - V_{sol}) + \gamma A_{sol} \tag{2.2}$$

where p_{sol} and p_{liq} are the pressures of a bulk solid and liquid respectively with chemical potential μ. Notice that the chemical potential , and the temperature are homogeneous properties (the molecules can diffuse) whereas the density and pressure are inhomogeneous[76].

The way to proceed to evaluate γ is as follows.

- The value of F is computed
- A dividing surface of radius R is chosen so that $V_{sol} = 4/3\pi R^3$ and $A_{sol} = 4\pi R^2$
- The value of γ is obtained for the chosen dividing surface using Eq.2.2

Therefore, the value of γ is not unique as it depends on the value of the chosen dividing surface. Two important surfaces are R_e (for which the number of excess particles is zero) yielding γ_e; and R_s, giving rise to γ_s, which is the value for which γ is minimum and for which the Laplace equation is satisfied.

As the reader may have noticed, the only way to determine γ is to determine the free energy of the system. This has been done only in a couple of cases for the liquid-vapor interface by Binder and coworkers and can be regarded as a tour de force[2,5,21,23,27].

In the past, we have used an approximate approach denoted as Seeding[61] to circumvent the computation of free energies[49,62]. With NpT simulations of critical clusters alongside a "judicious" order parameter to label the particles as liquid and solid alongside CNT we obtained reasonable estimates of γ and the nucleation rate[49,62]. By judicious we mean that the chosen order parameter is able to predict the free energy barrier and the nucleation rate obtained from rigorous techniques (for instance US[44,45] or metadynamics[77]). For HS, the combination of the order parameter of Lechner-Dellago $\bar{q_6}$[74] and the mislabeling criterion[61] meets this requirement[62]. According to CNT, the free energy barrier ΔG and the surface free energy γ for the pressure $\langle p^* \rangle$ can be estimated by means of the following expressions:

$$\Delta G = \langle N_{sol} \rangle \frac{\Delta\mu}{2}, \tag{2.3}$$

$$\gamma = \left(\frac{3\langle N_{sol} \rangle \rho_{sol}^2 |\Delta\mu|^3}{32\pi} \right)^{1/3}, \tag{2.4}$$

where ρ_{sol} is the density of the solid phase (at $\langle p^* \rangle$ since in CNT the solid is assumed to be incompressible) and $\Delta\mu \equiv \mu_{liq} - \mu_{sol}$ is the difference between the chemical potentials of the bulk liquid μ_{liq} and that of the bulk solid μ_{sol} when both are at the same pressure (this difference is not zero, as the equilibrium in the NVT ensemble arises from the higher pressure of the solid phase due to the presence of the curved interface). The variables ρ_{liq} and ρ_{sol} are obtained from the equations of state that are computed from simulations of the bulk phases along the isotherm of interest while $\Delta\mu$ is computed via thermodynamic integration $\Delta\mu = \int_{p_{coex}}^{p} [1/\rho_{sol}(p') - 1/\rho_{liq}(p')]dp'$ starting from the coexistence point where the chemical potential of both phases are equal[78]. The values of γ thus obtained in this work from solid clusters equilibrated in the NVT ensemble (NVT-Seeding) are compared to those obtained in Ref.[49,62] (NpT-Seeding) in Fig. 2.8. As expected from Fig. 2.6, that shows the equivalence of clusters in both ensembles, γ is the same in both cases.

The clusters obtained in this work in the NVT ensemble are at stable/metastable equilibrium. Therefore the value of γ_s for a certain value of R_s it is the value of the interfacial free energy obtained for this radius at the equilibrium pressure $\langle p^* \rangle$. Although one usually speaks on the variation of γ_s with R_s one should rather speak on the variation of γ_s with the pair R_s and $\langle p^* \rangle$ because it is not possible to change R_s and $\langle p^* \rangle$ independently for a system that is at equilibrium.

2.4.4. Variation of γ with Curvature and the Tolman Length.

It should be emphasized that the values of R and γ that are used in CNT are those of the surface of tension, i.e. R_s and γ_s[5,22,79]. In fact, it is simple to show that if one assumes that the chemical potential of the bulk liquid ($\mu_{liq}(p_{liq})$) is identical to that of the stable/critical solid cluster ($\mu_{sol}(p_{sol})$) (which makes sense after the results presented in the previous sections) and uses the Laplace equation (which is restricted to the surface of tension) to estimate the difference of pressures, one obtains the main equations of CNT (after assuming that the density of the solid does not change much with pressure). This indicates that R_s and γ_s are indeed the ones obtained when applying CNT.[5,22,79] Thus, values labeled as R_c and γ_{CNT} in our previous work should be identified with R_s and γ_s.

It is obvious from the results of Fig. 2.8 that the value of γ_s is not constant (showing the failure of the capillarity approximation). Recently, we used the following expression to describe the variation of γ_s with the cluster radius[49]:

$$\gamma_s = \gamma_{0,T}\left(1 - 2\frac{\delta_T}{R_s}\right), \tag{2.5}$$

where δ_T is a fitting parameter and $\gamma_{0,T}$ is the interfacial free energy at coexistence for a flat interface. We showed that this expression correctly describes the γ variation for critical hard sphere clusters. The blue line in Fig. 2.8 is the fit obtained in Ref.[49]. It describes well the data coming from either ensemble, which further demonstrates the equivalence between clusters equilibrated in the NVT ensemble and critical clusters obtained in the NpT ensemble. The parameters are $\gamma_{0,T} = 0.576kT/\sigma^2$, the interfacial

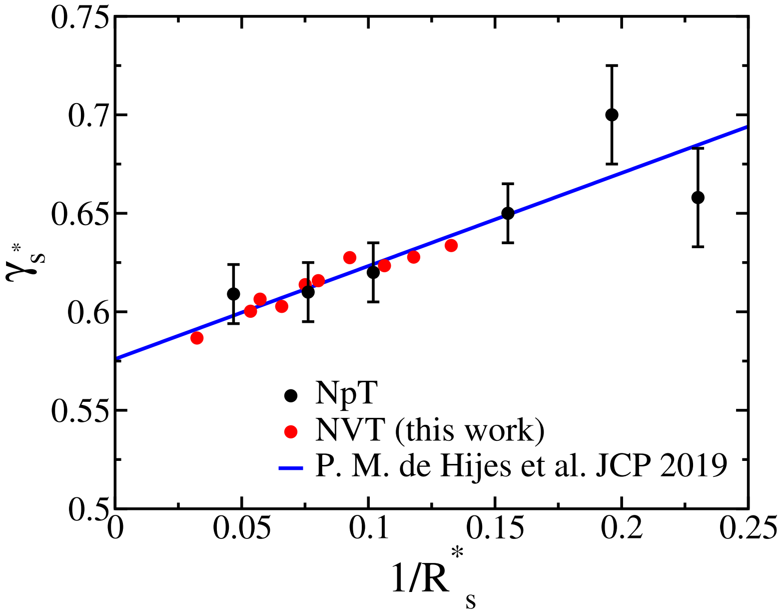

Figure 2.8: Interfacial free energy against the inverse of the radius of the cluster from both equilibrium results of this work (labeled as NVT) and from nucleation studies of our previous work[49,62] (labeled as NpT). Also shown: linear expression proposed in previous work[49] in solid blue line.

free energy at coexistence ($p^* = 11.648$) averaged over several planes[80,81], and $\delta_T = -0.41\sigma$. It is worth noting that, for HS in contact with a smooth spherical hard wall, a similar value of δ_T was reported from a theoretical study using Density Functional Theory[18] (although the value of $\gamma_{0,T}$ was found to be different indicating that there are differences in the value of $\gamma_{0,T}$ between a hard structureless spherical wall and a solid cluster of ordered hard spheres).

What is the physical meaning of the fitting parameter δ_T? Since this parameter is a distance we can compare it with the Tolman length, δ_{Tolman}[1,50]:

$$\delta_{Tolman} \equiv \lim_{\frac{1}{R_s}\to 0} \delta \tag{2.6}$$

where δ is the difference between the equimolar and the surface of tension radii:

$$\delta = R_e - R_s \tag{2.7}$$

The radius R_e of the (spherical) Gibbs dividing surface is obtained simply from the equation

$$N = \rho_{sol}[(4/3)\pi R_e^3] + \rho_{liq}[V - (4/3)\pi R_e^3]. \tag{2.8}$$

The previous expression only requires the knowledge of the bulk densities of the solid and fluid phases (ρ_{sol} and ρ_{liq} respectively) . On the other hand, R_s can be calculated from:

Label	R_s^*	R_e^*	$\delta^* \equiv (R_e^* - R_s^*)$
I	7.535	7.419	-0.1154
II	8.481	8.407	-0.0742
III	9.402	9.362	-0.0404
IV	10.791	10.543	-0.2478
V	12.461	12.265	-0.1965
VI	13.322	13.111	-0.2108
VII	15.200	14.996	-0.2035
VIII	17.467	17.213	-0.2538
IX	18.700	18.448	-0.2521
X	30.927	30.571	-0.3563

Table 2.2: Radius associated to the dividing surfaces from our results from equilibrium clusters. R_s is computed with Eq. (2.9) and corresponds to the radius of the sphere containing a number of particles corresponding to the equilibrium one, as reported in Tab. 2.1. R_e corresponds to the sphere's radius of the equimolar dividing surface (Gibbs dividing surface). δ is, by definition, the difference between the previous radii.

$$R_s = [3\langle N_{sol}\rangle/(4\pi\rho_{sol})]^{1/3}. \tag{2.9}$$

The values of δ are reported in Table 2.2. We found that δ is negative and its value changes with the radius of the solid cluster (i.e. with the equilibrium pressure). An analogous change of δ has been observed by Binder and coworkers in studies on the vapor-liquid interface[2,5,21,23,27]. In Fig.2.9 we have fitted the values of δ as a function of $1/R_s$ obtaining the value $\delta_{Tolman} = -0.41\sigma$ when $1/R_s$ goes to zero (i.e. for planar interface). The obtained value coincides with δ_T obtained from 2.5. Therefore, δ_T is an estimate of the Tolman length.

2.4.5. Application of Equilibrium Clusters to Study Nucleation.

We have developed in the last years an approximate route denoted as Seeding to determine nucleation rates, J. By performing NpT runs, the size of the solid critical cluster N_{sol} (at a certain T and p) is determined, and J is estimated from the expressions of CNT:

$$J = \rho_{liq}\sqrt{\frac{|\Delta\mu|}{6\pi kTN_{sol}}}f^{+}exp[(-\Delta\mu N_{sol})/(2kT)], \tag{2.10}$$

where f^{+} is the attachment rate which will be approximated as

$$f^{+} = 24D_{liq}(N_{sol})^{(2/3)}/\lambda^2, \tag{2.11}$$

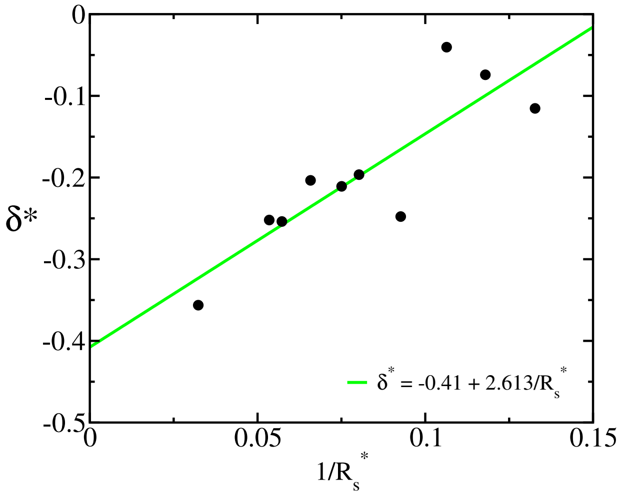

Figure 2.9: δ^* as function of $1/R_s^*$ for the different stable clusters of the NVT runs. Green dashed curve is a linear fit of the data.

where λ is the attachment length which for HS can be approximated[62] as $\lambda \simeq (\sigma/4)$ and D_{liq} the diffusion coefficient of the fluid at the pressure p. In previous work, we have shown that this set of equations (with the input from simulations) provides an excellent description of the values of J (including those for HS). We could denote this approach as NpT-seeding as a number of runs are performed at N, p, and T constant.

However, the results of Fig.6.2 indicate that there is a new way of doing Seeding. Instead of inserting a solid cluster in an equilibrated fluid and performing a number of NpT runs to determine at which pressure the cluster is critical, one can equilibrate the solid cluster in the NVT ensemble. In this way, the size of the solid cluster at the pressure $\langle p^* \rangle$ is obtained from a single equilibrium run. After this is done, one can use the machinery of Seeding (or more precisely Eq.2.10) to estimate J. We shall denote this approach as NVT-Seeding. We shall now estimate nucleation rates, simply using the results for the equilibrium solid clusters presented in Table 2.1 (plus performing additional simulations to estimate $\Delta\mu$ and D_{liq}). All the results required to determine J from the equilibrium solid clusters of this work are presented in Table 2.3

Values of the nucleation rate J computed in this work are presented in the last column of Table 2.3, whereas in Fig. 2.10 we compare them with our previous work[49,62] as well as other numerical[44,46] and experimental[82–85] independent estimations. Given that J goes to zero when the pressure tends to its coexistence value, in Fig. 2.10, we show only the highest nucleation rates. The results obtained for J from the equilibrium clusters of this work, agree quite well with previous results obtained from simulation techniques[44,46,47,62,86]. However the results of this work clearly contradict those found in experiments, providing further evidence that the experimental values presented as homogeneous nucleation rates are probably affected by heterogeneous nucleation events, as recently suggested in Ref.[87]. Previously mentioned nucleation studies of HS sampled the region of high pressures, typically above $p^* > 15$ (i.e. $\phi = (\pi/6)\rho^* > 0.52$). The results of this work expand the study to lower pressures (i.e. between $p^* = 12$ and

Label	ρ^*_{liq}	ρ^*_{sol}	$\lvert\Delta\mu\rvert/kT$	γ^*	$\Delta G/kT$	$D_{liq}/(\sigma^2/\tau)$	$f^+/(6D_{liq}/\sigma^2)$	$\log_{10}[J/(6D_{liq}/\sigma^5)]$
I	0.970	1.074	0.1566	0.634	150.7	0.0183	9904	-63
II	0.967	1.071	0.1383	0.628	189.1	0.0190	12520	-79
III	0.964	1.068	0.1242	0.623	230.9	0.0195	15360	-97
IV	0.962	1.065	0.1092	0.628	306.0	0.0201	20192	-130
V	0.959	1.061	0.0931	0.617	400.5	0.0207	26869	-171
VI	0.958	1.060	0.0869	0.614	456.3	0.0209	30684	-195
VII	0.956	1.057	0.0750	0.603	583.3	0.0213	39879	-250
VIII	0.954	1.055	0.0658	0.606	775.0	0.0217	52594	-333
IX	0.953	1.054	0.0609	0.600	879.3	0.0219	60242	-378
X	0.949	1.049	0.0362	0.587	2350.6	0.0228	164176	-1017

Table 2.3: Results from NVT-seeding calculations as obtained from the simulations of this work.

$p^* = 13.2$ (i.e. $0.5 < \phi < 0.515$), closer to the coexistence pressure.

The NVT-seeding approach does not only work for nucleation of solid HS. We have also shown recently that this approach is also working for an entirely different problem (the cavitation of a bubble in a Lennard-Jones fluid at negative pressures)[30]. This NVT-seeding approach allows to study easily nucleation along isotherms (NpT-seeding can be implemented easily both along isobars and along isotherms). However, it has two drawbacks. The first one is that it cannot be applied to small solid clusters as it is impossible to have them in a stable configuration in the NVT ensemble. The second is that there may be finite size effects, as the ratio $\langle N_{sol}\rangle/N$ cannot be changed at will. For instance for a solid cluster of HS at equilibrium in the NVT ensemble with $\langle N_{sol}\rangle = 3200$ particles we found $\langle N_{sol}\rangle/N = 0.16$. In the NpT-seeding approach, this ratio can be made arbitrarily low (we typically set it to $\langle N_{sol}\rangle/N < 0.05$ in our previous work). We found that the pressure at which the cluster was critical in the NVT system was $p^* \sim 12.95$ whereas it was found to be $p^* \sim 13.05$ in the NpT ensemble when $\langle N_{sol}\rangle/N$ was small. The finite size effects on HS is not dramatic (less than one per cent for the pressure at which the cluster is critical) but one should be aware of their presence.

2.5. Conclusions

In this work, we extend the simulations pioneered by Binder and coworkers[2,5,19–27] and recently used by Richard et al. also for HS to study a curved interface[14]. In particular, we have considered the possibility of having a stable spherical solid cluster in equilibrium with a fluid, for the hard spheres system. We were able to obtain equilibrium for up to ten different clusters with sizes ranging from 1900 to 130000 particles.

After the equilibrium configuration was found, we launched NpT runs and found that the clusters were critical at the average pressure found in the NVT run. Accordingly, all properties that can be inferred from critical clusters in unstable equilibrium

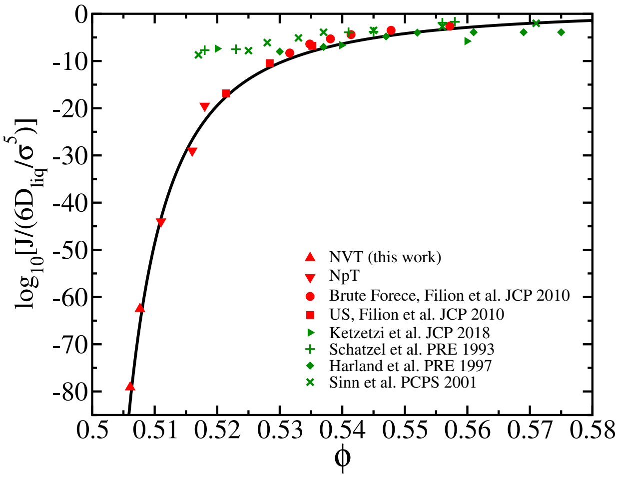

Figure 2.10: Nucleation rate against volume fraction (defined as $\phi \equiv \rho^* \pi/6$) from different sources. Experimental and numerical results are shown in green and red, respectively. The black line is a fit using CNT equations accounting for the interfacial free energy variation with the radius of the cluster as proposed in Ref.[49]. As stated in the caption of Fig. 2.8 points labeled as NpT in the legend come from previous work[49,62].

with the fluid in the NpT ensemble coincide with those obtained from clusters in stable/metastable equilibrium in the NVT ensemble. We show this equivalence for the cluster radius as well as for γ and the nucleation rate obtained from a Seeding analysis (CNT fed by microscopic parameters of the clusters measured in the simulations). Therefore, whereas the system is in a minimum of F in the NVT ensemble, the fact that the solid cluster is critical indicates that the system is in a maximum of G in the NpT ensemble. This is in agreement with a recent NVT-Seeding study of bubble cavitation[30].

In addition, we study the variation of γ with R_s, the relevant dividing surface in CNT. Recently, we showed by means of simulations of critical clusters in the NpT ensemble that such variation is well described by a linear fit of γ versus $1/R_s$ and obtained a characteristic length δ_T as a fitting parameter[49]. In this paper we show that the fit obtained in Ref.[49] works well for clusters equilibrated in the NVT ensemble as well. Moreover, we obtain the Tolman length as the difference between R_e, the Gibbs dividing surface, and R_s in the limit of very large clusters. We obtain $R_e - R_s$ for the clusters equilibrated in the NVT ensemble and extrapolate the difference to infinite radius. With this procedure we estimate the Tolman length, δ_{Tolman}. We find that δ_{Tolman} coincides with the δ_T parameter obtained from the fit of γ_s versus $(1/R_s)$ above mentioned.

We hope this work will encourage further research on the fascinating (but arguably difficult) issue of the change of the interfacial free energy between two phases separated by a curved interface.

2.6. Acknowledgments

This work was funded by Grant FIS2016-78117-P of the MEC and by project UCM-GR17-910570 from UCM. P. M. de H. acknowledges financial support from the FPI grant No. BES-2017-080074. J. R. E. acknowledges funding and support from the Oppenheimer Research Fellowship and from the Emmanuel College Research Fellowship. V.B. acknowledges the support from the European Commission through the Marie Skłodowska-Curie Fellowship No. 748170 ProFrost. C.V would like to thank Dr. Mario Alvarez and Dr. Aurora Rodriguez for their help in the last two years. Without them this work would have not been possible. We would like to dedicate this paper to the memory of Prof. John Rowlinson who passed away in 2018.

Bibliography

[1] Edgar M Blokhuis and Joris Kuipers. Thermodynamic expressions for the tolman length. *J. Chem. Phys.*, 124(7):074701, 2006.

[2] Benjamin J Block, Subir K Das, Martin Oettel, Peter Virnau, and Kurt Binder. Curvature dependence of surface free energy of liquid drops and bubbles: A simulation study. *J. Chem. Phys.*, 133(15):154702, 2010.

[3] J. G. Sampayo, A. Malijevsky, E. A. Muller, E. de Miguel, and G. Jackson. Evidence for the role of fluctuations in the thermodynamics of nanoscale drops and the implications in computations of the surface tension. *J. Chem. Phys.*, 132:141101, 2010.

[4] A. Malijevsky and G. Jackson. A perspective on the interfacial properties of nanoscopic liquid drops. *J. Phys. Condens. Matt.*, 24:464121, 2012.

[5] A Tröster, M Oettel, B Block, P Virnau, and K Binder. Numerical approaches to determine the interface tension of curved interfaces from free energy calculations. *J. Chem. Phys.*, 136(6):064709, 2012.

[6] Hai Ming Lu and Qing Jiang. Size-dependent surface tension and tolman's length of droplets. *Langmuir*, 21(2):779–781, 2005.

[7] S. M. Thompson, K. E. Gubbins, J. P. R. B. Walton, R. A. R. Chantry, and J. S. Rowlinson. A molecular dynamics study of liquid drops. *J. Chem. Phys.*, 81:530, 1984.

[8] Bingqing Cheng and Michele Ceriotti. Communication: Computing the tolman length for solid-liquid interfaces. *J. Chem. Phys.*, 148(23):231102, 2018.

[9] Gabriel V Lau, Ian J Ford, Patricia A Hunt, Erich A Müller, and George Jackson. Surface thermodynamics of planar, cylindrical, and spherical vapour-liquid interfaces of water. *J. Chem. Phys.*, 142(11):114701, 2015.

[10] J. Vrabec, G. K. Kedia, G. Fuchs, and H. Hasse. Comprehensive study of the vapour-liquid coexistence of the truncated and shifted lennard-jones fluid including planar and spherical interface properties. *Mol. Phys.*, 104:1509, 2006.

[11] O. Wilhelmsen, D. Bedeaux, and D. Reguera. Tolman length and rigidity constants of the lennard-jones fluid. *J. Chem. Phys.*, 142:064706, 2015.

[12] M. N. Joswiak, R Do, M. F. Doherty, and B. Peters. Energetic and entropic components of the tolman length for mw and tip4p/2005 water nanodroplets. *J. Chem. Phys.*, 145:204703, 2016.

[13] J. W. P. Schmelzer, A. S. Abyzov, and V. G. Baidakov. Entropy and the tolman parameter in nucleation theory. *Entropy*, 21:670, 2019.

[14] David Richard and Thomas Speck. Crystallization of hard spheres revisited. ii. thermodynamic modeling, nucleation work, and the surface of tension. *J. Chem. Phys.*, 148(22):224102, 2018.

[15] KGSH Gunawardana and Xueyu Song. Theoretical prediction of crystallization kinetics of a supercooled lennard-jones fluid. *J. Chem. Phys.*, 148(20):204506, 2018.

[16] Azat O Tipeev. Comment on 'theoretical prediction of crystallization kinetics of a supercooled lennard-jones fluid [j. chem. phys. 148, 204506 (2018)]'. *J. Chem. Phys.*, 151(1):017101, 2019.

[17] KGSH Gunawardana and Xueyu Song. Response to 'comment on theoretical prediction of crystallization kinetics of a supercooled lennard-jones fluid [j. chem. phys. 151, 017101 (2019)]'. *J. Chem. Phys.*, 151(1):017102, 2019.

[18] P. Bryk, R. Roth, K. R. Mecke, and S. Dietrich. Hard-sphere fluids in contact with curved substrates. *Phys. Rev. E*, 68:031602, 2003.

[19] Manuel Schrader, Peter Virnau, and Kurt Binder. Simulation of vapor-liquid coexistence in finite volumes: A method to compute the surface free energy of droplets. *Phys. Rev. E*, 79(6):061104, 2009.

[20] M Schrader, P Virnau, D Winter, T Zykova-Timan, and K Binder. Methods to extract interfacial free energies of flat and curved interfaces from computer simulations. *Eur. Phys. J. Spec. Top.*, 177(1):103–127, 2009.

[21] Kurt Binder, Benjamin J Block, Peter Virnau, and Andreas Tröster. Beyond the van der waals loop: What can be learned from simulating lennard- jones fluids inside the region of phase coexistence. *Am. J. Phys.*, 80(12):1099–1109, 2012.

[22] Antonia Statt, Peter Virnau, and Kurt Binder. Finite-size effects on liquid-solid phase coexistence and the estimation of crystal nucleation barriers. *Phys. Rev. Lett.*, 114(2):026101, 2015.

[23] A Tröster and K Binder. Positive tolman length in a lattice gas with three-body interactions. *Phys. Rev. Lett.*, 107(26):265701, 2011.

[24] Peter Koß, Antonia Statt, Peter Virnau, and Kurt Binder. The phase coexistence method to obtain surface free energies and nucleation barriers: a brief review. *Mol. Phys.*, 116(21-22):2977–2986, 2018.

[25] Peter Koß, Antonia Statt, Peter Virnau, and Kurt Binder. Free-energy barriers for crystal nucleation from fluid phases. *Phys. Rev. E*, 96(4):042609, 2017.

[26] Peter Virnau, Fabian Schmitz, and Kurt Binder. The ensemble switch method and related approaches to obtain interfacial fre e energies between coexisting phases from simulations: a brief review. *Mol. Simulat.*, 42(6-7):549–562, 2016.

[27] Andreas Troster, Fabian Schmitz, Peter Virnau, and Kurt Binder. Equilibrium between a droplet and surrounding vapor: A discussion of finite size effects. *J. Phys. Chem. B*, 122(13):3407–3417, 2017.

[28] Luis G. MacDowell, Peter Virnau, Marcus MÃ¼ller, and Kurt Binder. The evaporation/condensation transition of liquid droplets. *J. Chem. Phys.*, 120:5293, 2004.

[29] Luis G MacDowell, Vincent K Shen, and Jeffrey R Errington. Nucleation and cavitation of spherical, cylindrical, and slablike droplets and bubbles in small systems. *J. Chem. Phys.*, 125(3):034705, 2006.

[30] P Rosales-Pelaez, I Sanchez-Burgos, C Valeriani, C Vega, and E Sanz. Seeding approach to nucleation in the nvt ensemble: the case of bubble cavitation in overstretched lennard jones fluids. *Phys. Rev. E*, 101:022611, 2020.

[31] J. R. Espinosa, C. Navarro, E. Sanz, C. Valeriani, and C. Vega. On the time required to freeze water. *J. Chem. Phys.*, 145(21):211922, 2016.

[32] D. T. Limmer and D. Chandler. Time scales of supercooled water and implications for reversible polyamorphism. *Mol. Phys.*, 113:2799, 2015.

[33] Jeremy C. Palmer, Fausto Martelli, Yang Liu, Roberto Car, Athanassios Z. Panagiotopoulos, and Pablo G. Debenedetti. Metastable liquid-liquid transition in a molecular model of water. *Nature*, 510(7505):385–388, 2014.

[34] John Shipley Rowlinson and Benjamin Widom. *Molecular theory of capillarity*. Oxford University Press, 1982.

[35] For a general interface the Laplace equations is $\Delta p = \gamma_s(1/R_1 + 1/R_2)$, where R_1 and R_2 represent the principal radii of curvature.

[36] J. G. Kirkwood and F. P. Buff. The statistical mechanical theory of surface tension. *J. Chem. Phys.*, 17:338, 1949.

[37] G A Chapela, G Saville, S M Thompson, and J S Rowlinson. Computer simulation of a gas¿liquid surface. part 1. *J. Chem. Soc.*, 2:1133, 1977.

[38] Brian B. Laird, Ruslan L. Davidchack, Yang Yang, and Mark Asta. Determination of the solid-liquid interfacial free energy along a coexistence line by gibbs cahn integration. *J. Chem. Phys.*, 131(11):114110, 2009.

[39] T. Dreher, N. Pineau, E. Bourasseau, P. Malfreyt, L. Soulard, and C. A. Lemarchand. Anisotropic surface stresses of a solid/fluid interface: Molecular dynamics calculations for the copper/methane interface. *J. Chem. Phys.*, 151:244703, 2019.

[40] E. M. Blokhuis and D. Bedeaux. Pressure tensor of a spherical interface. *J. Chem. Phys.*, 97:3576, 1992.

[41] Luisa Ickes, Andre Welti, Corinna Hoose, and Ulrike Lohmann. Classical nucleation theory of homogeneous freezing of water: thermodynamic and kinetic parameters. *Phys. Chem. Chem. Phys.*, 17:5514–5537, 2015.

[42] Laszlo Granasy, Tamas Pusztai, and Peter F. James. Interfacial properties deduced from nucleation experiments: A cahn–hilliard analysis. *J. Chem. Phys.*, 117(13):6157–6168, 2002.

[43] J. W. P. Schmelzer, A. S. Abyzov, E. B. Ferreira, and V. M. Fokin. Curvature dependence of the surface tension and crystal nucleation in liquids. *Int. J. Appl. Glass Sci.*, 10:57, 2019.

[44] S. Auer and D. Frenkel. Prediction of absolute crystal-nucleation rate in hard-sphere colloids. *Nature*, 409:1020, 2001.

[45] S. Auer and D. Frenkel. Quantitative prediction of crystal-nucleation rates for spherical colloids: a computational approach. *Annu. Rev. Phys. Chem.*, 55:333, 2004.

[46] L. Filion, M. Hermes, R. Ni, and M. Dijkstra. Crystal nucleation of hard spheres using molecular dynamics, umbrella sampl ing, and forward flux sampling: A comparison of simulation techniques. *J. Chem. Phys.*, 133(24):244115, 2010.

[47] L. Filion, R. Ni, D. Frenkel, and M. Dijkstra. Simulation of nucleation in almost hard-sphere colloids: The discrepancy between experiment and simulation persists. *J. Chem. Phys.*, 134(13):134901, 2011.

[48] A. K. Sharma and F. A. Escobedo. Nucleus-size pinning for determination of nucleation free-energy barriers and nucleus geometry. *J. Chem. Phys.*, 148:184101, 2018.

[49] P Montero de Hijes, Jorge R Espinosa, Eduardo Sanz, and Carl os Vega. Interfacial free energy of a liquid-solid interface: Its change with curvat ure. *J. Chem. Phys.*, 151(14):144501, 2019.

[50] Richard C Tolman. The effect of droplet size on surface tension. *J. Chem. Phys.*, 17(3):333–337, 1949.

[51] N Bruot and F. Caupin. Curvature dependence of the liquid-vapor surface tension beyond the tolman approximation. *Phys. Rev. Lett.*, 116:056102, 2016.

[52] D. Turnbull. Formation of crystal nuclei in liquid metals. *J. Appl. Phys.*, 21(10):1022–1028, 1950.

[53] D. Turnbull. Kinetics of solidification of supercooled liquid mercury droplets. *J. Chem. Phys.*, 20:411, 1952.

[54] M. Volmer and A. Weber. Keimbildung in ubersattigten gebilden. *Z. Phys. Chem.*, 119:277, 1926.

[55] R. Becker and W. Doring. Kinetische behandlung der keimbildung in ubersattigten dampfen. *Ann. Phys.*, 416:719–752, 1935.

[56] J Gibbs. *The Collected Works. Vol. 1. Thermodynamics.* Yale University Press, 1948.

[57] K. F. Kelton and A. L. Greer. *Nucleation in Condensed Matter.* Pergamon,Elsevier,Oxford, 2010.

[58] S. Jungblut and C. Dellago. Pathways to self-organization: Crystallization via nucleation and growth. *Eur. Phys. J. E*, 39:77, 2016.

[59] Xian-Ming Bai and Mo Li. Calculation of solid-liquid interfacial free energy: A classical nucleation theory based approach. *J. Chem. Phys.*, 124(12):124707, 2006.

[60] Brandon C. Knott, Valeria Molinero, Michael F. Doherty, and Baron Peters. Homogeneous nucleation of methane hydrates: Unrealistic under realistic conditions. *J. Am. Chem. Soc.*, 134:19544–19547, 2012.

[61] E. Sanz, C. Vega, J. R. Espinosa, R. Caballero-Bernal, J. L. F. Abascal, and C. Valeriani. Homogeneous ice nucleation at moderate supercooling from molecular simulation. *J. Am. Chem. Soc.*, 135(40):15008–15017, 2013.

[62] Jorge R. Espinosa, Carlos Vega, Chantal Valeriani, and Eduardo Sanz. Seeding approach to crystal nucleation. *J. Chem. Phys.*, 144:034501, 2016.

[63] Jorge R. Espinosa, Alberto Zaragoza, Pablo Rosales-Pelaez, Caridad N avarro, Chantal Valeriani, Carlos Vega, and Eduardo Sanz. Interfacial free energy as the key to the pressure-induced deceleration o f ice nucleation. *Phys. Rev. Lett.*, 117:135702, 2016.

[64] Y Sun, H Song, F Zhang, L Yang, Z Ye, M. I. Mendelev, C. Wang, and K. Ho. Overcoming the time limitation in molecular dynamics simulation of crystal nucleation: a persistent-embryo approach. *Phys.Rev.Lett.*, 120:085703, 2018.

[65] Azat O Tipeev, Edgar D Zanotto, and José P Rino. Diffusivity, interfacial free energy, and crystal nucleation in a supercool ed lennard-jones liquid. *J. Phys. Chem. C*, 122(50):28884–28894, 2018.

[66] Nils ER Zimmermann, Bart Vorselaars, Jorge R Espinosa, David Quigley, William R Smith, Eduardo Sanz, Carlos Vega, and Baron Peters. Nacl nucleation from brine in seeded simulations: Sources of uncertainty in rate estimates. *J. Chem. Phys.*, 148(22):222838, 2018.

[67] J. R. Espinosa, E. Sanz, C. Valeriani, and C. Vega. Homogeneous ice nucleation evaluated for several water models. *J. Chem. Phys.*, 141:18C529, 2014.

[68] Alberto Zaragoza, Maria M. Conde, Jorge R. Espinosa, Chantal Valeri ani, Carlos Vega, and Eduardo Sanz. Competition between ices ih and ic in homogeneous water freezing. *J. Chem. Phys.*, 143(13):134504, 2015.

[69] J. Jover, A. J. Haslam, A. Galindo, G. Jackson, and E. A. Muller. Pseudo hard-sphere potential for use in continuous molecular-dynamics simulation of spherical and chain molecules. *J. Chem. Phys.*, 137(14):144505, 2012.

[70] B. Hess, C. Kutzner, D. van der Spoel, and E. Lindahl. Algorithms for highly efficient, load-balanced, and scalable molecular simulation. *J. Chem. Theory Comput.*, 4:435–447, 2008.

[71] P Rosales-Pelaez, P Montero de Hijes, E Sanz, and C Valeriani. Avalanche mediated devitrification in a glass of pseudo hard-spheres. *J. Stat. Mech.: Theory Exp.*, 2016(9):094005, 2016.

[72] Jorge R Espinosa, Eduardo Sanz, Chantal Valeriani, and Carlos Vega. On fluid-solid direct coexistence simulations: The pseudo-hard sphere model. *J. Chem. Phys.*, 139(14):144502, 2013.

[73] J. R. Espinosa, C. Vega, and E. Sanz. The mold integration method for the calculation of the crystal-fluid interfacial free energy from simulations. *J. Chem. Phys.*, 141(13):134709, 2014.

[74] Wolfgang Lechner and Christoph Dellago. Accurate determination of crystal structures based on averaged local bond order parameters. *J. Chem. Phys.*, 129(11):114707, 2008.

[75] D. Frenkel and B. Smit. *Understanding Molecular Simulation.* Academic Press, London, 1996.

[76] J. S. Rowlinson. Thermodynamics of inhomogeneous systems. *Pure Appl. Chem.*, 65:873, 1993.

[77] Alessandro Barducci, Giovanni Bussi, and Michele Parrinello. Well-tempered metadynamics: A smoothly converging and tunable free-energy method. *Phys. Rev. Lett.*, 100:020603, Jan 2008.

[78] C Vega, E Sanz, J L F Abascal, and E G Noya. Determination of phase diagrams via computer simulation: methodology and applications to water, electrolytes and proteins. *J. Phys.: Condens. Matter*, 20(15):153101, 2008.

[79] D. Kashchiev. *Nucleation: Basic Theory with Applications.* Butterworth-Heinemann, Oxford, 2000.

[80] Ruslan L. Davidchack, James R. Morris, and Brian B. Laird. The anisotropic hard-sphere crystal-melt interfacial free energy from fluctuations. *J. Chem. Phys.*, 125:094710, 2006.

[81] Ruslan L Davidchack and Brian B Laird. Crystal structure and interaction dependence of the crystal-melt interfacial free energy. *Phys. Rev. Lett.*, 94(8):086102, 2005.

[82] Stefania Ketzetzi, John Russo, and Daniel Bonn. Crystal nucleation in sedimenting colloidal suspensions. *J. Chem. Phys.*, 148(6):064901, 2018.

[83] Klaus Schätzel and Bruce J Ackerson. Density fluctuations during crystallization of colloids. *Phys. Rev. E*, 48(5):3766, 1993.

[84] C Sinn, A Heymann, A Stipp, and T Palberg. Solidification kinetics of hard-sphere colloidal suspensions. In *Trends in Colloid and Interface Science XV*, pages 266–275. Springer, 2001.

[85] J. L. Harland and W. van Megen. Crystallization kinetics of suspensions of hard colloidal spheres. *Phys. Rev. E*, 55:3054, 1997.

[86] David Richard and Thomas Speck. Crystallization of hard spheres revisited. i. extracting kinetics and free energy landscape from forward flux sampling. *J. Chem. Phys.*, 148:124110, 2018.

[87] J. R. Espinosa, C. Vega, C. Valeriani, D. Frenkel, and E. Sanz. Heterogeneous versus homogeneous crystal nucleation of hard spheres. *Soft Matter*, 15:9599, 2019.

Chapter 3

The Young-Laplace equation for a solid-liquid interface

P. Montero de Hijes[1], K. Shi[2], E. G. Noya[3], E. E. Santiso[2], K. E. Gubbins[2], E. Sanz[1], and C. Vega[1]

[1] Faculty of Chemistry, Chemical Physics Department, Universidad Complutense de Madrid, Plaza de las Ciencias, Ciudad Universitaria, Madrid 28040, Spain

[2] Department of Chemical and Biomolecular Engineering, North Carolina State University, Raleigh, North Carolina 27606, United States

[3] Instituto de Química Física Rocasolano, Consejo Superior de Investigaciones Científicas, CSIC, Calle Serrano 119, 28006 Madrid, Spain

3.1. Abstract

The application of the Young-Laplace equation to a solid-liquid interface is considered. Computer simulations show that the pressure inside a solid cluster of hard spheres is smaller than the external pressure of the liquid (both for small and large clusters). That would suggest a negative value for the interfacial free energy. We show that in a Gibbsian description of the thermodynamics of a curved solid-liquid interface in equilibrium, the choice of the thermodynamic (rather than mechanical) pressure is required, as suggested by Tolman for the liquid-gas scenario. With this definition, the interfacial free energy is positive, and the values obtained are in excellent agreement with previous results from nucleation studies. Although for a curved fluid-fluid interface there is no distinction between mechanical and thermal pressures (for a sufficiently large inner phase), in the solid-liquid they do not coincide, as hypothesized by Gibbs.

3.2. Introduction

Under certain conditions (i.e. constant number of particles N, volume V, and temperature T) it is possible to have a spherical phase in equilibrium with another phase around it. There, the Helmholtz free energy F is a local/global minimum representing a metastable/stable equilibrium state[1–8]. This equilibrium implies that T and chemical potential μ are homogeneous. Thus, $\nabla T(\mathbf{r}) = 0$ and $\nabla \mu(\mathbf{r}) = 0$ where $\mathbf{r}$ is the position vector. However, the number density $\rho(\mathbf{r}) = dN(\mathbf{r})/dV(\mathbf{r})$ and the pressure tensor $\mathbf{p}(\mathbf{r})$ are inhomogeneous[9,10]. By taking the center of mass of the cluster (COM) as origin and using spherical coordinates,

$$\mathbf{p}(\mathbf{r}) = \mathbf{p_N}(\mathbf{r})[\mathbf{e_r}\mathbf{e_r}] + \mathbf{p_T}(\mathbf{r})[\mathbf{e}_\theta\mathbf{e}_\theta + \mathbf{e}_\phi\mathbf{e}_\phi], \tag{3.1}$$

where $\mathbf{e_r}$, $\mathbf{e}_\theta$, and $\mathbf{e}_\phi$ are the unitary vectors. Then, the condition of mechanical equilibrium, $\nabla \cdot \mathbf{p} = 0$, implies[9–11]

$$p_T(r) = p_N(r) + \frac{r}{2}\frac{dp_N}{dr}. \tag{3.2}$$

In the late 70's and 80's, Rusanov, Rowlinson, Gubbins and Telo da Gamma and coworkers, pioneered the application of computer simulations to study fluid-fluid spherical interfaces at equilibrium[1,11,12]. Lately, there has been a revival in the study of these systems[5,6,8,13–27], including also solid-fluid curved interfaces[4,7,28–31]. In fact, we have recently shown that the stable equilibrium observed in the NVT ensemble is an unstable equilibrium in the NpT ensemble that corresponds to a maximum in the Gibbs free energy G. Thus, nucleation can be studied via both stable and unstable equilibrium as they are two sides of the same coin[7,8].

The best thermodynamic description of a system with a curved interface in equilibrium can be found in the book of Rowlinson and Widom[9,32]. Following in the spirit of Gibbs, one assumes two macroscopic phases that are homogeneous up to the interface and accounts for an additional contribution due to the interface itself. Taking into account that μ is homogeneous,

$$F = N\mu - p_{int}\frac{4}{3}\pi R^3 - p_{ext}(V - \frac{4}{3}\pi R^3) + 4\pi R^2\gamma, \tag{3.3}$$

where γ is the interfacial free energy, R the radius of the spherical phase, and p_{int} and p_{ext} the respective internal and external pressures.

At a molecular scale there is some arbitrariness in determining R. Since F, μ, p_{int}, and p_{ext} are fixed, changing R also changes γ. There are two popular choices for R. The first is the Gibbs dividing surface, $R = R_e$, for which the number of excess particles is zero (meaning that particles belong either to the solid or to the liquid, but not to the interfacial region). The second is the surface of tension, $R = R_s$, for which γ is a minimum (γ_s).

Actually, by taking the notational derivative (i.e. an arbitrary change in R without any physical change in the system) one obtains[9,32]:

$$p_{int} - p_{ext} = \frac{2\gamma}{R} + \left[\frac{d\gamma}{dR}\right]. \tag{3.4}$$

By definition, $[d\gamma/dR] = 0$ when $R = R_s$ leading to the celebrated Young-Laplace equation:

$$p_{int} - p_{ext} = \frac{2\gamma_s}{R_s} \tag{3.5}$$

Since γ_s is positive, this equation shows that the pressure inside the spherical phase is higher than outside and the difference depends on γ_s and R_s. Simulation studies of fluid-fluid phases by Gubbins and coworkers[11] and Vrabec and coworkers[33] have confirmed the higher pressure of the internal phase. However, this equation has not been tested for a solid-fluid curved interface. This is the goal of this letter.

3.3. Methodology

Recently, we simulated several solid clusters in equilibrium with a liquid[7] via the pseudo-hard-sphere PHS continuous potential[34] (hereafter simply HS) which allows to simulate with the standard molecular dynamics package GROMACS[35].

Here, for three selected clusters labeled as IV, VII, and VIII in our previous work[7] (see Ref.[7] for further details on the size of these solid clusters and the way they were obtained using NVT simulations), we launch new trajectories (in the NVT ensemble) saving configurations very often allowing us to compute the pressure tensor. Since the definition of the pressure tensor is locally arbitrary, we choose to use the Irving-Kirkwood[36] convention in which the forces between two particles act in the line connecting them. Further detail can be found in the supplementary material (SM). In addition, density profiles are provided.

The simulation details including interaction potential, GROMACS set up, and order parameter to label particles as solid or liquid are exactly the same as in our previous work[7]. We shall use here reduced units. Lengths are given in units of σ (i.e. the hard sphere diameter), densities as $\rho = N/V\sigma^3$, pressures in units of (kT/σ^3), interfacial free energies in units of kT/σ^2, and chemical potentials in units of kT. Pressure profiles are computed up to half of the simulation box $L/2$ whereas density profiles, following Ref.[37], cover the whole system.

3.4. Results

The density profile and the normal and tangential components of the pressure tensor are presented in Fig.3.1. The values of the densities of the solid and the liquid when they reach a plateau, and that of the pressure (far from the interface) are presented in Table 3.4. These are obtained by averaging the data from the corresponding plateaus.

Close to the interface the normal and tangential components of the pressure tensor are different, albeit far from it both are identical. Surprisingly, the pressure inside

Label	R_s	ρ_{sol}	ρ_{liq}	p_{sol}	p_{liq}	Δp
IV	10.791	1.0613	0.9619	12.6046	12.7437	-0.1391
VII	15.20	1.0548	0.9560	12.3053	12.4047	-0.0994
VIII	17.467	1.0529	0.9541	12.2199	12.3003	-0.0804

Table 3.1: Densities and pressures determined at the respective plateaus in the density and pressure profiles. The difference in pressure is also given as $\Delta p = p_{sol} - p_{liq}$. The notation of IV, VII, and VIII refers to the clusters labeled in this way in Ref.[7].

(solid) is smaller than outside (liquid). This result, in principle, contradicts the Young-Laplace equation. Notice though that having a lower pressure for the solid phase does not violate the mechanical equilibrium condition which only requires a certain relation between p_N and p_T (Eq.3.2).

This is opposite to the fluid-fluid curved interface. Actually, all previous studies on curved interfaces with fluid phases found higher pressure for the internal phase[1,11,12]. Here, for a solid spherical cluster we found lower pressure in the internal phase. One may think that this behavior is peculiar for HS, for which there are no attractive forces. However, recently, Gunawardana and Song[31] have reported a similar behavior for a solid cluster of Lennard-Jones particles surrounded by liquid.

Interestingly, one can already learn the behavior of the curved interface by analyzing the behavior of the pressure tensor for the planar interface. It turns out that in the interfacial region of a planar interface $p_T < p_N$ for fluid-fluid interfaces[38] and $p_T > p_N$ for solid-fluid interfaces[39]. Thus, a simple analysis of the behavior of the pressure tensor for the planar interface is sufficient to know if one will have higher or lower pressure in the internal spherical phase (see Eq.3.2). It is also interesting to point out that the pressure of the external phase, p_{ext}, is identical to the average pressure of the system, $\langle p \rangle$, obtained from the virial equation applied to the entire system provided that the normal and tangential components are identical at $L/2$, as demonstrated in the SM.

Although one must accept the fact that the pressure inside a solid cluster is smaller than the pressure outside, the consequence of this appears to be dramatic as this would imply (apparently) from the Young-Laplace equation that γ is negative[40]. The Young-Laplace equation is explained in any textbook of physics, and now we have a problem about how to use it in the case of a solid cluster surrounded by liquid. How to reconcile the results of this work with the Young-Laplace equation? The key was provided by Tolman in his celebrated paper discussing the variation of γ with R in a droplet. In particular, there is a remark by Tolman[41] which we believe is highly important in this context. The remark is as follows (adapting his notation to this paper):

"In applying Eqs. (2.2) and (2.3) to very small droplets, it is to be noted that p_{int} and ρ_{int} are to be taken as the pressure and density for a large mass of internal phase in a condition at the temperature of interest to give the same value of μ as that of the vapor

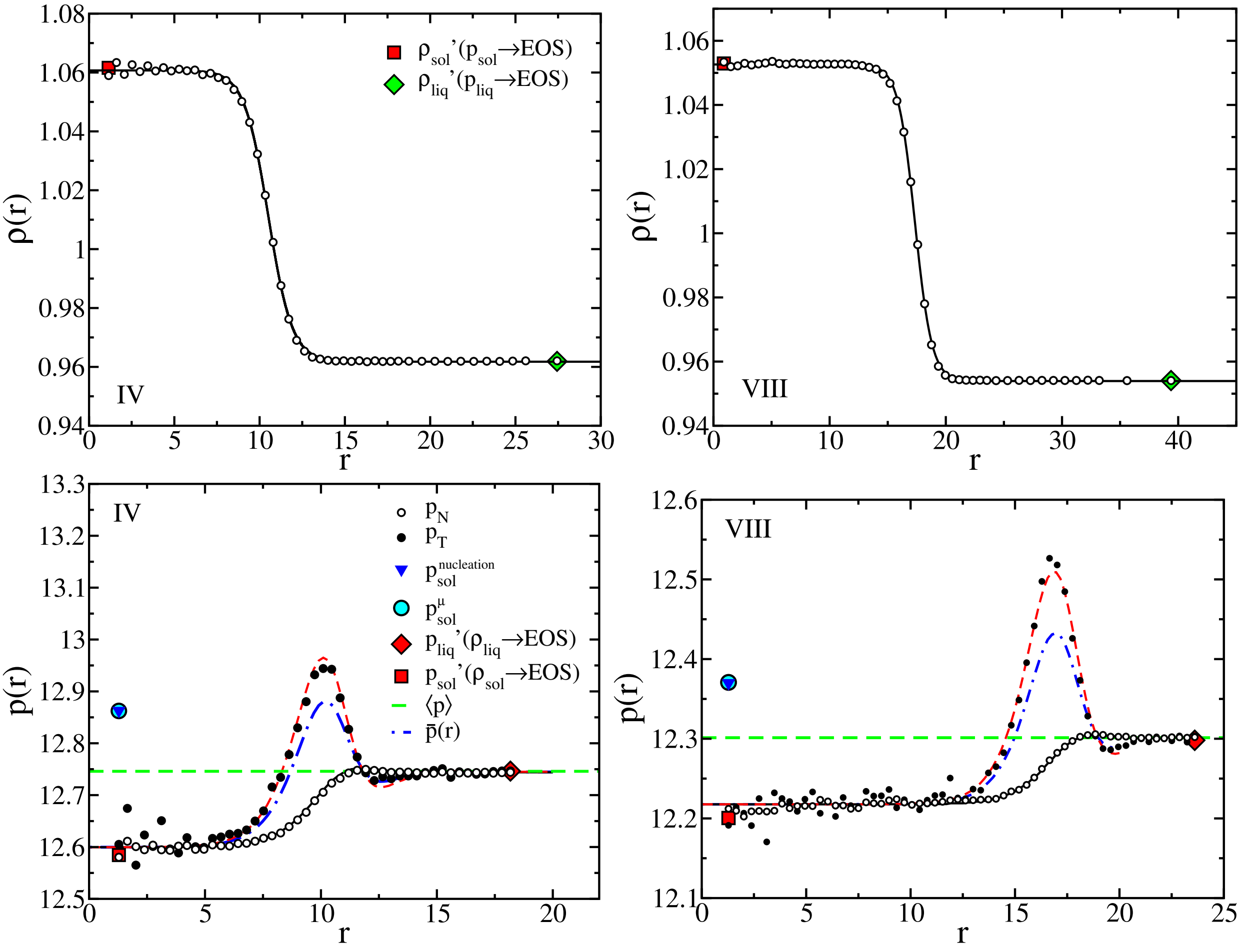

Figure 3.1: Radial density (top) and pressure (bottom) profiles from the COM for clusters IV (left) and VIII (right). For the meaning of p_{sol}^{μ} see the main text. $\langle p \rangle$ is the average pressure of the system as obtained from the virial theorem. $\bar{p}(r)$ is the average pressure at a distance r as given by $(2/3)p_T(r) + (1/3)p_N(r)$. The solid black line is a fit to p_N data, while the red dashed line is obtained from Eq.3.2 using the p_N fit. In the radial density plot we show the value ρ'_{sol}, which would be the density of a bulk solid at p_{sol}, and ρ'_{liq}, which would be the density of a bulk liquid at p_{liq}. In the pressure profile we show p'_{sol}, which would be the pressure of a bulk solid having the density ρ_{sol}, and p'_{liq}, which would be the density of a bulk liquid having the density ρ_{liq}. The value labeled as $p_{sol}^{nucleation}$ corresponds to $p_{sol}^{nucleation} = p_{liq} + 2\gamma_s/R_s$ when using the value of γ_s and R_s from nucleation studies[7].

(cf. Gibbs, reference 1, p. 253).”

Notice that Tolman was describing the equilibrium between a droplet of liquid in contact with its vapor. However, it also applies for the solid-liquid interface as we are about to show. Therefore, when using the formalism of Gibbs[42], the pressure of the internal spherical phase should not be taken as its actual value, but rather from that of a bulk having the same μ as the external phase. Similar reasoning was also used by ten Wolde and Frenkel[43].

Determining the exact value of μ of inhomogeneous systems of high density is very difficult[44] (notice though some recent progress[45]). Thus, we do not know the exact value of μ for the three systems considered in this work. However, to illustrate our main point this is not crucial. We shall assume that the external liquid has bulk behavior so that μ in the system corresponds to that of a bulk liquid at p_{liq}. In the inset of Fig.3.2 a), $\mu(p)$ for solid and liquid bulks are presented (obtained via thermodynamic integration[46] from $p = 11.648$ which is the coexistence pressure[47] where μ is identical in both phases).

Taking, for instance, system VIII where $p_{liq} = 12.3003$ and $p_{sol} = 12.2199$, it is possible to determine μ for a bulk liquid phase at this pressure, and also the pressure of a solid that has the same value of μ, which we found to be $p^{\mu}_{sol} = 12.37$. The superscript μ reminds us that this pressure is not the mechanical pressure of the solid, but rather the pressure of a bulk solid that has the same μ as that of a bulk liquid at p_{liq}. We shall denote this as the thermodynamical pressure (as opposed to the mechanical pressure p_{sol}). Notice that $p^{\mu}_{sol} > p_{liq} > p_{sol}$. This finding suggests that the cluster must be different to a perfect bulk at the same pressure p_{sol}, otherwise, μ could not be homogeneous and no equilibrium could be reached. In order to find differences, we followed the evolution of the closest particles to the COM finding that the solid cluster is a “living” structure that can melt in a certain region and grow in another while keeping the size approximately constant. As can be seen in Fig. 3.2 b), the selected particles ended up quite close to the interface and some of them changed their neighbor. This is likely due to the presence of vacancies in the cluster that lead to a relative diffusion. By computing such diffusion for the cluster as well as for solid bulks with and without vacancies at p^{VIII}_{sol}, we could estimate the cluster to have about one vacancy per four thousand particles (1/4000). More relevant is the distribution of distances from a given particle to its 12th closest neighbor considering only particles that fulfill COM $< r < 10\sigma$ in order to avoid surface effects (setting the upper limit in 7σ did not produce any difference). As shown in Fig. 3.2 c), such distribution is shifted to higher distances with respect to a bulk with and without vacancies indicating a tiny expansion in the cluster lattice. Further work is needed to completely understand this. Nevertheless, it is clear that the cluster is not identical to a bulk solid at the same mechanical pressure.

Therefore, for the solid-liquid interface the Young-Laplace equation must be written as:

$$p^{\mu}_{sol} - p_{liq} = \frac{2\gamma_s}{R_s} \tag{3.6}$$

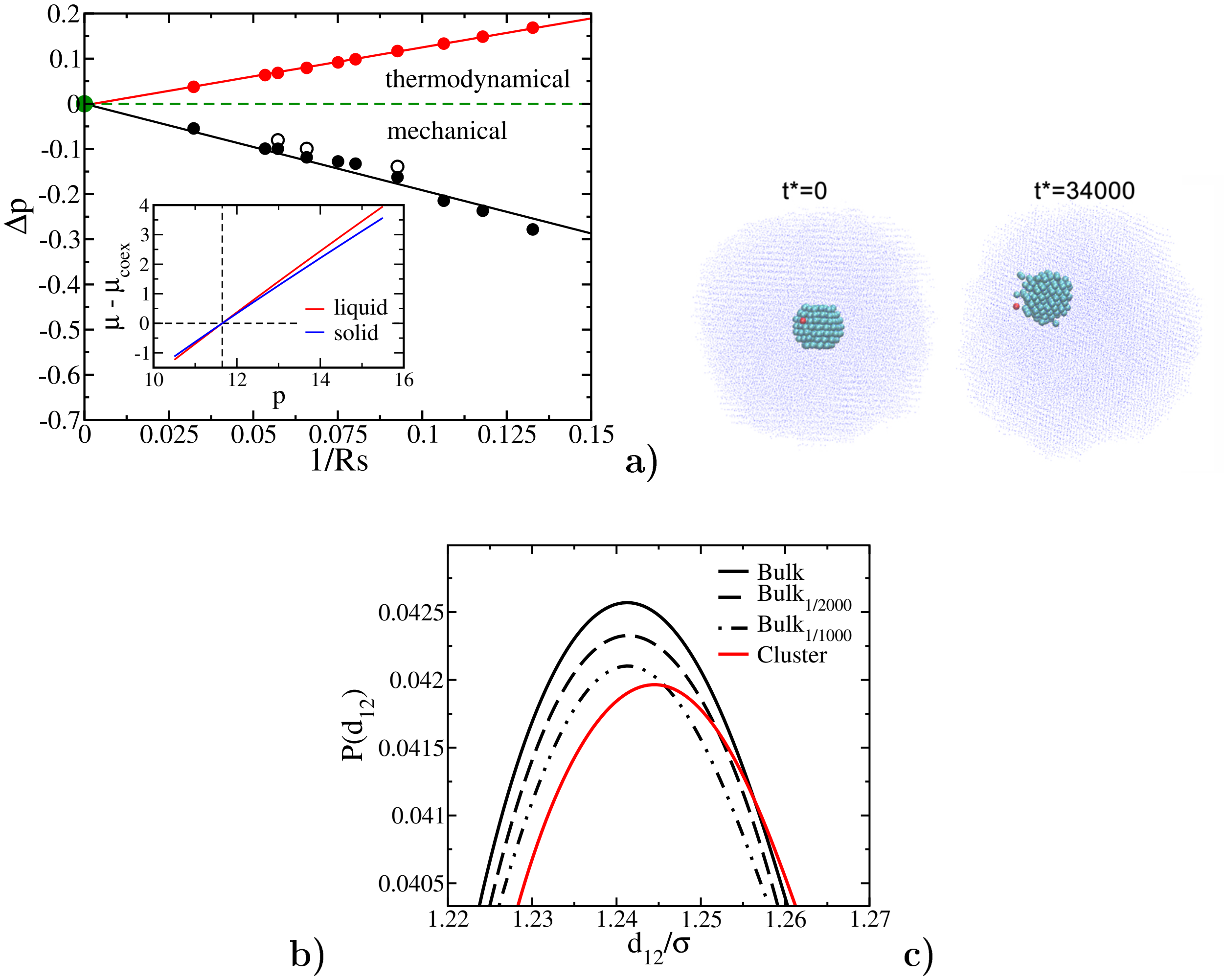

Figure 3.2: a) Difference in pressure between the solid cluster and the liquid as a function of $1/R_s$. Upper curve $p^{\mu}_{sol} - p_{liq}$. Lower curve $p_{sol} - p_{liq}$. Note that there are two sets for the mechanical Δp. Solid black circles are estimated (for all clusters in Ref.[7]) by using the respective densities and the equation of state (EOS), rather than by performing a more costly pressure tensor calculation, as was done for the empty circles. The former is systematically smaller than the latter suggesting that the cluster differs slightly from a bulk. In the inset of this panel, the chemical potential of both phases is shown. b) Snapshots of the solid cluster VIII in the initial configuration and after some time. Only solid particles within the system are shown. We followed the ten closest particles to the COM and their first coordination shells (cyan and red spheres). The remaining solid particles are shown as blue dots. In red, an example solid particle that changed neighbor. c) Maximum in the probability distribution function of the closest twelth neighbor considering cluster VIII and solid bulks with and without vacancies at p^{VIII}_{sol}. The ratios $1/1000$ and $1/2000$ mean the proportion of vacancy per number of particles for the considered bulks. Only the particles at COM $< r < 10\sigma$ were considered.

Label	R_s	p^{μ}_{sol}	Δp^{μ}	$2\gamma_s/R_s$[7]
IV	10.791	12.8627	0.1190	0.1164
VII	15.20	12.4846	0.0799	0.0793
VIII	17.467	12.3700	0.0697	0.0694

Table 3.2: Thermodynamic pressure of the solid and the difference with the pressure of the liquid phase (from Table 3.4). By using the values of γ_s from nucleation studies we estimated the term $2\gamma_s/R_s$, and found it to be in excellent agreement with the difference in pressure obtained when using p^{μ}.

In Table 3.2 the value of p^{μ}_{sol} for the three systems considered in this work is presented along with the difference in pressure $\Delta p^{\mu} = p^{\mu}_{sol} - p_{liq}$.

As can be seen, Δp^{μ} is positive. Thus, by using Tolman's suggestion one recovers a "normal" Young-Laplace equation. In previous work where the same clusters (IV, VII, and VIII) were studied, we obtained the values of γ_s from nucleation studies. Since, according to Eq.3.50, Δp^{μ} corresponds to $2\gamma_s/R_s$, it is of interest to analyze whether our previously reported values of γ_s and R_s are consistent with this difference of pressures. As shown in Table 3.2, results are fully consistent. Thus, the physical meaning of $2\gamma_s/R_s$ obtained for the values of γ_s and R_s from nucleation studies[7,48] is now clear. Note that for a fluid-fluid interface there is no difference between p^{μ}_{int} and p_{int} (for a sufficiently large inner phase) whereas in a solid-liquid system we could not find such agreement even for very large clusters. We have plotted the difference in pressure between solid and liquid as a function of $1/R_s$ in Fig. 3.2 a). As can be seen, there is no evidence that this difference can become positive for a certain value of R_s.

The idea that for the solid-liquid interface the difference in pressure between the phases may not lead to γ was already insinuated by Gibbs. Later, Cahn[49], Cammarata[50,51], and others[52] suggested that the strain, which is present in solids and not in fluids, was behind this.

3.5. Conclusions

In summary, we have computed the pressure tensor for a HS system at constant N, V and T where one has a stable solid cluster in contact with a liquid away from coexistence conditions. We found that the internal pressure (solid) is lower than the external one (liquid). That would lead to a negative γ. However, as suggested by Tolman (and insinuated by Gibbs), defining a thermal pressure for inner phase, which corresponds to that of a solid with the same chemical potential as the external liquid, allows to recover a normal Young-Laplace equation, where the pressure of the internal phase is higher, leading to a positive γ. The values of γ from this scheme are in excellent agreement with recent results from nucleation studies. Thus, for a solid-liquid interface one should distinguish between the mechanical and the thermodynamic pressure. This distinction is not so necessary for a fluid-fluid curved interface as they are comparable[25,51]. However, it is crucial in understanding the meaning of the Young-Laplace equation for a solid-fluid interface. Computer simulations have been the key to solve this subtle issue.

3.6. Acknowledgments

This work was funded by grants FIS2016-78117-P and PID2019-105898GB-C21 of the MEC, by project UCM-GR17-910570 from UCM, and by the USA National Science Foundation under Award No. CBET-1855465. PMdH acknowledges financial support from the FPI grant No. BES-2017-080074.

Supplementary Material

See the supplementary material for a description of the system and its interaction potential, details on the pressure tensor calculation, values for the fitting parameters as well as the demonstration that the average pressure in the system equals the external pressure. Additional figures and information can also be found.

Data Availability

The data that support the findings of this work are available within the article, and its supplementary material.

Bibliography

[1] DJ Lee, MM Telo da Gama, and KE Gubbins. A microscopic theory for spherical interfaces: liquid drops in the canonical ensemble. *The Journal of chemical physics*, 85(1):490–499, 1986.

[2] Anatoly I Rusanov. The thermodynamics of processes of new-phase formation. *Russ. Chem. Rev.*, 33:385–399, 1964.

[3] AK Shchekin, K Koga, and NA Volkov. The effect of a finite number of monomers available for aggregation at nucleation and micellization in a fixed volume. *J. Chem. Phys.*, 151(24):244903, 2019.

[4] Peter Koß, Antonia Statt, Peter Virnau, and Kurt Binder. The phase coexistence method to obtain surface free energies and nucleation barriers: a brief review. *Mol. Phys.*, 116(21-22):2977–2986, 2018.

[5] VG Baidakov. Phase equilibria in a microheterogeneous liquid–gas system: Gibbs capillary model. *Chemical Physics*, 525:110407, 2019.

[6] VG Baidakov and SP Protsenko. Computer simulation of nucleation in a liquid under tension. In *Doklady Physics*, volume 49, pages 69–72. Springer, 2004.

[7] P Montero de Hijes, Jorge R Espinosa, Valentino Bianco, Eduardo Sanz, and Carlos Vega. Interfacial free energy and tolman length of curved solid-liquid interfaces from equilibrium studies. *J.Phys.Chem.C*, 124:8795, 2020.

[8] P Rosales-Pelaez, I Sanchez-Burgos, C Valeriani, C Vega, and E Sanz. Seeding approach to nucleation in the nvt ensemble: the case of bubble cavitation in overstretched Lennard-Jones fluids. *Phys. Rev. E*, 101:022611, 2020.

[9] John Shipley Rowlinson and Benjamin Widom. *Molecular theory of capillarity.* Oxford University Press, 1982.

[10] J. S. Rowlinson. Thermodynamics of inhomogeneous systems. *Pure Appl. Chem.*, 65:873, 1993.

[11] S. M. Thompson, K. E. Gubbins, J. P. R. B. Walton, R. A. R. Chantry, and J. S. Rowlinson. A molecular dynamics study of liquid drops. *J. Chem. Phys.*, 81:530, 1984.

[12] AI Rusanov and EN Brodskaya. The molecular dynamics simulation of a small drop. *Journal of Colloid and Interface Science*, 62(3):542–555, 1977.

[13] A Tröster, M Oettel, B Block, P Virnau, and K Binder. Numerical approaches to determine the interface tension of curved interfaces from free energy calculations. *J. Chem. Phys.*, 136(6):064709, 2012.

[14] Benjamin J Block, Subir K Das, Martin Oettel, Peter Virnau, and Kurt Binder. Curvature dependence of surface free energy of liquid drops and bubbles: A simulation study. *J. Chem. Phys.*, 133(15):154702, 2010.

[15] Manuel Schrader, Peter Virnau, and Kurt Binder. Simulation of vapor-liquid coexistence in finite volumes: A method to compute the surface free energy of droplets. *Phys. Rev. E*, 79(6):061104, 2009.

[16] M Schrader, P Virnau, D Winter, T Zykova-Timan, and K Binder. Methods to extract interfacial free energies of flat and curved interfaces from computer simulations. *Eur. Phys. J. Spec. Top.*, 177(1):103–127, 2009.

[17] Kurt Binder, Benjamin J Block, Peter Virnau, and Andr eas Tröster. Beyond the van der waals loop: What can be learned from simulating Lennard-Jones fluids inside the region of phase coexistence. *Am. J. Phys.*, 80(12):1099–1109, 2012.

[18] A Tröster and K Binder. Positive tolman length in a lattice gas with three-body interactions. *Phys. Rev. Lett.*, 107(26):265701, 2011.

[19] Peter Virnau, Fabian Schmitz, and Kurt Binder. The ensemble switch method and related approaches to obtain interfacial fre e energies between coexisting phases from simulations: a brief review. *Mol. Simulat.*, 42(6-7):549–562, 2016.

[20] Andreas Troster, Fabian Schmitz, Peter Virnau, and Kurt Binder. Equilibrium between a droplet and surrounding vapor: A discussion of finite size effects. *J. Phys. Chem. B*, 122(13):3407–3417, 2017.

[21] Luis G. MacDowell, Peter Virnau, Marcus MÃ¼ller, and Kurt Binder. The evaporation/condensation transition of liquid droplets. *J. Chem. Phys.*, 120:5293, 2004.

[22] Luis G MacDowell, Vincent K Shen, and Jeffrey R Errington. Nucleation and cavitation of spherical, cylindrical, and slablike droplets and bubbles in small systems. *J. Chem. Phys.*, 125(3):034705, 2006.

[23] Øivind Wilhelmsen, Dick Bedeaux, Signe Kjelstrup, and David Reguera. Thermodynamic stability of nanosized multicomponent bubbles/droplets: The square gradient theory and the capillary approach. *J. Chem. Phys.*, 140(2):024704, 2014.

[24] J. G. Sampayo, A. Malijevsky, E. A. Muller, E. de Miguel, and G. Jackson. Evidence for the role of fluctuations in the thermodynamics of nanoscale drops and the implications in computations of the surface tension. *J. Chem. Phys.*, 132:141101, 2010.

[25] A. Malijevsky and G. Jackson. A perspective on the interfacial properties of nanoscopic liquid drops. *J. Phys. Condens. Matt.*, 24:464121, 2012.

[26] Gabriel V Lau, Ian J Ford, Patricia A Hunt, Erich A Müller, and George Jackson. Surface thermodynamics of planar, cylindrical, and spherical vapour-liquid interfaces of water. *J. Chem. Phys.*, 142(11):114701, 2015.

[27] Sa Hoon Min and Max L Berkowitz. Bubbles in water under stretch-induced cavitation. *The Journal of chemical physics*, 150(5):054501, 2019.

[28] Antonia Statt, Peter Virnau, and Kurt Binder. Finite-size effects on liquid-solid phase coexistence and the estimation of crystal nucleation barriers. *Phys. Rev. Lett.*, 114(2):026101, 2015.

[29] Peter Koß, Antonia Statt, Peter Virnau, and Kurt Binder. Free-energy barriers for crystal nucleation from fluid phases. *Phys. Rev. E*, 96(4):042609, 2017.

[30] David Richard and Thomas Speck. Crystallization of hard spheres revisited. ii. thermodynamic modeling, nucleation work, and the surface of tension. *J. Chem. Phys.*, 148(22):224102, 2018.

[31] KGSH Gunawardana and Xueyu Song. Theoretical prediction of crystallization kinetics of a supercooled Lennard-Jones fluid. *J. Chem. Phys.*, 148(20):204506, 2018.

[32] S. Kondo. Thermodynamical fundamental equation for spherical interface. *J.Chem.Phys.*, 25:662, 1956.

[33] J. Vrabec, G. K. Kedia, G. Fuchs, and H. Hasse. Comprehensive study of the vapour-liquid coexistence of the truncated and shifted Lennard-Jones fluid including planar and spherical interface properties. *Mol. Phys.*, 104:1509, 2006.

[34] J. Jover, A. J. Haslam, A. Galindo, G. Jackson, and E. A. Muller. Pseudo hard-sphere potential for use in continuous molecular-dynamics simulation of spherical and chain molecules. *J. Chem. Phys.*, 137(14):144505, 2012.

[35] B. Hess, C. Kutzner, D. van der Spoel, and E. Lindahl. Algorithms for highly efficient, load-balanced, and scalable molecular sim ulation. *J. Chem. Theory Comput.*, 4:435–447, 2008.

[36] J. H. Irving and J. G. Kirkwood. The statistical mechanical theory of transport processes. iv. the equations of hydrodynamics. *J. Chem. Phys.*, 18(X):817, 1950.

[37] Markus Deserno. *How to calculate a three-dimensional g(r) under periodic boundary conditions*, 2004. www.cmu.edu/biolphys/deserno/pdf/gr$_p$*eriodic.pdf*.

[38] A. Trokhymchuk and J. Alejandre. Computer simulations of liquid/vapor interface in Lennard-Jones fluids: Some questions and answers. *J. Chem. Phys.*, 111(X):8510, 1999.

[39] R. L. Davidchack and B. Laird. Simulation of the hard-sphere crystal–melt interface. *J. Chem. Phys.*, 108(X):9452, 1998.

[40] Azat O Tipeev. Comment on ‘theoretical prediction of crystallization kinetics of a supercooled Lennard-Jones fluid [j. chem. phys. 148, 204506 (2018)]’. *J. Chem. Phys.*, 151(1):017101, 2019.

[41] Richard C Tolman. The effect of droplet size on surface tension. *J. Chem. Phys.*, 17(3):333–337, 1949.

[42] J Gibbs. *The Collected Works. Vol. 1. Thermodynamics.* Yale University Press, 1948.

[43] Pieter Rein ten Wolde and Daan Frenkel. Computer simulation study of gas-liquid nucleation in a Lennard-Jones system. *J.Chem.Phys.*, 109:9901, 1998.

[44] J. G. Powles, S. E. Baker, and W. A. B. Evans. The chemical potential in atomically inhomogeneous fluids in external force fields by computer simulation. *J. Chem. Phys.*, 101(X):4098, 1994.

[45] C. Perego, O. Valsson, and M. Parrinello. Chemical potential calculations in non-homogeneous liquids. *J. Chem. Phys.*, 149(X):072305, 2018.

[46] C Vega, E Sanz, J L F Abascal, and E G Noya. Determination of phase diagrams via computer simulation: methodology and applications to water, electrolytes and proteins. *J. Phys.: Condens. Matter*, 20(15):153101, 2008.

[47] Jorge R Espinosa, Eduardo Sanz, Chantal Valeriani, and Carlos Vega. On fluid-solid direct coexistence simulations: The pseudo-hard sphere model. *J. Chem. Phys.*, 139(14):144502, 2013.

[48] P Montero de Hijes, Jorge R Espinosa, Eduardo Sanz, and Carlos Vega. Interfacial free energy of a liquid-solid interface: Its change with curvature. *J. Chem. Phys.*, 151(14):144501, 2019.

[49] John W Cahn. Surface stress and the chemical equilibrium of small crystals—i. the case of the isotropic surface. *Acta Metallurgica*, 28(10):1333–1338, 1980.

[50] R. C. Cammarata and K. Sieradzki. Surface and interface stresses. *Annu. Rev. Mater. Sci*, 24(X):215, 1994.

[51] R. C. Cammarata. Generalized thermodynamics of surfaces with applications to small solid systems. *Solid State Physics*, 61(X):1, 2009.

[52] Brian B. Laird, Ruslan L. Davidchack, Yang Yang, and Mark Asta. Determination of the solid-liquid interfacial free energy along a coexistence line by Gibbs-Cahn integration. *J. Chem. Phys.*, 131(11):114110, 2009.

3.7. Supporting Material

Equilibrium between a solid cluster and the fluid phase for hard spheres

In NVT runs it is possible to have an equilibrium between a solid cluster and the fluid phase. This has been shown in previous work.[1] In Fig.3.3 an equilibrium configuration is shown for the system labeled as IV in Ref.[1]

In the Gibbsian formalism one assumes that the interface has zero volume, but it may contain molecules which are denoted as excess particles. For a system of N particles, the number of internal (N_{int}), external (N_{ext}), and excess molecules (N_{exc}) are defined from the relation:

$$N_{exc} = N - N_{int} - N_{ext} = N - 4/3\pi R^3 \rho_{int} - (V - 4/3\pi R^3)\rho_{ext} \tag{3.7}$$

Since the chemical potential μ is uniform in the system, it holds that

$$(N_{int} + N_{ext} + N_{exc})\mu = N\mu \tag{3.8}$$

and that explains the origin of the term $N\mu$ in the expression of F of the main text.

Pressure tensor profile for spherical drop of liquid in contact with the vapor in the Lennard-Jones system

The pressure tensor profile of a liquid-gas curved interface is different from that presented in the main text for a solid-liquid curved interface. Here we present a figure from Ref.[2] to illustrate this point. As can be seen the tangential component of the pressure is smaller than the normal one in the proximity of the interface. That explains why the pressure of the liquid is higher than that of the vapor for a liquid-gas interface. Notice also that for a gas-liquid curved interface (e.g. a bubble inside a liquid) the pressure of the internal phase is also higher than the external pressure.[3] Thus, for a fluid-fluid curved interface the pressure of the internal phase is always higher than that of the external phase.

Spherical Pressure Tensor by the Irving-Kirkwood Definition

Derivation

The detailed derivation for the spherical pressure tensor has been discussed by Tjatjopoulos and Mann[4], but they only presented results for the normal pressure and one of the tangential components. Here we will present a full derivation for three diagonal elements in the spherical pressure tensor.

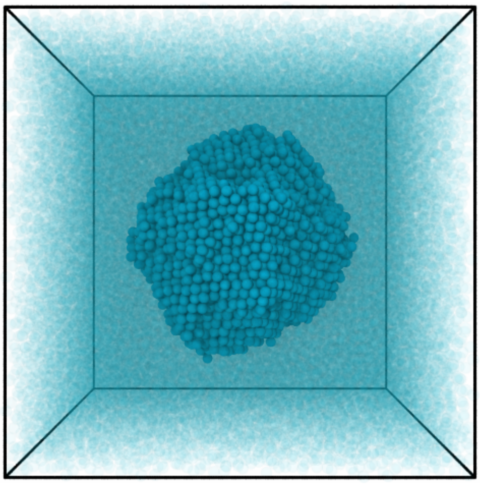

Figure 3.3: Snapshot

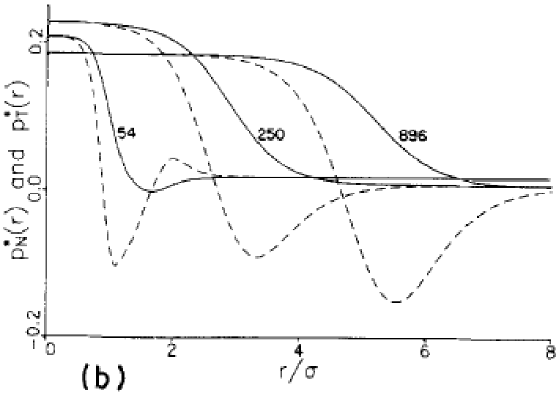

Figure 3.4: Pressure tensor profile of a Lennard-Jones spherical droplet at $T^* = 0.71$ (i.e. fluid-vapor interface). Dashed lines stand for the tangential pressure. Solid lines: Normal pressure. Figure adapted from Ref.[2]

In spherical coordinates, (r, θ, φ), due to the symmetry of the droplet, the local pressure tensor can be written as

$$\mathbf{p}\left(r\right) = p_N\left(r\right)\hat{e}_r\hat{e}_r + p_T\left(r\right)\left(\hat{e}_\theta\hat{e}_\theta + \hat{e}_\varphi\hat{e}_\varphi\right), \tag{3.9}$$

where $p_N = p_{rr}$ is the normal pressure in the radial direction; $p_T = p_{\theta\theta} = p_{\varphi\varphi}$ is the tangential pressure and the polar component, $p_{\theta\theta}$, is equivalent to the azimuthal component, $p_{\varphi\varphi}$. The orthogonal unit vectors are

$$\hat{e}_r = \begin{pmatrix} \sin\theta\cos\varphi \\ \sin\theta\sin\varphi \\ \cos\theta \end{pmatrix} \hat{e}_\theta = \begin{pmatrix} \cos\theta\cos\varphi \\ \cos\theta\sin\varphi \\ -\sin\theta \end{pmatrix} \hat{e}_\varphi = \begin{pmatrix} -\sin\varphi \\ \cos\varphi \\ 0 \end{pmatrix}. \tag{3.10}$$

If a system is under the condition of hydrostatic equilibrium and there is no external field, we have $\nabla \cdot \mathbf{p} = 0$, i.e.,

$$p_T\left(r\right) = p_N\left(r\right) + \frac{r}{2}\frac{dp_N\left(r\right)}{dr}. \tag{3.11}$$

The total pressure tensor is composed of two parts: the kinetic part and the configurational part. The kinetic part is well defined and is given by $\mathbf{p}^K\left(r\right) = \rho\left(r\right)k_BT\mathbf{1}$, where $\rho\left(r\right)$ is the number density at a radial position r; k_B is the Boltzmann constant, T is temperature and $\mathbf{1}$ is the second order unit tensor. For pairwise interactions, the configurational part is given by[5]

$$\mathbf{p}^C\left(\mathbf{r}\right) = \frac{1}{2}\left\langle \sum_{i\neq j}\mathbf{F}_{ij}\int_{C_{ij}} d\tilde{l}\delta\left(\mathbf{r} - \tilde{l}\right)\right\rangle, \tag{3.12}$$

where $\langle ... \rangle$ is the ensemble average; $\mathbf{F}_{ij}$ is the force vector between ij particle pair, and $\tilde{l}$ is a path vector integrated over the contour C_{ij}; prefactor $1/2$ is to account for double counting of particles. This integral contour is not uniquely defined. Here we adopt the choice of Irving and Kirkwood[2,6] which is a straight line connecting two interacting molecules. And such a path is given by

$$\tilde{l} = \mathbf{r}_i + \alpha\mathbf{r}_{ij}, \tag{3.13}$$

where position vector $\mathbf{r}_{ij} = \mathbf{r}_j - \mathbf{r}_i$. Parameters α varies from 0 to 1. Differentiating the contour vector $\tilde{l}$ gives,

$$d\tilde{l} = \mathbf{r}_{ij}d\alpha. \tag{3.14}$$

The delta function in Eq. 3.12 can be rewritten in spherical coordinates as

$$\delta\left(\mathbf{r} - \tilde{l}\right) = \frac{1}{r^2\sin\theta}\delta\left(r - r_l\right)\delta\left(\theta - \theta_l\right)\delta\left(\varphi - \varphi_l\right). \tag{3.15}$$

Substituting Eq. 3.15 into Eq. 3.12 gives

$$\mathbf{p}^C(\mathbf{r}) = \frac{1}{2}\left\langle \sum_{i\neq j} \frac{\mathbf{r}_{ij}}{r_{ij}} f_{ij} \frac{1}{r^2 \sin\theta} \int_{C_{ij}} d\tilde{l} \delta(r - r_l)\,\delta(\theta - \theta_l)\,\delta(\varphi - \varphi_l) \right\rangle, \tag{3.16}$$

where r_{ij} is the scalar distance between ij-pair; f_{ij} is the ij-pair force for isotropic interactions.

Normal (Radial) Pressure p_N

The normal pressure is only a function of the radial distance r. We need to perform an average of the normal pressure over both polar and azimuthal angles so as to integrate out unnecessary variables (θ, φ),

$$p_N^C(r) = \frac{1}{4\pi} \int_0^{2\pi} d\varphi \int_0^{\pi} \sin\theta d\theta \left[\hat{e}_r \cdot \mathbf{p}^C(\mathbf{r}) \cdot \hat{e}_r\right]. \tag{3.17}$$

The bracket double dot product term in Eq. 3.17 essentially takes the diagonal element p_{rr}^C out of the 2nd-order pressure tensor. Substituting Eq. 3.16 into Eq. 3.17 gives,

$$p_N^C(r) = \frac{1}{8\pi r^2} \left\langle \sum_{i\neq j} \int_0^{2\pi} d\varphi \int_0^{\pi} d\theta \int_{C_{ij}} d\tilde{l} \cdot \hat{e}_r \frac{\mathbf{r}_{ij} \cdot \hat{e}_r}{r_{ij}} f_{ij} \delta(r - r_l)\,\delta(\theta - \theta_l)\,\delta(\varphi - \varphi_l) \right\rangle. \tag{3.18}$$

Since

$$\int_{a-\varepsilon}^{a+\varepsilon} f(\alpha)\,\delta(\alpha - a)\,d\alpha = f(a), \varepsilon > 0, \tag{3.19}$$

we can perform the integration over polar and azimuthal angles and Eq. 3.18 becomes

$$p_N^C(r) = \frac{1}{8\pi r^2} \left\langle \sum_{i\neq j} \int_{C_{ij}} d\tilde{l} \cdot \hat{e}_{r,l} \frac{\mathbf{r}_{ij} \cdot \hat{e}_{r,l}}{r_{ij}} f_{ij} \delta(r - r_l) \right\rangle, \tag{3.20}$$

where $\hat{e}_{r,l}$ is the radial unit vector with $\theta = \theta_l$ and $\varphi = \varphi_l$. Using the differential in Eq. 3.14 and using the identity,

$$\int_c^d f(\alpha) d\alpha = \int_{-\infty}^{+\infty} f(\alpha) H(\alpha - c)\, H(d - \alpha)\, d\alpha. \tag{3.21}$$

Eq. 3.20 becomes

$$\begin{aligned} p_N^C(r) &= \frac{1}{8\pi r^2}\left\langle \sum_{i\neq j}\int_0^1 d\alpha \frac{(\mathbf{r}_{ij}\cdot\hat{e}_{r,l})^2}{r_{ij}} f_{ij}\delta(r-r_l)\right\rangle \\ &= \frac{1}{8\pi r^2}\left\langle \sum_{i\neq j}\int_{-\infty}^{+\infty} d\alpha \frac{(\mathbf{r}_{ij}\cdot\hat{e}_{r,l})^2}{r_{ij}} f_{ij}H(\alpha)H(1-\alpha)\delta(r-r_l)\right\rangle, \end{aligned} \tag{3.22}$$

where $H(x)$ is the Heaviside step function ($x \geq 0$, $H(x) = 1$; $x < 0$, $H(x) = 0$). Applying Eq. 3.19 and the identity

$$\delta[f(\alpha)] = \sum_k \frac{1}{|f'(\alpha_k)|}\delta(\alpha-\alpha_k), \tag{3.23}$$

where $f'(\alpha) = df/d\alpha$ and α_k is a simple root of $f(\alpha_k) = 0$, to Eq. 3.22 yields

$$\begin{aligned} p_N^C(r) &= \frac{1}{8\pi r^2}\left\langle \sum_{i\neq j}\int_{-\infty}^{+\infty} d\alpha \frac{(\mathbf{r}_{ij}\cdot\hat{e}_{r,l})^2}{r_{ij}} f_{ij}H(\alpha)H(1-\alpha)\sum_k \frac{1}{|\mathbf{r}_{ij}\cdot\hat{e}_{r,l}|}\delta(\alpha-\alpha_k)\right\rangle \\ &= \frac{1}{8\pi r^2}\left\langle \sum_{i\neq j}\sum_k \frac{|\mathbf{r}_{ij}\cdot\hat{e}_{r,\alpha_k}|}{r_{ij}} f_{ij}H(\alpha_k)H(1-\alpha_k)\right\rangle, \end{aligned} \tag{3.24}$$

recalling $r_l(\alpha) = \sqrt{(x_i+\alpha x_{ij})^2 + (y_i+\alpha y_{ij})^2 + (z_i+\alpha z_{ij})^2}$ and α_k are the roots of a quadratic equation, $r = r_l$, i.e.,

$$(\mathbf{r}_{ij})^2\alpha^2 + 2\alpha\mathbf{r}_i\cdot\mathbf{r}_{ij} + (\mathbf{r}_i)^2 - r^2 = 0. \tag{3.25}$$

If the discriminant of Eq. 3.25 is smaller than zero, there is no contribution to the surface r; if the discriminant is equal to zero, contour $\tilde{l}$ is tangent to the spherical surface of radius r, and $\mathbf{r}_{ij}\cdot\hat{e}_{r,\alpha_k} = 0$ thus there is no contribution to the surface r either. Only if the discriminant is larger than zero, the force between ij-pair then contributes to the local pressure. The radial unit vector $\hat{e}_{r,\alpha_k}$ at $\alpha = \alpha_k$ is given by

$$\hat{e}_{r,\alpha_k} = \begin{pmatrix} (x_i+\alpha_k x_{ij})/r \\ (y_i+\alpha_k y_{ij})/r \\ (z_i+\alpha_k z_{ij})/r \end{pmatrix}. \tag{3.26}$$

Because the contour from i to j and the contour from j to i are physically equivalent, we can further simplify Eq. 3.24 and do the summation over pairs ($i < j$),

$$p_N^C(r) = \frac{1}{4\pi r^2}\left\langle \sum_{i<j}\sum_{k=1}^{2} \frac{|\mathbf{r}_{ij}\cdot\hat{e}_{r,\alpha_k}|}{r_{ij}} f_{ij}H(\alpha_k)H(1-\alpha_k)\right\rangle. \tag{3.27}$$

Combining the kinetic and configurational contributions together, the total normal pressure is

$$p_N\left(r\right) = \rho\left(r\right) k_B T + \frac{1}{4\pi r^2}\left\langle \sum_{i<j} \sum_{k=1}^{2} \frac{\left|\mathbf{r}_{ij} \cdot \hat{e}_{r,\alpha_k}\right|}{r_{ij}} f_{ij} H\left(\alpha_k\right) H\left(1-\alpha_k\right) \right\rangle . \tag{3.28}$$

Polar Pressure $p_{\theta\theta}$

The local polar pressure only depends on the radial distance r, an integration over the polar and azimuthal angles must be carried out in a similar manner to Eq. 3.17. The polar pressure component is given by

$$p^{C}_{\theta\theta}\left(r\right) = \frac{1}{4\pi}\int_0^{2\pi} d\varphi \int_0^{\pi} \sin\theta d\theta \left[\hat{e}_\theta \cdot \mathbf{p}^{C}\left(\mathbf{r}\right) \cdot \hat{e}_\theta\right] . \tag{3.29}$$

Applying Eq. 3.16 gives

$$p^{C}_{\theta\theta}\left(r\right) = \frac{1}{8\pi r^2}\left\langle \sum_{i \neq j} \int_0^{2\pi} d\varphi \int_0^{\pi} d\theta \int_{C_{ij}} d\tilde{l} \cdot \hat{e}_\theta \frac{\mathbf{r}_{ij} \cdot \hat{e}_\theta}{r_{ij}} f_{ij} \delta\left(r - r_l\right) \delta\left(\theta - \theta_l\right) \delta\left(\varphi - \varphi_l\right) \right\rangle . \tag{3.30}$$

Integrating out variable θ and φ leads to

$$p^{C}_{\theta\theta}\left(r\right) = \frac{1}{8\pi r^2}\left\langle \sum_{i \neq j} \int_{C_{ij}} d\tilde{l} \cdot \hat{e}_{\theta,l} \frac{\mathbf{r}_{ij} \cdot \hat{e}_{\theta,l}}{r_{ij}} f_{ij} \delta\left(r - r_l\right) \right\rangle , \tag{3.31}$$

where $\hat{e}_{\theta,l}$ is the polar unit vector with $\theta = \theta_l$ and $\varphi = \varphi_l$. Now, replacing the line element $d\tilde{l}$ in Eq. 3.31 with Eq. 3.14 results in

$$p^{C}_{\theta\theta}\left(r\right) = \frac{1}{8\pi r^2}\left\langle \sum_{i \neq j} \int_0^{1} d\alpha \frac{\left(\mathbf{r}_{ij} \cdot \hat{e}_{\theta,l}\right)^2}{r_{ij}} f_{ij} \delta\left(r - r_l\right) \right\rangle . \tag{3.32}$$

Applying the identity (Eq. 3.23) to above Eq. 3.32 and carrying out the integration yields,

$$p^{C}_{\theta\theta}\left(r\right) = \frac{1}{8\pi r^2}\left\langle \sum_{i \neq j} \sum_{k=1}^{2} \frac{\left(\mathbf{r}_{ij} \cdot \hat{e}_{\theta,\alpha_k}\right)^2}{\left|\mathbf{r}_{ij} \cdot \hat{e}_{r,\alpha_k}\right|} \frac{f_{ij}}{r_{ij}} H\left(\alpha_k\right) H\left(1-\alpha_k\right) \right\rangle , \tag{3.33}$$

where

$$\hat{e}_{\theta,\alpha_k} = \begin{pmatrix} (x_i + \alpha_k x_{ij})(z_i + \alpha_k z_{ij})/(r d_{xy}) \\ (y_i + \alpha_k y_{ij})(z_i + \alpha_k z_{ij})/(r d_{xy}) \\ -d_{xy}/r \end{pmatrix}, \tag{3.34}$$

and $d_{xy} = \sqrt{(x_i + \alpha_k x_{ij})^2 + (y_i + \alpha_k y_{ij})^2}$; α_k are roots of Eq. 3.25. Thus, the local polar pressure is given by

$$p_{\theta\theta}(r) = \rho(r) k_B T + \frac{1}{4\pi r^2} \left\langle \sum_{i<j} \sum_{k=1}^{2} \frac{(\mathbf{r}_{ij} \cdot \hat{e}_{\theta,\alpha_k})^2}{|\mathbf{r}_{ij} \cdot \hat{e}_{r,\alpha_k}|} \frac{f_{ij}}{r_{ij}} H(\alpha_k) H(1-\alpha_k) \right\rangle. \tag{3.35}$$

Azimuthal Pressure $p_{\varphi\varphi}$

Following the similar derivation as shown above, we can obtain the local azimuthal pressure in a form of

$$p_{\varphi\varphi}(r) = \rho(r) k_B T + \frac{1}{4\pi r^2} \left\langle \sum_{i<j} \sum_{k=1}^{2} \frac{(\mathbf{r}_{ij} \cdot \hat{e}_{\varphi,\alpha_k})^2}{|\mathbf{r}_{ij} \cdot \hat{e}_{r,\alpha_k}|} \frac{f_{ij}}{r_{ij}} H(\alpha_k) H(1-\alpha_k) \right\rangle, \tag{3.36}$$

where

$$\hat{e}_{\varphi,\alpha_k} = \begin{pmatrix} -(y_i + \alpha_k y_{ij})/d_{xy} \\ (x_i + \alpha_k x_{ij})/d_{xy} \\ 0 \end{pmatrix}. \tag{3.37}$$

We note that the configurational part (second term on the right) in Eq. 3.36 is equivalent to Eq. (20) in Ref.[4] although they have different appearance. Unlike the method in Ref.[4] that takes an average over a number of φ-surface in computation, here we have already averaged over all possible φ analytically through integration. The final tangential pressure is calculated by $p_T(r) = [p_{\theta\theta}(r) + p_{\varphi\varphi}(r)]/2$.

Results and Discussions: Critical Nucleus in Liquids

In this section, we present the pressure profile for critical nucleus in liquids. The pseudo-hard sphere potential u_{PHS} is of Mie type (50-49) and is given by the expression[7]:

$$u_{PHS}(r) = \begin{cases} 50\left(\frac{50}{49}\right)^{49} \epsilon \left[\left(\frac{\sigma}{r}\right)^{50} - \left(\frac{\sigma}{r}\right)^{49}\right] + \epsilon & r < \left(\frac{50}{49}\right)\sigma \\ 0 & r \geq \left(\frac{50}{49}\right)\sigma \end{cases} \tag{3.38}$$

where σ represents the hard sphere diameter and ϵ is the depth of the potential. It has been shown in previous work[7] that the properties of the PHS are quite close to that of the HS system when the reduced temperature $T^* = T/(\epsilon/k) = 1.5$. To simulate the PHS potential we shall use the parameters of the Lennard-Jones potential of Ar, namely $\sigma = 3.405$ Å, $\varepsilon/k = 119.80667$ K. Simulations were performed at $T = 179.71$ K ($T^* = 1.5$). Results, in reduced units of pressure (i.e in units of kT/σ^3) are shown in the main text. The discrete p_N data were fitted to a hyperbolic equation[2,8]

$$p_N\left(r\right) = \frac{1}{2}\left(p_{sol} + p_{liq}\right) + \frac{p_{liq}}{2}\tanh\left[2\left(r - r_{liq}\right)/d_{liq}\right] - \frac{p_{sol}}{2}\tanh\left[2\left(r - r_{sol}\right)/d_{sol}\right], \tag{3.39}$$

where subscript ‘sol’ denotes the solid, ‘liq’ denotes the liquid; p_{sol} and p_{liq} are the normal pressure of the bulk solid and that of the bulk liquid, respectively; r_{sol} and r_{liq} are the radial positions of the inflection points on the normal pressure profile for the corresponding phase; d_{sol} and d_{liq} are the width of the interface for the corresponding phase. Fitting parameters are listed in Table 3.3.

The discrete data of p_T is not fitted. Instead, we estimate its functionality by applying the hyperbolic form of p_N along with the fit parameters to equation 3.11.

We show here the table from the main text on the values for pressure and density on the solid cluster and surrounding liquid. The values are obtained by linear regression only in the plateaus, hence, they slightly differ from the asymptotic values obtained from our previous fit.

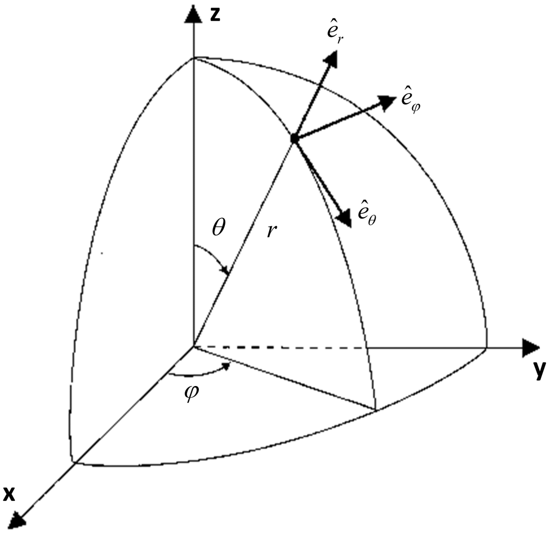

Figure 3.5: Spherical coordinate system with corresponding unit vectors in each direction.

Label	p_{sol}	p_{liq}	r_{sol}	r_{liq}	d_{sol}	d_{liq}
IV	12.5996	12.7444	10.8752	10.8546	3.77093	3.78267
VII	12.3053	12.4039	15.5184	15.5037	3.83847	3.84728
VIII	12.2177	12.3005	17.6211	17.6094	4.01175	4.01468

Table 3.3: Parameters of the fit to p_N. Pressure in reduced units (i.e in units of kT/σ^3). Distances in reduced units (i.e in units of σ).

Label	R_s	ρ_{sol}	ρ_{liq}	p_{sol}	p_{liq}	Δp
IV	10.791	1.0613	0.9619	12.6046	12.7437	-0.1391
VII	15.20	1.0548	0.9560	12.3053	12.4047	-0.0994
VIII	17.467	1.0529	0.9541	12.2199	12.3003	-0.0804

Table 3.4: From the main text, densities and pressures (for the solid and fluid) as determined by the respectively plateaus in the density and pressure profiles. The difference in pressure is also given as $\Delta p = p_{sol} - p_{liq}$. The notation of IV,VII and VIII refers to the clusters labeled in this way in Ref.[1]. Results are given in reduced units.

Cluster VII

In the main text, we show the profiles for clusters IV and VIII. Here we show cluster VII which is intermediate in size between the other two.

Theorem of the mean pressure: $< p >= p_{ext}$

It is simple to show that the average pressure obtained by appliying the virial theorem to the entire inhomogeneous system (in the NVT ensemble) $< p >$, or integrating the pressure tensor over the entire volume, is identical to the pressure of the external phase p_{ext} provided that both the normal and tangent components of the pressure tensor are identical at L/2 (half the value of the simulation box). We shall locate the center of mass of the solid cluster in the center of the simulation box. That it holds :

$$\langle p \rangle = p_{ext} \tag{3.40}$$

Let us prove this. Firsly one defines a local pressure as :

$$\overline{p}(r) = \frac{1}{3}\left[p_N(r) + 2p_T(r)\right] \tag{3.41}$$

We shall assume that beyond $L/2$ (in the corners of the simulation box) the normal and tangential components are equal and its value is p_{ext}. What is of interest is to determine the average pressure in the region between the center of mass of the solid cluster and $L/2$ and to show if this average is just p_{ext}. We shall now determine the average pressure by integration of the local net pressure over the spherical region with radius $L/2$:

$$\langle \overline{p} \rangle = \frac{24}{L^3}\int_0^{L/2} r^2 \overline{p}(r)\, dr \tag{3.42}$$

Substitution of equation 3.41 within equation 3.42 gives

$$\langle \overline{p} \rangle = \frac{8}{L^3}\left[\int_0^{L/2} r^2 \left(p_N(r) + 2 \cdot p_T(r)\right)\, dr\right] \tag{3.43}$$

Now, the mechanical equilibrium condition $\nabla \cdot \mathbf{p}$ implies

$$p_T(r) = p_N(r) + \frac{r}{2}\frac{dp_N}{dr} \tag{3.44}$$

Substitution in equation 3.43 gives

$$\begin{aligned}\langle\overline{p}\rangle &= \frac{8}{L^3}\left[\int_0^{L/2} r^2 p_N(r)\,dr + 2\int_0^{L/2} r^2 p_N(r)\,dr + \int_{p(0)}^{p(L/2)} r^3\,dp_N\right] = \\ &= \frac{8}{L^3}\left[3\int_0^{L/2} r^2 p_N(r)\,dr + \int_{p(0)}^{p(L/2)} r^3\,dp_N\right]\end{aligned} \tag{3.45}$$

. By solving the second integral by parts, (i.e. $u = r^3$, $du = 3r^2dr$; $dv = dp_N$; $v = p_N$), one finds

$$\langle\overline{p}\rangle = \frac{8}{L^3}\left[3\int_0^{L/2} r^2 p_N(r)\,dr + r^3 p_N(r)|_0^{L/2} - 3\int_0^{L/2} r^2 p_N(r)\,dr\right] = \frac{8}{L^3}\left[\frac{L^3}{8}\cdot p_N(L/2)\right] \tag{3.46}$$

Thus,

$$\langle\overline{p}\rangle = p_N(L/2) = p_{ext} \tag{3.47}$$

In general at $L/2$ both the tangential and normal components are identical and they have already reached the value of the plateau of the pressure for the external phase and one may conclude that :

$$\langle\overline{p}\rangle = p_{ext} \tag{3.48}$$

The lower pressure of the normal component inside the cluster is exactly compensated by the higher pressure of the two tangential components. Thus the average pressure of the system (as given by the virial equation) will be identical to the pressure of the external phase. To derive this equation it was only needed to apply the equation of mechanical equilibrium and to assume that at $L/2$ the system has already reached the pressure of the external phase.

Crystal-Liquid Equations of State

The equations of state can be described by quadratic fits $p = \sum_{i=1}^{n} c_i\rho^i$. The corresponding parameters are presented below.

Assuming that the chemical potential of the inhomogeneous system μ is close to the chemical potential of a bulk solid at p_{sol}.

In the main text we assumed that the chemical potential μ (which strictly speaking must be determined in independent calculations) can be taken from that of a bulk fluid phase at p_{ext}. Here we shall analyze what would happen if the value of μ of the

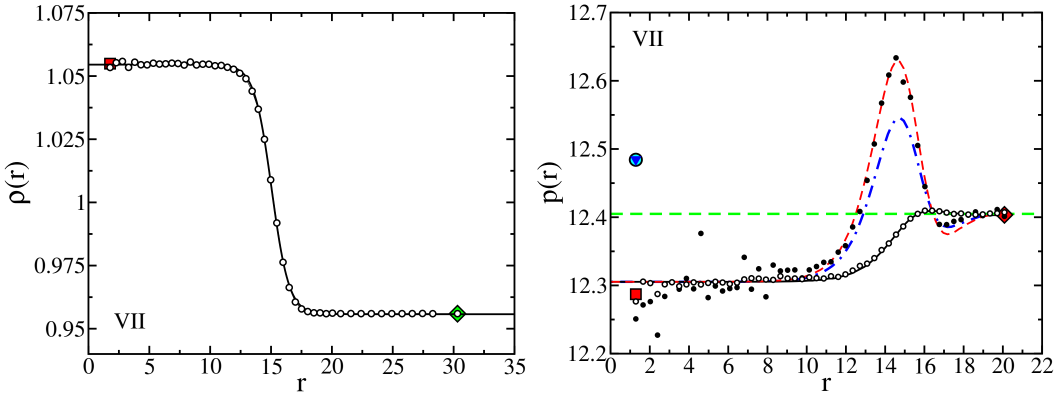

Figure 3.6: Radial density (left) and pressure (right) profiles from the COM for cluster VII. See caption in Fig. 1 of main text for explanation.

Phase	c_0	c_1	c_2
Crystal	132.175	-271.979	150.094
Liquid	97.6991	-235.516	153.029

Table 3.5: Paremeters of the fits to the equations of state of both solid and liquid.

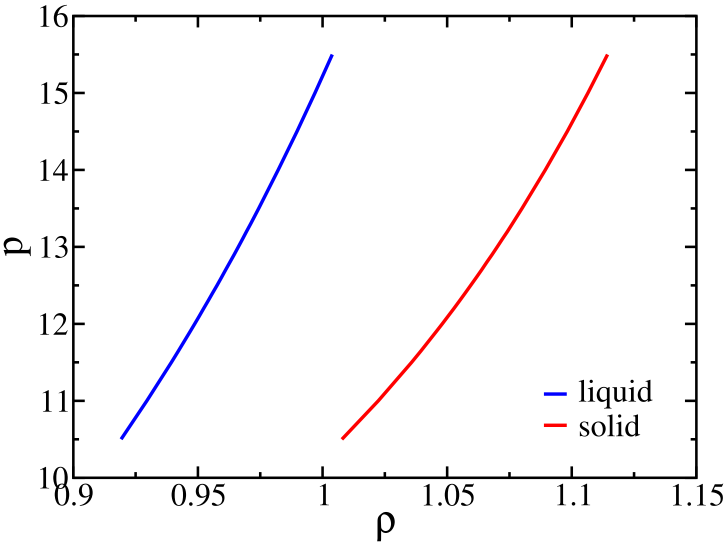

Figure 3.7: Equations of state.

Label	R_s	p_{sol}	p^{μ}_{liq}	$\Delta p^{\mu} = p_{sol} - p^{\mu}_{liq}$	$2\gamma_s/R_s$
IV	10.791	12.6046	12.523	0.0816	0.1164
VII	15.200	12.3053	12.250	0.0553	0.0793
VIII	17.467	12.2199	12.165	0.0549	0.0694

Table 3.6: Pressure of the solid and thermodynamic pressure of the fluid, obtained by assuming that the chemical potential of the inhomogeneous system μ can be estimated from that of a bulk solid at p_{sol}. By using the values of γ_s from nucleation studies we estimate the term $2\gamma_s/R_s$ and found to be in fair agreement with the difference in pressure obtained when using the thermodynamic pressure for the fluid. The notation of IV, VII, and VIII refers to the clusters labeled in this way in Ref.[1]. Results are given in reduced units.

inhomeneous system were closer to the properties of a bulk solid at p_{sol}. If this is the case then, it would be necessary to introduce p^{μ}_{liq} as the pressure of a bulk fluid with the same chemical potential as the bulk solid at p_{sol}. The Gibbsian formalism in this case would read:

$$F = N \ \ \mu - p_{sol}\frac{4}{3}\pi R^3 - p^{\mu}_{liq}(V - \frac{4}{3}\pi R^3) + 4\pi R^2 \gamma \tag{3.49}$$

Since F is invariant to arbitrary changes in R one then obtains (for the choice of R that leads to a minimum of γ):

$$p_{sol} - p^{\mu}_{liq} = \frac{2\gamma_s}{R_s} \tag{3.50}$$

In Table 3.6 the value of p^{μ}_{liq} for the three systems considered in this work (IV, VII, VIII) is presented and also the difference in pressure $\Delta p^{\mu} = p_{sol} - p^{\mu}_{liq}$. The value of $2\gamma_s/R_s$ from nucleation studies is also shown. As can be seen, Δp^{μ} is in fair agreement with $2\gamma_s/R_s$. The agreement with the value $2\gamma_s/R_s$ from nucleation studies is somewhat worse than that presented in the main text, strongly suggesting that the chemical potential of the inhomogeneous system μ is probably closer to that of the bulk liquid external phase.

Probably if μ were calculated rigorously it would correspond to an intermediate case (neither that of the bulk fluid at p_{liq} nor that of the bulk solid at p_{sol} but at some intermediate value probably closer to the first one). In this case it would be necessary to introduce the thermodynamic pressures for both phases. However the expected value of Δp^{μ} would be intermediate between the value of the main paper and that presented in this Appendix and close to the value $2\gamma_s/R_s$ obtained from nucleation studies.

Bibliography

[1] P Montero de Hijes, Jorge R Espinosa, Valentino Bianco, Eduardo Sanz, and Carlos Vega. Interfacial free energy and tolman length of curved solid-liquid interfaces from equilibrium studies. *J.Phys.Chem.C*, 124(X):8795, 2020.

[2] S. M. Thompson, K. E. Gubbins, J. P. R. B. Walton, R. A. R. Chantry, and J. S. Rowlinson. A molecular dynamics study of liquid drops. *J. Chem. Phys.*, 81:530, 1984.

[3] P Rosales-Pelaez, I Sanchez-Burgos, C Valeriani, C Vega, and E Sanz. Seeding approach to nucleation in the nvt ensemble: the case of bubble cavitation in overstretched lennard jones fluids. *Phys. Rev. E*, 101:022611, 2020.

[4] George J Tjatjopoulos and J. Adin Mann. The pressure tensor of an inhomogeneous fluid. *Molecular Physics*, 60(6):1425–1432, 4 1987.

[5] Christopher G. Gray, Keith E. Gubbins, and Christopher G. Joslin. Sec. 8.3 Pressure Tensor. In *Theory of Molecular Fluids. Vol. 2: Applications*, pages 928–942. Oxford University Press, 2011.

[6] J. H. Irving and John G. Kirkwood. The Statistical Mechanical Theory of Transport Processes. IV. The Equations of Hydrodynamics. *The Journal of Chemical Physics*, 18(6):817–829, 6 1950.

[7] J. Jover, A. J. Haslam, A. Galindo, G. Jackson, and E. A. Muller. Pseudo hard-sphere potential for use in continuous molecular-dynamics si mulation of spherical and chain molecules. *J. Chem. Phys.*, 137(14):144505, 2012.

[8] Jadran Vrabec, Gaurav Kumar Kedia, Guido Fuchs, and Hans Hasse. Comprehensive study of the vapour–liquid coexistence of the truncated and shifted Lennard–Jones fluid including planar and spherical interface properties. *Molecular Physics*, 104(9):1509–1527, 5 2006.

Chapter 4

On the thermodynamics of curved interfaces and the nucleation of hard spheres in a finite system

P. Montero de Hijes[1] and C. Vega[1]

[1]Departamento de Química Física, Facultad de Ciencias Químicas, Universidad Complutense de Madrid, 28040 Madrid, Spain

4.1. Abstract

A theoretical description of crystal critical nuclei of hard spheres (spherical, cylindrical or planar) in stable equilibrium with its melt is performed. We determine the Helmholtz free energy of the system as a function of the size of the cluster by means of the formalism of the thermodynamics of curved interfaces. The variation of the interfacial free energy with the radius of the cluster and the distance between equimolar and tension surfaces are inputs from simulation results of nucleation studies. This is possible because equilibrium clusters in the canonical ensemble become critical in the isothermal-isobaric ensemble. We show that under certain conditions, one may have several local minima in the free energy profile, one for the homogeneous fluid, and others for the spherical, cylindrical, and planar clusters. At each local minima we find no difference in chemical potential between the phases. At local maxima we also find equal chemical potential albeit in this case the nucleus is unstable. The theory allows us to describe the stable solid clusters found in simulations. Therefore, we can use it for any combination of total number of particles, volume and/or global density as long as a minimum in the Helmholtz free energy occurs. We also study under which conditions the absolute minimum in the free energy corresponds to a homogeneous liquid or to a heterogeneous system having either spherical, cylindrical or planar geometry. This work shows that the thermodynamics of curved interfaces at equilibrium can be used to describe nucleation in a finite system.

Chapter 5

Equivalence between condensation and boiling in a Lennard Jones fluid

I. Sanchez-Burgos[1], P. Montero de Hijes[1], P. Rosales-Pelaez[1], C. Vega[1], and E. Sanz[1]

[1]Departamento de Química Física, Facultad de Ciencias Químicas, Universidad Complutense de Madrid, 28040 Madrid, Spain

5.1. Abstract

Condensation and boiling are phase transitions highly relevant to industry, geology or atmospheric science. These phase transitions are initiated by the nucleation of a drop in a supersaturated vapor and of a bubble in an overstretched liquid respectively. The surface tension between both phases, liquid and vapor, is a key parameter in the development of such nucleation stage. Whereas the surface tension can be readily measured for a flat interface, there are technical and conceptual limitations to obtain it for the curved interface of the nucleus. On the technical side, it is quite difficult to observe a critical nucleus in experiments. From a conceptual point of view, the interfacial free energy depends on the choice of the dividing surface, being the surface of tension the one relevant for nucleation. We bypass the technical limitation by performing simulations of a Lennard Jones fluid where we equilibrate critical nuclei (both drops and bubbles). Regarding the conceptual hurdle, we find the relevant cluster size by searching the radius that correctly predicts nucleation rates and nucleation free energy barriers when combined with Classical Nucleation Theory. With such definition of the cluster size we find the same value of the surface tension for drops and bubbles of a given radius. Thus, condensation and boiling can be viewed as two sides of the same coin. Finally, we combine the data coming from drops and bubbles to obtain, via two different routes, estimates of the Tolman length, a parameter that allows describing the curvature dependence of the surface tension in a theoretical framework.

5.2. Introduction

Understanding first order phase transitions is of great importance to many fields, ranging from biology[1], to atmospheric science[2], physics[3], geology[4] or industry[5,6].

In the absence of impurities or external surfaces, first order phase transitions start with the emergence of a nucleus of the stable phase in the bulk of the parent metastable phase[7,8]. A nucleus is "critical" if it is big enough so that it has 50 per cent chances to either grow or redissolve.

Although the emerging phase is more stable, the presence of an unfavourable interface between the nucleus and the parent phase can delay to a great extent the phase transition. Thus, for instance, alkane vapors can be saturated thousands of times over their vapor pressure before condensation takes place[9], alkane liquids can be substantially superheated above the boiling temperature[10–12] or liquid water can be supercooled up to $\sim$ 60 K below melting until it freezes[13–16].

Therefore, the surface tension, γ, or the free energy per unit area between both phases, plays a key role in the development of first order phase transitions. Whereas γ can be readily measured for a flat interface at equilibrium –at least between fluid phases[17]– it cannot be directly probed for curved interfaces, which is the relevant case for nucleation. Moreover, the fact that critical nuclei are nanoscopic objects makes it very difficult to observe them in experiments, let alone measuring their γ. The usual strategy is to infer γ by combining a theoretical description of nucleation with measurements of the nucleation rate (the number of nuclei that appear per unit of time and volume)[7,17–19]. This approach relies on the validity of theoretical approximations that are difficult to assess.

Computer simulations do have access to the time and length scales relevant for the observation of critical nuclei. However, whereas the methodology and theoretical framework for computing γ for flat interfaces is very well established[20–29], that for curved interfaces is still under development[30–32]. One of the key issues is that γ for curved interfaces depends on the location of the interface, that can be defined in different ways[32,33]. The current situation is that the dependence of γ with the curvature of the interface is contradictory between different groups[18,30–32,34–44]

In this work we address fundamental questions regarding the liquid-vapor interface with computer simulations. It has been shown in different simulation works that spherical nuclei can be equilibrated at constant volume and temperature in finite systems[35,44–53]. Recently, we showed with simulations of bubbles[54] and crystals[55] that nuclei thus equilibrated are critical, in agreement with Density Functional Theory (DFT) predictions[56,57]. On the other hand, we have extensively developed in the past years the so-called Seeding method[58–61] to study nucleation phenomena. This method consists in obtaining with simulations the properties of critical clusters and "plug" them in the Classical Nucleation Theory (CNT) formalism[62–65] to obtain predictions of the nucleaiton rate and of the γ curvature dependence. This approach has been successful for a wide range of systems[54,58,59,61,66–70] and we use it here for the first time to study condensation. In particular, we apply Seeding at constant volume both to condensation and to cavitation for a Lennard Jones model.

Since Seeding relies on CNT, it is necessary to validate it by comparing its predictions with independent calculations that do not rely on such framework. We do so by computing nucleation rates via Umbrella Sampling (US)[71,72] and direct brute force simulations[73] as well as by testing the consistency of the γ-curvature dependence obtained via Seeding with the value for a flat interface.

All consistency tests are successfully passed for our Seeding simulations provided that the nucleus surface is identified with that where the density is the average between the density of both phases ("equi-density" surface). Therefore, we identify the equidensity surface with the surface of tension. On the other hand, we directly compare the condensation of liquid drops in a supersaturated vapor with the cavitation of vapor bubbles in an overstretched liquid. We find that, for a given temperature, drops and bubbles of the same radius have the same γ when using the equidensity definition of the surface of tension. Finally, we estimate the Tolman lenght[74], a parameter useful to predict the γ-curvature dependence, via two different routes, as recently proposed in[55].

5.3. Simulation details

The Lennard Jones model potential, as well as the simulation details, are the same as in our previous work[54,70]. In particular, we study the truncated and force-shifted Lennard-Jones (TSF-LJ) potential[75], a model for which the vapor-liquid transition has been previously investigated[70,75–77]:

$$U_{TSF-LJ}(r) = U_{LJ}(r) - U_{LJ}(r_c) - (r - r_c)U'_{LJ}(r_c), \tag{5.1}$$

where $U_{LJ}(r)$ is the standard 12-6 Lennard-Jones potential and $U'_{LJ}(r)$ is its first derivative. The interaction potential is truncated and shifted at $r_c = 2.5\sigma$, being σ the particle's diameter and ϵ the depth of the un-truncated Lennard-Jones potential. Unless otherwise specified, all magnitudes in this work are given in Lennard-Jones reduced units[54]. Thus, the reported temperatures are reduced by ϵ/k_B, distances by σ, densities by σ^{-3}, pressures by ϵ/σ^3, times by $\tau = \sqrt{m\sigma^2/\epsilon}$ (being m the particle mass), interfacial free energies by ϵ/σ^2 and nucleation rates by $1/(\tau\sigma^3)$.

We use cubic boxes with periodic boundary condition and the Molecular Dynamics (MD) LAMMPS package[78] to perform all simulations of this work. The equations of motion are integrated with a leap-frog algorithm[79].

In the MD Seeding simulations we used a time-step of 0.0012. The system was kept at constant temperature using the Nosé-Hover thermostat[80] with a relaxation time of 0.46.

For the MD simulations used within the Umbrella Sampling scheme we set the time step for the integration of the motion equations to 0.0012. The relaxation times for the Nose-Hover thermostat and barostat were 0.46 and 1.6 respectively.

All simulations are carried out at T=0.785. The coexistence pressure at such temperature for the model is p_{coex}=0.0267. We determined this value, refined with respect to that of 0.026 previously published[75], by running long ($4 \cdot 10^5$ τ) MD NVT simulations with an elongated box (50 x 17 x 17) where the vapor and the liquid were put at contact at the temperature of interest. The average pressure normal to the interface in such simulation corresponds to p_{coex}.

5.4. Seeding of condensation

This work is based on a recent publication where we demonstrate how to compute bubble nucleation rates in an overstretched Lennard-Jones fluid by equilibrating critical bubbles in the NVT ensemble, an approach we call "NVT-Seeding"[54]. The Seeding method, originally developed to study crystal nucleation[58–61], and more recently applied to vapor cavitation[54,70,81], consists in combining CNT[62–65] with computer simulations to estimate nucleation free energy barrier heights, ΔG_c, interfacial free energies, γ, and, most importantly, nucleation rates, J.

According to CNT, the Gibbs free energy barrier for the nucleation of a spherical liquid drop is given by the following expression:

$$\Delta G = \gamma A - V\Delta p \tag{5.2}$$

Where V and A are the volume and the area of the drop respectively. By maximizing Eq. 5.2 assuming a spherical drop shape one obtains both the height of the nucleation free energy barrier,

$$\Delta G_c = \frac{2\pi R_c^3 \Delta p}{3}, \tag{5.3}$$

where R_c is the critical droplet radius and Δp is the pressure difference between the interior of the drop and the surrounding vapor, and the number of particles in the critical drop,

$$N_c = (32\pi\rho_l\gamma^3)/(3\Delta p^3), \tag{5.4}$$

where ρ_l is the critical drop number density and γ is the liquid-vapor surface tension. By substituting in the equation above N_c by the droplet volume $(4/3\pi R_c^3)$ times ρ_l one recovers the Laplace equation:

$$\Delta p = \frac{2\gamma}{R_c}. \tag{5.5}$$

This derivation shows that the Laplace equation, which is valid when the droplet surface is located at the the surface of tension, is implicit in CNT. Consequently, R_c should be identified with the radius of tension, R_s. This is an important point that we will use later on in the paper.

The CNT prediction for the nucleation rate of drops is given by[7]:

$$J = A_0\rho_{vap}\exp\left(-\frac{\Delta G_c}{k_B T}\right), \tag{5.6}$$

where k_B is the Boltzmann constant, ρ_{vap} is the density of the vapor phase that multiplied by $\exp\left(-\frac{\Delta G_c}{k_B T}\right)$ gives the number density of critical clusters and A_0 is a kinetic pre-factor.

A_0 is computed as the product of the Zeldovich factor, Z, and the rate of attachment to the critical nucleus, f^{+}[7,63]:

$$A_0 = Zf^{+}. \tag{5.7}$$

Z takes into account the establishment of a steady state and, according to CNT, is given by[7,62,63]:

$$Z = \sqrt{\frac{|\Delta G(N)''|_{N_c}}{2\pi k_B T}} = \sqrt{\frac{\Delta p}{6\pi k_B T \rho_l N_c}} = \sqrt{\frac{\Delta p}{8\pi^2 k_B T \rho_l^2 \cdot R_c^3}} \tag{5.8}$$

where N_c is the number of particles in the drop and $|\Delta G_c(N)''|_{N_c}$ is the curvature of $\Delta G(N)$ evaluated at the barrier top.

The attachment rate, f^{+}, can be estimated by multiplying the collision frequency of the vapor per unit of wall area given by the kinetic theory of gasses (ktg) by the area of the critical bubble:

$$f^{+}_{ktg} = \sqrt{\frac{k_B T}{2\pi m}} \left(\frac{6\sqrt{\pi} N_c}{\rho_l}\right)^{2/3} \tag{5.9}$$

where the subscript "*ktg*" stresses the fact that this expression of the attachment rate is based on the kinetic theory of gasses.

Combining this equation with 5.8, 5.4, and 5.5, the following kinetic pre-factor is obtained:

$$A_0^{ktg} = \sqrt{\frac{\Delta p R_c}{\pi m}} \frac{\rho_{vap}}{\rho_l}. \tag{5.10}$$

The equations above are quite powerful, because only R_c, Δp and the density of both phases are required to obtain key nucleation parameters as free energy barriers, interfacial free energies and ınucleation rates. The Seeding method consists in performing simulations of a cluster of the stable phase surrounded by the mestastable phase (a liquid drop surrounded by supersaturated vapor in our case as shown in Fig. 5.1) to compute R_c, Δp, ρ_l and ρ_{vap} in order to get "cheap" estimates of ΔG_c, γ and, most importantly, J through the expressions above.

The main drawback of Seeding is that the definition of R_c is not unique. Therefore, the resulting free energy barrier depends on the specific definition of R_c. This contrasts with rigorous simulation methods like Umbrella Sampling[73,82] or with theoretical approaches like DFT[83–85] where the nucleation free energy does not depend on the criterion chosen to measure the nucleus size, which can be estimated *a posteriori* via, e. g. the nucleation theorem[86–88] (although in the particular case of DFT an approximate functional needs to be proposed so that the results do also contain approximations). To assess the suitability of our choice to compute R_c we complement Seeding with Umbrella Sampling simulations.

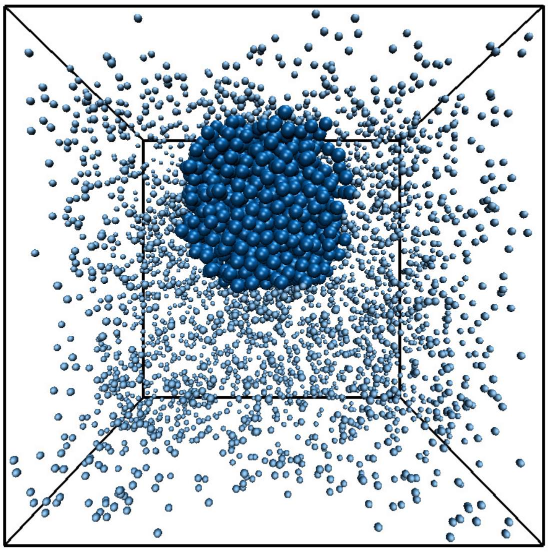

Figure 5.1: Snapshot of a critical drop equilibrated in the NVT ensemble at T=0.785 surrounded by supersaturated vapor. The droplet radius is about 6.8 and the density of the surrounding vapor 0.0550.

5.4.1. R_c, Δp, ρ_l and ρ_{vap}

We use the NVT ensemble to run the simulations of the drops given that in such ensemble critical nuclei are naturally equilibrated and stabilised for long times[54,55]. We equilibrate drops in 10 different systems. The edge of the cubic simulation box, L, and the total number of particles in each system, N_T, are reported in Table 5.1. A large number of particles is used to minimize finite size effects[52,54,89]. Each system was simulated for about 10^3 Lennard Jones times of equilibration and $2 \cdot 10^5$ of production.

To prepare the initial configuration we cut a spherical liquid drop from a bulk liquid simulation and insert it in a bulk vapor box removing the overlapping vapor particles. The liquid drop is cut with a certain tentative radius, but the precise number of particles in each phase is not crucial given that equilibrium is reached along the course of the NVT simulation.

From a simulation of a drop surrounded by supersaturated vapor one can obtain an average radial density profile starting from the center of the drop as that shown in Fig. 5.2 (to find the drop centre in each configuration we use a similar strategy to that described in our previous work[54] consisting in this case in identifying the maxima of density profiles computed along each cartesian coordinate). Following Refs.[54,70], we obtain R_c from such density profile as the distance at which the density is average between the liquid and the vapor plateaux. This is indicated with a vertical dashed line in Fig. 5.2. We refer to this way of obtaining R_c as the “equi-density” criterion. The R_c's thus obtained in our NVT-Seeding simulations are also reported in Table 5.1. Other definitions of R_c are in principle as valid as the equi-density criterion[70,84,85]. We argue later on in the paper that our R_c definition is a good one because it makes

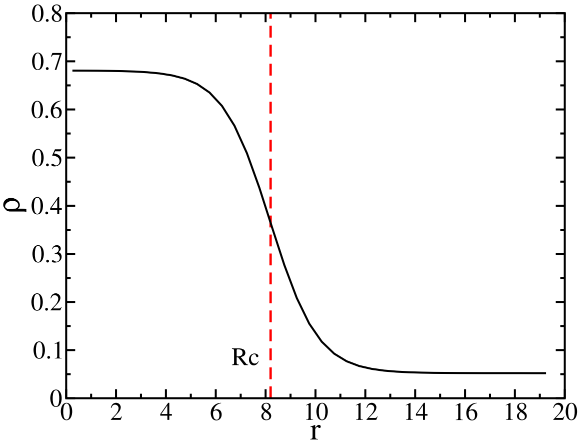

Figure 5.2: Density profile of a critical drop equilibrated in the NVT ensemble at T=0.785 surrounded by supersaturated vapor. The droplet radius, indicated by a red vertical line in the figure, is given by the point at which $\rho(r)$ takes an average value between both plateaux (equi-density criterion). The density profile corresponds to the system labelled as IV in Table 5.1

.

Seeding predictions consistent with independent calculations of γ, J or ΔG_c.

To get $\Delta p = p_l - p_{vap}$ we obtain first the vapor density, ρ_{vap}, by counting the number of particles outside a sphere concentric with the drop but with a larger radius (we use a sphere radius 7σ larger than that of the drop, but we have checked for a few selected cases that any value beyond $\sim 5\sigma$ gives the same result). ρ_{vap} is given by the number of particles outside the sphere divided by the L^3 minus the sphere volume. We then use the bulk vapor equation of state to infer p_{vap} from ρ_{vap}. We report p_{vap} and ρ_{vap} in Table 5.1. We have checked for all studied systems that p_{vap} coincides with the overall virial pressure of the system. On the other hand, p_l is obtained, as in our previous work[54,70], by assuming equal chemical potential between the critical drop and the surrounding vapor:

$$\int_{p_{coex}}^{p_{vap}} \frac{1}{\rho_{vap}(p)} dp = \int_{p_{coex}}^{p_l} \frac{1}{\rho_l(p)} dp \tag{5.11}$$

where p_{coex} is the coexistence pressure and $\rho_{vap}(p)$ and $\rho_l(p)$ are the bulk vapor and bulk liquid number densities at pressure p. In Table 5.1 we report p_l and Δp for all studied systems. Once p_l is known, ρ_l, also reported in the table, can be easily computed from the bulk liquid equation of state. In all cases, this computation of ρ_l, based on the equality of chemical potential between both phases, is consistent with that obtained from the density profiles. For instance, for system IV we get $\rho_l = 0.0680$, which is fully consistent with the first plateau observed in the density profile shown in Fig. 5.2. This means that the mechanical pressure and the thermodynamic pressure inside the drop coincide, a matter of current debate for solid-liquid nucleation[90].

There has been much simulation, theoretical and experimental work devoted to study

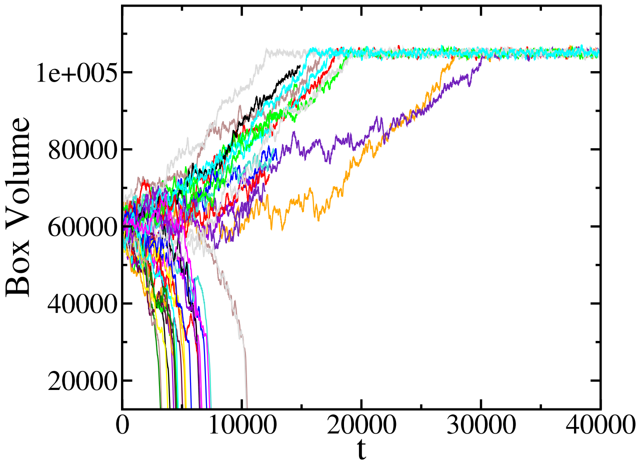

Figure 5.3: Box volume versus time in NpT simulations starting from 40 configurations taken from the NVT-Seeding simulation labelled as IX in Table 5.1. The imposed pressure is the average viral pressure of the NVT-Seeding run.

the formation of nuclei confined at constant volume[32,44,48,91–99]. In Refs.[54,55] we showed with simulations that nuclei equilibrated in the NVT ensemble are critical because they have equal chances to grow or shrink when simulated in the NpT ensemble at the same temperature and at the average pressure along the NVT run. Based on this result, we opted to study here drop nucleation in the NVT ensemble, where statistics is better because clusters remain stable for very long times[54]. Stabilising nuclei to gain time to study their properties is something quite desirable. An alternative strategy to the use of constant volume simulations is to pin the nucleus to a heterogeneous solid substrate[100].

Despite having already shown the equivalence between stable (NVT) and critical (NpT) nuclei for cavitation[54], we check here for one of the NVT-Seeding simulations if the drops equilibrated at constant volume and temperature do correspond to a Gibbs free energy maximum. In Fig. 5.3 we show the evolution of the box volume in NpT simulations started from 40 independent configurations gathered along the NVT-Seeding trajectory labelled as IX in Table 5.1. The imposed pressure is the average virial pressure along the NVT-Seeding run. Roughly, in 50 per cent of the cases the box expands (the drop dissolves) and in the other half of the cases the box shrinks (the drop grows). This result supports the use of NVT to study drop condensation in the same manner we did for bubble cavitation and cystal nucleation[54,55]. Furthermore, the equivalence between clusters equilibrated at constant volume and critical nuclei has been recently proven with DFT theoretical arguments for crystallization (see supplementary material of Ref.[57]).

Having computed R_c, Δp and ρ_{vap} and ρ_l we have everything needed to obtain γ, ΔG_c and J according to the equations presented in section 5.4. We report the values for these variables in Table 5.1 and plot them in fig. 5.4(a)-(c) versus the vapor pressure with black dots. In the following section we comment each of these graphs.

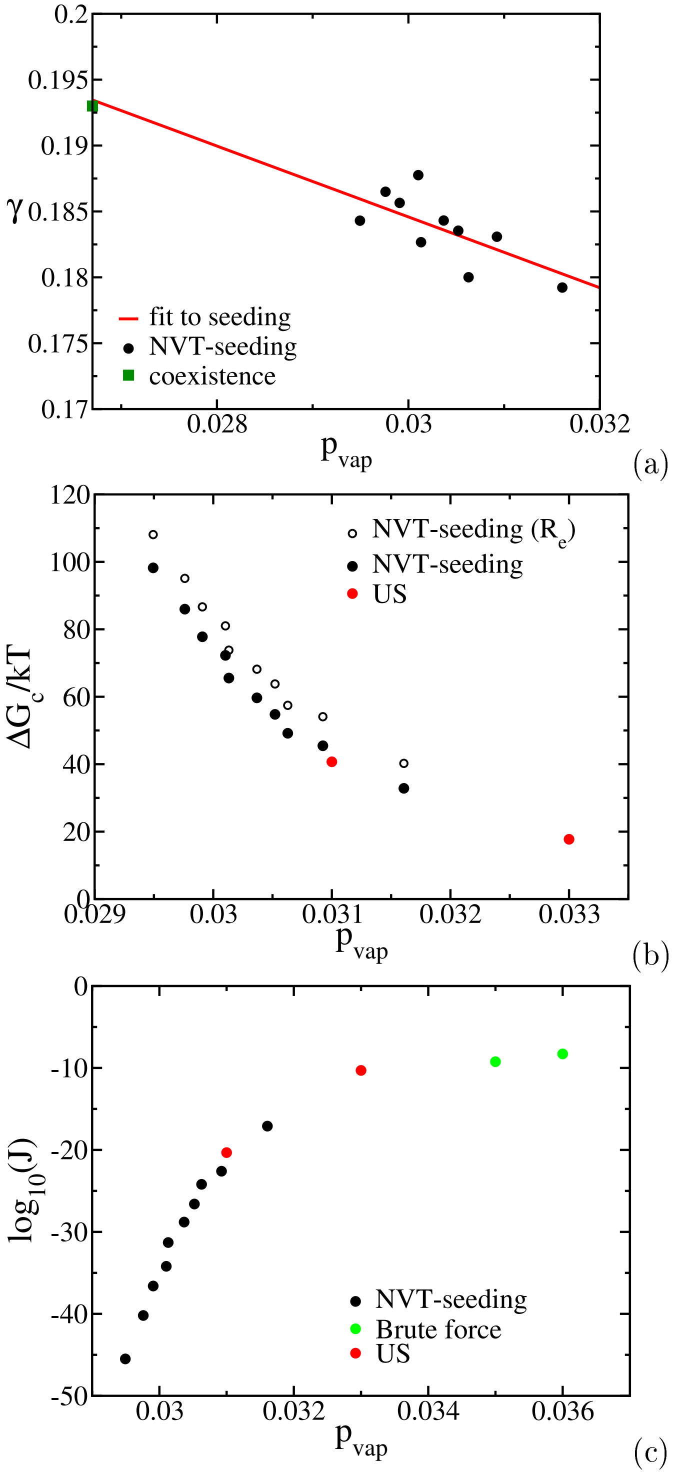

Figure 5.4: (a) γ vs vapor pressure obtained from NVT-Seeding data of droplets surrounded by supersaturated vapor. The surface tension at coexistence (p=0.0267) is included[70]. (b) ΔG_c vs vapor pressure. NVT-Seeding and US data are compared. Empty black symbols correspond to Seeding predictions when the Gibbs dividing (equi-molar) –instead of the equi-density– surface is employed to identify the cluster radius. (c) Nucleation rate versus vapor pressure as obtained from NVT-Seeding, US and spontaneous nucleation.

Label	L	N_T	ρ_l	ρ_{vap}	p_l	p_{vap}	Δp	R_c	γ	$\Delta G_c/(k_B T)$	A_0^{ktg}	A_0^{af}	$\log_{10}(J)$
I	38.019	3774	0.6833	0.05690	0.09279	0.03161	0.0612	5.86	0.1792	32.8	0.028		−17.1
II	39.160	4291	0.6811	0.05496	0.0846	0.03092	0.0537	6.82	0.1831	45.5	0.028		−22.6
III	39.160	4373	0.6801	0.05414	0.08095	0.03063	0.0503	7.15	0.1800	49.2	0.027		−24.2
IV	39.160	4510	0.6797	0.05384	0.07961	0.03052	0.0491	7.48	0.1835	54.8	0.027	0.030	−26.6
V	39.160	4623	0.6792	0.05342	0.07769	0.03037	0.0473	7.79	0.1843	59.7	0.027		−28.8
VI	39.160	4796	0.6782	0.05277	0.07468	0.03013	0.0446	8.20	0.1827	65.5	0.027	0.036	−31.3
VII	39.160	4964	0.6783	0.05269	0.07432	0.03010	0.0442	8.49	0.1878	72.3	0.027		−34.2
VIII	39.160	5163	0.6776	0.05216	0.07181	0.02991	0.0419	8.86	0.1856	77.8	0.027		−36.6
IX	39.160	5435	0.6771	0.05176	0.06989	0.02976	0.0401	9.30	0.1865	86.0	0.026		−40.2
X	85.264	34519	0.6761	0.05105	0.06638	0.02949	0.0369	9.99	0.1843	98.2	0.026		−45.5

Table 5.1: NVT-Seeding data for the different drops studied in this work at T=0.785.

5.4.2. γ, ΔG_c and J

γ

As shown in Fig. 5.4 (a) the prediction we obtain from Seeding is that γ decreases as the vapor supersaturation increases. This trend is in agreement with previous work[35,47]. Accordingly, using the capillarity approximation (i. e., that γ is pressure independent) would be erroneous. The green square in Fig. 5.4(a) corresponds to the surface tension at coexistence[70] obtained through the pressure tensor[101] in an NVT simulation of a liquid and a vapor at contact. The trend of the Seeding data is fully consistent with the coexistence value, as shown by the linear fit in the figure. This is a good consistency test, although the γ values provided by Seeding could still be incorrect despite the fact that they extrapolate correctly to coexistence. Therefore, a test for Seeding predictions away from coexistence is needed.

ΔG_c

To further test our Seeding results we compare ΔG_c obtained with Seeding with that computed via Umbrella Sampling. In Fig. 5.4(b), where we plot ΔG_c versus the vapor pressure, black solid dots correspond to Seeding and red ones to US (details on US calculations are described in section 5.5). Whereas Seeding predictions rely on the validity of CNT and on a proper definition of R_c, Umbrella Sampling calculations are rigorous and independent on the criterion to identify the nucleus size[73]. On the other hand Seeding is much "cheaper" than US from a computational point of view. As a matter of fact, Seeding has access to much higher nucleation barriers than US. The accordance between Seeding and US shown in Fig. 5.4 is excellent, which gives us great confidence on Seeding predictions. The choice of the equi-density surface to identify the drop radius has proven correct. If we use another criterion, such as the Gibbs (equi-molar) dividing surface, the agreement between Seeding and Umbrella Sampling deteriorates (empty black symbols in Fig. 5.4 (b)). To compute R_e, the radius associated to the Gibbs dividing surface, we use $N_T = N_l + N_{vap}$ where $N_l = 4/3\pi R_e^3\rho_l$

and $N_{vap} = [V_T - (4/3\pi R_e^3)]\rho_{vap}$, where V_T is the volume of the simulation box and the densities ρ_l and ρ_{vap} are obtained as described in Sec. 5.4.

In a recent publication on cavitation (nucleation of bubbles instead of drops) we compared the performance of different criteria to identify the cluster radius and found that the equi-density criterion also made Seeding predictions consistent with other rigorous calculations[70]. Therefore, identifying the critical drop radius with the equi-density distance seems to be quite general for condensation-evaporation transitions.

J

Once ΔG_c is known computing J via Eq. 5.6 is quite straight forward. The kinetic pre-factor A_0 given by the kinetic theory of gases, Eq. 5.10, depends on parameters we already have under control: Δp, R_c and the density of both phases. The values of A_0 computed via Eq. 5.10, A_0^{ktg}, are reported in Table 5.1.

These A_0 values are approximate since they rely on the validity of the kinetic theory of gasses to estimate the attachment rate (see section 5.4). We therefore have to check A_0^{ktg} by computing the attachment rate with an alternative approach. Following the work by Auer and Frenkel[102], the attachment rate can be computed from the diffusion of N, the number of particles in the liquid drop, around the critical drop[102]:

$$f_{af}^{+} = \frac{\langle (N(t) - N(0))^2 \rangle_{Nc}}{2t}, \tag{5.12}$$

where the average is performed over several trajectories starting from a critical drop configuration. The af subscript stresses the fact that this expression of the attachment rate is based on the work by Auer and Frenkel.

To compute N we follow[103]. We count as neighbors all particles within a 1.625 distance of a tagged particle. Particles with 8 or more neighbors are labelled as “liquid”. Two liquid particles belong to the same drop if their mutual distance is less than 1.625. An example of the calculation of f^+ according to equation 5.12 is illustrated in Fig. 5.5. Typically, $\langle N(t) - N(0) \rangle_{N_c}$ is obtained by averaging 20 NpT runs started from independent configurations of the critical drop, coming either from NVT-Seeding or from Umbrella Sampling simulations (see section 5.5). In these runs, the pressure is fixed to the virial value of the simulations were the critical clusters were previously equilibrated. According to Eq. 5.12, the slope of Fig. 5.5 divided by 2 gives f^+. Multiplying such f^+ by the Zeldovich factor we get an estimate of the kinetic pre-factor, A_0^{af}, that does not rely on the kinetic theory of gases. A_0^{af} is reported it in Table 5.1 for a couple of critical clusters generated with NVT-Seeding (systems IV and VI). A_0^{af} is very close to A_0^{ktg}. This agreement suggests the validity of the kinetic theory of gases to estimate the attachment rate and makes the theoretical framework that supports the Seeding technique quite powerful given that, since A_0^{ktg} can be used, only R_c, Δp and the density of both phases are required to get accurate estimates of J in a wide range of orders of magnitude. Note in Fig. 5.4(c) that Seeding (black dots) has access to J values many orders of magnitude lower than US (red dots).

Label	N_T	$\langle V \rangle$	p_v	ρ_v	$\log_{10}(J)$
BF-1	4000	57145	0.035	0.0700	-9.235
BF-2	4000	53456	0.036	0.0748	-8.287

Table 5.2: Data corresponding to the brute force calculations.

Label	L	N_T	$\Delta G_c/(k_B T)$	A_0^{af}	$\log_{10}(J)$
US-1	39.112	4000	17.7	0.041	-10.3
US-2	38.501	4000	40.7	0.039	-20.3

Table 5.3: Data corresponding to the US calculations.

The green dots in Fig. 5.4(c) correspond to rate estimates obtained in brute force NPT molecular simulation runs performed at high supersaturations where condensation occurs spontaneously from an unseeded vapor. In such cases the nucleation rate can be estimated as $J = 1/(t < V >)$, where $< V >$ is the average volume before nucleation and t is the nucleation time averaged over a number of independent trajectories (typically 20 in our case). N_T, V, the vapor pressure and density, and J for the two states where we studied spontaneous condensation are reported in Table 5.2. In Fig. 5.4(c) we show that J estimates from Seeding and from spontaneous nucleation are consistent with each other, which further indicates the ability of Seeding to predict nucleation rates. It is worth mentioning here that NVT-Seeding and spontaneous nucleation are complementary techniques. On the one hand, the former does not have access to such high supersaturations given the difficulty to equilibrate small clusters in the NVT ensemble[54,55]. That said, it would be nonsense using Seeding where nucleation occurs spontaneously in a straightforward manner. On the other hand, spontaneous nucleation is limited to a narrow window of nucleation rates (that enabled by computational time) whereas Seeding has access to extremely low rates.

We would like to end this section by discussing finite size effects, which could be present if a nucleus sees its replica through periodic boundary conditions. On the one hand, we made sure that the density of the outer phase reaches a plateau before L/2 by looking at radial density profiles such as that shown in Fig. 5.2. On the other hand, we note that the box side of system X is more than twice than those of the other systems. By looking at Figs. 5.4 (a), (b) and (c) one can see that the results from system X are fully consistent with those inferred from the other systems, which strongly supports the absence of noticeable finite size effects in our simulations.

5.5. Umbrella Sampling

As previously indicated, to validate the Seeding results we used the US technique. We followed Refs.[103,104] to compute ΔG_c for two different vapor pressures: p=0.031 and

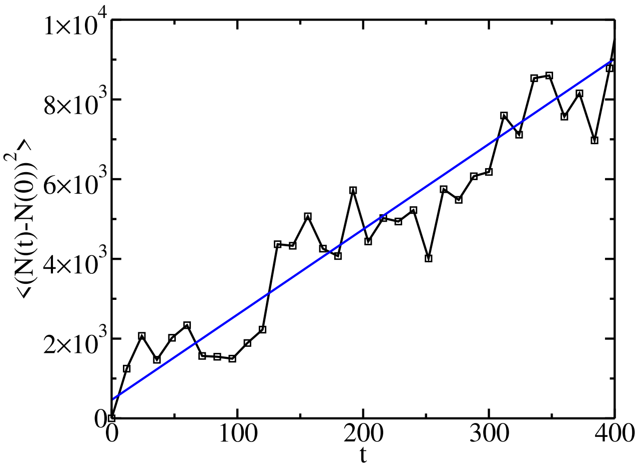

Figure 5.5: Time dependence of the mean squared deviation of the number of particles in the critical drop for system VI in Table 5.1. Half the slope of this plot gives the attachment rate according to Eq. 5.12

.

p=0.033. Details on the simulation box size and number of particles in the systems used to perform the US calculations are given in Table 5.3.

The free energy associated to the formation of an N particle cluster drop can be obtained from:

$$\Delta G(N) = -k_B T \ln[P(N)], \tag{5.13}$$

where $P(N)$ is the probability distribution of N. Our criterion to compute N is described in Section 5.4.2. It is important to note that even though different criteria may give different N for a given configuration, the height of an US free energy barrier does not depend on the criterion to determine the cluster size[73]. Therefore, contrary to what happens in Seeding, the US method does not depend on the specific criterion to determine the nucleus size. This is why it is important to validate the Seeding method with other tecniques such us US.

With conventional NpT simulations at the selected pressures $P(N)$ can only be sampled up to $N \sim 40$ while the critical cluster is much larger in this regime. To sample the rest of the free energy barrier a biasing potential, U_{bias}, is added to the original hamiltonian:

$$U_{bias} = \frac{1}{2} k_{bias} \left(N - N_0\right)^2, \tag{5.14}$$

where N_0 controls the cluster size around which the sampling will be centred and k the width of such sampling. Tens of overlapping sampling "windows" centered at different N_0 values are required to reconstruct the whole free energy barrier. The effect of the bias potential on the calculation of the free energy barrier is removed as follows[71]:

$$\Delta G(N) = -k_B T \ln \left\langle \frac{\chi_N}{e^{-U_{bias}/(k_B T)}} \right\rangle + C \tag{5.15}$$

where χ_N is the fraction of clusters with N particles that appear within a certain window and C is a constant. The constant is obtained by gluing together the first part of the energy barrier evaluated without the biasing potential (Eq. 5.13) with the rest of the windows. The result is the whole free energy barrier.

To compute each window we use the hybrid Molecular Dynamics-Monte Carlo scheme labelled as HMC(nM-NpT)/US in Ref.[104]. From the starting configuration, random velocities are assigned to every particle according to a Maxwell-Boltzmann distribution and a short (Δt 19.2 Lennard Jones times) MD simulation is run for generating a new configuration, which is accepted with probability $\min[1, \exp[-(U_{bias}(\Delta t) - U_{bias}(0))/(k_B T)]]$. Either in case of acceptance or rejection new random velocities are assigned at the beginning of each short MD cycle. For each window, 10000 of such cycles were performed for equlibration and 60000 to obtain the free energy barrier. We used $k_{bias} = 0.04 k_B T$ in the biasing potential (Eq. 5.14), which gives an acceptance rate of $\sim 25\%$.

In figure 5.6 we plot both free energy barriers, being $\Delta G_c = 17.7 k_B T$ for p=0.033 and $\Delta G_c = 40.7 k_B T$ for p=0.031 (also reported in Table 5.3). As already discussed, the agreement between US and Seeding is excellent (see Fig. 5.4(b)).

Additionally, we compute the kinetic pre-factor A_0^{af} (Eq. 5.7) to obtain the nucleation rate (Eq. 5.6). To do that, we launch tens of unbiased trajectories from independent configurations at the barrier top in order to compute the attachment rate via Eq. 5.12. The Zeldovich factor (Eq. 5.8) can be obtained by numerically calculating the curvature of $\Delta G(N)$ at the barrier top. We report A_0^{af} thus calculated and the corresponding J in Table 5.3. As previously discussed, J from US is fully consistent with that coming from Seeding (see Fig. 5.4 (c)).

In summary, we have compared Seeding, that relies on the theoretical assumptions by CNT and ktg and depends on the criterion employed to determine the cluster size, with US, that does not have these limitations. We have obtained an excellent agreement between both techniques. This is very good news because Seeding is much more efficient than US and has access to much lower values of the nucleation rate.

5.6. Condensation vs boiling

5.6.1. Comparison for a given R_c

We have studied quite recently the nucleation of bubbles for the same Lennard Jones model employed here[54]. Since the study was performed at the same temperature, the question that naturally arises is whether bubbles and drops with the same radius have the same interfacial properties. To establish the comparison we have repeated the analysis performed in Ref.[54] because in such work we used 0.026 as the coexistence pressure instead of 0.0267. We took the 0.026 value from a paper published more than a decade ago[75]. However, we have recomputed more carefully the coexistence pressure at $T = 0.785$ and obtain $p = 0.0267$ instead, which is the value we use in this work. The

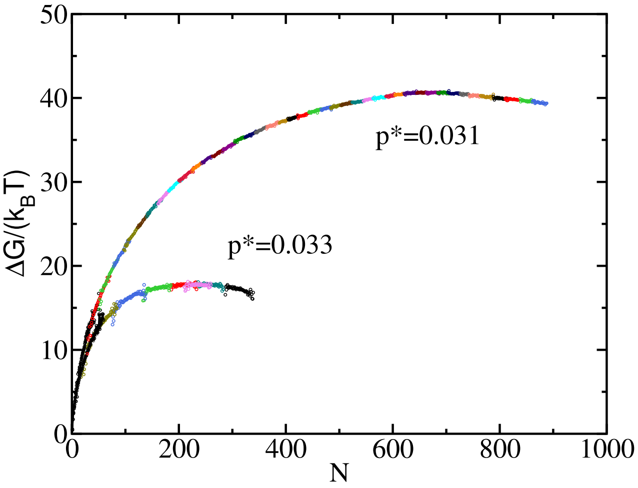

Figure 5.6: Free energy for two different pressures (p=0.031 and p=0.033) versus the number of particles in the drop as obtained from US calculations. The different colours represent the different windows performed.

Label	L	N_T	$\rho_{\rm vap}$	ρ_l	$p_{\rm vap}$	p_l	Δp	R_c	γ	$\Delta G_c/(k_BT)$	A_0^{BK}	$\log_{10}(J)$
I	36.731	30795	0.03765	0.6453	0.02365	−0.02601	0.0497	7.35	0.1826	52.7	0.341	−23.5
II	36.731	30342	0.03834	0.6484	0.02398	−0.01914	0.0431	8.50	0.1832	70.6	0.342	−31.3
III	36.731	29760	0.03875	0.6501	0.02419	−0.01503	0.0392	9.53	0.1869	90.6	0.345	−40.0
IV	36.731	29034	0.03907	0.6514	0.02433	−0.01191	0.0362	10.52	0.1906	112.5	0.348	−49.5
V	36.731	28147	0.03949	0.6530	0.02453	−0.00776	0.0323	11.50	0.1857	131.1	0.344	−57.6
VI	36.731	27082	0.03972	0.6539	0.02464	−0.00558	0.0302	12.45	0.1881	155.7	0.346	−68.3

Table 5.4: NVT-Seeding data for the different bubbles studied in this work at T=0.785.

difference is subtle, but given that the pressure inside the nucleating phase is obtained by integrating from the coexistence pressure (see Eq. 5.11) it is very important to use an accurate value for the latter.

The simulation data for different bubbles equilibrated at T=0.785 in the NVT ensemble are reported in Table 5.4. The values of R_c corresponding to each system (obtained with the equi-density criterion as discussed in section 5.4.1 and in Ref.[54]) are very close to those recently reported by ourselves[54]. However, the values of Δp here reported are not identical to those of Ref.[54] due to the coexistence pressure issue discussed above. In Fig.5.7(a) we plot Δp vs $1/R_c$ for bubbles and and drops at T=0.785. Drops and bubbles of the same size have the same Δp, which is perhaps the most important result of the paper. Note that, for a given R_c, the pressures of the external and the internal phases are not the same if one compares cavitation and condensation. What is the same is the pressure difference between the internal and the external phases. For instance, let's focus on the case of drop VII and bubble II, both with $R_c \approx 8.5$. In Fig. 5.8 we compare their radial density profiles. The density of the liquid inside the drop is different from that of the liquid outside the bubble. Also, the density of

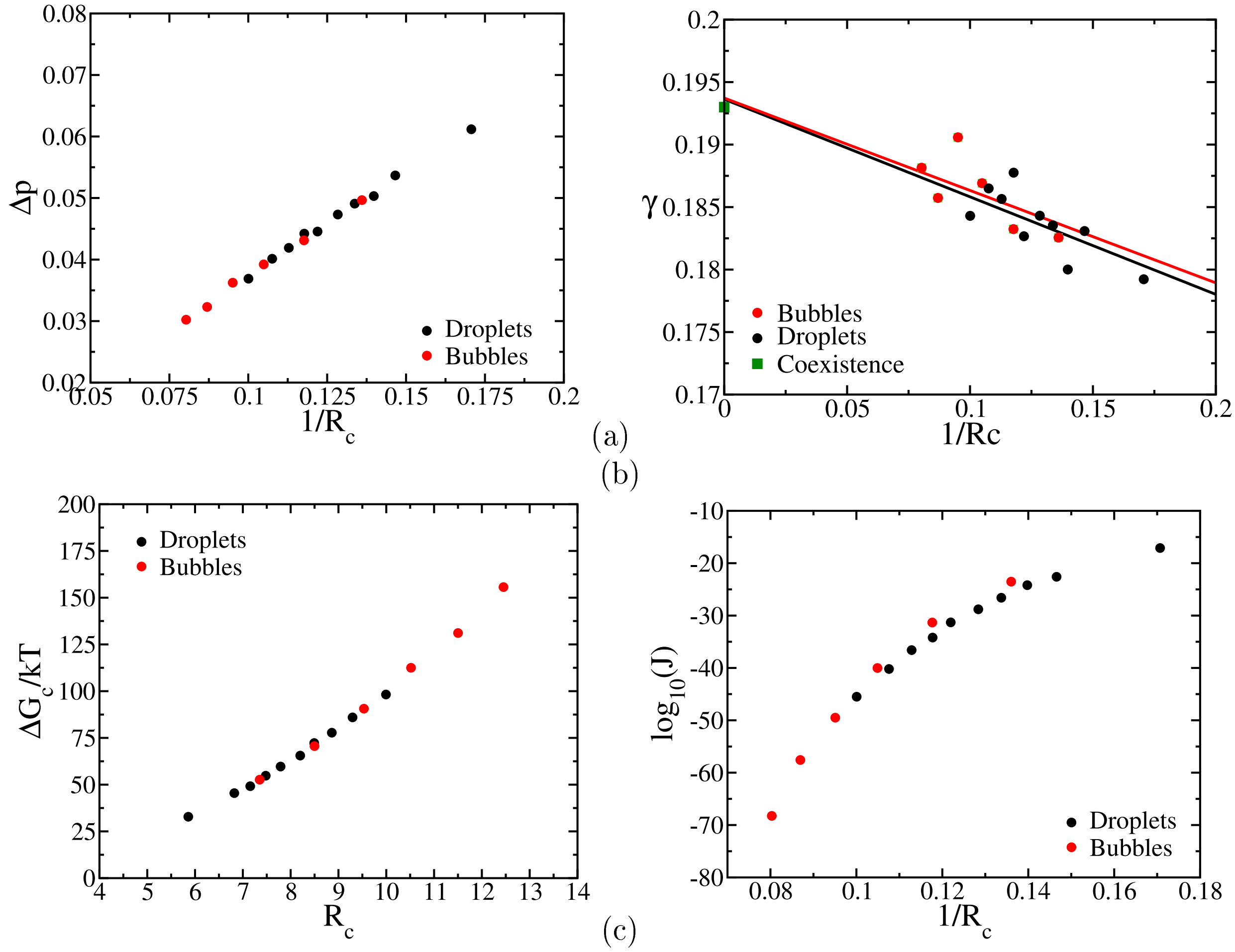

(a)
(b)

(c)
(d)

Figure 5.7: (a) Δp vs. $1/R_c$, (b) γ vs. $1/R_c$, (c) ΔG_c vs. R_c, and (d) $log_{10}J$ vs. $1/R_c$ for droplets (black symbols) and bubbles (red symbols) as obtained from NVT-Seeding.

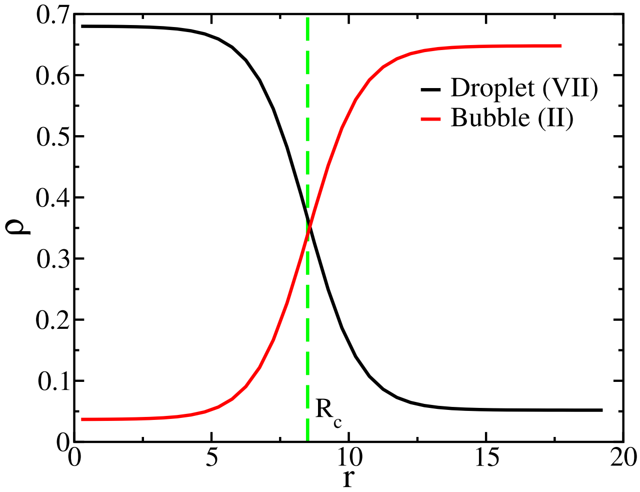

Figure 5.8: Radial density profiles of drop VII and bubble II, compared. They have almost identical radius, R_c.

the vapor inside the bubble is different from that of the vapor outside the drop. The bubble is surrounded by a liquid of pressure -0.01914 whereas the drop by a vapor of pressure 0.0301: the pressures of the external phases do not even have the same sign. The bubble and the drop also have very different pressures: 0.02398 and 0.07432 respectively. Despite the fact that the external and the internal pressures are very different, Δp is not: 0.043 and 0.044 for the bubble and the drop respectively.

According to the Laplace equation, that $\Delta p(R_c)$ is the same for drops and bubbles, implies that γ must be the also same regardless the identity of the internal and the external phases. In Fig. 5.7 (b) we plot γ vs $1/R_c$ for bubbles and drops and find that, indeed, they have the same γ within our statistical noise. Of course, attending to Eq. 5.3, ΔG_c, that only depends on R_c and Δp, is also the same for a given R_c, as illustrated in Fig. 5.7(c).

The nucleation rate for bubbles with a given R_c is close to the corresponding drop, but is not exactly the same, given that the kinetic pre-factor is not identical. In the case of bubble nucleation we have carefully assessed[70] that the following expression by Blander and Katz (BK) provides a good approximation for A_0:

$$A_0^{BK} = \sqrt{\frac{\Delta p R_c}{\pi m}}, \tag{5.16}$$

which is very similar, but with a missing (ρ_{vap}/ρ_l) factor with respect to the *ktg* expression we use for drop condensation (Eq. 5.10). The A_0^{BK} values we use in our Seeding predictions of bubble cavitation are reported in Table 5.4 alongside the resulting values of J obtained as $J = \rho_l A_0^{BK} \exp[-\Delta G_c/(k_B T)]$. As it can be seen in Fig. 5.7(d), the rate for bubbles and drops for a given R_c is quite similar, although it is systematically lower for the latter due to the ρ_{vap}/ρ_l factor previously mentioned.

Condensation and cavitation have already been compared in the literature[32,35,43,48,105–107]. However, there are only few cases in which γ has been compared for a given temperature as a function of the droplet/bubble size[32,35] as we do in this work. Establishing such comparison in experiments is difficult because it is not possible to detect the critical nucleus. In simulations the nucleus can be visualized, but computing γ is a hard task. It requires either computing the free energy of a system with the nucleus inside[32,34] or, more easily, computing the nucleus size and using a theory to infer γ[60,108] as we do in this work. In either approach, one has to deal with the arbitrariness of establishing a location for the interface.

In our case, we found in a recent work by "trial and error" that the equi-density surface gives good results for cavitation[70]. By "good results" we mean that Seeding predictions of nucleation are consistent with those coming from independent methods that do not rely on a precise definition of the nucleus size. In this work we have demonstrated that the same criterion to locate the interface is successful in condensation. Therefore, one of our main findings is that the equi-density surface is the one that provides good predictions when CNT is used both for cavitation and for condensation. This means that the equi-density surface can be identified with the surface of tension, which is the one for which CNT works and the Laplace equation holds (see section 5.4)[47,49,55,109] . We believe that identifying the surface of tension with the equi-density surface both for cavitation and condensation is an important finding of our work. This leads to the relevant conclusion that condensation and cavitation are two sides of the same coin in the sense that they share the same surface tension.

In Ref.[35] γ was found to be quite different for both phenomena, but the comparison was not established for the surface of tension but for the equimolar surface. In Ref.[32], however, the comparison was established for the first time for the surface of tension and, although γ was similar for condensation and cavitation, there were significant differences that need to be further investigated in order to match our work with that of Ref.[32].

5.6.2. Comparison for a given metastability degree

In Ref.[83] it was proposed in a DFT study that the work of formation of critical bubbles studied at different temperatures collapse when plotted against the metastability degree, X_m, quantified as:

$$X_m = \frac{\mu_{nuc} - \mu_{coex}}{\mu_{spinodal} - \mu_{coex}} \tag{5.17}$$

where μ_{nuc} is the chemical potential of the parent phase at the conditions where nucleation is studied, μ_{coex} is the coexistence chemical potential at the same temperature and at coexistence pressure, and $\mu_{spinodal}$ is the chemical potential at the same temperature but at the pressure where spinodal decomposition takes place. To estimate the spinodal pressure we run NpT simulations of the bulk liquid and vapor phases with 4000 particles. We estimate the spinodal decomposition pressure as that for which we the system undergoes a phase transition without any induction period, right after the start of the simulation. Both chemical potential differences in Eq. 5.17 can be easily obtained by numerically integrating the molar volume along pressure at constant

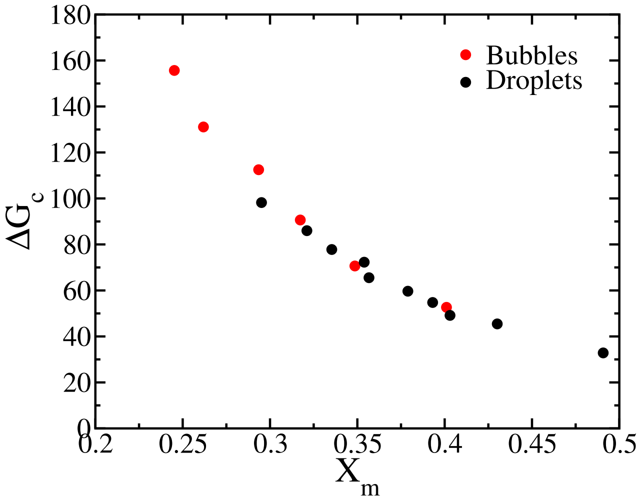

Figure 5.9: Nucleation free energy barrier for drops and bubbles (see legend) as a function of the metastability degree, X_m, defined in Eq. 5.17.

temperature. The denominator is the maximum possible metastability whereas the numerator is the actual metastability of the state where nucleation is studied. Therefore, X_m varies from 0 at coexistence, to 1 at spinodal decomposition. The mestastability degree above described can be computed for drop as well as for bubble nucleation. Therefore, we have the chance to compare nucleation free energy barriers for drops and bubbles as a function of X_m. The comparison, shown in Fig. 5.9, reveals the interesting conclusion that ΔG_c for bubble and drop nucleation is the same for a given metastbility degree. Therefore, not only nucleation barriers at different temperatures can be collapsed via the metastability degree as proposed in Ref.[83], but also bubble and drop nucleation data match for a given metastability degree.

5.6.3. Tolman Length

Since bubbles and drops of the same radius have the same interfacial properties, we can use the data coming from both systems altogether in order to compute the Tolmann Lenght, δ_T, which is defined as[34,74]:

$$\delta_{Tolman} = \lim_{R_s \to \infty} (R_e - R_s) \tag{5.18}$$

where R_e is the Gibbs equi-molar radius and R_s is the radius of the surface of tension. We identify R_s with R_c (the equi-density radius) given that (i) we obtain good predictions of nucleation when we use R_c and (ii) R_s is the radius that enters CNT[47,49,55,109]. To underline the fact that we identify R_c with R_s we label R_c as $R_{s=c}$ in the following figures. R_e can be easily computed from the radial density profiles[55,70]. In Fig. 5.10(a) we show $R_e - R_{s=c}$ versus $1/R_{s=c}$ for all data (either bubbles or drops) coming from this work. The extrapolation to $1/R_{s=c} = 0$ provides an estimate of δ_{Tolman}, indicated with an empty blue dot in the figure. We obtain $\delta_{Tolman} = 0.15 \pm 0.02$. We showed in a

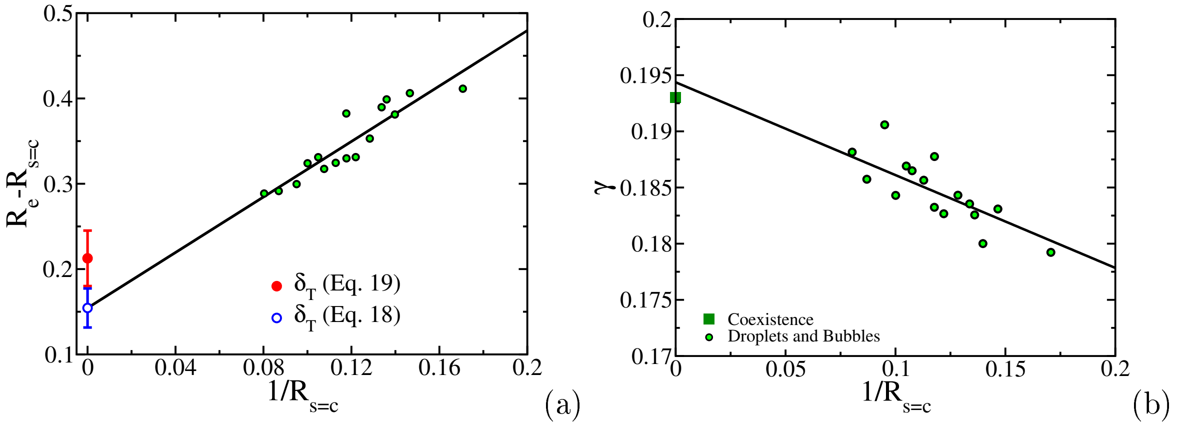

Figure 5.10: (a) $R_e - R_{s=c}$ and (b) γ vs. $1/R_{s=c}$ for drops and bubbles together.

recent paper, in which we analysed spherical hard sphere crystals in equilibrium with the fluid, that δ_{Tolman} can be also estimated by fitting γ to the following expression:

$$\gamma = \gamma_0 \left(1 - 2\frac{\delta_T}{R_s}\right), \tag{5.19}$$

where γ_0 is the value of γ at coexistence at the temperature of interest and δ_T is the fitting parameter that serves as an estimate for δ_{Tolman}[55]. This approach is similar in spirit to those that include γ given by Eq. 5.19 in CNT to fit free energy barriers obtained by rare event methods[84,110]. Again, we identify here R_s with R_c. Consequently, we use the γ data coming from such radius (that reported in Tables 5.1 and 5.4) to obtain an estimate of δ_T with the expression above. The data of γ vs $1/R_{s=c}$ are shown in green in Fig. 5.10(b). The solid line is a linear fit of γ vs $1/R_{s=c}$ which includes γ_0 (the green square in the figure). The δ_T value coming from such fit, $\delta_T = 0.21 \pm 0.03$, is shown with a red dot in Fig. 5.10(a). Both values, δ_{Tolman} obtained via Eq. 5.18 (blue dot in Fig. 5.10(a)) and δ_T coming from Eq. 5.19 (red dot the same figure), are consistent with each other within the statistical uncertainty of our estimates. This corroborates the idea, recently checked for the first time for hard sphere crystals[55], that the Tolman lenght can be obtained either from Eq. 5.19 or from Eq. 5.18. Hence, this idea seems to be a general one pertaining not only to the crystal-fuid equilibrium but also to the liquid-vapor one.

This study may shed some light in the intense literature debate about the magnitude and sign of the Tolman length[18,30–32,34–44]. We obtain a Tolman length of about twenty per cent the particle diameter. Its sign is positive, which means that γ decreases when one moves away from coexistence at constant temperature.

5.7. Conclusions

The main conclusions we draw from our work are the following:

a) We have used NVT-Seeding to investigate droplet nucleation in a supersaturated Lennard-Jones vapor. The results obtained from this technique are consistent with: (i) independent calculations of the nucleation free energy barrier performed with Umbrella Sampling (ii) the surface tension of a flat interface obtained from the pressure tensor in a vapor-liquid coexistence simulation (iii) the drop nucleation rate obtained both with US and in brute force spontaneous nucleation simulations.

b) NVT-Seeding requires defining the radius of a droplet equilibrated in the NVT ensemble. The radius definition that passes the consistency tests mentioned in the previous paragraph is that given by the surface where the density is average between that of the interior and that of the exterior phases. Such radius definition was also successful in our earlier studies of bubble nucleation[54,70]. Therefore, we identify this "equi-density" radius with the radius of tension, R_s.

c) The good performance of Seeding strongly supports the use of CNT to describe nucleation. However, the capillarity approximation (that γ is curvature independent) does not provide good results. A γ dependent on the curvature of the critical nucleus must be plugged into the the theory. Therefore, the theory, although powerful, requires the involvement of simulations given that the γ-curvature dependence is obtained by computing the size of the critical cluster at different pressures.

d) The kinetic theory of gases provides very good estimates of the kinetic pre-factor of the condensation nucleation rate. This makes the theoretical framework very powerful given that only the size of the critical cluster, the density of the external phase and the bulk phases equations of state are needed to estimate nucleation rates.

e) We compare NVT-Seeding results of droplets with those obtained for bubbles and find that, for a given temperature, bubbles and droplets of the same radius have, within the accuracy of our method, the same pressure difference with the surrounding medium. Therefore, bubbles and droplets of the same size have the same surface tension and the same nucleation free energy barrier. In this respect, condensation and boiling can be seen as two sides of the same coin. Such duality is only verified if the size of the critical nucleus (either a bubble or a drop) is determined with the equi-density radius (our empirical definition of the surface of tension).

f) We estimate the Tolman length, δ_T, by extrapolating to infinite-size drops/bubbles the difference between the equimolar radius, R_e, and R_s. Such δ_T is consistent with that obtained by linearly fitting $\gamma(1/R_c)$, in accordance with our recent work of hard sphere crystals[55].

5.8. Acknowledgments

This work was funded by grants FIS2016/78117-P and PID2019-105898GB-C21 of the MEC. The authors acknowledge the computer resources and technical assistance provided by the RES. P. R. thanks a doctoral grant from UCM. P. M. H. acknowledges financial support from the FPI grant no. BES- 671 2017-080074. We also thank the reviewers of this work for their suggestions.

Bibliography

[1] G. J. Morris and E. Acton. Controlled ice nucleation in cryopreservation–a review. *Cryobiology*, 66:85, 2013.

[2] Will Cantrell and Andrew Heymsfield. Production of ice in tropospheric clouds: A review. *Bulletin of the American Meteorological Society*, 86(6):795–808, 2005.

[3] P. G. Debenedetti. *Metastable liquids: Concepts and Principles.* Princeton University Press, 1996.

[4] Keith T. Smith. Water ice cliffs on mars. *Science*, 359(6372):172–172, 2018.

[5] R. W. Hartel. *Crystallization in foods.* Springer, New York, 2001.

[6] H G Brittain(Ed.). *Polymorphism in Pharmaceutical Solids.* Marcel Dekker, New York, 1999.

[7] K. F. Kelton. *Crystal Nucleation in Liquids and Glasses.* Academic, Boston, 1991.

[8] Vladimir Pavlovich Skripov. *Metastable liquids.* Wiley, 1974.

[9] Barbara E Wyslouzil and Judith Wölk. Overview: Homogeneous nucleation from the vapor phasethe experimental science. *The Journal of chemical physics*, 145(21):211702, 2016.

[10] P. V. Skripov and A. P. Skripov. The phenomenon of superheat of liquids: in memory of Vladimir P. Skripov. *International Journal of Thermophysics*, 31(4-5):816–830, 2010.

[11] EV Lipnyagov, AL Gurashkin, AA Starostin, and PV Skripov. Going to spontaneous boiling-up onset. *Journal of Engineering Thermophysics*, 27(3):307–318, 2018.

[12] VP Skripov. Metastable states. *J. Non-Equilib. Thermodyn*, 17(3):193–236, 1992.

[13] A. Manka, H. Pathak, S. Tanimura, J. Wolk, R. Strey, and B. E. Wyslouzil. Freezing water in no man's land. 14:4505–4516, 2012.

[14] Andrew J Amaya and Barbara E Wyslouzil. Ice nucleation rates near ~ 225 K. *The Journal of chemical physics*, 148(8):084501, 2018.

[15] Xiao Liang Hu and Angelos Michaelides. Water on the hydroxylated (0 0 1) surface of kaolinite: From monomer adsorption to a flat 2d wetting layer. *Surface Science*, 602(4):960–974, 2008.

[16] Ashutosh Bhabhe, Harshad Pathak, and Barbara E. Wyslouzil. Freezing of heavy water (D_2O) nanodroplets. *The Journal of Physical Chemistry A*, 117(26):5472–5482, 2013.

[17] Luisa Ickes, Andre Welti, Corinna Hoose, and Ulrike Lohmann. Classical nucleation theory of homogeneous freezing of water: thermodynamic and kinetic parameters. *Phys. Chem. Chem. Phys.*, 17:5514–5537, 2015.

[18] Nicolas Bruot and Frédéric Caupin. Curvature dependence of the liquid-vapor surface tension beyond the tolman approximation. *Physical review letters*, 116(5):056102, 2016.

[19] Laszlo Granasy, Tamas Pusztai, and Peter F. James. Interfacial properties deduced from nucleation experiments: A cahn–hilliard analysis. *J. Chem. Phys.*, 117(13):6157–6168, 2002.

[20] John G Kirkwood and Frank P Buff. The statistical mechanical theory of surface tension. *The Journal of Chemical Physics*, 17(3):338–343, 1949.

[21] G.J. Gloor, G. Jackson, F.J. Blas, and E. de Miguel. Test-area simulation method for the direct determination of the interfacial tension of systems with continuous or discontinuous potentials. 123:134703, 2005.

[22] J. Q. Broughton and G. H. Gilmer. Molecular dynamics investigation of the crystal–fluid interface. VI. Excess surface free energies of crystal–liquid systems. *J. Chem. Phys.*, 84(10):5759–5768, 1986.

[23] J. J. Hoyt, Mark Asta, and Alain Karma. Method for computing the anisotropy of the solid-liquid interfacial free energy. *Phys. Rev. Lett.*, 86:5530–5533, Jun 2001.

[24] Alessandro Laio and Michele Parrinello. Escaping free-energy minima. 99:12562, 2002.

[25] Stefano Angioletti-Uberti, Michele Ceriotti, Peter D. Lee, and Mike W. Finnis. Solid-liquid interface free energy through metadynamics simulations. *Phys. Rev. B*, 81:125416, Mar 2010.

[26] L. A. Fernandez, V. Martin-Mayor, B. Seoane, and P. Verrocchio. Equilibrium fluid-solid coexistence of hard spheres. *Phys. Rev. Lett.*, 108:165701, Apr 2012.

[27] T. Zykova-Timan, D. Ceresoli, U. Tartaglino, and E. Tosatti. Why are alkali halide surfaces not wetted by their own melt? *Phys. Rev. Lett.*, 94:176105, May 2005.

[28] S. Auer and D. Frenkel. Prediction of absolute crystal-nucleation rate in hard-sphere colloids. *Nature*, 409:1020, 2001.

[29] J. R. Espinosa, C. Vega, and E. Sanz. The mold integration method for the calculation of the crystal-fluid int erfacial free energy from simulations. *J. Chem. Phys.*, 141(13):134709, 2014.

[30] Gabriel V Lau, Ian J Ford, Patricia A Hunt, Erich A Müller, and George Jackson. Surface thermodynamics of planar, cylindrical, and spherical vapour-liquid interfaces of water. *J. Chem. Phys.*, 142(11):114701, 2015.

[31] Bingqing Cheng and Michele Ceriotti. Communication: Computing the tolman length for solid-liquid interfaces. *The Journal of chemical physics*, 148(23):231102, 2018.

[32] Kurt Binder, Benjamin J Block, Peter Virnau, and Andreas Tröster. Beyond the van der waals loop: What can be learned from simulating lennard-jones fluids inside the region of phase coexistence. *American Journal of Physics*, 80(12):1099–1109, 2012.

[33] John Shipley Rowlinson and Benjamin Widom. *Molecular theory of capillarity.* Oxford University Press, 1982.

[34] Edgar M Blokhuis and Joris Kuipers. Thermodynamic expressions for the tolman length. *The journal of chemical physics*, 124(7):074701, 2006.

[35] Benjamin J Block, Subir K Das, Martin Oettel, Peter Virnau, and Kurt Binder. Curvature dependence of surface free energy of liquid drops and bubbles: A simulation study. *The Journal of chemical physics*, 133(15):154702, 2010.

[36] José G Sampayo, Alexandr Malijevskỳ, Erich A Müller, Enrique de Miguel, and George Jackson. Communications: Evidence for the role of fluctuations in the thermodynamics of nanoscale drops and the implications in computations of the surface tension. *J. Chem. Phys.*, 132(14):141101, 2010.

[37] Alexandr Malijevskỳ and George Jackson. A perspective on the interfacial properties of nanoscopic liquid drops. *Journal of Physics: Condensed Matter*, 24(46):464121, 2012.

[38] Hai Ming Lu and Qing Jiang. Size-dependent surface tension and tolman's length of droplets. *Langmuir*, 21(2):779–781, 2005.

[39] S. M. Thompson, K. E. Gubbins, J. P. R. B. Walton, R. A. R. Chantry, and J. S. Rowlinson. A molecular dynamics study of liquid drops. 81:530, 1984.

[40] Jadran Vrabec, Gaurav Kumar Kedia, Guido Fuchs, and Hans Hasse. Comprehensive study of the vapour–liquid coexistence of the truncated and shifted lennard–jones fluid including planar and spherical interface properties. *Molecular physics*, 104(09):1509–1527, 2006.

[41] Øivind Wilhelmsen, Dick Bedeaux, and David Reguera. Tolman length and rigidity constants of the lennard-jones fluid. *The Journal of chemical physics*, 142(6):064706, 2015.

[42] Mark N Joswiak, Ryan Do, Michael F Doherty, and Baron Peters. Energetic and entropic components of the tolman length for mw and tip4p/2005 water nanodroplets. *The Journal of chemical physics*, 145(20):204703, 2016.

[43] Jürn WP Schmelzer, Alexander S Abyzov, and Vladimir G Baidakov. Entropy and the tolman parameter in nucleation theory. *Entropy*, 21(7):670, 2019.

[44] David Richard and Thomas Speck. Crystallization of hard spheres revisited. ii. thermodynamic modeling, nucleation work, and the surface of tension. *The Journal of chemical physics*, 148(22):224102, 2018.

[45] Manuel Schrader, Peter Virnau, and Kurt Binder. Simulation of vapor-liquid coexistence in finite volumes: A method to compute the surface free energy of droplets. *Physical Review E*, 79(6):061104, 2009.

[46] Mitsuhiro Matsumoto and Kotaro Tanaka. Nano bubble-size dependence of surface tension and inside pressure. *Fluid dynamics research*, 40(7-8):546, 2008.

[47] A Tröster, M Oettel, B Block, P Virnau, and K Binder. Numerical approaches to determine the interface tension of curved interfaces from free energy calculations. *The Journal of chemical physics*, 136(6):064709, 2012.

[48] Luis G MacDowell, Vincent K Shen, and Jeffrey R Errington. Nucleation and cavitation of spherical, cylindrical, and slablike droplets and bubbles in small systems. *J. Chem. Phys.*, 125(3):034705, 2006.

[49] Antonia Statt, Peter Virnau, and Kurt Binder. Finite-size effects on liquid-solid phase coexistence and the estimation of crystal nucleation barriers. *Physical review letters*, 114(2):026101, 2015.

[50] Peter Koß, Antonia Statt, Peter Virnau, and Kurt Binder. The phase coexistence method to obtain surface free energies and nucleation barriers: A brief review. *Molecular Physics*, 116(21-22):2977–2986, 2018.

[51] KGSH Gunawardana and Xueyu Song. Theoretical prediction of crystallization kinetics of a supercooled lennard-jones fluid. *The Journal of chemical physics*, 148(20):204506, 2018.

[52] Johannes Zierenberg and Wolfhard Janke. Exploring different regimes in finite-size scaling of the droplet condensation-evaporation transition. *Physical Review E*, 92(1):012134, 2015.

[53] Johannes Zierenberg, Philipp Schierz, and Wolfhard Janke. Canonical free-energy barrier of particle and polymer cluster formation. *Nature Communications*, 8(1):14546, 2017.

[54] Pablo Rosales-Pelaez, Ignacio Sanchez-Burgos, Chantal Valeriani, Carlos Vega, and Eduardo Sanz. Seeding approach to nucleation in the n v t ensemble: The case of bubble cavitation in overstretched lennard jones fluids. *Physical Review E*, 101(2):022611, 2020.

[55] Pablo Montero de Hijes, Jorge R Espinosa, Valentino Bianco, Eduardo Sanz, and Carlos Vega. Interfacial free energy and tolman length of curved liquid–solid interfaces from equilibrium studies. *The Journal of Physical Chemistry C*, 124(16):8795–8805, 2020.

[56] James F Lutsko and Julien Lam. Classical density functional theory, unconstrained crystallization, and polymorphic behavior. *Physical Review E*, 98(1):012604, 2018.

[57] James F Lutsko. How crystals form: A theory of nucleation pathways. *Science advances*, 5(4):eaav7399, 2019.

[58] E. Sanz, C. Vega, J. R. Espinosa, R. Caballero-Bernal, J. L. F. Abascal, and C. Valeriani. Homogeneous ice nucleation at moderate supercooling from molecular simulation. *J. Am. Chem. Soc.*, 135(40):15008–15017, 2013.

[59] Brandon C. Knott, Valeria Molinero, Michael F. Doherty, and Baron Peters. Homogeneous nucleation of methane hydrates: Unrealistic under realistic conditions. *J. Am. Chem. Soc.*, 134:19544–19547, 2012.

[60] Xian-Ming Bai and Mo Li. Calculation of solid-liquid interfacial free energy: A classical nucleation theory based approach. *J. Chem. Phys.*, 124(12):124707, 2006.

[61] Jorge R. Espinosa, Carlos Vega, Chantal Valeriani, and Eduardo Sanz. Seeding approach to crystal nucleation. 144:034501, 2016.

[62] M. Volmer and A. Weber. Keimbildung in ubersattigten gebilden. *Z. Phys. Chem.*, 119:277, 1926.

[63] R. Becker and W. Doring. Kinetische behandlung der keimbildung in ubersattigten dampfen. *Ann. Phys.*, 416:719–752, 1935.

[64] J. W. Gibbs. On the equilibrium of heterogeneous substances. *Trans. Connect. Acad. Sci.*, 3:108–248, 1876.

[65] J. W. Gibbs. On the equilibrium of heterogeneous substances. *Trans. Connect. Acad. Sci.*, 16:343–524, 1878.

[66] Alberto Zaragoza, Maria M. Conde, Jorge R. Espinosa, Chantal Valeri ani, Carlos Vega, and Eduardo Sanz. Competition between ices ih and ic in homogeneous water freezing. *J. Chem. Phys.*, 143(13):134504, 2015.

[67] Jorge R. Espinosa, Alberto Zaragoza, Pablo Rosales-Pelaez, Caridad N avarro, Chantal Valeriani, Carlos Vega, and Eduardo Sanz. Interfacial free energy as the key to the pressure-induced deceleration o f ice nucleation. *Phys. Rev. Lett.*, 117:135702, 2016.

[68] Jorge R. Espinosa, Guiomar D. Soria, Jorge Ramirez, Chantal Valeriani, Carlos Vega, and Eduardo Sanz. Role of salt, pressure, and water activity on homogeneous ice nucleation. *J. Phys. Chem. Lett.*, 8:4486, 2017.

[69] Jorge R Espinosa, Carlos Vega, and Eduardo Sanz. Homogeneous ice nucleation rate in water droplets. *The Journal of Physical Chemistry C*, 122(40):22892–22896, 2018.

[70] P Rosales-Pelaez, MI Garcia-Cid, C Valeriani, C Vega, and E Sanz. Seeding approach to bubble nucleation in superheated lennard-jones fluids. *Physical Review E*, 100(5):052609, 2019.

[71] Glenn M Torrie and John P Valleau. Monte carlo free energy estimates using non-boltzmann sampling: Application to the sub-critical lennard-jones fluid. *Chemical Physics Letters*, 28(4):578–581, 1974.

[72] J. S. van Duijneveld and D. Frenkel. Computer simulation study of free energy barriers in crystal nucleation. 96:4655, 1992.

[73] L. Filion, M. Hermes, R. Ni, and M. Dijkstra. Crystal nucleation of hard spheres using molecular dynamics, umbrella sampling, and forward flux sampling: A comparison of simulation techniques. *J. Chem. Phys.*, 133(24):244115, 2010.

[74] Richard C Tolman. The effect of droplet size on surface tension. *The journal of chemical physics*, 17(3):333–337, 1949.

[75] Zun-Jing Wang, Chantal Valeriani, and Daan Frenkel. Homogeneous bubble nucleation driven by local hot spots: A molecular dynamics study. *The Journal of Physical Chemistry B*, 113(12):3776–3784, 2008.

[76] Kyoko K Tanaka, Hidekazu Tanaka, Raymond Angelil, and Jürg Diemand. Simple improvements to classical bubble nucleation models. *Physical review E*, 92(2):022401, 2015.

[77] Stacey L Meadley and Fernando A Escobedo. Thermodynamics and kinetics of bubble nucleation: Simulation methodology. *The Journal of chemical physics*, 137(7):074109, 2012.

[78] S. Plimpton. Fast parallel algorithms for short-range molecular dynamics. *J. Comput. Phys.*, 117:1, 1995.

[79] R. W. Hockney, S. P. Goel, and J Eastwood. Quiet high resolution computer models of a plasma. *J. Comp. Phys.*, 14:148–158, 1974.

[80] Shuichi Nosé. A unified formulation of the constant temperature molecular dynamics methods. 81:511, 1984.

[81] VG Baidakov and KR Protsenko. Molecular dynamics simulation of cavitation in a lennard-jones liquid at negative pressures. *Chemical Physics Letters*, 760:138030, 2020.

[82] C. Valeriani, E. Sanz, and D. Frenkel. Rate of homogeneous crystal nucleation in molten NaCl. 122:194501, 2005.

[83] Vincent K Shen and Pablo G Debenedetti. Density-functional study of homogeneous bubble nucleation in the stretched lennard-jones fluid. *The Journal of Chemical Physics*, 114(9):4149–4159, 2001.

[84] Mirko Gallo, Francesco Magaletti, Davide Cocco, and Carlo Massimo Casciola. Nucleation and growth dynamics of vapour bubbles. *Journal of Fluid Mechanics*, 883:A14, 2020.

[85] James F Lutsko. Density functional theory of inhomogeneous liquids. iii. liquid-vapor nucleation. *The Journal of Chemical Physics*, 129(24):244501, 2008.

[86] Dimo Kashchiev. On the relation between nucleation work, nucleus size, and nucleation rate. 76:5098, 1982.

[87] Dimo Kashchiev. Forms and applications of the nucleation theorem. *The Journal of chemical physics*, 125(1):014502, 2006.

[88] Jan Wedekind and David Reguera. What is the best definition of a liquid cluster at the molecular scale? *The Journal of chemical physics*, 127(15):154516, 2007.

[89] S Marchio, S Meloni, A Giacomello, C Valeriani, and CM Casciola. Pressure control in interfacial systems: Atomistic simulations of vapor nucleation. *The Journal of chemical physics*, 148(6):064706, 2018.

[90] P Montero de Hijes, K Shi, EG Noya, EE Santiso, KE Gubbins, E Sanz, and C Vega. The young–laplace equation for a solid–liquid interface. *The Journal of Chemical Physics*, 153(19):191102, 2020.

[91] Olivier Vincent and Philippe Marmottant. On the statics and dynamics of fully confined bubbles. *Journal of Fluid Mechanics*, 827:194–224, 2017.

[92] Dominik Marti, Yves Krüger, Dominik Fleitmann, Martin Frenz, and Jaro Rička. The effect of surface tension on liquid–gas equilibria in isochoric systems and its application to fluid inclusions. *Fluid phase equilibria*, 314:13–21, 2012.

[93] Jan Wedekind, David Reguera, and Reinhard Strey. Finite-size effects in simulations of nucleation. *The Journal of Chemical Physics*, 125(21):214505, 2006.

[94] David Reguera and Howard Reiss. Fusion of the extended modified liquid drop model for nucleation and dynamical nucleation theory. *Physical review letters*, 93(16):165701, 2004.

[95] D. Reguera, R. K. Bowles, Y. Djikaev, and H. Reiss. Phase transitions in systems small enough to be clusters. 118:340, 2003.

[96] P. Koss, A. Statt, P. Virnau, and K. Binder. Free energy barriers for crystal nucleation from fluid phases. *arXiv*, -:1705.08216, 2017.

[97] Arthur Jing-Min Yang. The thermodynamical stability of the heterogeneous system with a spherical interface. *The Journal of chemical physics*, 82(4):2082–2085, 1985.

[98] Mirko Gallo, Francesco Magaletti, and Carlo Massimo Casciola. Thermally activated vapor bubble nucleation: The landau-lifshitz–van der waals approach. *Physical Review Fluids*, 3(5):053604, 2018.

[99] Mirko Gallo, Francesco Magaletti, and Carlo Massimo Casciola. Heterogeneous bubble nucleation dynamics. *Journal of Fluid Mechanics*, 906, 2020.

[100] Qianxiang Xiao, Yawei Liu, Zhenjiang Guo, Zhiping Liu, Daan Frenkel, Jure Dobnikar, and Xianren Zhang. What experiments on pinned nanobubbles can tell about the critical nucleus for bubble nucleation. *The European Physical Journal E*, 40(12):1–6, 2017.

[101] JPRB Walton, DJ Tildesley, JS Rowlinson, and JR Henderson. The pressure tensor at the planar surface of a liquid. *Molecular physics*, 48(6):1357–1368, 1983.

[102] S. Auer and D. Frenkel. Numerical prediction of absolute crystallization rates in hard-sphere colloids. 120:3015, 2004.

[103] Pieter Rein ten Wolde and Daan Frenkel. Computer simulation study of gas-liquid nucleation in a Lennard-Jones system. 109:9901, 1998.

[104] M. A. Gonzalez, E. Sanz, C. McBride, J. L. F. Abascal, C. Vega, and C. Valeriani. Nucleation free-energy barriers with hybrid monte-carlo/umbrella sampling. *Phys. Chem. Chem. Phys.*, 16:24913–24919, 2014.

[105] Robert Guermeur, Francis Biquard, and Christian Jacolin. Density profiles and surface tension of spherical interfaces. numerical results for nitrogen drops and bubbles. *The Journal of chemical physics*, 82(4):2040–2051, 1985.

[106] Luis G. MacDowell, Peter Virnau, Marcus Müller, and Kurt Binder. The evaporation/condensation transition of liquid droplets. 120:5293, 2004.

[107] F. Caupin. Escaping the no man's land: Recent experiments on metastable liquid water. *Journal of Non-Crystalline Solids*, 407:441–448, 2015.

[108] R. G. Pereyra, I. Szleifer, and M. A. Carignano. Temperature dependence of ice critical nucleus size. *J. Chem. Phys.*, 135:034508, 2011.

[109] D. Kashchiev. *Nucleation: Basic Theory with Applications.* Butterworth-Heinemann, Oxford, 2000.

[110] Georg Menzl, Miguel A Gonzalez, Philipp Geiger, Frédéric Caupin, José LF Abascal, Chantal Valeriani, and Christoph Dellago. Molecular mechanism for cavitation in water under tension. *Proceedings of the National Academy of Sciences*, 113(48):13582–13587, 2016.

Chapter 6

Anomalous behavior in the nucleation of ice at negative pressures

Valentino Bianco[1], P. Montero de Hijes[1], Cintia P. Lamas[1], Eduardo Sanz[1], and Carlos Vega[1]

[1]Departamento de Química Física, Facultad de Química, Universidad Complutense de Madrid, Ciudad Universitaria, Madrid 28040, Spain

6.1. Abstract

Ice nucleation is a phenomenon that, despite the relevant implications for life, atmospheric sciences and technological applications, is far from being completely understood, especially under extreme thermodynamic conditions. In this work we present a computational investigation of the homogeneous ice nucleation at negative pressures. By means of the *seeding technique* we estimate the size of the ice critical nucleus N_c for the TIP4P/Ice water model. This is done along the isotherms 230 K, 240 K, and 250 K, from positive to negative pressures until reaching the liquid-gas kinetic stability limit (where cavitation cannot be avoided). We find that N_c is non-monotonic upon depressurization, reaching a minimum at negative pressures in the doubly metastable region of water. According to classical nucleation theory we establish the nucleation rate J and the surface tension γ, revealing a retracing behavior of both when the liquid-gas kinetic stability limit is approached. We also predict a reentrant behavior of the homogeneous nucleation line. The re-entrance of these properties is related to the re-entrance of the coexistence line at negative pressure, revealing new anomalies of water. The results of this work suggest the possibility of having metastable samples of liquid water for long times at negative pressure provided that heterogeneous nucleation is suppressed.

6.2. Introduction

Ice formation is possibly the most important liquid-to-solid transition, being relevant in cryo-biology, food storage, material science, and Earth science[1–8]. Homogeneous nucleation is the mechanism through which thermal fluctuations in a pure liquid below coexistence induce the formation of crystal nuclei that, when sufficiently large (critical size), trigger the crystallization.

At ambient pressure and a few kelvins below coexistence, the size of the critical nucleus N_c is huge and the probability of forming spontaneously in pure supercooled water is negligible[9,10]. Consequently, in nature, ice is formed essentially via heterogeneous nucleation[11].

Several investigations have addressed the behavior of supercooled liquid water at negative pressure[12–20], with little attention paid to ice nucleation[21,22]. Here, we fill this gap by exploring the homogeneous ice nucleation from positive to negative pressure P at constant temperature T.

By means of molecular dynamic simulations of the TIP4P/Ice water model[23] – probably the best atomistic model to study ice properties and with a well known phase diagram[23,24]– we reveal that the isothermal variation of N_c is non-monotonic. For any isothermal path, a minimum is always observed at $P < 0$. This retracing behavior is linked to the re-entrance of the coexistence line.

6.3. Simulation Details

All the simulations have been performed using GROMACS[25], adopting: i) a time step of 2 fs; ii) the Noose-Hoover thermostat with a relaxation time of 1 ps; iii) the Parrinello-Rahman barostat with a relaxation time of 2 ps; iv) the particle-mesh-Ewald algorithm of order 4, with Fourier spacing of 0.1 nm to solve the electrostatic interaction; v) a cutoff of 0.9 nm both for the Lennard-Jones and Coulomb interactions; vi) long range corrections to the Lennard-Jones interaction.

6.4. Results

Given the polymorphism of ice, we investigate the most stable structure. According to Matsui et al.[26], Ih is clearly the most stable ice up to extreme negative pressures, where ice Ih and the recently discovered ice XVI[27] are close in terms of stability. Hence, first we determine the solid-liquid coexistence lines for ice Ih and ice XVI for the TIP4P/Ice model via direct coexistence simulations [see the Supporting Material (SM)[28]]. The T-P loci of the coexistence lines are shown in Fig. 6.1a. For $P > -3000$ bar the ice XVI coexistence line is lower than the Ih coexistence line, meaning that the Ih structure is more stable than the ice XVI for this pressure range. The triple point water-Ih-ice

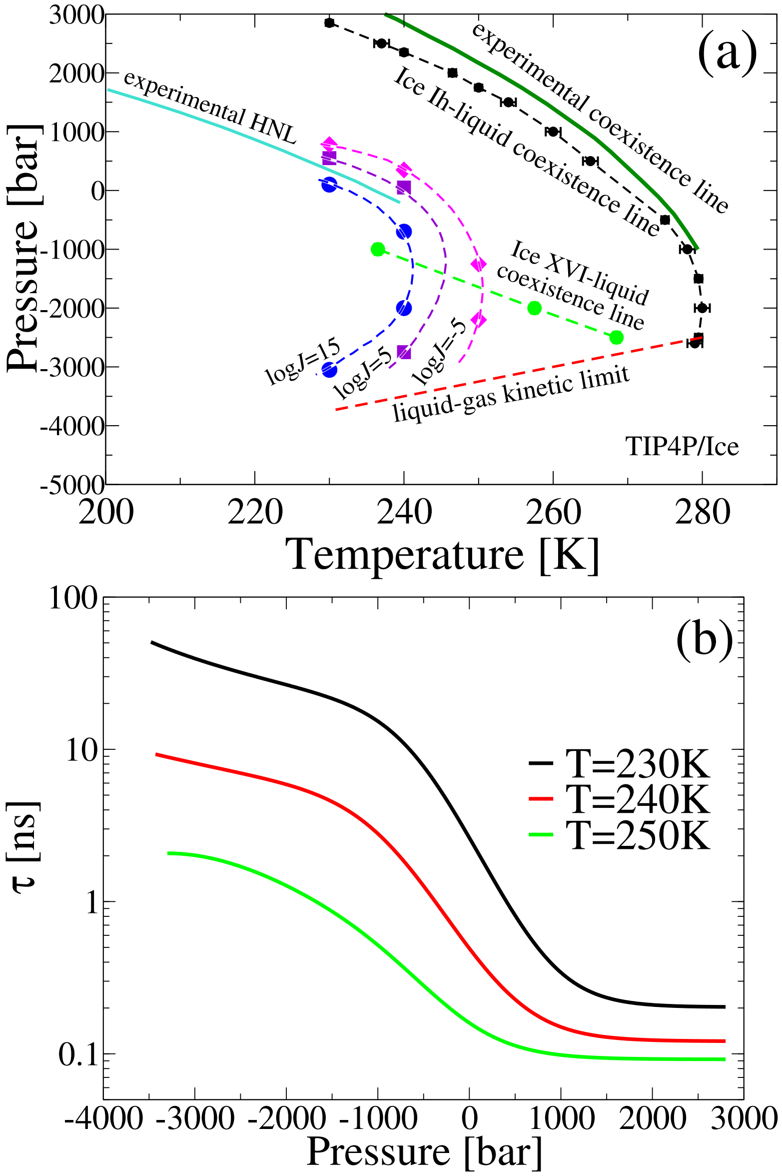

Figure 6.1: (a) Phase diagram in the $T-P$ plane of the TIP4P/Ice water model showing: i) the ice Ih-liquid coexistence line (black points); ii) the liquid-gas kinetic limit (red dashed line); iii) the iso-lines with constant logarithm of the nucleation rate: $\log_{10} J/(m^{-3}s^{-1}) = 15, 5, -5$ (see Fig. 6.4b). iv) the fitting of experimental homogeneous nucleation line (HNL)[22] and ice Ih-liquid coexistence proposed by Marcolli[21]; v) the ice XVI-liquid coexistence curve (green points). The HNL (where the formation of ice can not be avoided) from experiments corresponds approximately to an iso-line $\log_{10} J/(m^{-3}s^{-1}) = 15$[9]. (b) Relaxation time $\tau \equiv (0.31\ \mathrm{nm})^2/(6D)$ to diffuse the square of the diameter of a water molecule as a function of P.

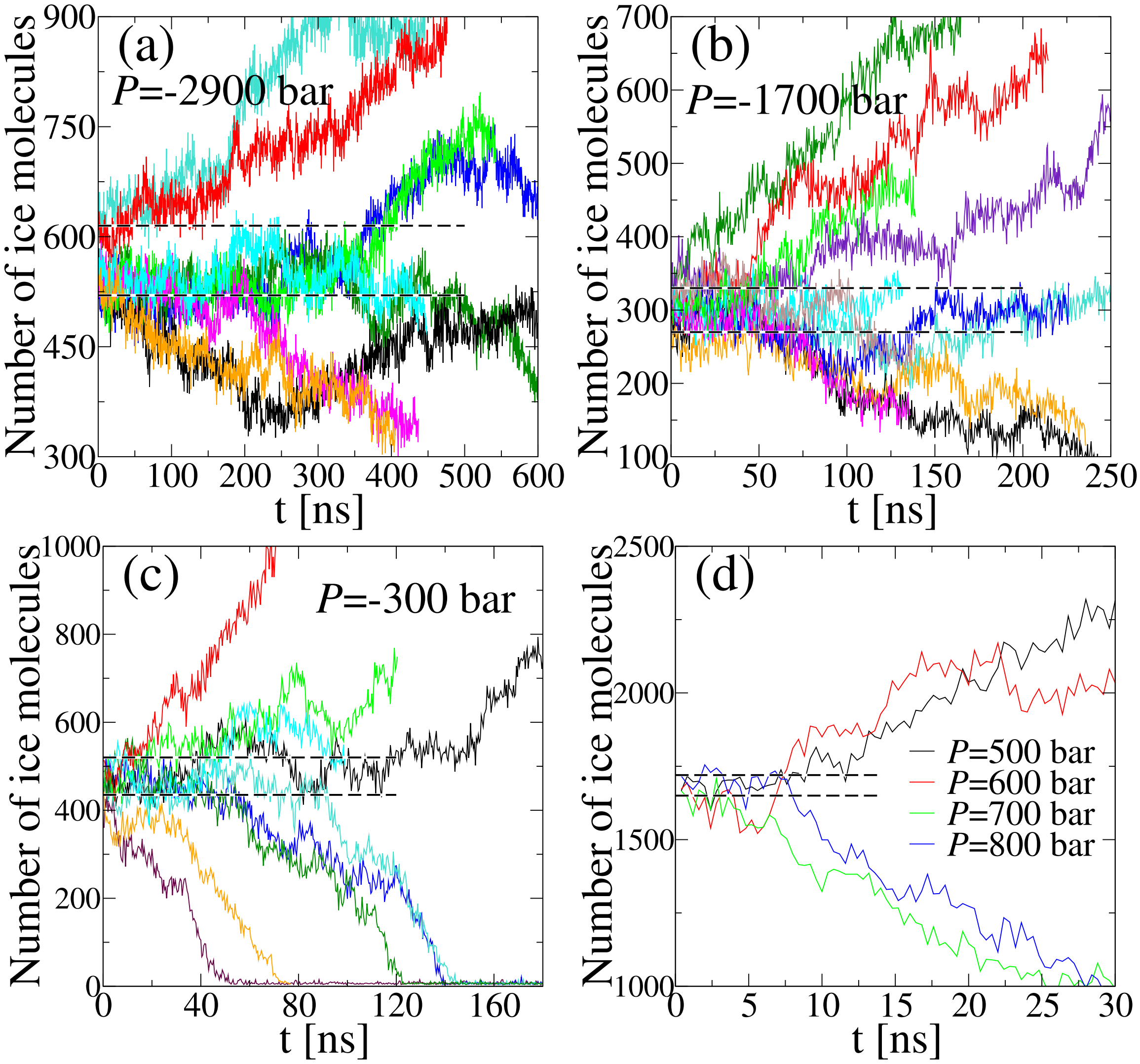

Figure 6.2: Time evolution of the ice seed along the isotherm $T = 240$ K at: (a) $P = -2900$ bar; (b) $P = -1700$ bar; (c) $P = -300$ bar; (d) different positive pressures. Dashed lines mark the boundaries of the estimated critical size N_c (established as the difference between the size of the largest seed melting and the smallest seed growing). In a-c P was constant and we changed the size of the initial ice cluster. In d), the initial size of the cluster was identical but it was studied at different P. From the results of d) one estimates that the cluster is critical at $P \sim 650\,$bar.

XVI is estimated at $P \sim -3000$ bar and $T \sim 278$ K, similar to what has been found for the TIP4P/2005 water model[29]. Therefore, we have conducted our investigation with ice Ih, although for $P < -3000$ bar the nucleation of ice XVI could be relevant.

We then estimate the liquid-gas kinetic stability limit defined as the $T - P$ locus where 2000 liquid water molecules were stable for at least 100 ns. For any thermodynamic state in this work it is possible to reach a metastable equilibrium, as the relaxation time is smaller than 40 ns (Fig. 6.1b). As can be seen, before this stability limit is reached, there is a re-entrance of the coexistence line with a turning point $dT/dP = 0$ at $P \sim -2000$ bar and $T \sim 280$ K. In 1982, Speedy conjectured a re-entering behavior of the liquid-gas spinodal[30]. This has been recently demonstrated to be the case for colloidal systems[31] but ruled out for water[32] as further seen in this work. Nevertheless, Henderson and Speedy later conjectured a reentrance in the coexistence line[15] (also suggested by Bridgman in 1912[33]). Speedy's estimation of the turning point of the coexistence line occurring at $P \sim -1750\,\mathrm{bar}$ and $T \sim 283\,\mathrm{K}$[15] is surprisingly close to our numerical finding.

Although experimentally inaccessible for large (in absolute value) negative pressures, the possible re-entrance of the solid-liquid coexistence line affects the kinetic and thermodynamic properties of the accessible metastable region of the supercooled water's phase diagram at negative pressure. This phenomenon resembles what has been largely discussed in the last decades about the origin of water's anomalies[7,19,34–44]. There, the possible presence of a second liquid-liquid critical point in a low T-high P region of the phase diagram (confirmed recently for the TIP4P/Ice model[24] although experimentally prohibitive) would determine the increase of the fluctuations (and related thermodynamic response functions) in the accessible metastable region of the phase diagram.

To evaluate N_c we follow the *seeding* computational approach, introduced by Bai and Li[45], and widely adopted in nucleation studies[11,46–60] (see SM for details). This scheme consists in introducing a spherical crystal seed of a given size into a bulk of supercooled liquid and let it evolve at constant T and P. Seeds whose size is larger than $N_c(T, P)$ grow spanning the entire system, while those below $N_c(T, P)$ melt. When the size is critical, the crystal seed can grow or melt with equal probability. Hence, by comparing the time evolution of the size of the crystal seeds at certain T and P, it is possible to establish N_c (within a certain resolution). One can either study seeds differing in size at fixed state point $T - P$ (Fig. 6.2a-c) or a given seed at different $T - P$ (Fig. 6.2d).

We investigate the $T = (230, 240, 250)$ K isotherms with $N \sim 46000$ water molecules. For any T we explore $P \in [-3500 : 2400]$ bar, i.e. from the liquid-gas kinetic stability limit at negative pressures up to the melting point at positive pressures. The number of ice molecules is determined according to the Lechner-Dellago order parameter $\bar{q}_6$[61], with cutoff distance of 3.5 . Molecules (within the cutoff distance) above the threshold $\bar{q}_{6,t}$ are labeled as ice, whereas those with smaller values are labeled as liquid. The value of $\bar{q}_{6,t}$ which depends on P and T is determined according to the mislabeling criterion[47] (see the SM for details). In Fig. 6.2 we show the time evolution of the number of ice particles in the crystal seed along the isotherm $T = 240$ K, with runs spanning in some cases up to the μs. On average any N_c has been identified by means of ~ 10 independent runs. All the estimated N_c along the three isotherms are presented in Fig. 6.3c and reported in the SM. As shown in Fig. 6.3c, from positive pressures, N_c largely decreases upon decreasing P, reaching a quasi-constant value at negative P. By further decreasing P we find that N_c increases again. In all cases the minimum value of N_c is observed at $P < 0$. In particular, we find that the minimum value of N_c is ~ 150 for $T = 230$ K, ~ 310 for $T = 240$ K, and ~ 800 for $T = 250$ K. From $N_c(T,P)$ we can extract the P-dependence of the surface tension $\gamma(T,P)$ following the classical nucleation theory (CNT). Indeed, according to CNT, γ can be expressed as[48]

$$\gamma(T,P) = \left[\frac{3\rho_{\text{ice}}(T,P)^2|\Delta\mu(T,P)|^3 N_c(T,P)}{32\pi}\right]^{1/3}, \qquad (6.1)$$

being $\rho_{\text{ice}}(T,P)$ the ice density at (T,P), and $\Delta\mu(T,P) \equiv \mu_{\text{liq}}(T,P) - \mu_{\text{ice}}(T,P)$ the difference in chemical potential between water (μ_{liq}) and ice (μ_{ice}). As discussed in the SM (see Fig. 3 and Table II), $\Delta\mu$ can be computed by thermodynamic integration. In Fig. 6.3a we report $\Delta\mu$ along the isotherms of interest, showing a retracing behavior whose maximum value is always reached at $P < 0$. The maxima of $\Delta\mu$ are observed at $(T = 230\,\text{K}, P \sim -1160\,\text{bar})$, $(T = 240\,\text{K}, P \sim -1405\,\text{bar})$, and $(T = 250\,\text{K}, P \sim -1605\,\text{bar})$, roughly coinciding with the thermodynamic state points where $N_c(P)$ exhibits a minimum. The presence of the maximum of $\Delta\mu$ is due to the crossing of ice and liquid water densities along the corresponding isotherm as shown in Fig. 6.3a inset (see also Fig. 3(c-e) of the SM). From Eq. 6.1 we obtain γ which is shown in Fig. 6.4a. As can be seen, γ decreases upon decreasing P, reaching a quasi-constant value at negative P, then increasing again at largely (in absolute value) negative P. We can extract the values of γ at $P = 1$ bar: $\gamma \sim 20\,\text{mJ/m}^2$ for $T = 230$ K, $\gamma \sim 21\,\text{mJ/m}^2$ for $T = 240$ K, and $\gamma \sim 24\,\text{mJ/m}^2$ for $T = 250$ K. These values are in agreement with the fitting expression for $\gamma(T, P = 1\,\text{bar})$ reported in Ref.[48,52] ($\gamma = 19.1$, 21.8, $24.5\,\text{mJ/m}^2$ respectively).

Following Becker and Döring[62] we can express the nucleation rate $J(T,P)$ as

$$J(T,P) = \rho_{\text{liq}} f^+ Z \exp(-\Delta G_c/k_B T) \qquad , \qquad (6.2)$$

where ρ_{liq} is the density of the liquid phase, and $\Delta G_c = N_c|\Delta\mu(T,P)|/2$ is the free energy barrier associated to the formation of a critical cluster. Also, k_B is the Boltzmann constant and $Z \equiv \sqrt{|\Delta\mu|/(6\pi k_B T N_c)}$ is the Zeldovich factor which depends on the curvature of ΔG around the barrier top and is related to the width of the critical region. The attachment rate f^+ can be approximated as $f^+ = 24DN_c^{2/3}/\lambda^2$, where D is the diffusion coefficient of the supercooled water (shown in Fig. 6.3b) and $\lambda = 3.8$ according to previous work[46]. Such an approximation succesfully works at positive pressure[46]. We test it at negative pressure by computing f^+ rigorously as in Ref.[63] from $\langle (N(t) - N(0))^2 \rangle = 2f^+t$, at $T = 240$ K for $P = -300, -1700, -2900$ bar finding good agreement, as reported in SM (the deviations do not affect the resulting value of J).

The P-dependence of ΔG_c is shown in Fig. 6.3d. Then, we estimate J via Eq. 6.2. In Fig. 6.4b, the returning of J at negative P is revealed. The maxima of J are found

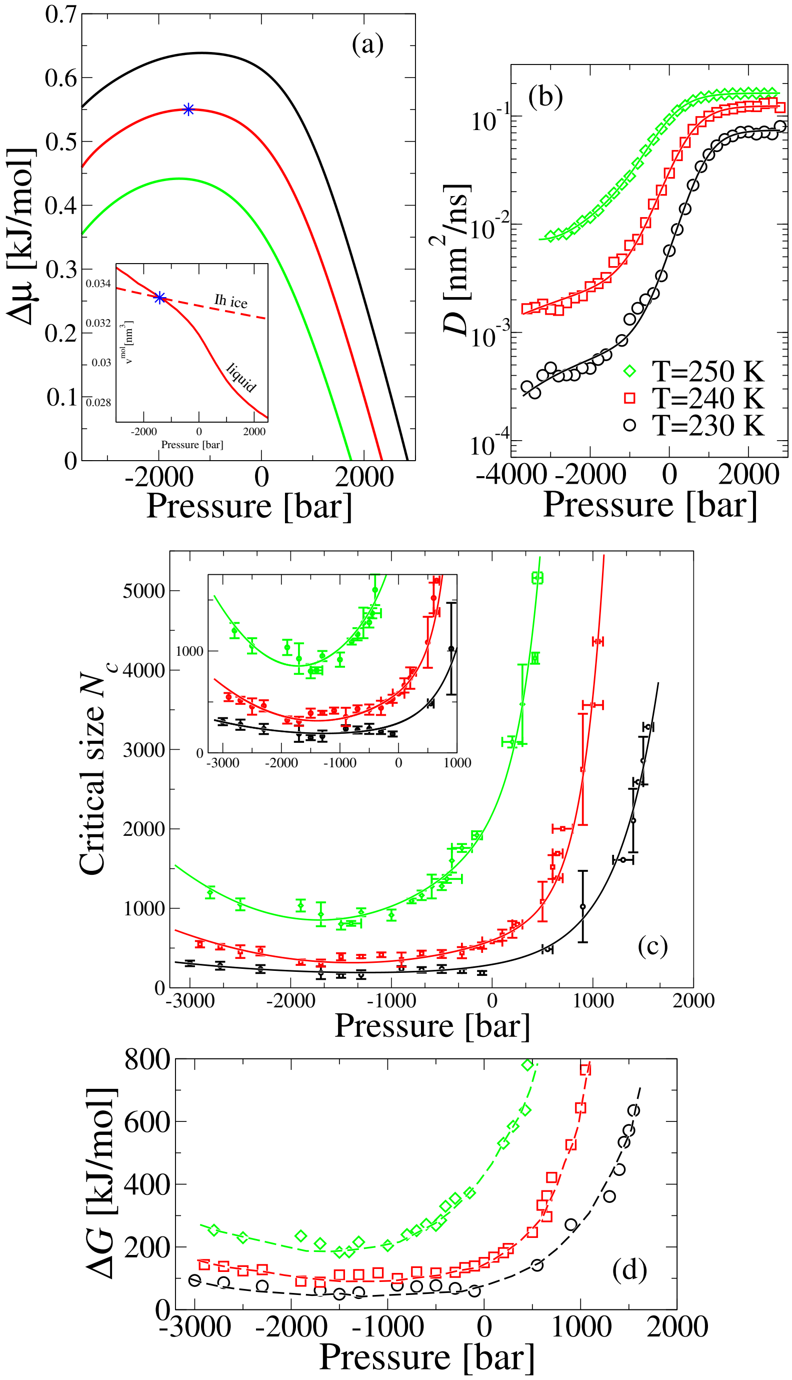

Figure 6.3: Different observables as a function of P along the isotherms $T = 230$ K, $T = 240$ K, and $T = 250$ K (legend for all panels in (b)): (a) Difference in chemical potential $\Delta\mu$. Volume per molecule of Ih ice and liquid water at $T = 240$ K in inset. Blue star indicators are at the same P. (b) Diffusion coefficient D. Lines are fitting curves reported in the SM. (c) Size of the ice critical nucleus N_c. Inset zooms on the region where the minima are observed. Lines are fitting functions given in the SM. (d) Gibbs free energy barrier ΔG (zoom in at the minima including error bars in SM). Dashed lines are guides for the eye.

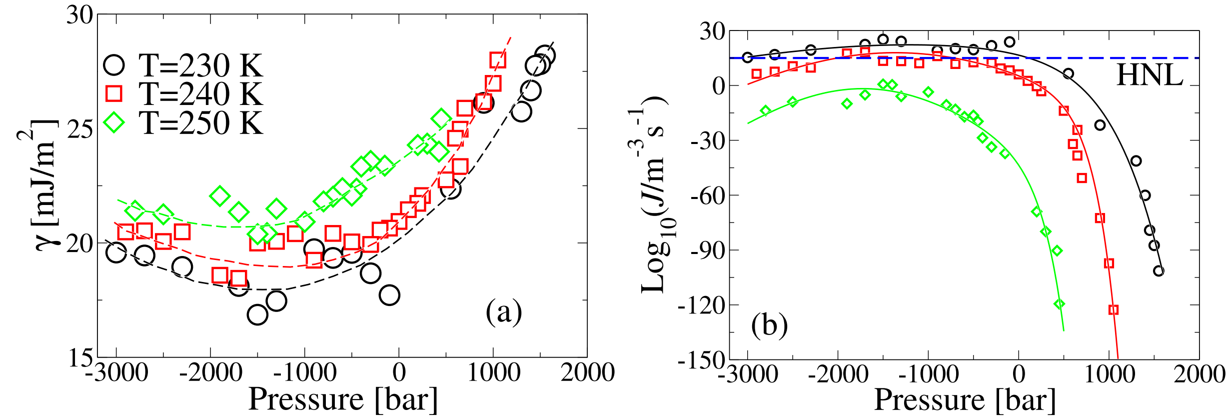

Figure 6.4: Isothermal variations (at 230 K, 240 K, and 250 K) with P of: (a) Surface tension γ. Dashed lines are guides for the eye. (b) The logarithm of J (zoom in at the maxima including error bars in SM). Same legend than (a). Dashed blue line marks the homogeneous nucleation line (HNL) given by $\log_{10} J/(\text{ m}^{-3} \text{ s}^{-1}) = 15$. Continues lines are analytical expression according to Eq. (6.2), using the fitting curves $\rho_{\text{liq}}(T,P)$ shown in Fig 2 of the SM and and $D(T,P)$ and $N_c(T,P)$ shown in Fig. 6.3b and 6.3c respectively, all reported in the SM. By estimating the (T,P) state points where $\log_{10} J/(\text{ m}^{-3} \text{ s}^{-1})$ $= 15, 5, -5$ we have drawn the iso-J lines shown in Fig. 6.1.

at $P < 0$ for all the explored T and mark the (T,P) conditions where homogeneous nucleation occurs more easily as recently suggested by Marcolli[21]. In this particular case, $J \sim 10^{22}$ $\text{m}^{-3}\text{s}^{-1}$ for ($T = 230$ K, $P \sim -1200$ bar), $J \sim 10^{18}$ $\text{m}^{-3}\text{s}^{-1}$ for ($T = 240$ K, $P \sim -1350$ bar), and $J \sim 10^{-1}$ $\text{m}^{-3}\text{s}^{-1}$ for ($T = 250$ K, $P \sim -1750$ bar). Accordingly, the estimated surviving time τ of a water droplet with volume $V_{\text{ice}} \sim 5$ cm^3 characteristic of the inclusion experiments at negative P[13,18] is $\tau \equiv (JV_{\text{ice}})^{-1} \sim 2\times10^{-17}$ s at $T = 230$ K, $\tau \sim 2\times10^{-13}$ s at $T = 240$ K, and $\tau \sim 2\times10^{6}$ s at $T = 250$ K. Thus, this work suggests that 245 K - 250 K is the minimum T at which one can study macroscopic samples of water at $P < 0$ without freezing the entire sample in a few seconds.

Finally, we compute the iso-nucleation rate lines for TIP4P/Ice (representing the loci of points in the $P - T$ plane where the nucleation rates have identical values). They are presented in Fig. 6.1 for $\log_{10} J/(\text{ m}^{-3} \text{ s}^{-1}) = 15, 5, -5$. As can be seen, the iso-nucleation rate lines present reentrant behavior. The curve $\log_{10} J/(\text{ m}^{-3} \text{ s}^{-1}) = 15$ is of particular interest as it can be regarded as an estimate of the experimental homogeneous nucleation line (HNL)[9] where freezing of droplets of a few microns occurs in a few seconds and cannot be avoided, thus, representing the solid-liquid limit of stability. In the 230 K isotherm, $\log_{10} J/(\text{ m}^{-3} \text{ s}^{-1}) = 15$ occurs at $P = 1$ bar (see also Fig. 6.1). The results of this work suggest that the HNL presents reentrant behavior, another anomaly of water arising at the confluence of low T and negative P[64,65] that, to the best of our knowledge, has not been reported before.

6.5. Conclusions

In conclusion, we use computer simulations of the TIP4P/Ice water model to estimate the size of the critical nucleus N_c along three isotherms $T = 230\,\mathrm{K}$, $T = 240\,\mathrm{K}$, and $T = 250\,\mathrm{K}$. We cover from typical positive coexistence pressures until approaching the liquid-gas kinetic stability curve (under 100 ns of observation). We show how N_c does not change monotonically exhibiting a minimum at negative P and increasing again in the vicinity of the stability limit. Accordingly, the nucleation rate J and the surface tension γ show a retracing behavior, with a maximum of J and a minimum of γ both occurring at negative P. Our findings reveal new water anomalies as the retracing behavior of N_c, γ and J along the isotherms when going from positive to negative pressures. We also predict anomalous behavior of the homogeneous nucleation line, which again presents reentrant behavior at negative pressures. This can be regarded as a smoking gun of the re-entrance of the melting curve which can be evaluated experimentally only up to moderate values of negative pressures[13,15–18].

6.6. Acknowledgments

The authors acknowledge the project PID2019-105898GB-C21 of the MEC. V. B. acknowledges the support from the European Commission through the Marie Skłodowska-Curie Fellowship No. 748170 ProFrost. P.M.d.H. acknowledges the financial support from the FPI grant no. BES-2017-080074. C.P.L thanks MEC for a predoctoral FPU grant FPU18/03326 and also Ayuntamiento de Madrid for a Residencia de Estudiantes grant. The authors acknowledge the computer resources and technical assistance provided by the RES and the Vienna Scientific Cluster (VSC).

Bibliography

[1] A. Gettelman, X. Liu, S. J. Ghan, H. Morrison, S. Park, A. J. Conley, S. A. Klein, J. Boyle, D. L. Mitchell, and J.-L. F. Li. Global simulations of ice nucleation and ice supersaturation with an improved cloud scheme in the Community Atmosphere Model. *Journal of Geophysical Research*, 115(D18):D18216, sep 2010.

[2] I. Coluzza, J. Creamean, M.J. Rossi, H. Wex, P.A. Alpert, V. Bianco, Y. Boose, C. Dellago, L. Felgitsch, J. Fröhlich-Nowoisky, H. Herrmann, S. Jungblut, Z.A. Kanji, G. Menzl, B. Moffett, C. Moritz, A. Mutzel, U. Pöschl, M. Schauperl, J. Scheel, E. Stopelli, F. Stratmann, H. Grothe, and D.G. Schmale. Perspectives on the future of ice nucleation research: Research needs and Unanswered questions identified from two international workshops. *Atmosphere*, 8(8):138, 2017.

[3] Jan Nitzbon, Sebastian Westermann, Moritz Langer, Léo C. P. Martin, Jens Strauss, Sebastian Laboor, and Julia Boike. Fast response of cold ice-rich permafrost in northeast Siberia to a warming climate. *Nature Communications*, 11(1):2201, dec 2020.

[4] G. John Morris and Elizabeth Acton. Controlled ice nucleation in cryopreservation – A review. *Cryobiology*, 66(2):85–92, apr 2013.

[5] Maya Bar Dolev, Ido Braslavsky, and Peter L. Davies. Ice-Binding Proteins and Their Function. *Annual Review of Biochemistry*, 85(1):515–542, jun 2016.

[6] K. Broekaert, M. Heyndrickx, L. Herman, F. Devlieghere, and G. Vlaemynck. Seafood quality analysis: Molecular identification of dominant microbiota after ice storage on several general growth media. *Food Microbiology*, 28(6):1162–1169, sep 2011.

[7] John Russo, Flavio Romano, and Hajime Tanaka. New metastable form of ice and its role in the homogeneous crystallization of water. *Nature Materials*, 13(7):733–739, jul 2014.

[8] R. Bintanja, G. J. van Oldenborgh, S. S. Drijfhout, B. Wouters, and C. A. Katsman. Important role for ocean warming and increased ice-shelf melt in Antarctic sea-ice expansion. *Nature Geoscience*, 6(5):376–379, may 2013.

[9] Jorge R. Espinosa, Alberto Zaragoza, Pablo Rosales-Pelaez, Caridad Navarro, Chantal Valeriani, Carlos Vega, and Eduardo Sanz. Interfacial Free Energy as the Key to the Pressure-Induced Deceleration of Ice Nucleation. *Physical Review Letters*, 117(13):135702, sep 2016.

[10] Haiyang Niu, Yi Isaac Yang, and Michele Parrinello. Temperature Dependence of Homogeneous Nucleation in Ice. *Physical Review Letters*, 122(24):245501, jun 2019.

[11] E. Sanz, C. Vega, J. R. Espinosa, R. Caballero-Bernal, J. L. F. Abascal, and C. Valeriani. Homogeneous Ice Nucleation at Moderate Supercooling from Molecular Simulation. *Journal of the American Chemical Society*, 135(40):15008–15017, oct 2013.

[12] JL Green, DJ Durden, GH Wolf, and CA Angell. WATER AND SOLUTIONS AT NEGATIVE-PRESSURE - RAMAN-SPECTROSCOPIC STUDY TO -80 MEGA-PASCALS . *Science*, 249:649, 1990.

[13] Mouna El Mekki Azouzi, Claire Ramboz, Jean-François Lenain, and Frédéric Caupin. A coherent picture of water at extreme negative pressure. *Nature Physics*, 9(1):38–41, jan 2013.

[14] PA Netz, FW Starr, HE Stanley, and MC Barbosa. Static and dynamic properties of stretched water . *J. Chem. Phys.*, 115:344, 2001.

[15] Stephen J. Henderson and Robin J. Speedy. Melting temperature of ice at positive and negative pressures. *The Journal of Physical Chemistry*, 91(11):3069–3072, may 1987.

[16] Q Zheng, DJ Durben, GH Wolf, and CA Angell. Liquids at Large Negative Pressures: Water at the Homogeneous Nucleation Limit. *Science*, 254(5033):829–832, 1991.

[17] A. R. Imre, H. J. Maris, and P. R. Williams. *Liquids Under Negative Pressure : Proceedings of the NATO Advanced Research Workshop of Liquids Under Negative Pressure Budapest, Hungary 23-25 February 2002.* Springer Netherlands, 2002.

[18] F. Caupin. Escaping the no man's land: Recent experiments on metastable liquid water. *Journal of Non-Crystalline Solids*, 407:441–448, 2015.

[19] Paola Gallo, Katrin Amann-Winkel, Charles Austen Angell, Mikhail Alexeevich Anisimov, Frédéric Caupin, Charusita Chakravarty, Erik Lascaris, Thomas Loerting, Athanassios Zois Panagiotopoulos, John Russo, Jonas Alexander Sellberg, Harry Eugene Stanley, Hajime Tanaka, Carlos Vega, Limei Xu, and Lars Gunnar Moody Pettersson. Water: A Tale of Two Liquids. *Chemical Reviews*, 116(13):7463–7500, 2016.

[20] P Montero de Hijes, E Sanz, L Joly, C Valeriani, and F Caupin. Viscosity and self-diffusion of supercooled and stretched water from molecular dynamics simulations . *J. Chem. Phys.*, 149:094503, 2018.

[21] Claudia Marcolli. Ice nucleation triggered by negative pressure. *Scientific Reports*, 7(1):16634, dec 2017.

[22] H. Kanno, R. J. Speedy, and C. A. Angell. Supercooling of water to -92^{o}c under pressure. *Science*, 189(4206):880–881, 1975.

[23] J. L. F. Abascal, E. Sanz, R. García Fernández, and C. Vega. A potential model for the study of ices and amorphous water: TIP4P/Ice. *The Journal of Chemical Physics*, 122(23):234511, jun 2005.

[24] Pablo G Debenedetti, F. Sciortino, and H. Zerze. Second critical point in two realistic models of water. *Science*, 369:289, 2020.

[25] Berk Hess, Carsten Kutzner, David van der Spoel, and Erik Lindahl. GROMACS 4: Algorithms for Highly Efficient, Load-Balanced, and Scalable Molecular Simulation. 4(3):435–447, 2008.

[26] Takahiro Matsui, Takuma Yagasaki, Masakazu Matsumoto, and Hideki Tanaka. Phase diagram of ice polymorphs under negative pressure considering the limits of mechanical stability. *The Journal of chemical physics*, 150(4):041102, 2019.

[27] Andrzej Falenty, Thomas C Hansen, and Werner F Kuhs. Formation and properties of ice xvi obtained by emptying a type sii clathrate hydrate. *Nature*, 516(7530):231–233, 2014.

[28] See Supplemental Material at http://link.aps.org/ supplemental/10.1103/PhysRevLett.126.015704 for a detailed description of the numerical methods and results (seeding, direct coexistence, mislabeling, thermodynamic integration and attachment rates) of this work and the fitting curves shown in the main text.

[29] MM Conde, C Vega, GA Tribello, and B Slater. The phase diagram of water at negative pressures: Virtual ices. *The Journal of chemical physics*, 131(3):034510, 2009.

[30] Robin J. Speedy. Stability-limit conjecture. An interpretation of the properties of water. *The Journal of Physical Chemistry*, 86(6):982–991, mar 1982.

[31] L. Rovigatti, V. Bianco, J.M. Tavares, and F. Sciortino. Communication: Reentrant limits of stability of the liquid phase and the Speedy scenario in colloidal model systems. *Journal of Chemical Physics*, 146(4):041103, 2017.

[32] Pablo G. Debenedetti. Supercooled and glassy water. *Journal of Physics: Condensed Matter*, 15(45):R1669—-R1726, 2003.

[33] Percy Williams Bridgman. Water, in the liquid and five solid forms, under pressure. 47(13):441–558, 1912.

[34] R. J. Speedy and C. A. Angell. Isothermal compressibility of supercooled water and evidence for a thermodynamic singularity at -45 degrees c. *J. Chem. Phys.*, 65:851–858, 1976.

[35] P H Poole, F Sciortino, Ulrich Essmann, and H. Eugene Stanley. Phase-Behavior Of Metastable Water. *Nature*, 360(6402):324–328, nov 1992.

[36] Chae Un Kim, Buz Barstow, Mark W Tate, and Sol M Gruner. Evidence for liquid water during the high-density to low-density amorphous ice transition. *Proceedings of the National Academy of Sciences*, 106(12):4596, 2009.

[37] Kevin Stokely, Marco G Mazza, H. Eugene Stanley, and Giancarlo Franzese. Effect of hydrogen bond cooperativity on the behavior of water. *Proceedings of the National Academy of Sciences of the United States of America*, 107:1301–1306, 2010.

[38] Valentino Bianco and Giancarlo Franzese. Critical behavior of a water monolayer under hydrophobic confinement. *Scientific reports*, 4:4440, 2014.

[39] Jeremy C Palmer, Fausto Martelli, Yang Liu, Roberto Car, Athanassios Z Panagiotopoulos, and Pablo G Debenedetti. Metastable liquid-liquid transition in a molecular model of water. *Nature*, 510(7505):385–8, jun 2014.

[40] Gaël Pallares, Mouna El Mekki Azouzi, Miguel A González, Juan L Aragones, JoséL. F Abascal, Chantal Valeriani, and Frédéric Caupin. Anomalies in bulk supercooled water at negative pressure. *Proceedings of the National Academy of Sciences*, 111(22):7936–7941, 2014.

[41] Anders Nilsson and Lars GM Pettersson. The structural origin of anomalous properties of liquid water . *Nature Communications*, 6:8998, 2015.

[42] Fivos Perakis, Katrin Amann-Winkel, Felix Lehmkühler, Michael Sprung, Daniel Mariedahl, Jonas A. Sellberg, Harshad Pathak, Alexander Späh, Filippo Cavalca, Daniel Schlesinger, Alessandro Ricci, Avni Jain, Bernhard Massani, Flora Aubree, Chris J. Benmore, Thomas Loerting, Gerhard Grübel, Lars G. M. Pettersson, and Anders Nilsson. Diffusive dynamics during the high-to-low density transition in amorphous ice. *Proceedings of the National Academy of Sciences*, 114(31):8193, jun 2017.

[43] Valentino Bianco and Giancarlo Franzese. Hydrogen bond correlated percolation in a supercooled water monolayer as a hallmark of the critical region. *Journal of Molecular Liquids*, 285:727–739, apr 2019.

[44] Paola Gallo, Thomas Loerting, and Francesco Sciortino. Supercooled water: A polymorphic liquid with a cornucopia of behaviors. *The Journal of Chemical Physics*, 151(21):210401, dec 2019.

[45] Xian-Ming Bai and Mo Li. Test of classical nucleation theory via molecular-dynamics simulation. *The Journal of Chemical Physics*, 122(22):224510, jun 2005.

[46] J R Espinosa, E Sanz, C Valeriani, and C Vega. Homogeneous ice nucleation evaluated for several water models. *The Journal of chemical physics*, 141(18):18C529, nov 2014.

[47] Jorge R. Espinosa, Carlos Vega, Chantal Valeriani, and Eduardo Sanz. Seeding approach to crystal nucleation. *The Journal of Chemical Physics*, 144(3):034501, jan 2016.

[48] J. R. Espinosa, C. Navarro, E. Sanz, C. Valeriani, and C. Vega. On the time required to freeze water. *The Journal of Chemical Physics*, 145(21):211922, dec 2016.

[49] Jorge R. Espinosa, Carlos Vega, and Eduardo Sanz. Homogeneous Ice Nucleation Rate in Water Droplets. *The Journal of Physical Chemistry C*, 122(40):22892–22896, oct 2018.

[50] Yuri Lifanov, Bart Vorselaars, and David Quigley. Nucleation barrier reconstruction via the seeding method in a lattice model with competing nucleation pathways. *The Journal of Chemical Physics*, 145(21):211912, dec 2016.

[51] Fabio Leoni, Rui Shi, Hajime Tanaka, and John Russo. Crystalline clusters in mW water: Stability, growth, and grain boundaries. *The Journal of Chemical Physics*, 151(4):044505, jul 2019.

[52] P Montero de Hijes, Jorge R Espinosa, Eduardo Sanz, and Carlos Vega. Interfacial free energy of a liquid-solid interface: Its change with curvature. *The Journal of Chemical Physics*, 151(14):144501, 2019.

[53] P. Montero de Hijes, Jorge. R. Espinosa, Valentino Bianco, Eduardo Sanz, and Carlos Vega. Interfacial Free Energy and Tolman Length of Curved Liquid–Solid Interfaces from Equilibrium Studies. *The Journal of Physical Chemistry C*, 124(16):8795 – 8805, apr 2020.

[54] P Montero de Hijes, K Shi, EG Noya, EE Santiso, KE Gubbins, E Sanz, and C Vega. The young–laplace equation for a solid–liquid interface. *The Journal of Chemical Physics*, 153(19):191102, 2020.

[55] Azat O Tipeev, Edgar D Zanotto, and Jose P Rino. Diffusivity, interfacial free energy, and crystal nucleation in a supercooled lennard-jones liquid. *The Journal of Physical Chemistry C*, 122(50):28884–28894, 2018.

[56] Brandon C. Knott, Valeria Molinero, Michael F. Doherty, and Baron Peters. Homogeneous Nucleation of Methane Hydrates: Unrealistic under Realistic Conditions. *Journal of the American Chemical Society*, 134(48):19544–19547, dec 2012.

[57] Rodolfo G Pereyra, Igal Szleifer, and Marcelo A Carignano. Temperature dependence of ice critical nucleus size. *The Journal of chemical physics*, 135(3):034508, 2011.

[58] Tonnishtha Dasgupta, Gabriele M. Coli, and Marjolein Dijkstra. Tuning the Glass Transition: Enhanced Crystallization of the Laves Phases in Nearly Hard Spheres. *ACS Nano*, 14(4):3957–3968, apr 2020.

[59] Haiyang Niu, Luigi Bonati, Pablo M. Piaggi, and Michele Parrinello. Ab initio phase diagram and nucleation of gallium. *Nature Communications*, 11(1):2654, dec 2020.

[60] Nils ER Zimmermann, Bart Vorselaars, David Quigley, and Baron Peters. Nucleation of nacl from aqueous solution: Critical sizes, ion-attachment kinetics, and rates. *Journal of the American Chemical Society*, 137(41):13352–13361, 2015.

[61] Wolfgang Lechner and Christoph Dellago. Accurate determination of crystal structures based on averaged local bond order parameters. *The Journal of Chemical Physics*, 129(11):114707, sep 2008.

[62] R. Becker and W. Döring. Kinetische Behandlung der Keimbildung in übersättigten Dämpfen. *Annalen der Physik*, 416(8):719–752, jan 1935.

[63] Stefan Auer and Daan Frenkel. Prediction of absolute crystal-nucleation rate in hard-sphere colloids. *Nature*, 409(6823):1020–1023, 2001.

[64] Y Elia Altabet, Rakesh S Singh, Frank H Stillinger, and Pablo G Debenedetti. Thermodynamic anomalies in stretched water. *Langmuir*, 33(42):11771–11778, 2017.

[65] Vincent Holten, Chen Qiu, Emmanuel Guillerm, Max Wilke, Jaroslav Ricka, Martin Frenz, and Frédéric Caupin. Compressibility anomalies in stretched water and their interplay with density anomalies. *The journal of physical chemistry letters*, 8(22):5519–5522, 2017.

6.7. Supporting Material

Direct coexistence simulations

To determine the solid-liquid equilibrium line we place a block of ice Ih consisting of 4032 molecules in contact with an equal number of liquid molecules. We perform NPT simulations, with anisotropic P to relax the crystal structure, counting the number of solid molecules in time. Along an isobar, if T is larger than the coexistence temperature the ice melts, hence the number of solid particles decreases in time. On the other hand, for T below the coexistence temperature the number of solid molecules increases in time. The coexistence T is determined when, for independent trajectories, the ice shows equal probability of melting or growing.

Seeding simulations

The purpose of this technique is to find the critical nucleus size at a certain temperature T and pressure P. Given that the critical nucleus is situated at the top of the energy barrier, it is in unstable equilibrium and the probability for the nucleus to grow or to shrink is equally 50%. Therefore, by inserting a crystal seed of a given size N within the bulk liquid and tracking its evolution with time over multiple independent runs, we can estimate if N is larger than the crytical size N_c (meaning that all the crystal seeds grow) or if it is smaller (in which case all the seeds melt). When $N \sim N_c$ we expect to observe the ice growing for half of the trayectories, and melting for the remaining ones.

Introduced in 2005[1], the *seeding* technique's popularity has grown over the last few years being extensively applied in nucleation studies[2–16]. The *seeding* scheme can be used in two distinct ways: tracking several seeds differing in size at a given (T, P) or studying a seed with a fixed size at different (T, P). We found that the first protocol is more suitable when the critical size does not change significantly with the thermodynamic state point (i.e. $\partial N_c/\partial P \sim 0$ or $\partial N_c/\partial T \sim 0$) and we adopted it to identify N_c at most of the negative pressures. On the other hand, the second protocol (fixed seed simulated at different (T, P)) works well when the critical size is sensitive to changes of T and/or P, as observed at positive pressures, and has been adopted in this regime.

To create the initial configuration for a single *seeding* run we first equilibrate separately bulk liquid water and bulk ice at the T and P of interest. Then, we create a spherical cavity of radius R within the bulk liquid water and insert in the empty space a spherical seed of a slightly smaller radius extracted from the bulk ice. The system is quickly equilibrated at constant volume for ~ 10 ps keeping the ice-molecules motionless, which allows us to equilibrate the interface. Finally, we simulate the system in the NPT ensemble, where the pressures is applied isotropically.

In the following we show the estimation of N_c according to our *seeding* simulations.

230 K				240 K				250 K			
N_c	ΔN_c	P	Δ_P	N_c	ΔN_c	P	Δ_P	N_c	ΔN_c	P	Δ_P
3284	0	1550	50	4360	0	1050	50	5160	70	450	50
2860	300	1500	0	3560	0	1000	100	4150	70	425	25
2590	0	1450	50	2750	700	900	0	3570	500	300	0
2105	400	1400	0	2003	0	700	100	3095	70	200	100
1610	0	1300	100	1690	0	650	50	1920	50	-150	50
1022	450	900	0	1380	0	650	50	1760	50	-300	100
485	0	550	50	1520	150	600	0	1600	150	-400	0
186	25	-100	0	1085	250	500	0	1370	50	-450	150
210	25	-300	0	797	0	250	50	1280	50	-500	0
236	50	-500	0	734	105	200	0	1275	150	-600	0
225	35	-700	0	662	70	100	0	1164	60	-700	0
237	35	-900	0	582	0	1	100	1093	30	-800	0
165	55	-1300	0	531	40	-100	0	915	70	-1000	0
150	25	-1500	0	503	0	-200	100	950	50	-1300	0
189	80	-1700	0	442	70	-300	0	810	30	-1400	100
235	50	-2300	0	425	50	-500	0	802	70	-1500	0
277	50	-2700	0	432	35	-700	0	925	150	-1700	0
307	35	-3000	0	353	90	-900	0	1035	75	-1900	0
				415	30	-1100	0	1050	75	-2500	0
				393	20	-1300	0	1200	75	-2800	0
				390	45	-1500	0				
				310	45	-1700	0				
				323	35	-1900	0				
				462	55	-2300	0				
				455	80	-2500	0				
				516	35	-2700	0				
				548	40	-2900	0				

Table 6.1: Seeding results. ΔN_c and Δ_P are the uncertainty of the critical nucleus size and pressure respectively.

Mislabeling calculation

In Fig. 6.5 we report the % of mislabeled solid and liquid molecules, according to the threshold $\bar{q}_{6,t}$ of the $\bar{q}_6$ order parameter. The value of $\bar{q}_{6,t}$ is determined from the crossing of the mislabeling curves of ice and liquid water in the bulk. For any P the optimal value of $\bar{q}_{6,t}$ is well fitted by the expression $\bar{q}_{6,t}(P) = a_{q6}(T) - b_{q6}(T)\exp(c_{q6}(T)P)/[d_{q6}(T) + \exp(c_{q6}(T)P)]$ (see Fig. 2 of SM). The fitting parameters are reported in Tab. 6.2.

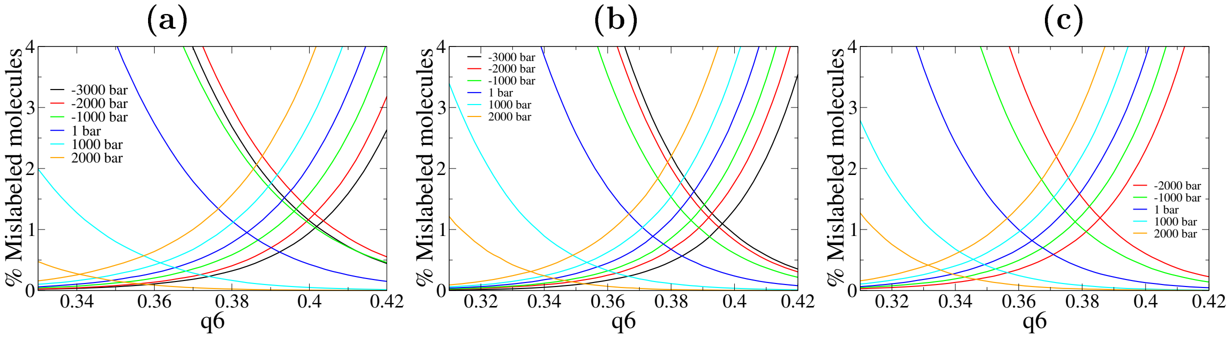

Figure 6.5: Percentage of mislabeled molecules for each phase at $T =$ 230 K (a), $T = 240$ K (b) and $T = 250$ K (c). Data are over equilibrium simulations of 3820 molecules in the liquid phase, and 4032 molecules in the solid Ih phase.

T [K]	$a_{q6}(T)$	$b_{q6}(T)$	$c_{q6}(T)$	$d_{q6}(T)$
230	0.401839	0.0765991	0.00127229	3.29737
240	0.396191	0.0772493	0.00106575	2.35767
250	0.392375	0.0776309	0.000938774	1.7289

Table 6.2: Fitting parameters for the $\bar{q}_{6,t}$.

Calculation of $\Delta\mu$

The difference between the chemical potentials of the liquid phase μ_l and the solid phase μ_s along an isotherm, at the desired pressure P, is given by

$$\Delta\mu(P) \equiv \mu_l(P) - \mu_s(P) = \int_{P_{\text{coex}}}^{P} [v_{\text{liq}}^{\text{mol}}(P') - v_{\text{ice}}^{\text{mol}}(P')]dP' \quad , \tag{6.3}$$

being P_{coex} the coexistence pressure at the temperature T, $v_{\text{liq}}^{\text{mol}}$ the molecular volume of the liquid phase, $v_{\text{ice}}^{\text{mol}}$ the molecular volume of the solid phase. The P dependence of $v_{\text{liq}}^{\text{mol}}$ and $v_{\text{ice}}^{\text{mol}}$ are shown in Fig. 6.7a,b. Data are fitted with 9_{th} order polynomials, whose coefficient are reported in Tab 6.3. It is worth noting that, along the isotherms of the liquid phase shown in Fig. 6.7a, the volume data cross each other at positive pressures and negative pressures. This is due to the presence of a temperature of

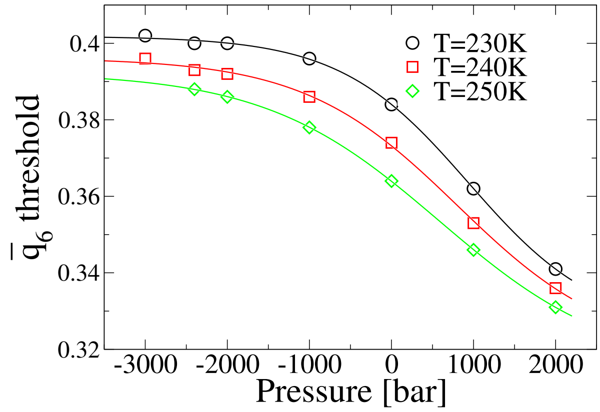

Figure 6.6: Threshold $\bar{q}_{6,t}$ for the $\bar{q}_6$ order parameter as function of P, for different temperatures. Curves are fitted according to the expression reported in the SM.

maximum density and a temperature of minimum density, both observed upon isobaric cooling. According to our data, we have that $v_{\text{liq}}^{\text{mol}}(T = 240\,\text{K}) = v_{\text{liq}}^{\text{mol}}(T = 250\,\text{K})$ both at $P \sim 1500$ bar and $P \sim -2070$ bar, and $v_{\text{liq}}^{\text{mol}}(T = 230\text{ K}) = v_{\text{liq}}^{\text{mol}}(T = 240\text{ K})$ both at $P \sim 1650$ bar and $P \sim -1890$ bar. The crossing at positive pressures indicates the presence of a maximum in density, along the point $(T \sim 245\text{ K}, P \sim 1500\text{ bar})$ and $(T \sim 235\,\text{K}, P \sim 1650\,\text{bar})$, while the crossing at negative pressure points out the presence of a minimum in density at $(T \sim 245\text{K}, P \sim -2070\text{bar})$ and $(T \sim 235\text{K}, P \sim -1890\text{bar})$. Moreover, as shown in Fig. 6.7c-e, $v_{\text{liq}}^{\text{mol}}$ and $v_{\text{ice}}^{\text{mol}}$ intersects at fixed T, marking the maximum of $\Delta\mu$ shown in Fig. 5a of the main text. We found that $v_{\text{liq}}^{\text{mol}} = v_{\text{ice}}^{\text{mol}}$ at $(T = 230\text{ K}, P \sim -1110\text{ bar})$, $(T = 240\text{ K}, P \sim -1420\text{ bar})$ and $(T = 250\,\text{K}, P \sim -1605\,\text{bar})$.

v [nm^3]	T [K]	$a_v(T)$ ($\times 10^{-34}$)	$b_v(T)$ ($\times 10^{-31}$)	$c_v(T)$ ($\times 10^{-27}$)	$d_v(T)$ ($\times 10^{-24}$)	$e_v(T)$ ($\times 10^{-20}$)	$f_v(T)$ ($\times 10^{-17}$)	$g_v(T)$ ($\times 10^{-13}$)	$h_v(T)$ ($\times 10^{-10}$)	$i_v(T)$ ($\times 10^{-6}$)	$l_v(T)$ ($\times 10^{-2}$)
$v_{\text{ice}}^{\text{mol}}$	250	0	0	0	0	0	0	0	0.0676672	-0.287745	3.29197
$v_{\text{ice}}^{\text{mol}}$	240	0	0	0	0	0	0	0	0.0634812	-0.280247	3.28709
$v_{\text{ice}}^{\text{mol}}$	230	0	0	0	0	0	0	0	0.0607871	-0.273831	3.28217
$v_{\text{liq}}^{\text{mol}}$	250	0	3.53928	1.56695	-5.80737	-2.9843	3.84266	2.24401	-1.1388	-2.04296	3.08979
$v_{\text{liq}}^{\text{mol}}$	240	0	7.91325	1.33479	-17.2535	-2.80532	13.7737	2.29159	-4.77538	-2.08529	3.13703
$v_{\text{liq}}^{\text{mol}}$	230	2.46393	10.0899	-5.35123	-24.2833	3.44422	21.2156	-0.0287716	-8.12152	-1.80442	3.18724

Table 6.3: Coefficient of the polynomial fit for the molecular volume v^{mol} of liquid and solid phases, shown in Fig. 6.7. The fitting polynomial as function of P is $a_v(T)P^9 + b_v(T)P^8 + c_v(T)P^7 + d_v(T)P^6 + e_v(T)P^5 + f_v(T)P^4 + g_v(T)P^3 + h_v(T)P^2 + i_v(T)P + l_v(T)$.

Fit of N_c

The pressure dependence of the ice critical size N_c has been fitted according to the expression $N_c(T,P) = a_{N_c}(T)P^2 + b_{N_c}(T)P + c_{N_c}(T) + d_{N_c}(T)\exp[e_{N_c}(T)(P + h_{N_c}(T))]$.

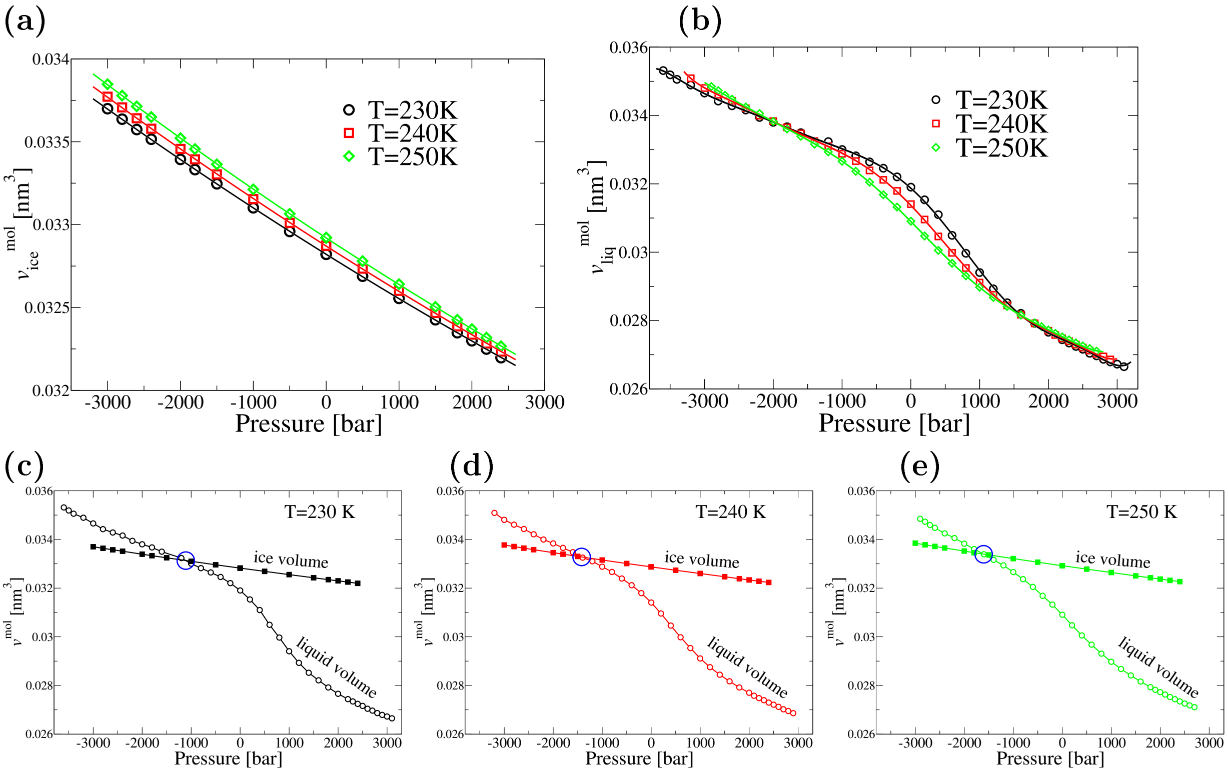

Figure 6.7: Molecular volume of ice Ih v_{ice}^{mol} (a) and liquid water v_{liq}^{mol} (b) as function of pressure, for different temperatures. Data are calculated with NPT runs spanning up to 200 ns of a bulk liquid phase of 3840 molecules, and a bulk of 4032 ice molecules. Lines are polynomial fits described in the text and in TAB. 6.3. Panels (c-e) show the molecular volume v^{mol} of liquid (open circles) and solid phase (full squares) at $T = 230$ K (c), $T = 240$ K (d) and $T = 250$ K (e). Blue circles mark the crossing between $v_{\text{ice}}^{\text{mol}}$ and $v_{\text{liq}}^{\text{mol}}$.

The fitting parameters are shown in Tab. 6.4

T [K]	$a_{N_c}(T)$ $(\times 10^{-4})$	$b_{N_c}(T)$	$c_{N_c}(T)$ $(\times 10^{2})$	$d_{N_c}(T)$	$e_{N_c}(T)$ $(\times 10^{-3})$	$h_{N_c}(T)$ $(\times 10^{3})$
230	0.341809	0.0797471	2.35066	0.85	2.46	1.72
240	1.32674	0.368069	5.7071	9.5	4.6	0.22
250	3.3502	1.147	18.3463	0.3	4.5	1.57

Table 6.4: Fitting parameters of the curves $N_c(T, P)$.

Fit of D

The pressure dependence of the diffusion coefficient $D(T, P)$ is given by $D(T, P) = a_D(T) + \exp[b_D(T)P]/\{c_D(T) + d_D(T)\exp[b_D(T)P]\} + [e_D(T)P + f_D(T)P^2]/\{1 + \exp[h_D(T)P]\}$, with parameters shown in Tab. 6.5

T [K]	$a_D(T)$ ($\times 10^{-4}$)	$b_D(T)$ ($\times 10^{-3}$)	$c_D(T)$	$d_D(T)$	$e_D(T)$ ($\times 10^{-7}$)	$f_D(T)$ ($\times 10^{-12}$)	$h_D(T)$ ($\times 10^{-3}$)
230	8.99447	3.00448	193.8014	13.68375	1.7342152	0	125.5709
240	34.87718	2.630391	28.8107	8.2971	5.737374	7.8152591	34.16511
250	311.085	2.4591358	8.3357863	7.5807725	145.64959	2217.4348	2.824802

Table 6.5: Fitting parameters of the curves $D(T, P)$.

Attachment rate f^+

The attachment rate f^+ can be rigoursly computed from the expression proposed by Auer and Frenkel[17]

$$f^+_{AF} = \frac{\langle (N(t) - N(0))^2 \rangle}{2t} \tag{6.4}$$

and approximated by the equation

$$f^+ = \frac{24 D N_c^{2/3}}{\lambda^2} \tag{6.5}$$

where D is the diffusion coefficient of the supercooled liquid, N_c the size of the critical nucleus, and $\lambda \equiv 3.8$ is a characteristic length of the order of a molecular diameter[4]. In a previous work, we have applied this approximation in nucleation of ice at positive pressures finding good agreement with the rigourous procedure[4]. Here, we test it at negative pressures, also finding good agreement as can be seen in Table 6.6. In particular, along the 240 K isotherm, we calculate f^+ for three different negative pressures: -300 bar, -1700 bar, and -2900 bar.

P (bar)	f^+_{AF} (ns^{-1})	f^+ (ns^{-1})
-300	129.5	111.4
-1700	22.1	16.6
-2900	15.0	13.9

Table 6.6: Attachment rate computed according the rigourous Eq. 6.4 and approximated by the Eq. 6.5.

Error bars for ΔG and $log_{10}J$

In Fig. 6.8, we have a closer look at the minima of ΔG and maxima of $log_{10}J$. We also include error bars. As can be seen, the uncertainty is not enough to cover the non-monotonic behavior.

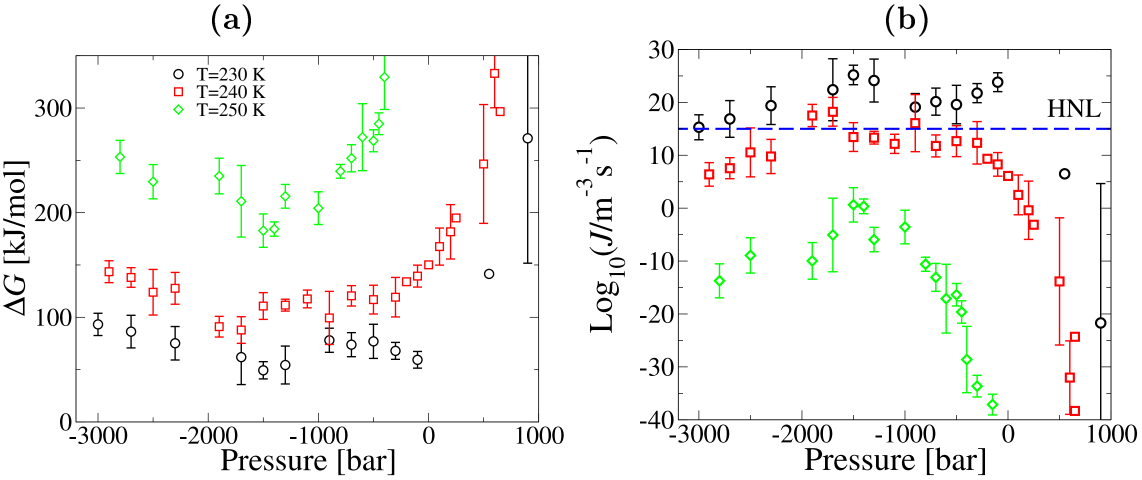

Figure 6.8: Zoom in Fig. 3d) and 4b) from main text. Here, a) free energy barrier ΔG and b) the logarithm of the nucleation rate J. Error bars are included. The same legend applies in both panels.

Bibliography

[1] Xian-Ming Bai and Mo Li. Test of classical nucleation theory via molecular-dynamics simulation. *The Journal of Chemical Physics*, 122(22):224510, jun 2005.

[2] E. Sanz, C. Vega, J. R. Espinosa, R. Caballero-Bernal, J. L. F. Abascal, and C. Valeriani. Homogeneous Ice Nucleation at Moderate Supercooling from Molecular Simulation. *Journal of the American Chemical Society*, 135(40):15008–15017, oct 2013.

[3] Jorge R. Espinosa, Carlos Vega, and Eduardo Sanz. Homogeneous Ice Nucleation Rate in Water Droplets. *The Journal of Physical Chemistry C*, 122(40):22892–22896, oct 2018.

[4] J R Espinosa, E Sanz, C Valeriani, and C Vega. Homogeneous ice nucleation evaluated for several water models. *The Journal of chemical physics*, 141(18):18C529, nov 2014.

[5] Jorge R. Espinosa, Carlos Vega, Chantal Valeriani, and Eduardo Sanz. Seeding approach to crystal nucleation. *The Journal of Chemical Physics*, 144(3):034501, jan 2016.

[6] J. R. Espinosa, C. Navarro, E. Sanz, C. Valeriani, and C. Vega. On the time required to freeze water. *The Journal of Chemical Physics*, 145(21):211922, dec 2016.

[7] Nils ER Zimmermann, Bart Vorselaars, David Quigley, and Baron Peters. Nucleation of nacl from aqueous solution: Critical sizes, ion-attachment kinetics, and rates. *Journal of the American Chemical Society*, 137(41):13352–13361, 2015.

[8] Brandon C. Knott, Valeria Molinero, Michael F. Doherty, and Baron Peters. Homogeneous Nucleation of Methane Hydrates: Unrealistic under Realistic Conditions. *Journal of the American Chemical Society*, 134(48):19544–19547, dec 2012.

[9] Yuri Lifanov, Bart Vorselaars, and David Quigley. Nucleation barrier reconstruction via the seeding method in a lattice model with competing nucleation pathways. *The Journal of Chemical Physics*, 145(21):211912, dec 2016.

[10] Fabio Leoni, Rui Shi, Hajime Tanaka, and John Russo. Crystalline clusters in mW water: Stability, growth, and grain boundaries. *The Journal of Chemical Physics*, 151(4):044505, jul 2019.

[11] Rodolfo G Pereyra, Igal Szleifer, and Marcelo A Carignano. Temperature dependence of ice critical nucleus size. *The Journal of chemical physics*, 135(3):034508, 2011.

[12] P Montero de Hijes, Jorge R Espinosa, Eduardo Sanz, and Carlos Vega. Interfacial free energy of a liquid-solid interface: Its change with curvature. *The Journal of Chemical Physics*, 151(14):144501, 2019.

[13] P. Montero de Hijes, Jorge. R. Espinosa, Valentino Bianco, Eduardo Sanz, and Carlos Vega. Interfacial Free Energy and Tolman Length of Curved Liquid–Solid Interfaces from Equilibrium Studies. *The Journal of Physical Chemistry C*, 124(16):8795 – 8805, apr 2020.

[14] Azat O Tipeev, Edgar D Zanotto, and Jose P Rino. Diffusivity, interfacial free energy, and crystal nucleation in a supercooled lennard-jones liquid. *The Journal of Physical Chemistry C*, 122(50):28884–28894, 2018.

[15] Tonnishtha Dasgupta, Gabriele M. Coli, and Marjolein Dijkstra. Tuning the Glass Transition: Enhanced Crystallization of the Laves Phases in Nearly Hard Spheres. *ACS Nano*, 14(4):3957–3968, apr 2020.

[16] Haiyang Niu, Luigi Bonati, Pablo M. Piaggi, and Michele Parrinello. Ab initio phase diagram and nucleation of gallium. *Nature Communications*, 11(1):2654, dec 2020.

[17] Stefan Auer and Daan Frenkel. Prediction of absolute crystal-nucleation rate in hard-sphere colloids. *Nature*, 409(6823):1020–1023, 2001.

Chapter 7

Ice growth rate: Temperature dependence and effect of heat dissipation

P. Montero de Hijes[1], J. R. Espinosa[1], C. Vega[1], and E. Sanz[1]

[1]Departamento de Química Física, Facultad de Ciencias Químicas, Universidad Complutense de Madrid, 28040 Madrid, Spain

7.1. Abstract

The transformation of liquid water into solid ice is arguably the most important phase transition on Earth. A key aspect of such transformation is the speed with which ice grows once it is nucleated. There are contradictory experimental results as to whether the ice growth rate shows a maximum on cooling. Previous simulation results point to the existence of such maximum. However, simulations were performed at constant temperature with the aid a thermostat that dissipates the heat released at the ice-water interface unrealistically fast. Here, we perform simulations of ice growth without any thermostat. Large systems are required to perform these simulations at constant overall thermodynamic conditions (pressure and temperature). We obtain the same growth rate as in previous thermostated simulations. This implies that the dynamics of ice growth is not affected by heat dissipation. Our results strongly support the experiments predicting the existence of a maximum in the ice growth rate. By using the Wilson-Frenkel kinetic theory we argue that such maximum is due to a competition between an increasing crystallization thermodynamic driving force and a decreasing molecular mobility on cooling.

7.2. Introduction

The transformation of supercooled water into ice is one of the most important phase transitions on Earth. It involves two stages. Initially, a process known as nucleation where a solid ice nucleus must appear after overcoming a free energy barrier. Nucleation can be heterogeneous in presence of impurities[1–5] or homogeneous[6–8] in case of pure water. The emergence of a critical ice nucleus enables other molecules to join. That is the second stage known as crystal growth and it is the framework of this article.

Understanding and, hence, learning to control the growth of ice is important for various and diverse disciplines like climate science (precipitation and albedo)[9], aviation technology[10], cryopreservation[11,12], food industry[13] or material science[14].

Despite the importance of water and the ubiquitous character of the water-to-ice transition, there are still large discrepancies and uncertainties in experimental measurements of the ice growth rate[15–19]. There are even qualitative differences in the temperature dependence of the growth rate: whereas some experiments support the existence of a maximum[19] and some others deny it[17].

Fortunately, experimental research can be complemented with computer simulations. Nowadays there are several water models that accurately describe the behaviour of real water[20–22]. Simulation estimates of the ice growth rate using different water models[23–28] point to the existence of a maximum in the ice growth rate.

However, there is one remaining issue that questions the validity of these simulations: they were carried out at constant temperature with the aid of a thermostat that dissipates the freezing heat released at the interface as ice grows within a small relaxation time (typically a few ps). One may wonder whether an artificially quick heat dissipation due to the use of a thermostat may affect the dynamics of ice growth[18,27].

In this paper we compare simulations of ice growth previously performed in the NpT ensemble (with thermostat) with new ones performed in this work in the NVE ensemble (with no thermostat). Ice growth simulations in the NVE ensemble are more akin to experiments because the heat released by freezing is not removed by a thermostat. Using the NVE ensemble poses a computational challenge, though, given that large systems are required to avoid temperature or pressure drifts during the course of the simulation.

Within the accuracy of our simulations we find that the use of a thermostat does not alter the rate of ice growth. This implies that latent heat dissipation is faster than ice growth. Thus, our work confirms the existence of a maximum in the ice growth rate predicted in previous simulations and serves as a guide to solve the discrepancies between different experimental measurements. We also check that the Wilson-Frenkel theory[29–32] quite accurately predicts the growth rate estimated in our simulations. Therefore, one can understand the maximum in the growth rate as a result of the competition between thermodynamics (chemical potential difference between both phases) and kinetics (diffusion coefficient).

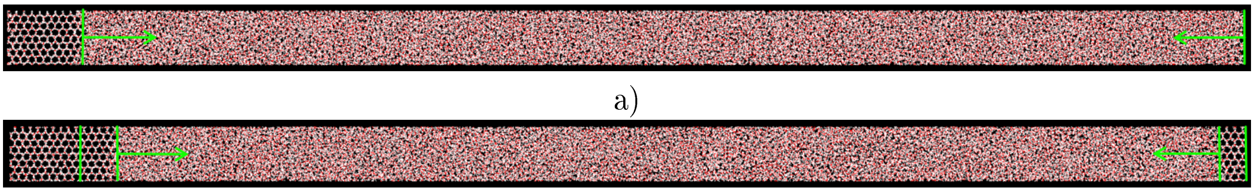

a)

b)

Figure 7.1: a) Initial configuration of a typical simulation for computing the growth rate, being the thermodynamic conditions 257 K and 1 bar. b) The same system after 13 ns, showing how both the left and right interfaces have moved toward the liquid. The plane exposed to the liquid is the secondary prismatic $\{1\bar{2}10\}$.

7.3. Methods and simulation details

Molecular dynamics simulations were performed using the GROMACS package[33] while water was simulated with the TIP4P/Ice model[34]. Such model accurately reproduces water properties especially when solid phases are present and its melting point is 270 K[26,27,35], very close to the experimental value of 273.15 K[36]. The computational work had two main stages. The aim of the first one was to prepare well equilibrated configurations. A small block of ice containing $N^i_{ice} \approx 1000$ water molecules was set in contact with a large bath of $N^i_{bath} \approx 20760$ water molecules. The total number of molecules involved in the simulation was always $N = 21760$. During this stage, simulations were done in the NpT ensemble in order to set temperature and pressure at the values of interest. These are, pressure always $P \sim 1$ bar and temperatures $T = 265$, 257, 251 and 243 K corresponding to supercoolings $\Delta T = 5$, 13, 19 and 27 K. The second stage consisted in simulations in the NVE ensemble of the configurations prepared in the first stage. After the preparation, N^i_{ice} as well as N^i_{bath} could have slightly changed so that these initial values during the production stage depend on the run. The plane that the ice block exposed to the liquid water was the secondary prismatic $\{1\bar{2}10\}$. A representation of the system that was created with VMD[37] can be seen in Figure 7.1.

In both the preparation and the production stages the LJ term of the potential and the real part of the electrostatic potential were truncated at 12.5 Å. We used PME[38] to deal with the long range electrostatic corrections with 0.1 nm Fourier spacing and a 4^{th} order interpolation polynomial. In order to constraint the geometry of the molecule the LINCS algorithm[39] was used.

During the NpT simulation stage a velocity-rescale thermostat[40] and an anisotropic Parrinello-Rahman barostat[41] were used with a relaxation time of 0.5 ps in both cases. The time step was set to 2 fs and runs lasted until the systems were equilibrated (around 2 ns). In the NVE simulations it was crucial to use a short integration time, 0.2 fs in our case, to maintain the energy constant along the trajectories. Runs lasted until the size of the ice block was almost twice the initial one for a given trajectory. The time needed for this was 13 ns for the fastest (257 K) and 22 ns for the slowest case (242

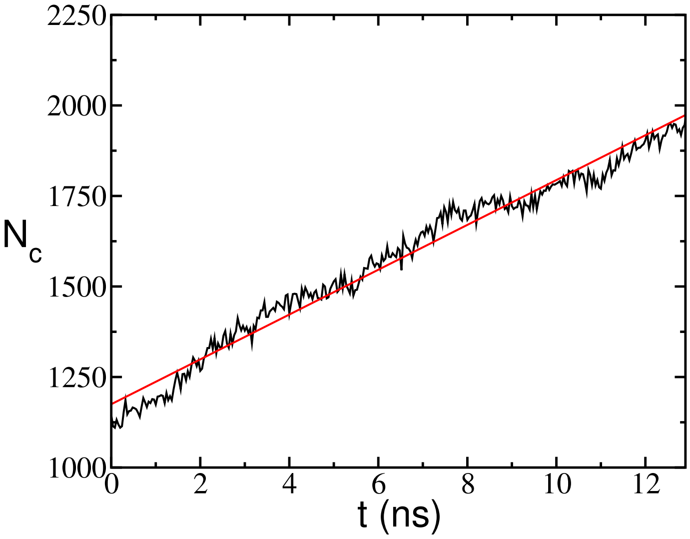

Figure 7.2: Number of particles in the biggest cluster of ice-like molecules, N_c, as a function of time for T=257 K.

K). Both the short integration time step and the large system size required make of these simulations a computational challenge. We needed a 24-core machine for about a month in order to get a single estimate of the growth rate. We obtained the growth rate for 4 different state points. Two independent estimates were made for each state point to improve statistics.

In what concerns to the analysis of the simulations, once the ice block had grown sufficiently, we obtained the growth rate u as:

$$u = \frac{\Delta L_{ice}}{2\tau} \tag{7.1}$$

where ΔL_{ice} is the distance grown by ice and τ is the simulation time. The factor of 2 comes from the fact that there are two interfaces growing under periodic boundary conditions.

ΔL_{ice} can be estimated as:

$$\Delta L_{ice} = \frac{\Delta N_c}{\rho_{ice} A} \tag{7.2}$$

where ΔN_c is the number of molecules that incorporate into the ice phase during the simulation, A is the area of the section and ρ_{ice} is the ice number density at (T,P).

To compute the number of molecules in the ice phase, N_c, we employed the widely used $\overline{q}_6$ order parameter[42] with a cutoff of 3.5 Å to label ice-like and liquid-like molecules in the system (see Refs.[43–45] for details on the implementation of the $\overline{q}_6$ order parameter for water).

An example of the evolution of N_c during the course of one of our simulations is given in Fig. 7.2. The slope of the curve is proportional to the growth rate.

7.4. Results

7.4.1. Validity of the NVE calculations

As explained in the introduction, we use the NVE ensemble to simulate the dissipation of freezing heat during ice growth more realistically than when a thermostat is employed. Working in the NVE ensemble is tricky, though. To avoid significant energy, pressure or temperature drifts, and hence be able to compare our results with experiments or thermostated simulations, the molecular dynamics time step must be short and the system must be large (see previous section). In particular, the number of water molecules that incorporates into the ice phase during the simulation must be small as compared to the total number of liquid molecules (see Fig. 7.1 for a snapshot). In this way, neither the heat released by freezing will change much the overall temperature, nor the expansion due to freezing will cause a large pressure raise.

To asses the validity of our NVE simulations, we follow the evolution of the total energy, temperature and pressure. In Figure 7.3 we show these variables for one trajectory initially at 257 K and 1 bar. As Figure 7.3 a) shows, the total energy in the system is well conserved. Temperature is shown in panel b) and increases about 2 K along the course of the 13 ns simulation due to the freezing process. The growth rate determined in the simulations is assigned to the average temperature of the run rather than to the initial one. Consequently, we have a temperature uncertainty of about ±1 K in each determination of the growth rate. Note that if the runs were not interrupted and crystallization continued, the temperature would keep raising and, at some point, the growth rate would change according to the new thermodynamic conditions. Thus, the analysis must be restricted to time intervals where the growth rate is steady. In the bottom of Figure 7.3, panel c) we show the variation of pressure. Since the simulation volume is fixed and ice occupies more space than liquid water pressure increases as the ice front moves forward. Another contribution to this effect could be brought by an increase in temperature. Anyway, the pressure raise is small and comparable to the fast, local pressure fluctuations. With this analysis we conclude that our simulation set up enables keeping pressure and temperature roughly constant during the time required to measure the growth rate.

7.4.2. NVE vs NpT

Having made sure that pressure and temperature are kept fairly constant along our NVE simulations, we can compare our results for the growth rate with those obtained by means of NpT simulations. Such comparison is established in Fig. 7.4 (a). Red symbols are the NVE results of this work and black and blue ones correspond to NpT simulations from Refs.[18;26;27]. In all cases, the TIP4P/Ice water model was used and the secondary prismatic ice plane was exposed to the liquid. As it can be seen in Figure 7.4, the results of both simulation ensembles are in very good agreement. The main conclusion that can be drawn from this successful comparison, which is the main

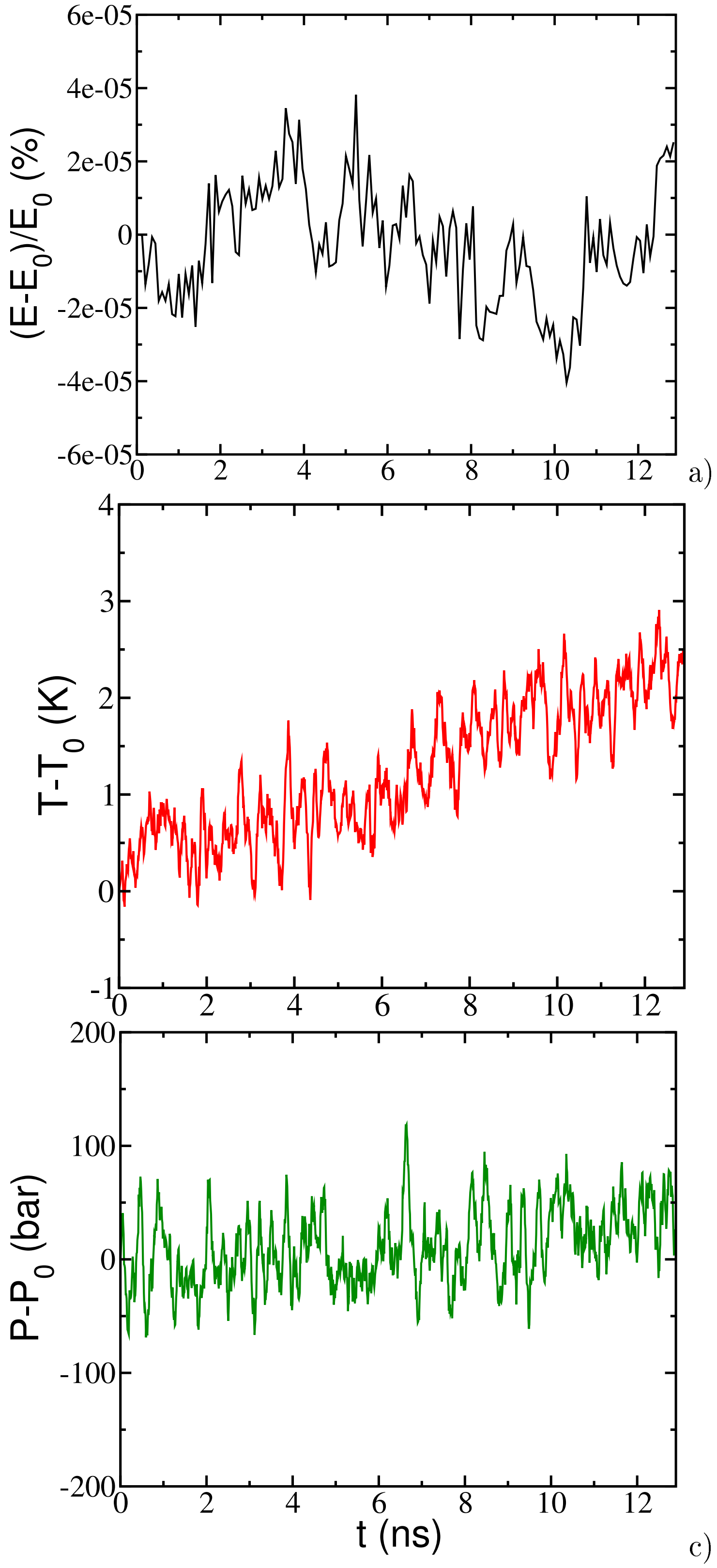

Figure 7.3: Time evolution of the relative change (in %) of the total energy, a), the temperature, b) and the pressure, c), for a system prepared at 257 K and 1 bar. All the panels share the same horizontal axis.

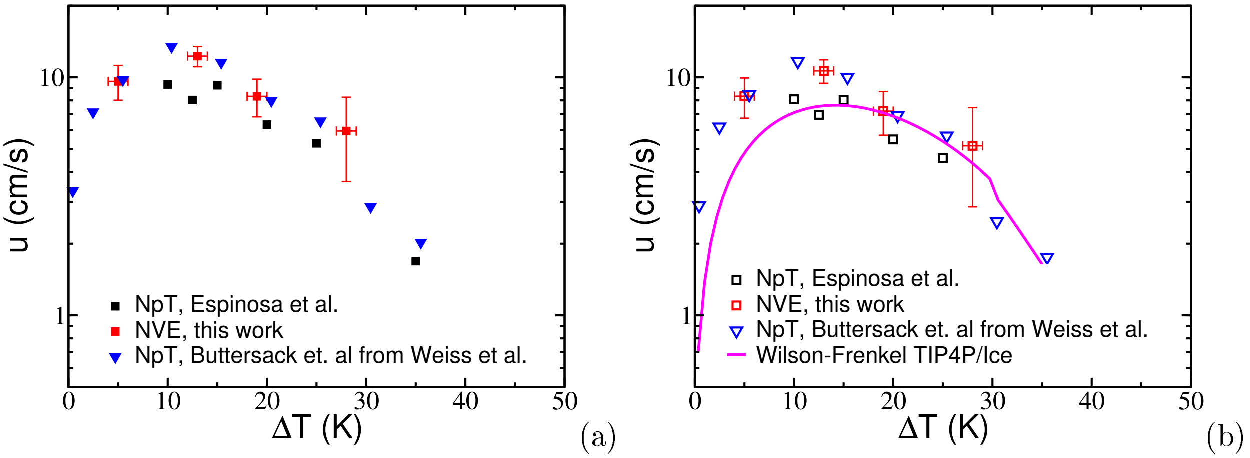

Figure 7.4: (a) Growth rate of ice in the secondary prismatic direction as a function of supercooling, using the TIP4P/Ice model, both in the NVE (this work) and NpT ensembles. Black squares have been taken from Ref.[26]. Blue triangles are a private communication from the authors of Ref.[27] to those of Ref.[18]. Error bars represent standard error. In (b) simulation data presented in (a) are multiplied by a factor of 13/15 in order to obtain an estimate of the growth rate averaged over all crystalline directions, as suggested in Ref.[26]. The magenta line corresponds to the Wilson-Frenkel theory using the TIP4P/Ice parameters (see main text).

result of this work, is that the freezing heat dissipation does not affect the dynamics of ice growth. This means that the timescale associated to the dissipation of the heat released in the interfacial region when ice grows is much shorter than that related to ice growth. In fact, as shown in Fig. 7.5, there are no significant temperature gradients along the direction perpendicular to the interface in the timescale of ice growth.

7.4.3. Maximum in the growth rate

In Fig. 7.4 (a) we show that the growth rate has a maximum for the TIP4P/Ice model. The same trend has been observed by Rozmanov et al. using the TIP4P/2005 model[24,25]. In this work we show that such behaviour is robust and independent of the use of a thermostat in the simulations.

Such maximum can be understood as a consequence of the competition between opposing thermodynamic and kinetic effects. On the one hand, upon cooling, the solid becomes increasingly more stable than the liquid, thus raising the thermodynamic driving force for ice growth. On the other hand, lowering the temperature slows down diffusion[46] and molecules take longer to incorporate into the growing ice phase. These competing factors give rise to the Wilson-Frenkel theory for the growth rate[30–32]:

$$u(T) = \frac{D(T)}{a}\left[1 - \exp\left(-\frac{|\Delta\mu(T)|}{k_B T}\right)\right] \tag{7.3}$$

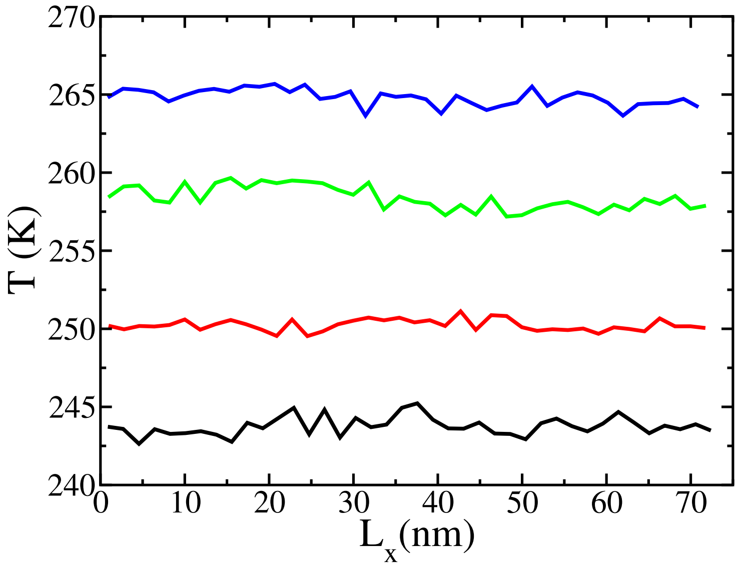

Figure 7.5: Temperature profile along the direction perpendicular to the interface for all systems simulated averaged over the last half of the simulation.

where $D(T)$ is the diffusion coefficient, a is a characteristic length –of the order of the molecular diameter– $\Delta\mu$ is the chemical potential difference between the solid and the liquid and k_B is the Botzmann constant. We can test the theory by using the equation above with the parameters of the TIP4P/Ice model. $D(T)$ and $\Delta\mu(T)$ are given in Ref.[26] and we take $a = 3$ Å , about one molecular diameter. The theory gives the magenta line in Fig. 7.4(b), which describes quite well the trend of the TIP4P/Ice simulation data, particularly so beyond the maximum. We stress that the magenta line is not a fit, but the theory combined with simulation parameters. Therefore, the view that the maximum in the growth rate is due to a competition between an increasing thermodynamic driving force and a decreasing mobility seems to be correct.

7.4.4. Experiments

In Fig, 7.6 we plot the results for the ice growth rate from different experimental groups. As mentioned in the introduction, there are strong discrepancies. Seminal work by Pruppacher et al.[16] was restricted to low supercooling, where there is no sign of a maximum in the growth rate (green triangles). Pruppacher's work is in good agreement with that by Buttersack et al.[18] (turquoise triangles). The work by Buttersack et al.[18], that extends to deeper supercooling, seems to be consistent with a maximum, although their data are quite scattered and no definite conclusion can be drawn in this respect. Sibkov et. al.[17], however, did not find a maximum but a sharp monotonic increase of the growth rate with the supercooling (orange squares). This result is in stark contrast with the work by Xu et al.[19] (green circles), who performed experiments up to very deep supercooling with water nanofilms. They see a monotonic decrease of the growth rate with the supercooling, a tendency consistent with the maximum.

In Fig. 7.6 we include the Wilson-Frenkel curve previously presented in Fig. 7.4(b), that describes pretty well the trend for the TIP4P/Ice simulation data. Such line is in very good agreement with the experiments by Xu et al. This agreement clearly supports the experiments that claim the existence of a maximum in the growth rate.

Before our work both simulations and experiments claiming the existence of such maximum were questioned for the way heat dissipation was dealt with. On the one hand, in simulations, the use of a thermostat instantly dissipates the heat released at the interfacial region while ice grows. On the other hand, the experiments by Xu et al. are performed with ultra-thin water films (nm thick), which would enable a faster heat dissipation than in experiments with large samples. Therefore, both the use of thermostats or of thin samples questioned the validity of the experimental and simulation works that support the existence of the maximum in the growth rate. However, the good agreement between NVE and NpT simulations shown in Fig. 7.4 proves that heat dissipation does not affect the ice growth dynamics. Therefore, our work is a strong support for the existence of a maximum in the ice growth rate. Our simulations with the TIP4P/Ice model predict the maximum to occur at 14 K below melting and at a growth rate of ca. 10 cm/s.

A comment is due on the comparison between simulations and ice growth experiments in large samples[16,17].

There, the mechanism of growth is dendritic and several fronts simultaneously grow. In this situation, only $\sim$ one third of the molecules initially engulfed in the dendritic branch are in the crystalline state[18]. The rest of the water molecules inside the dendritic ice network take longer time to crystallize. In our simulations we estimate the speed of growth of a single front growing in detriment of the liquid. Notice that dendritic developments cannot happen even when simulating the secondary prismatic plane due the limited size of the simulation box. In any case, our results disagree with those of Shibkov et al., since even if our system related to the slowest front in their dendritic front, it would not reach their reported growth rate. For instance, at 35 K of supercooling, they found a freezing velocity of 40 cm/s while in our calculations we find around 5 cm/s.

7.5. Summary and conclusions

We investigate the effect of heat dissipation in the dynamics of ice growth. For that purpose, we perform NVE simulations of a growing ice front in contact with supercooled water and compare the results with previous estimates in the NpT ensemble, where freezing heat dissipation is artificially fast due to the effect of a thermostat. First, we validate our NVE simulations, that must be performed with large systems and short time steps in order to avoid temperature and pressure drifts. Our NVE results are fully consistent with those previously obtained in the NpT ensemble. This agreement leads us to conclude that ice growth is not affected by the dissipation of freezing heat

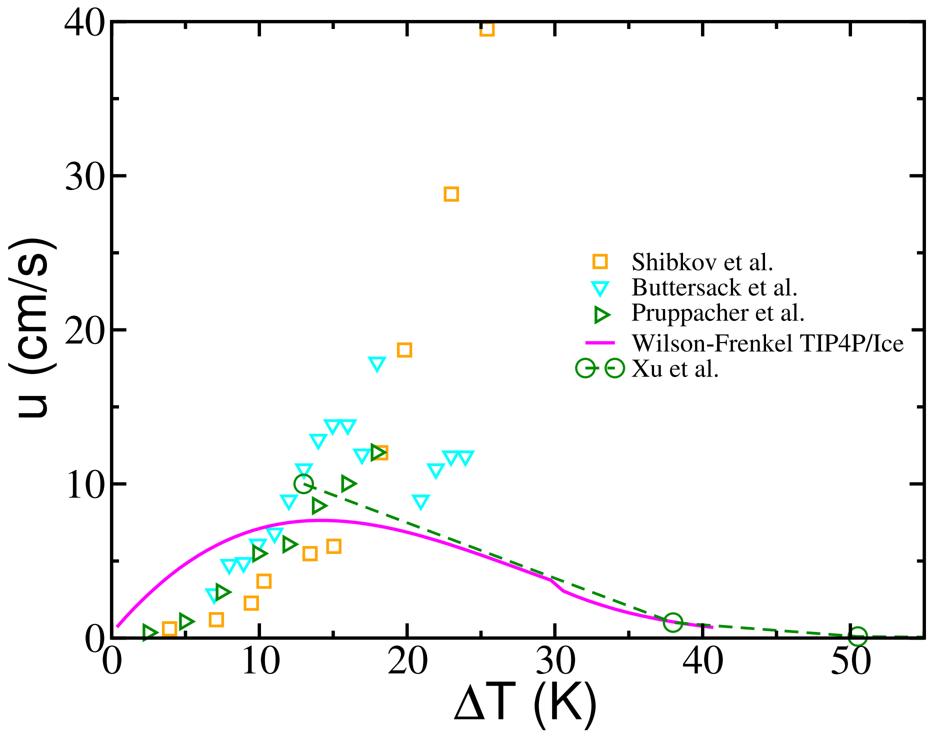

Figure 7.6: Rate of ice growth u as a function of supercooling. Symbols correspond to different experiments: laser-pulsed nanofilms by Xu et al.[19] (empty green circles connected by dashed green lines as a guide to the eye), thin layers by Shibkov et al.[17] (empty orange squares), droplets by Buttersak et al.[18] (cyan inverted triangles) and Pruppacher et al[16] (dark green triangles). The magenta line corresponds to the Wilson-Frenkel theory applied to the TIP4P/Ice water model as explained in the main text. This line describes quite well the simulation results for u (see Fig. 7.4(b)).

from the interfacial region. This statement implies the heat dissipation is much faster that ice growth. Our simulations support some experiments that show the existence of a maximum in the growth rate as a function of the supercooling and disagree with some others that predict a monotonic increase of the growth rate on cooling. We successfully apply the Wilson-Frenkel theory for crystal growth rates to the employed water model. The good performance of the theory suggests that the maximum in the growth rate is due to a competition between an increasing thermodynamic driving force for crystallization and a decreasing mobility of the molecules on cooling.

7.6. Acknowledgments

This work was funded by grant FIS2016/78117-P of the MEC. P.M.H. acknowledges an FPI BES-2017-080074 Ph.D. grant. The authors acknowledge the computer resources and technical assistance provided by the RES. J.R.E. acknowledges funding and support from Oppenheimer Research Fellowship.

Bibliography

[1] Guillaume Fraux and Jonathan P. K. Doye. Note: Heterogeneous ice nucleation on silver-iodide-like surfaces. *The Journal of Chemical Physics*, 141(21):216101, 2014.

[2] Benjamin J Murray, Theodore W Wilson, Steven Dobbie, Zhiqiang Cui, Sardar MRK Al-Jumur, Ottmar Möhler, Martin Schnaiter, Robert Wagner, Stefan Benz, Monika Niemand, et al. Heterogeneous nucleation of ice particles on glassy aerosols under cirrus conditions. *Nature Geoscience*, 3(4):233, 2010.

[3] Corinna Hoose, Jón Egill Kristjánsson, Jen-Ping Chen, and Anupam Hazra. A classical-theory-based parameterization of heterogeneous ice nucleation by mineral dust, soot, and biological particles in a global climate model. *Journal of the Atmospheric Sciences*, 67(8):2483–2503, 2010.

[4] Alexei Kiselev, Felix Bachmann, Philipp Pedevilla, Stephen J Cox, Angelos Michaelides, Dagmar Gerthsen, and Thomas Leisner. Active sites in heterogeneous ice nucleation: the example of k-rich feldspars. *Science*, 355(6323):367–371, 2017.

[5] Aleida J. Bermudez di Lorenzo, Marcelo A. Carignano, and Rodolfo G. Pereyra. A statistical study of heterogeneous nucleation of ice by molecular dynamics. *Chemical Physics Letters*, 635:45 – 49, 2015.

[6] B. J. Murray, S. L. Broadley, T. W. Wilson, S. J. Bull, R. H. Wills, H. K. Christenson, and E. J. Murray. Kinetics of the homogeneous freezing of water. *Phys. Chem. Chem. Phys.*, 12:10380, 2010.

[7] J. R. Espinosa, E. Sanz, C. Valeriani, and C. Vega. Homogeneous ice nucleation evaluated for several water models. *J. Chem. Phys.*, 141:18C529, 2014.

[8] R. G. Pereyra, I. Szleifer, and M. A. Carignano. Temperature dependence of ice critical nucleus size. *J. Chem. Phys.*, 135:034508, 2011.

[9] Will Cantrell and Andrew Heymsfield. Production of ice in tropospheric clouds: A review. *Bulletin of the American Meteorological Society*, 86(6):795–808, 2005.

[10] Stewart G Cober, George A Isaac, and J Walter Strapp. Characterizations of aircraft icing environments that include supercooled large drops. *Journal of Applied Meteorology*, 40(11):1984–2002, 2001.

[11] Xu Xue, Hai-Lan Jin, Zhi-Zhu He, and Jing Liu. Quantifying the growth rate and morphology of ice crystals growth in cryoprotectants via high-speed camera and cryomicroscope. *Journal of Heat Transfer*, 137(9):091020, 2015.

[12] Tadanori Sei, Takehiko Gonda, and Yoshiyasu Arima. Growth rate and morphology of ice crystals growing in a solution of trehalose and water. *Journal of crystal growth*, 240(1-2):218–229, 2002.

[13] Guillermo Petzold and José M Aguilera. Ice morphology: fundamentals and technological applications in foods. *Food Biophysics*, 4(4):378–396, 2009.

[14] Angelos Michaelides and Karina Morgenstern. Ice nanoclusters at hydrophobic metal surfaces. *Nature materials*, 6(8):597, 2007.

[15] J Hallett. Experimental studies of the crystallization of supercooled water. *Journal of the Atmospheric Sciences*, 21(6):671–682, 1964.

[16] H. R. Pruppacher. Interpretation of experimentally determined growth rates of ice crystals in supercooled water. *The Journal of Chemical Physics*, 47(5):1807–1813, 1967.

[17] A.A. Shibkov, M.A. Zheltov, A.A. Korolev, A.A. Kazakov, and A.A. Leonov. Crossover from diffusion-limited to kinetics-limited growth of ice crystals. *Journal of Crystal Growth*, 285(1):215 – 227, 2005.

[18] Tillmann Buttersack and Sigurd Bauerecker. Critical radius of supercooled water droplets: On the transition toward dendritic freezing. *The Journal of Physical Chemistry B*, 120(3):504–512, 2016.

[19] Yuntao Xu, Nikolay G. Petrik, R. Scott Smith, Bruce D. Kay, and Greg A. Kimmel. Growth rate of crystalline ice and the diffusivity of supercooled water from 126 to 262 K. *Proceedings of the National Academy of Sciences*, 113(52):14921–14925, 2016.

[20] Carlos Vega and Jose L. F. Abascal. Simulating water with rigid non-polarizable models: a general perspective. *Phys. Chem. Chem. Phys.*, 13:19663–19688, 2011.

[21] David C. Malaspina, Aleida J. Bermudez di Lorenzo, Rodolfo G. Pereyra, Igal Szleifer, and Marcelo A. Carignano. The water supercooled regime as described by four common water models. *The Journal of Chemical Physics*, 139(2):024506, 2013.

[22] German C. Picasso, David C. Malaspina, Marcelo A. Carignano, and Igal Szleifer. Cooperative dynamic and diffusion behavior above and below the dynamical crossover of supercooled water. *The Journal of Chemical Physics*, 139(4):044509, 2013.

[23] MA Carignano, PB Shepson, and I Szleifer. Molecular dynamics simulations of ice growth from supercooled water. *Molecular Physics*, 103(21-23):2957–2967, 2005.

[24] Dmitri Rozmanov and Peter G. Kusalik. Temperature dependence of crystal growth of hexagonal ice (ih). *Phys. Chem. Chem. Phys.*, 13:15501–15511, 2011.

[25] Dmitri Rozmanov and Peter G Kusalik. Anisotropy in the crystal growth of hexagonal ice, i h. *The Journal of chemical physics*, 137(9):094702, 2012.

[26] J. R. Espinosa, C. Navarro, E. Sanz, C. Valeriani, and C. Vega. On the time required to freeze water. *J. Chem. Phys.*, 145(21):211922, 2016.

[27] Volker C. Weiss, Markus Rullich, Christof Köhler, and Thomas Frauenheim. Kinetic aspects of the thermostatted growth of ice from supercooled water in simulations. *The Journal of Chemical Physics*, 135(3):034701, 2011.

[28] Alberto Zaragoza, Jorge R Espinosa, Regina Ramos, José Antonio Cobos, Juan Luis Aragones, Carlos Vega, Eduardo Sanz, Jorge Ramírez, and Chantal Valeriani. Phase boundaries, nucleation rates and speed of crystal growth of the water-to-ice transition under an electric field: a simulation study. *Journal of Physics: Condensed Matter*, 30(17):174002, 2018.

[29] Ramon Garcia-Fernandez, José L. F. Abascal, and Carlos Vega. The melting point of ice ih for common water models calculated from direct coexistence of the solid-liquid interface. *The Journal of Chemical Physics*, 124(14):144506, 2006.

[30] Harold W Wilson. Xx. on the velocity of solidification and viscosity of super-cooled liquids. *The London, Edinburgh, and Dublin Philosophical Magazine and Journal of Science*, 50(303):238–250, 1900.

[31] J Frenkel. Note on a relation between the speed of crystallization and viscosity. *Phisik. Zeit. Sowjetunion*, 1:498–510, 1932.

[32] JQ Broughton, GH Gilmer, and KA Jackson. Crystallization rates of a lennard-jones liquid. *Physical review letters*, 49(20):1496, 1982.

[33] Erik Lindahl, Berk Hess, and David van der Spoel. Gromacs 3.0: a package for molecular simulation and trajectory analysis. *J. Mol. Model.*, 7:306, 2001.

[34] J. L. F. Abascal, Eduardo Sanz, Ramon Garcia Fernandez, and Carlos Vega. A potential model for the study of ices and amorphous water: TIP4P/Ice. 122:234511, 2005.

[35] MM Conde, M Rovere, and P Gallo. High precision determination of the melting points of water tip4p/2005 and water tip4p/ice models by the direct coexistence technique. *The Journal of chemical physics*, 147(24):244506, 2017.

[36] Rainer Feistel and Wolfgang Wagner. A new equation of state for h 2 o ice ih. *Journal of Physical and Chemical Reference Data*, 35(2):1021–1047, 2006.

[37] William Humphrey, Andrew Dalke, and Klaus Schulten. Vmd: visual molecular dynamics. *Journal of molecular graphics*, 14(1):33–38, 1996.

[38] Ulrich Essmann, Lalith Perera, Max L. Berkowitz, Tom Darden, Hsing Lee, and Lee G. Pedersen. A smooth particle mesh ewald method. 103:8577, 1995.

[39] Berk Hess, Henk Bekker, Herman J. C. Berendsen, and Johannes G. E. M. Fraaije. Lincs: A linear constraint solver for molecular simulations. *J. Comput. Chem.*, 18(12):1463–1472, 1997.

[40] Giovanni Bussi, Davide Donadio, and Michele Parrinello. Canonical sampling through velocity rescaling. *The Journal of Chemical Physics*, 126(1):014101, 2007.

[41] M. Parrinello and A. Rahman. Polymorphic transitions in single crystals: A new molecular dynamics method. 52:7182, 1981.

[42] Wolfgang Lechner and Christoph Dellago. Accurate determination of crystal structures based on averaged local bond order parameters. *J. Chem. Phys.*, 129(11):114707, 2008.

[43] Jorge Benet, Luis G. MacDowell, and Eduardo Sanz. A study of the ice-water interface using the TIP4P/2005 water model. *Phys. Chem. Chem. Phys.*, 16:22159–22166, 2014.

[44] Alberto Zaragoza, Maria M. Conde, Jorge R. Espinosa, Chantal Valeri ani, Carlos Vega, and Eduardo Sanz. Competition between ices ih and ic in homogeneous water freezing. *J. Chem. Phys.*, 143(13):134504, 2015.

[45] E. Sanz, C. Vega, J. R. Espinosa, R. Caballero-Bernal, J. L. F. Abascal, and C. Valeriani. Homogeneous ice nucleation at moderate supercooling from molecular simulation. *J. Am. Chem. Soc.*, 135(40):15008–15017, 2013.

[46] P. G. Debenedetti. Supercooled and glassy water. 15:R1669–R1726, 2003.

Chapter 8

Viscosity and self-diffusion of supercooled and stretched water from molecular dynamics simulations

P. Montero de Hijes[1], E. Sanz[1], L. Joly[2], C. Valeriani[3], and F. Caupin[2]

[1]Departamento de Química Física, Facultad de Ciencias Químicas, Universidad Complutense de Madrid, 28040 Madrid, Spain

[2]Universite Lyon, Universite Claude Bernard Lyon 1, CNRS, Institut Lumiere Matiere, F-69622 Lyon, France

[3]Departamento de Estructura de la Materia, Física Térmica y Electrónica, Facultad de Ciencias Físicas, Universidad Complutense de Madrid, Madrid 28040, Spain

8.1. Abstract

Among the numerous anomalies of water, the acceleration of dynamics under pressure is particularly puzzling. Whereas the diffusivity anomaly observed in experiments has been reproduced in several computer studies, the parallel viscosity anomaly has received less attention. Here we simulate viscosity and the self-diffusion coefficient of the TIP4P/2005 water model over a broad temperature and pressure range. We reproduce the experimental behavior and find additional anomalies at negative pressure. The anomalous effect of pressure on dynamic properties becomes more pronounced upon cooling, reaching two orders of magnitude for viscosity at 220 K. We analyze our results with a dynamic extension of a thermodynamic two-state model, an approach which has proved successful in describing experimental data. Water is regarded as a mixture of interconverting species with contrasting dynamic behaviors, one being strong (Arrhenius) and the other fragile (non-Arrhenius). The dynamic parameters of the two-state models are remarkably close between experiment and simulations. The larger pressure range accessible to simulations suggests a modification of the dynamic two-state model, which in turn also improves the agreement with experimental data. Furthermore, our simulations demonstrate the decoupling between viscosity η and self-diffusion coefficient D as a function of temperature T. The Stokes-Einstein relation, which predicts a constant $D\eta/T$, is violated when T is lowered, in connection with the Widom line defined by an equal fraction of the two interconverting species. These results provide a unifying picture of thermodynamics and dynamics in water and call for experiments at negative pressure.

8.2. Introduction

Liquid water exhibits countless thermodynamic and dynamic peculiarities[1]. Among thermodynamic properties, well known anomalies are the negative expansion coefficient below 4^{o}C at ambient pressure, or the rapid increase in isothermal compressibility and isobaric heat capacity upon cooling. These anomalies become more pronounced in supercooled water[2,3]. Several dynamic properties are also anomalous, showing a non-monotonic pressure dependence. Below room temperature, the shear viscosity η reaches a minimum as a function of pressure[4–7], whose location has been recently tracked down to 244 K and 200 MPa, where η is reduced by 42% compared to its value at ambient pressure[8]. Diffusivity reaches a maximum as a function of pressure, which has been measured in supercooled water both for translation[9,10] and rotation[11,12]. Stretched water, or water at negative pressure, has also been studied, although less extensively (see Ref.[13] for a review). The temperature of maximum density increases from 4^{o}C at ambient pressure to 18^{o}C at -137 MPa, and a maximum in the isothermal compressibility of water along isobars has been revealed around -100 MPa and below 276 K[14]. A limit to experiments on metastable water is homogeneous nucleation of ice in supercooled water or of vapor in stretched water. At deeply metastable conditions, nucleation becomes unavoidable on the time scale needed to perform measurements. Because of the small sizes and short time scales involved, molecular dynamics (MD) simulations provide a powerful alternative to experiments for studying physical properties at even more extreme conditions. Extensive thermodynamic data are already available for several water models such as ST2[15,16] and TIP4P/2005[17–19]. The self-diffusion coefficient D has also been studied in simulations. Early simulations reproduced qualitatively the experimental behavior of D: first its anomalous density dependence for ST2[20] and SPC/E water[21] and later its maximum for SPC/E water[22–24]. A minimum in D at low density, not yet observed in experiments, has also been found in simulations of TIP4P[25] and SPC/E water[22,24,26]. Agarwal et al.[17] simulated D of water for five models, namely, SPC/E, mTIP3P, TIP4P, TIP5P, and TIP4P/2005. Although they all show a maximum in D as a function of density at low enough temperatures, only TIP4P/2005 gives a maximum at ambient temperature, as observed in experiments. All models give rise to a minimum in D at low density. One concern about the results for D is the possible existence of finite-size effects, with simulations involving for instance 256 molecules only[17]. Correcting for these effects requires the knowledge of the viscosity[27,28].

However, simulations of viscosity are scarce. Because of its lower computational cost, the structural relaxation time $\tau\alpha$ is often used as a proxy for η, as these two quantities are assumed to be proportional. However, Shi et al.[29] found that, for model atomic and molecular systems, $\tau\alpha/\eta$ is temperature dependent. The same issue was observed for a water model[30,31]. Coming back to direct simulations of η, we list here the important works relevant to our study. A minimum in the density dependence of η was obtained with TIP4P/2005[32] and BK3 water[33]. Values of D and η for TIP4P/2005 were also reported[34] in the range 260–400 K and 0.1–300 MPa and showed the maximum in D, whereas the minimum in η was hidden by the simulation uncertainties. To our knowledge, simulation data for η of TIP4P/2005 water at supercooled conditions are only available at ambient pressure[30] or at a density of 1000 kg m^{-3}[35]. We are aware of only two simulation studies of viscosity in the supercooled region under pressure. The first study by Dhabal et al.[36] reported D and η for the coarse-grained mW model (monatomic water), and the density dependence gave a minimum and a maximum for D and a minimum for η. However, because it omits the reorientation of hydrogen atoms, mW gives D three times higher and η three times lower than experimental values for water at ambient conditions. The second study simulated the more realistic WAIL potential[37], but the pressure range investigated (0–70 MPa) precluded the observation of a minimum in η. It is therefore of interest to perform simulations with a realistic water model, aimed at the direct determination of η in a broad pressure and temperature range. In particular, it should be possible to follow in the supercooled region the minimum in η seen at stable conditions and also to investigate if there is a maximum in η at low density, similar to the second extremum seen in simulations of D. In the present work, we have performed such simulations with TIP4P/2005 water. We have computed η and D at the same state points so that we were able to apply finite-size corrections to D at the same time.

An additional motivation of our work is to investigate the connection between thermodynamics and dynamics. In the case of real water, several studies have addressed this question using a two-state model for the theoretical frame[38–42]. In Ref.[8], an accurate thermodynamic two-state model[43] was successfully extended to describe dynamic data. As a similar thermodynamic two-state model is available for TIP4P/2005 water[19], we investigate here if its dynamic extension can also reproduce our simulated dynamic properties. Finally, obtaining simultaneous data on D and η is also useful to test their coupling. Indeed, in liquids at high temperatures, D and η are usually linked by the Stokes-Einstein (SE) relation, inspired by macroscopic hydrodynamics and linear response theory, which states that $D\eta/T$ is independent of temperature. Deviations are observed in supercooled liquids, usually around 1.3 T_g where T_g is the glass transition temperature; see for instance Ref.[44] for $D\eta/T$ vs. T for six glassformers. By contrast, at ambient pressure, water already exhibits a violation of the SE relation at room temperature (above $2T_g$); this violation increases upon cooling, with a relative deviation around 70% at 239 K[45]. Understanding the origin of this early SE violation in water is an active field of research[30,35,46] as for other anomalies of water that become more pronounced in the supercooled region[1].

8.3. Methods

8.3.1. Simulation Details

We have selected the TIP4P/2005 model for water[47], which is currently one of the best force fields available, describing nearly quantitatively many properties of water in a broad temperature and pressure range. Many thermodynamic quantities are available for TIP4P/2005 water and they have been successfully described within the two-state formalism by Biddle et al.[19] (see Sec. II B). We have performed NVT runs of TIP4P/2005 water simulated via the LAMMPS MD package[48]. N is set to 216 molecules and the temperature is kept constant via a Nose-Hoover thermostat. To remain consistent with the definition of TIP4P/2005[47], we used a 0.85 nm cutoff. Long-range Coulombic interactions were computed using the particle-particle particle-mesh method[49], and water molecules were held rigid using the SHAKE algorithm[50]. We simulated temperatures ranging from 220 to 300 K and densities from 800 to 1320 kg m^{-3}. We selected state points on a grid in the temperature-density plane, which includes the validity region of the thermodynamic two-state model by Biddle et al[19]. All state points have been simulated far beyond their characteristic time to ensure equilibration [see for instance Fig. 1(b) of Ref.[35] for characteristic times of TIP4P/2005 water at 1000 kg m^{-3}]. The run durations ranged from 25 ns at 1320 kg m^{-3} and 300 K to 88 ns at 960 kg m^{-3} and 220 K; at 920 kg m^{-3} and 220 K, a longer duration of 880 ns was used. For each state point, we obtained the shear viscosity η by averaging the five independent Green-Kubo integrals of the auto-correlation function of traceless stress tensor elements[51]. As these calculations were computationally expensive, optimized algorithms were used[52]. We calculated the self-diffusion coefficient D from the slope of the linear regression of the mean squared displacement $\langle r^2 \rangle$ in the diffusive regime. The slope is divided by 6 following the Einstein relation[53] $\langle r^2 \rangle = 6Dt$ to obtain D (note that center of mass corrections have been used). Because of hydrodynamic interactions between image boxes in a simulation with periodic boundary conditions, the raw value of D suffers from finite size effects. It has been shown on theoretical grounds and verified with simulations of boxes with different sizes[27,28] that the value for the self-diffusion in an infinite liquid can be calculated with the following formula:

$$D = D_{PBC} + 2.837 \frac{k_B T}{6\pi\eta L_{box}} \tag{8.1}$$

where D_{PBC} is the self-diffusion coefficient before finite size correction (that is in a cubic simulation box of side Lbox with periodic boundary conditions), k_B is the Boltzmann constant, T is the temperature, and η is the viscosity (previously obtained from the simulation). Tazi et al.[28] also simulated TIP4P/2005 water but for only one state point. They computed D_{PBC} for several box sizes L_{box} and used Eq. (1) to calculate D for the infinite liquid. From the slope of D_{PBC} vs. $1/L_{box}$, they also obtained an estimate of η, which was in perfect agreement with η directly calculated from the Green-Kubo integrals. This validates our procedure of first calculating η from the Green-Kubo integrals and D_{PBC} for one value of L_{box} (e.g., 1.863 nm for $\rho = 1000$ kg m^{-3}) and then using η and Eq. (1) to calculate D for the infinite liquid. Appendix A gives all simulations results for η (Table III) and for D (Table IV). We also present in Appendix A how uncertainties on η and D were estimated; their values are given in the tables.

8.3.2. Two-state model

Two-state models are popular explanations of the anomalies of water because anomalous behavior in such models stems from the variation of the fraction of each state, each having otherwise a normal behavior. For instance, Robinson and his colleagues provided a two-state description of density at ambient pressure[38], later extended to the pressure dependence of viscosity[39] and density[40]. A more comprehensive description was formulated by Tanaka[41,42] to account for the anomalous behavior of density, isothermal compressibility, isobaric heat capacity, and shear viscosity with a mixture of two states with fractions $f(T,P)$ and 1 - $f(T,P)$. The dynamic part of Tanaka's model describes the viscosity of water as a thermally activated process, whose activation energy E_a is the fraction-weighted average of the activation energy for each state, E_1 and E_2: $E_a = f(T,P)E_1 + [1 - f(T,P)]E_2$. In other words, the hypothetic pure liquids made of only one of the two states would have an Arrhenius behavior (constant E_1 and E_2), and the non-Arrhenius behavior of real water would arise from the variation of the fraction $f(T,P)$. Holten, Sengers, and Anisimov[43] developed an equation of state for water based on the two-state picture, which we will refer to as the HSA model. In the HSA model, water is considered as an athermal non-ideal "solution" of two rapidly inter-convertible states or structures: a low density state (LDS) and a high density state (HDS), with respective fractions f and 1 - f. The non-ideality of the solution drives a first-order phase transition between two distinct liquids at low temperatures, ending at a liquid-liquid critical point (LLCP) at $T_c = 228.2$ K and $P_c = 0$ MPa. We emphasize that there is currently no firmly established experimental proof of such a liquid-liquid transition and LLCP for real water, the main reason being that, in experiments, ice nucleates before reaching the putative two-phase region[13]. Nevertheless, the HSA model achieves a fit within experimental error of a comprehensive data set of thermodynamic properties (density, isothermal compressibility, thermal expansion coefficient, isobaric heat capacity, and speed of sound) in the range 200–310 K and 0.1–400 MPa. This equation of state is the current official guideline on thermodynamic properties of supercooled water[54]. Following Tanaka's example[41,42], the HSA model was recently extended to dynamic properties by Singh et al.[8], who additionally measured viscosity of supercooled water under pressure. Experimental data for stable and supercooled water below 300 K and between 0 and 400 MPa were included, not only for shear viscosity as Tanaka did[41,42] but also for the self-diffusion coefficient[9,10] and rotational correlation time[11,12]. It was observed that a mixture of two liquids following Arrhenius dynamics did not give satisfactory results. Instead, all properties could be reproduced within experimental uncertainty if the high density state was assumed to follow a fragile behavior. Eventually the following form was used to describe all three dynamic properties:

	Simulations		Experiment		
Quantity	Viscosity η	Self-diffusion coefficient D	Viscosity η	Self-diffusion coefficient D	Rotational correlation time τ_r
A_0	37.19 ± 1.32 μPa s	39 715 ± 950 $\mu m^2\ s^{-1}$	38.75 ± 0.63 μPa s	40 330 ± 320 $\mu m^2\ s^{-1}$	86.2 ± 3.0 fs
E_{LDS}/k_B (K)	1874 ± 56	2 034 ± 21	2262 ± 23	1 984 ± 21	2585 ± 53
E_{HDS}/k_B (K)	350.2 ± 10.2	288.0 ± 5.1	421.9 ± 3.2	402.2 ± 1.5	395.0 ± 5.5
Δv_{HDS} (10^{-30} m^3)	3.32 ± 0.25	3.80 ± 0.11	2.44 ± 0.08	1.79 ± 0.04	1.62 ± 0.13
T_0 (K)	145.86		147.75		
N_{points}	26	26	178	157	101
χ^2	3.30	7.54	1.57	1.48	0.82

Table 8.1: Best fit parameters of the original two-state model for dynamic properties [Eq. (2), applied to simulation set 1 (this work) and to the experiment.[8] A common temperature T_0 is used for the different dynamic properties. Uncertainties correspond to a 95% confidence interval. The number of points and reduced χ^2 are also given.

$$A(T,P) = A_0 \left(\frac{T}{T_{ref}}\right)^{\nu} exp\left\{\epsilon\left[[1-f(T,P)]\frac{E_{HDS}+\Delta v_{HDS}P}{k_B(T-T_0)} + f(T,P)\frac{E_{LDS}}{k_BT}\right]\right\}. \quad (8.2)$$

Here $T_{ref} = 273.15$ K (introduced to make T/T_{ref} dimensionless), ν accounts for the temperature variation of the average speed of the molecules[9] ($\nu = 1/2$ for $A = \eta$ or D, -1/2 for $A = \tau_r$[55]), and $\epsilon = 1$ for $A = \eta$ or τ_r and -1 for $A = D$. There are also 5 free parameters, as for Tanaka's viscosity model. Their physical meaning is as follows. A_0 is a global scale factor. LDS behaves like an Arrhenian liquid with activation energy E_{LDS}, whereas HDS behaves like a fragile liquid described by a Vogel-Tamann-Fulcher (VTF) law with parameters $E_{HDS} + \Delta v_{HDS}P$ and T_0. The energy appearing in the VTF law has a pressure dependence $\Delta v_{HDS}P$ coming from the difference in volume between the activated and initial state of the activated process.[41] A good fit, with good reduced χ^2 and residuals, could be obtained holding T_0 equal for the three properties (see Fig. 3 of Ref. 8). The best fit parameters are reproduced in Table I. They are relatively close between properties and have reasonable physical values. In particular, E_{LDS} is of the order of the hydrogen bond energy and Δv_{HDS} is around 5%-8% of the volume per molecule, around $301{\cdot}10^{-30}$ m^3 at $\rho = 1000$ kg m^{-3}.

One focus of the present paper is applying a two-state approach for simulation data. Recently, a set of thermodynamic properties of TIP4P/2005 water was successfully described with a two-state model similar to the HSA model.[19] Its validity region (Fig. 1 of Ref. 19) covers temperatures from 180 to 320 K and pressures from around -250 to 500 MPa. It predicts a liquid-liquid critical point at 182 K and 170 MPa. These values are close to previous estimates for TIP4P/2005.[56–59] Although the existence of such a critical point in TIP4P/2005 has been challenged,[60] a recent approach based on the potential energy landscape[61] also predicts a critical point. Inspired by the analysis performed on experimental data,[8] we have investigated if, for simulations, the two-state model presented in Ref. 19 could be extended to describe dynamic properties.

8.4. Results and discussion

8.4.1. Simulation results

Figure 1 shows the final results for η and D as a function of density for a series of isotherms. Our results compare well with those of Tazi et al.[28] for both η and D. Our uncorrected values for D agree well with Agarwal et al.[17] at high density. A slight discrepancy appears at low density and gets more pronounced at low temperatures. Note that the difference with Ref. 17 is that we could correct D for finite size effects because we have both η and D. Figure 2 shows a close-up to allow comparison with experimental data. The fits of Ref. 8 were used to represent the experimental data. Simulations reproduce well the fast temperature variation of η and D, together with their minimum and maximum as a function of density, respectively. This illustrates once more the good performance of the TIP4P/2005 model in reproducing the properties of experimental water. At lower densities, where no experiment is available at present, our simulations yield a maximum in η versus ρ and a minimum in D versus ρ. The minimum in D has been previously observed in simulations.[17,22,24–26,36] To our knowledge, the maximum in η is found here for the first time. The anomalous variation with density (decrease of η and increase of D) at a fixed temperature becomes more pronounced upon cooling, as observed in the experiment (Fig. 2). The anomalous change measured experimentally corresponds to a maximum factor 1.7 for η at 244 K[8] and 1.8 for D at 238 K.[9] Because the simulations reach lower temperatures and densities, the observed factors reach larger values. At 220 K, the anomalous change corresponds to a factor 98 for η and 30 for D; note that these values are lower bounds, as no low density extremum is present in the density range of our simulations at this temperature. To illustrate the fragile character of TIP4P/2005 water, Appendix B shows the variation of η and D with inverse temperature in a log-lin plot for each isochore (Arrhenius plots). Arrhenius behavior would correspond to straight lines. Instead, the curves exhibit a more rapid variation with decreasing temperature. The effect tends to be more pronounced at lower densities.

8.4.2. Two-state analysis

The analysis of the simulation data with the two-state model[19] presented in Sec. II B can be done only for state points in the validity region of the two-state model (between dashed vertical lines in Fig. 1). Therefore, only data with density between 920 and 1160 kg m^{-3} were considered. Because the dynamic two-state model [Eq. (2)] uses pressure as a variable, the pressure for each state point was calculated from its temperature and density using the thermodynamic two-state model.[19] As a first step, we have tried to reproduce the analysis of experimental data (see Sec. II B). To this end, we have selected a subset of simulation data, set 1, at positive pressure as in the experiment. Because its pressure was very close to zero, we also included in set 1 a data point at 280 K and -1.5 MPa. The fit to Eq. (2) and the corresponding residuals are shown in Fig. 3,

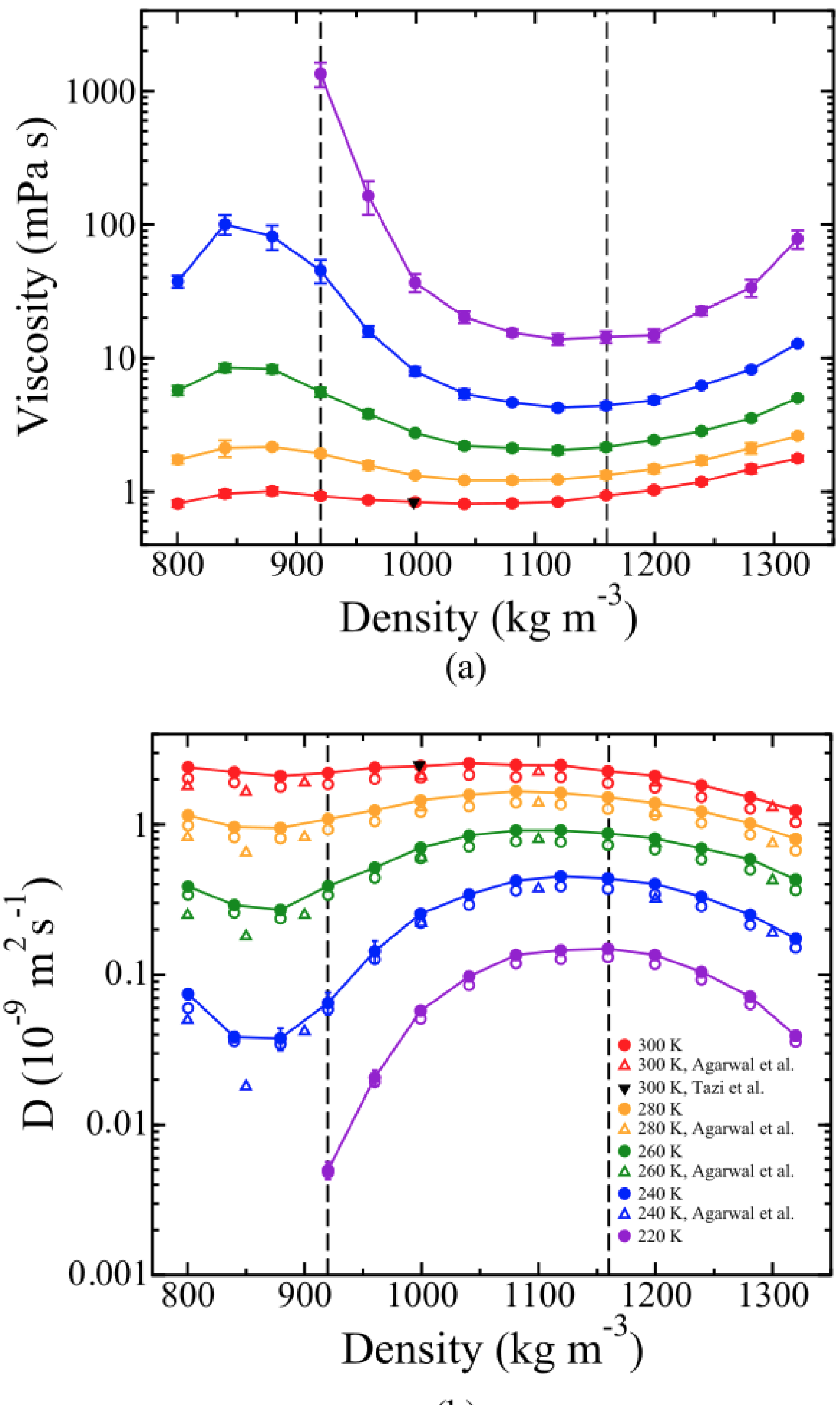

(a)

(b)

Figure 8.1: Density dependence of viscosity (a) and self-diffusion coefficient (b) along several isotherms. The data set for each isotherm (circles: this work; down triangle: Ref. 28; up triangles: Ref. 17) is shown with a distinct color and labeled with the temperature in K. In (b), the empty and filled symbols correspond to data before and after correction with Eq. (1), respectively. The solid lines connecting points are guides to the eye. The vertical dashed lines bracket the validity region of the two-state model from Ref. 19.

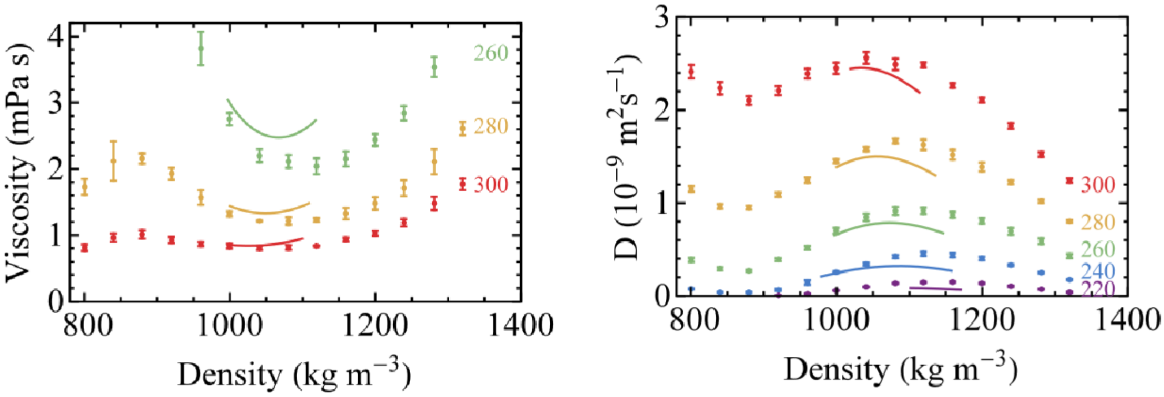

Figure 8.2: Details of the previous figure showing our simulations results (circles) on a linear vertical scale and experimental data 8 (solid lines, see the text for details).

which corresponds to the simulation equivalent of Fig. 3 of Ref. 8 for the experiments. Overall the fit quality is reasonable. The reduced residuals, defined as the difference between data and fit values divided by the data uncertainty, are acceptable, but a systematic deviation appears at low temperatures and low density. Table I gives the best fit parameters. It can be seen that, as noted in Ref. 8 for the experiment, and here as well for the simulation set 1, the values of E_{LDS}, E_{HDS}, and Δv_{HDS} are in the same range for the different dynamic quantities. Note that they cannot have a common value for all dynamic properties; otherwise, the SE relation would always hold. Moreover, the best fit parameters for the same dynamic quantity have similar values in simulations and in experiment. This confirms the good performance of the TIP4P/2005 model in reproducing the properties of experimental water. Remarkably, both in simulations and in experiment, the temperature T_0 is around 147 K and E_{LDS}/k_B is in the range 1900–2600 K, the typical energy of a hydrogen bond. The activation volume Δv_{HDS} is in the range 1.6–3.8·10^{-30} m^3. This is around 5%–12% of the volume per molecule in the liquid, which is around 30·10^{-30} m^3 at $\rho = 1000$ kg m^{-3}. As a second step, we attempted to fit all simulation data belonging to the validity region of the two-state model.[19] The fit to Eq. (2) deteriorates gradually when simulation data with lower density are successively added. Equation (2) cannot generate a low-density extremum in dynamic quantities. Figure 1 shows that these extrema lie outside the region of validity of the two-state model,[19] but still their vicinity might be responsible for the discrepancy. To improve the fit, we tried a number of other formulas, obtained by making simple changes to Eq. (2). In all our attempts, one point at 220 K and 920 kg m^{-3}, at the corner of the validity region, caused too large deviations, resulting in a reduced $\chi^2 = 2.21$ for η and 11.4 for D for our best fit with a modified equation. Yet this state point was well equilibrated, as we checked by performing an 880 ns-long simulation run. To keep the change to Eq. (2) to a minimum, we decided to discard this problematic point. We kept all other points in the region of validity of the two-state model[19] to form a second set of simulation data, set 2. We were able to improve the fit to set 2 by adding a volume term Δv_{LDS} in the activation energy for the LDS

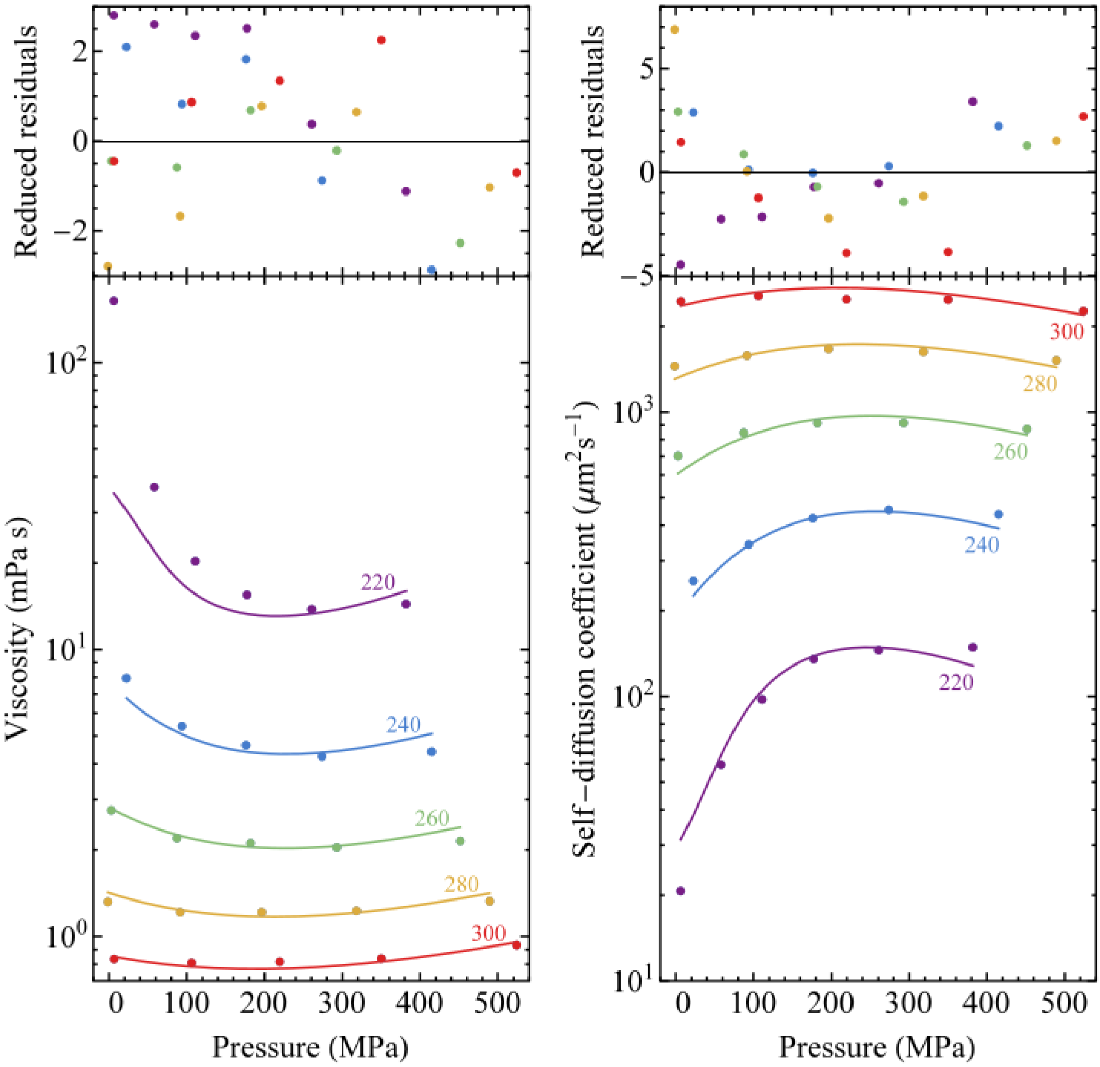

Figure 8.3: Pressure dependence of simulated dynamic properties (set 1) and original dynamic two-state model [Eq. (2)]. The best fits to Eq. (2) for the simulation set 1 are shown for viscosity (left) and self-diffusion coefficient (right). Best fit parameters are given in Table I. In the bottom panels, the differently colored curves labeled by the temperature in K correspond to the values calculated along isotherms. The top panels show the deviations between fitted values and data points, each normalized by the simulation uncertainty (one standard deviation).

	Simulations		Experiment		
Quantity	Viscosity η	Self-diffusion Coefficient D	Viscosity η	Self-diffusion Coefficient D	Rotational Correlation time τ_r
A_0	60.23 ± 2.02 μPa s	$24\,315 \pm 530$ $\mu m^2\ s^{-1}$	48.79 ± 1.16 μPa s	$37\,280 \pm 350$ $\mu m^2\ s^{-1}$	93.3 ± 3.8 fs
E_{LDS}/k_B (K)	2239 ± 53	2067 ± 22	2433 ± 28	2056 ± 30	2626 ± 71
Δv_{LDS} (10^{-30} m^3)	28.9 ± 2.8	28.5 ± 1.3	42.5 ± 4.0	16.6 ± 4.3	15.1 ± 14.8
E_{HDS}/k_B (K)	182.0 ± 10.5	164.0 ± 5.2	376.3 ± 4.5	382.0 ± 2.6	375.7 ± 9.3
Δv_{HDS} (10^{-30} m^3)	4.29 ± 0.19	3.7 ± 0.09	2.69 ± 0.08	1.94 ± 0.06	1.76 ± 0.20
T_0 (K)	158.55		149.18		
N_{points}	34	34	178	157	101
χ^2	1.61	2.01	0.94	1.40	0.85

Table 8.2: Best fit parameters of the modified two-state model for dynamic properties [Eq. (3), applied to simulation set 2 (this work) and to the experiment.[8] A common temperature T_0 is used for the different dynamic properties. Uncertainties correspond to a 95% confidence interval. The number of points and reduced χ^2 are also given.

(similar to Δv_{HDS} for the HDS), namely,

$$A(T,P) = A_0 \left(\frac{T}{T_{ref}}\right)^{\nu} exp\left\{\epsilon\left[[1-f(T,P)]\frac{E_{HDS}+\Delta v_{HDS}P}{k_B(T-T_0)} + f(T,P)\frac{E_{LDS}+\Delta v_{LDS}P}{k_BT}\right]\right\}. \tag{8.3}$$

An advantage of Eq. (3) over Eq. (2) is that the former is able to yield a second extremum at low density. This can be understood by studying the derivative of lnA with respect to pressure,

$$\left(\frac{\partial lnA}{\partial P}\right)_T = \epsilon\left\{[1-f(T,P)]\frac{\Delta v_{HDS}}{k_B(T-T_0)} + f(T,P)\frac{\Delta v_{LDS}}{k_BT} + \left(\frac{\partial f}{\partial P}\right)_T \times \left[\frac{E_{LDS}+\Delta v_{LDS}P}{k_BT} - \frac{E_{HDS}+\Delta v_{HDS}P}{k_B(T-T_0)}\right]\right\} \tag{8.4}$$

At high pressure, $f \to 0$ and $(\partial f/\partial P)_T \to 0$ so that the dynamic behavior is normal, tending toward that of a pure HDS liquid. At intermediate pressures, the $(\partial f/\partial P)_T$ term has a sign opposite to the others, and if its amplitude is sufficient (i.e., at low enough temperature), it causes the anomalous behavior of dynamic properties. When the pressure is sufficiently reduced, the $1-f$ term can dominate, causing the dynamic properties to recover a normal behavior. The fit to Eq. (3) and the corresponding residuals are shown in Fig. 4. The fit is good, with significantly better quality than the fit of set 1 to Eq. (2). The residuals are reasonable, although some bias remains at low temperatures and at the two lowest densities. There are several possible reasons for this discrepancy and for our need to discard the point at 220 K and 920 kg m^{-3}. The simple linear pressure dependence of the apparent activation energies in Eq. (3) might not be sufficient for the large pressure range investigated or some parameters of the

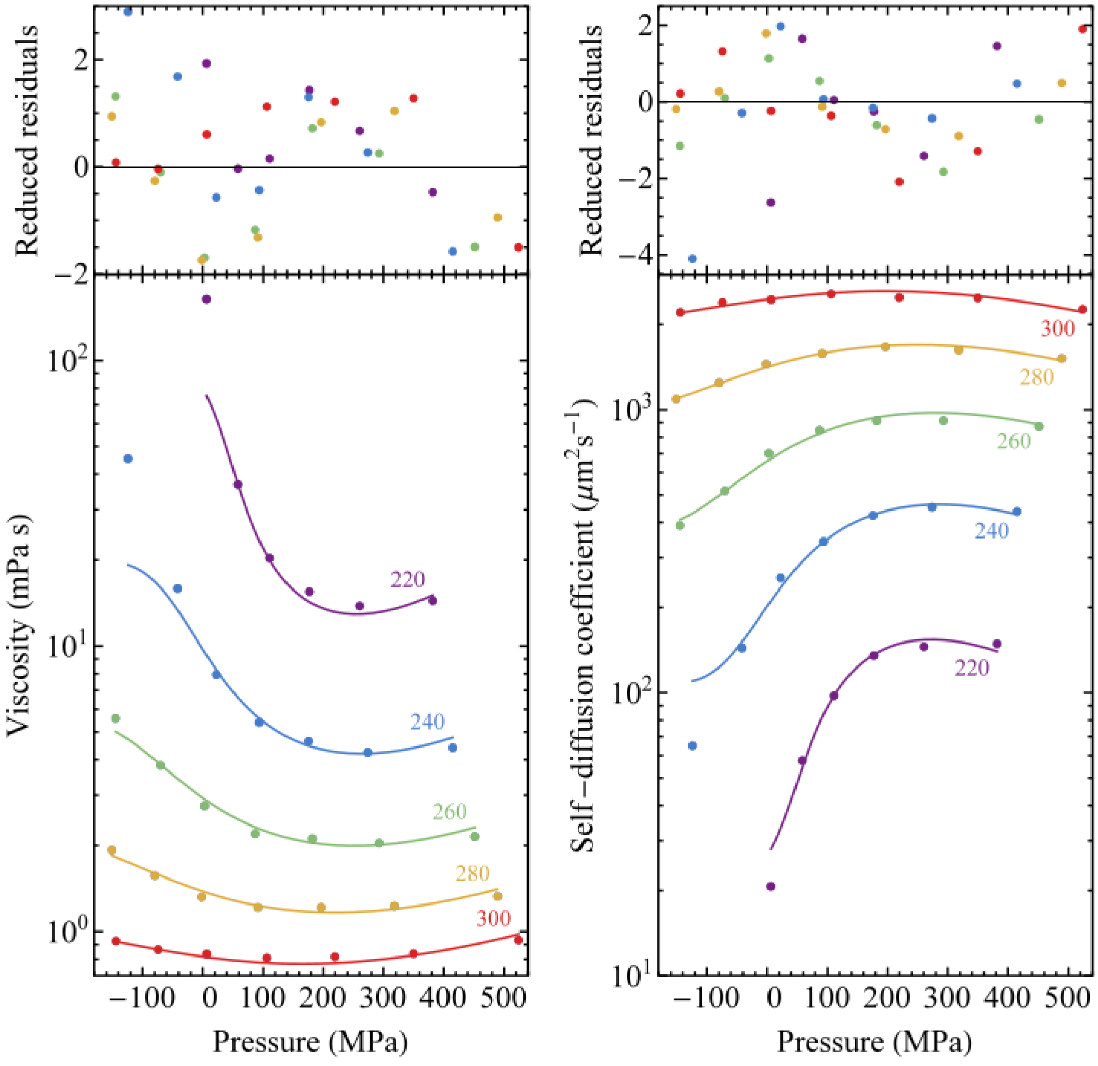

Figure 8.4: Pressure dependence of simulated dynamic properties (set 2) and modified dynamic two-state model [Eq. (3)]. The same as Fig. 3 for the fitting to Eq. (3) of the simulation set 2. Best fit parameters are given in Table II.

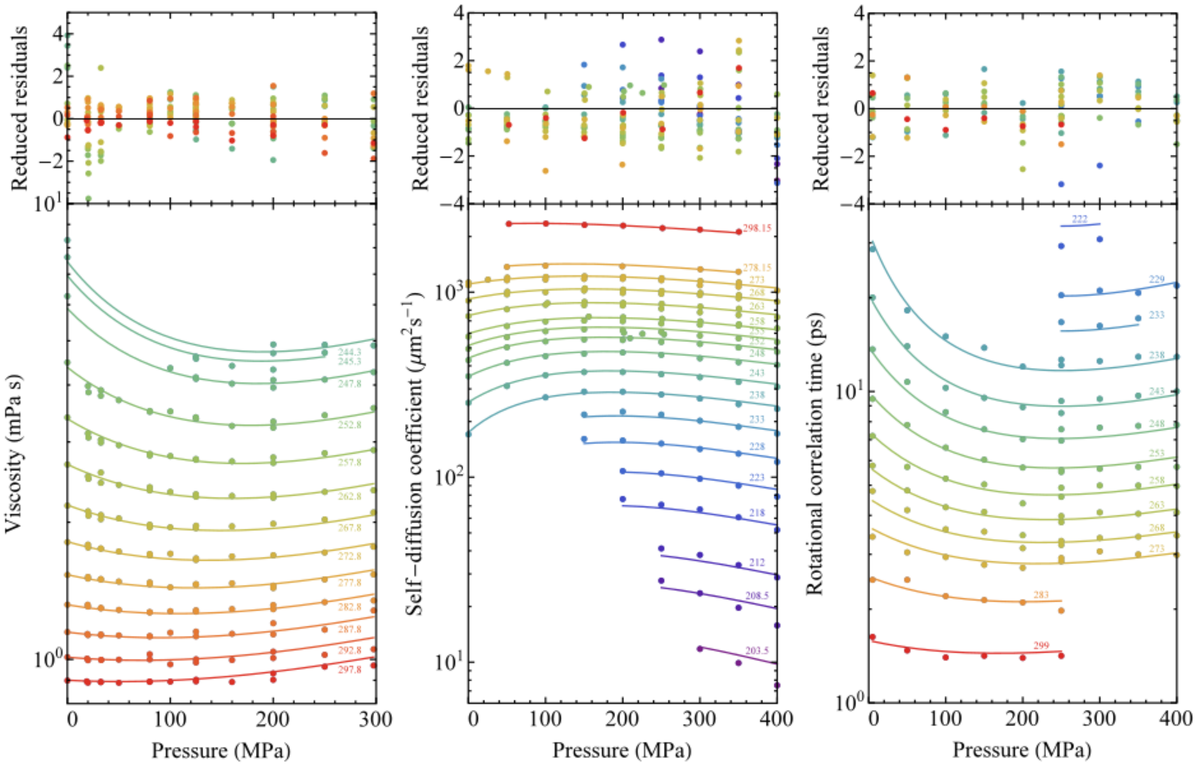

Figure 8.5: Pressure dependence of experimental dynamic properties and modified two-state model [Eq. (3)]. The best fits to Eq. (3) for the experimental data are shown for viscosity (left), self-diffusion coefficient (center), and rotational correlation time (right). Best fit parameters are given in Table II. In the bottom panels, the differently colored curves labeled by the temperature in K correspond to the values calculated along isotherms. The top panels show the deviations between fitted values and data points, each normalized by the experimental uncertainty (one standard deviation).

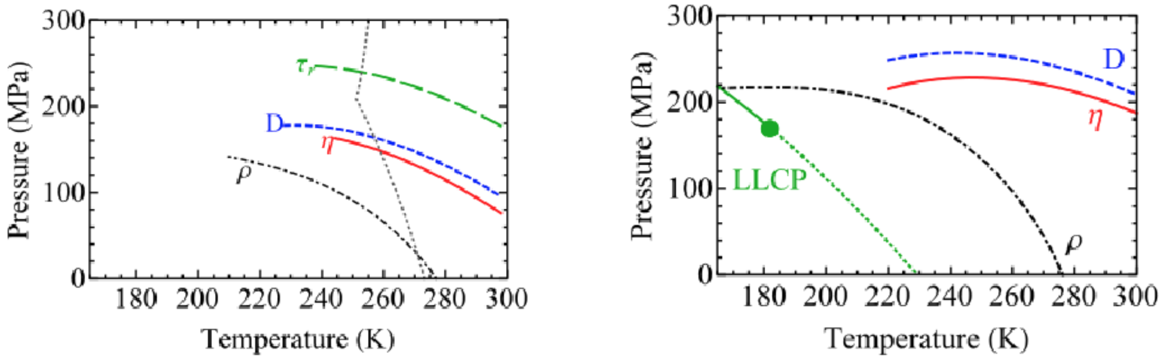

Figure 8.6: Extrema in density and dynamic properties. Left: Location in the pressure-temperature plane of the experimental extrema along isotherms for viscosity η (full red curve), self-diffusion coefficient D (short-dashed blue curve), rotational correlation time τ_r (long-dashed green curve), and density ρ (dashed-dotted black curve). The gray dotted curve shows the melting lines of ice Ih and ice III.[62] Adapted from Ref. 8, where experiments were fit with Eq. (2). Right: the same as left, but for the TIP4P/2005 model and Eq. (2) and including the liquid-liquid transition (solid green line), the LLCP, and the Widom line (dotted green line).[19].

thermodynamic two-state model (e.g., the location of the Widom line) might have to be modified, to improve the agreement with the dynamic data, without deteriorating the description of thermodynamic data. A simultaneous fit of both types of data is an interesting direction for future work. For comparison, we also performed the fit of experimental data to Eq. (3), as shown in Fig. 5. Table II gives the best fit parameters. Adding the Δv_{LDS} term also improves the fit to experiment, albeit only slightly, presumably because of the restricted pressure interval and small values of the LDS fraction in the experimentally covered range. The values of E_{LDS}, Δv_{LDS}, E_{HDS}, and Δv_{HDS} are in the same range for the different dynamic quantities. E_{LDS}/k_B, in the range 2000–2600 K, still has the order of the energy of a hydrogen bond, whereas Δv_{LDS}, E_HDS, and Δv_{HDS} are more different between simulations and experiment. For the experimental data, T_0 is around 149 K, nearly the same as for the fit to Eq. (2), whereas it is increased to 159 K for the fit of MD data. The activation volume Δv_{HDS} is slightly increased but remains small, while the activation volume Δv_{LDS} is rather large, in the range 15–42$\cdot 10^{-30}$ m^3. This value is similar to the volume per molecule in the liquid. In the model we propose, transport by a molecule in the LDS state would thus involve a considerable change in volume for the activated state. This is not unlikely, as the LDS state is sometimes viewed as a structure involving a tetrahedral arrangement of hydrogen bonded molecules, with low entropy and large volume.

We now discuss the value of T_0 appearing in the VTF-like behavior of the dynamics of the HDS state, Eqs. (2) and (3). T_0, at which the system would be arrested, has been related to the Kauzmann temperature[63] or the mode-coupling temperature.[64] In the former case, it is expected to be lower than T_g, whereas in the latter case,

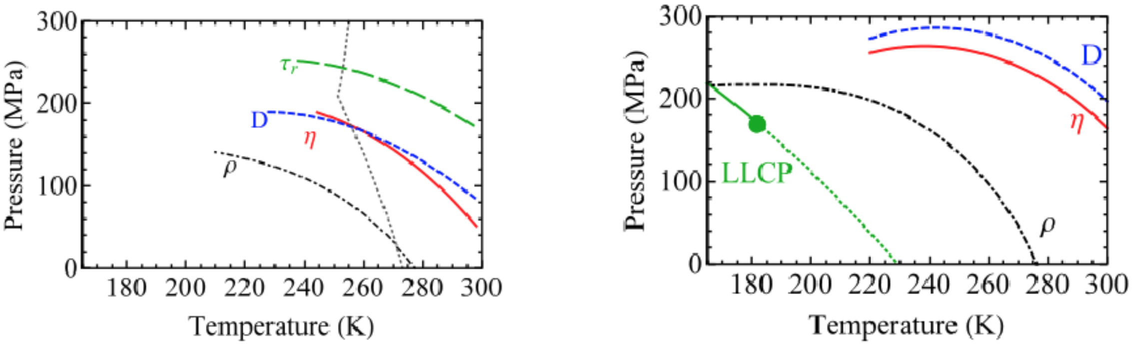

Figure 8.7: Extrema in density and dynamic properties. The same as the previous figure, except that the experimental dynamic data (left) were fit with Eq. (3) (Fig. 5 and Table II) and the TIP4P/2005 simulation set 2 (right) were fit with Eq. (3) (Fig. 4 and Table II).

T_0 should be higher than T_g , because of hopping processes. T_g for water has been reported below 145 K.[65] However, a recent comparison of the calorimetric features of the glass phases of several water isotopes[66] points toward a reinterpretation of the glass transition as an orientational glass transition. The true structural glass transition of water might therefore occur at a temperature above 145 K, which eludes observation because of crystallization upon further heating. We make the conservative statement that the best fit value for T_0 is close to T_g. Finally, we compare the lines of extrema for experiment and simulations, as derived from the fitting of experiment and simulation set 1 to Eq. (2) (Fig. 6) and of experiment and simulation set 2 to Eq. (3) (Fig. 7). The line of density maxima is also shown, together with the liquid-liquid transition and the Widom line for TIP4P/2005. All figures are qualitatively similar. We note that Fig. 6 does not show the intersection between the line of minima in η and of maxima in D for the fit to experiment nor the maxima of these lines for the fit to simulations, which can be seen in Fig. 7. We believe that these features are not significant and are rather due to inaccuracies of the fit in locating the rather shallow extrema (see Figs. 3–5). A robust result is the nested pattern formed by the lines. Part of this pattern was observed in previous simulations,[24,67,68] with the locus of maxima in D encircling the line of density maxima. The same arrangement of these lines was also observed for mW water, with, in addition, the locus of minima in η located in between them. However, mW does not reproduce quantitatively the dynamics of real water (see Sec. I). Here, with the more quantitative TIP4P/2005 water model, we find the lines of extrema in the same order as, and at a location close to, the experimental lines of extrema.

8.4.3. Stokes-Einstein relation

We are now in a position to test the SE relation by combining the simulation results. We choose to use directly the raw simulation data rather than the fits presented in Sec. III B because the simulations cover a larger range of temperature and pressure. Moreover, in their validity region, the fits exhibit systematic deviations which, although small for

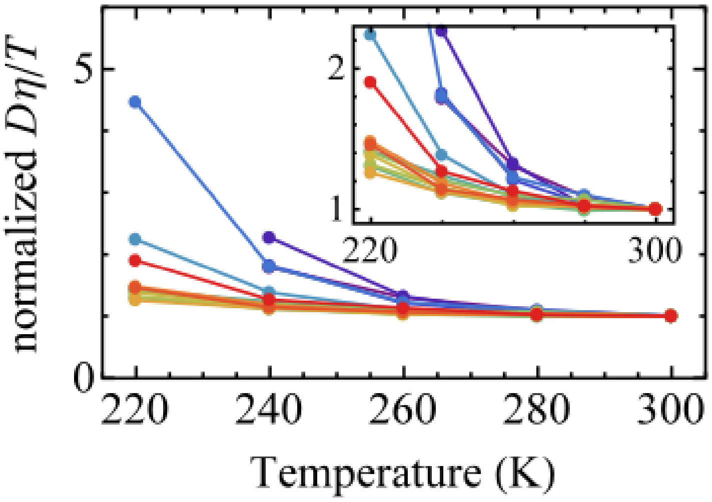

Figure 8.8: Temperature variation of the quantity $D\eta/T$ normalized by its value at 300 K for a series of isochores. The corresponding densities are listed in Appendix A, and the color code is the same as in Appendix B. The lines connecting data points are to guide the eye. The inset shows a zoom to emphasize the non-monotonic density variation.

the absolute values of η and D compared to the simulation uncertainties, result in an excessive underestimate of the product $D\eta$. To emphasize the temperature variation, $D\eta/T$ is usually normalized at a reference temperature, which is taken as 300 K in Fig. 8. For 1000 kg m^{-3}, the violation reaches 24% at 240 K, which is comparable to the violation of around 60% observed in the experiment at 240 K and atmospheric pressure. At a given temperature, the SE violation tends to become more pronounced at lower densities; however, the density dependence is not monotonic. Kumar et al.[69] studied the SE relation for two other models of water: TIP5P and ST2. Note that they used the structural relaxation time τ_α as a proxy for the shear viscosity η (see Sec. I). They related the SE violation to the existence of a LLCP in the supercooled liquid, and more particularly to the Widom line emanating from this LLCP, located at a temperature T_W depending on the pressure P. They found that, at pressures lower than the LLCP pressure, the $D\tau_\alpha/T$ curves for each pressure collapsed onto a master curve when plotted as a function of the distance to the Widom line, $T - T_W(P)$, instead of the temperature. We have tested this collapse. Strictly speaking, the Widom line is the locus of correlation length maxima associated with the LLCP. As a proxy for $T_W(P)$, Kumar et al. used the maxima of isobaric heat capacity along isobars, which asymptotically approaches the Widom line near the LLCP. Here instead, we use the two-state model presented in Sec. II B. For the 4 isochores having a density below the LLCP density, but still in the validity region of the two-state model, we use the two-state model to locate the Widom line as the locus of points where the LDS and HDS have equal fraction, 1/2. This is given by the roots of Eq. (4) of Ref. 19, which correspond to the two states having the same Gibbs free energy. Figure 9 shows the

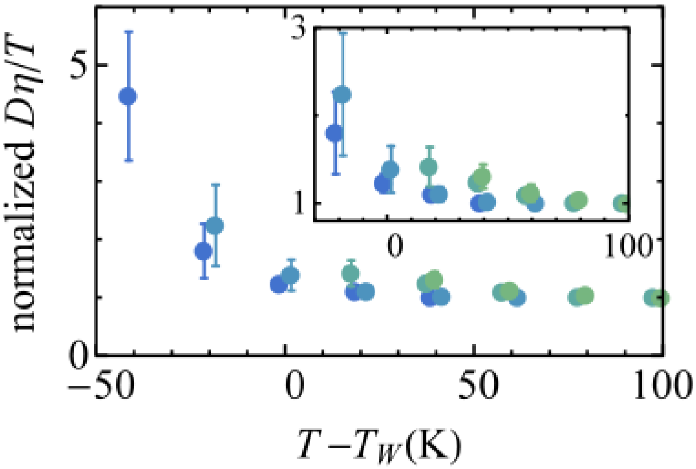

Figure 8.9: Temperature variation of the quantity $D\eta/T$ normalized by its value at 300 K, as a function of the distance to the Widom line $T-T_W(\rho)$ (see the text for details) for four isochores (from bottom to top: 920.050, 960.090, 999.260, and 1040.59 kg m^3). The inset points out the non-perfect collapse of the three isochores.

normalized $D\eta/T$ as a function of $T-T_W(P)$. We observe an approximate collapse, but a density dependence can still be seen. The normalization process used above removes the information about the absolute value of $D\eta/T$. If D was the diffusion coefficient of a macroscopic object obeying hydrodynamics in the Stokes regime, $D\eta/T$ would be related to the hydrodynamic diameter ϕ_h by

$$\phi_h = \frac{k_B T}{3\pi\eta D} \tag{8.5}$$

Figure 10 shows ϕ_h computed from the simulation data. At high temperatures, ϕ_h is 0.2–0.22 nm, nearly independent of (or only slightly decreasing with) density. To assess the validity of Eq. (5), ϕ_h should be compared to a molecular diameter determined independently. Several choices of this molecular diameter are possible (see for instance Ref.[70] for discussion in the case of the Lennard-Jones fluid). The volume per molecule in the liquid is around $30\cdot10^{-30}$ m^3 at $\rho = 1000$ kg m^{-3}, equivalent to a sphere of diameter 0.38 nm or 0.33 nm if one considers random close-packed spheres occupying 64% of space. The Lennard-Jones parameter for interaction between the oxygen sites of two molecules in TIP4P/2005 is 0.31589 nm.[47] All these values are close to ϕ_h. For a spherical object, a hydrodynamic diameter smaller than the physical diameter can be due to the slip boundary condition between the object and the ambient fluid.[71] This can vary the factor in the denominator of Eq. (5) from 3π (no slip) to 2π (perfect slip). Slip could thus explain the values of ϕ_h for water at high temperatures.[72] A change in slip boundary conditions may also explain changes in ϕ_h up to 50%, but cannot account for the large decrease at low temperatures, which can exceed a factor of 10. An explanation based on slippage only should thus be discarded. The behavior

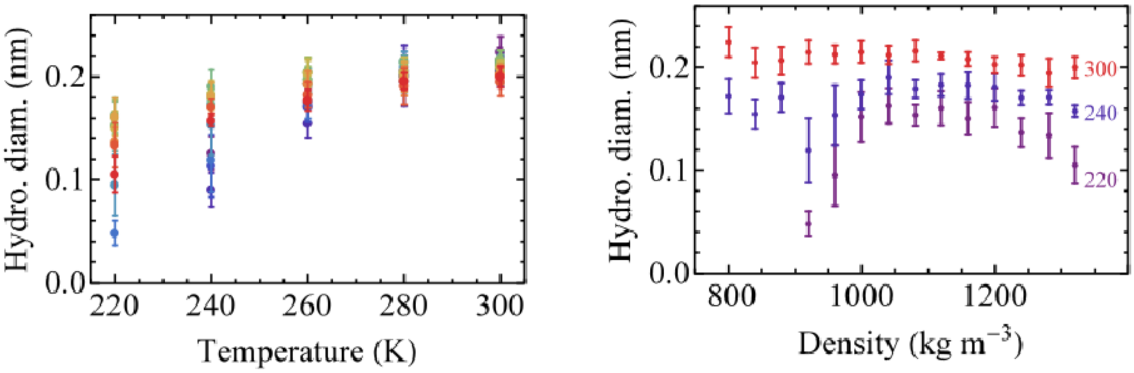

Figure 8.10: Left: Temperature dependence of the hydrodynamic diameter ϕ_h for a series of isochores with the same color code as in Appendix B. Right: Density dependence of the hydrodynamic diameter ϕ_h for three isotherms (labels give the temperature in K).

of water is reminiscent of many glassformers near their glass transition temperature T_g. In this case, the decoupling between D and η is due to the emergence of dynamic heterogeneities, that is, transient spatially correlated regions of particles with high and low mobility.[73,74] Emergence of these regions at low temperatures gives rise to a distribution of relaxation times broader than those at high temperatures. Because the different dynamic quantities result from different moments of the distribution, they start decoupling upon cooling. The SE violation in water has also been related to dynamic heterogeneities;[30,35,46,69,75,76] however, the discussion was based on simulations of τ_α rather than of η, and in contrast to usual glassformers for which the most mobile molecules cause the breakdown of the SE relation, all scales of mobility were involved in water. Further studies are needed to better understand the origin of the SE violation in water and its relation with the Widom line.

8.5. Conclusions

By performing extensive simulations of dynamic properties for the TIP4P/2005 water model, we have been able to reproduce nearly quantitatively all features observed for viscosity and the self-diffusion coefficient of real water at temperatures below ambient, including the supercooled region, and in a broad positive pressure range. Our simulations also go beyond the conditions which have been hitherto explored in experiments. At lower temperatures, the minimum in η and the maximum in D as a function of density or pressure are found to become even more pronounced. At negative pressure, a maximum in η and a minimum in D are observed. The dynamic extension of the thermodynamic two-state model available for TIP4P/2005 is able to accurately reproduce the simulation data. Inclusion of a pressure dependence in the activation energy of the low density state is necessary to fit the negative pressure data, pointing to a large activation volume for the dynamics of this state. The Stokes-Einstein relation is strongly violated as the system is cooled through the Widom line. Our study provides a unifying framework to interpret the thermodynamic and dynamic anomalies of water and calls for experiments on the dynamics of water at negative pressure.

8.6. Acknowledgments

P.M.H., E.S., and C.V. have been funded by Grant Nos. FIS2013/43209-P, FIS2016-78117-P, and FIS2016-78847-P of the MEC and the UCM/Santander Nos. 910570 and PR26/16-10B-2. P.M.H. acknowledges financial support from a FPI Ph.D. fellowship. L.J. acknowledges support from Institut Universitaire de France. This work was partially supported by CNRS (France) through a PICS program.

8.7. Appendix A: Simulation data

Tables III and IV give all the simulation results of this study with their uncertainty (one standard deviation). For viscosity (Table III), the uncertainty is the standard deviation of the five independent Green-Kubo integrals of the autocorrelation function of traceless stress tensor elements.[51] For self-diffusion (Table IV), the uncertainty was less straightforward to obtain and we proceeded as follows. At each temperature, for one in every three densities, we used the block averaging method on one of the trajectories. The selected trajectory was cut into four pieces with equal duration. For each piece, the self-diffusion coefficient for the finite system, D_{PBC}, was calculated from the slope of the mean squared displacement $\langle r^2 \rangle$ in the diffusive regime as explained in Sec. II A. The uncertainty on D_{PBC} was taken as the standard deviation of the four values thus obtained. Table IV gives the self-diffusion coefficient D for the infinite liquid, after correction for finite size effects using Eq. (1). The total uncertainty on the corrected D was calculated by propagating the uncertainty on D_{PBC} and η. Because the procedure was computationally costly, we applied it at every temperature, but only for one in every three densities. At each temperature, for each remaining density, we assumed that the relative uncertainty on D was equal to the relative uncertainty on D at the nearest density for which it was directly calculated with the above method. Hence, absolute uncertainties on D at the remaining densities were only calculated indirectly.

We note that, in order to get a more accurate estimate of the uncertainties, more simulations would be needed. The quantity χ^2 we use to assess the quality of the fits is quite sensitive to the uncertainty, because it involves dividing by the squared uncertainties. Therefore the absolute values for χ^2 could be modified if the uncertainty calculations were refined. Nevertheless, because fitting with the original or the modified two-state model uses the same definitions for the uncertainties, the comparison between the two fits is justified. Our results show that the modified model gives a better fit than the original one, and over a broader pressure range.

	Temperature (K)				
Density (kg m^{-3})	220	240	260	280	300
800.43		37.5 (3.8)	5.72 (0.45)	1.73 (0.12)	0.811 (0.046)
839.99		101 (17)	8.46 (0.61)	2.12 (0.30)	0.961 (0.062)
879.49		82 (17)	8.26 (0.59)	2.157 (0.077)	1.011 (0.062)
920.05	1348 (281)	45.3 (9.0)	5.58 (0.43)	1.929 (0.089)	0.926 (0.045)
960.09	164 (46)	15.9 (1.5)	3.82 (0.25)	1.57 (0.11)	0.864 (0.032)
999.26	36.8 (5.7)	7.94 (0.56)	2.753 (0.091)	1.320 (0.037)	0.834 (0.036)
1040.59	20.3 (2.0)	5.40 (0.41)	2.20 (0.10)	1.214 (0.014)	0.808 (0.028)
1080.66	15.5 (0.9)	4.64 (0.13)	2.114 (0.097)	1.215 (0.056)	0.816 (0.033)
1119.05	13.8 (1.3)	4.24 (0.15)	2.04 (0.12)	1.228 (0.028)	0.8368 (0.0092)
1159.29	14.4 (1.4)	4.40 (0.24)	2.15 (0.11)	1.327 (0.084)	0.933 (0.030)
1199.42	14.8 (1.6)	4.83 (0.28)	2.44 (0.09)	1.480 (0.093)	1.029 (0.037)
1239.28	22.6 (1.7)	6.23 (0.18)	2.84 (0.11)	1.71 (0.12)	1.189 (0.055)
1280.93	33.7 (5.0)	8.21 (0.23)	3.54 (0.15)	2.11 (0.19)	1.48 (0.10)
1319.79	78.2 (12)	12.81 (0.24)	5.02 (0.12)	2.61 (0.10)	1.770 (0.087)

Table 8.3: Simulation results for the shear viscosity η in mPa s. The uncertainty (one standard deviation) is given between parentheses.

	Temperature (K)				
Density (kg m^{-3})	220	240	260	280	300
800.43		0.0746 (0.0058)	0.387 (0.022)	1.152 (0.031)	2.413 (0.072)
839.99		0.0386 (*0.0030*)	0.291 (*0.017*)	0.963 (*0.026*)	2.235 (*0.067*)
879.49		0.0378 (*0.0063*)	0.270 (*0.011*)	0.949 (*0.021*)	2.103 (*0.046*)
920.05	0.004 97 (0.000 67)	0.065 (0.011)	0.390 (0.016)	1.089 (0.024)	2.209 (0.048)
960.09	0.020 7 (*0.002 8*)	0.144 (*0.024*)	0.517 (*0.021*)	1.246 (*0.028*)	2.392 (*0.052*)
999.26	0.057 6 (*0.002 0*)	0.255 (*0.010*)	0.701 (*0.032*)	1.450 (*0.021*)	2.450 (*0.061*)
1040.59	0.097 6 (0.003 3)	0.342 (0.014)	0.846 (0.039)	1.579 (0.023)	2.563 (0.064)
1080.66	0.135 3 (*0.004 6*)	0.423 (*0.017*)	0.914 (*0.042*)	1.666 (*0.025*)	2.492 (*0.062*)
1119.05	0.145 5 (*0.006 0*)	0.453 (*0.022*)	0.915 (*0.033*)	1.627 (*0.056*)	2.485 (*0.029*)
1159.29	0.149 0 (0.006 1)	0.437 (0.021)	0.872 (0.032)	1.519 (0.053)	2.264 (0.026)
1199.43	0.135 3 (*0.005 6*)	0.402 (*0.019*)	0.808 (*0.029*)	1.387 (*0.048*)	2.108 (*0.024*)
1239.28	0.104 4 (*0.007 3*)	0.331 (*0.010*)	0.695 (*0.037*)	1.224 (*0.020*)	1.828 (*0.033*)
1280.93	0.071 5 (0.005 0)	0.2504 (0.0076)	0.589 (0.031)	1.019 (0.017)	1.522 (0.027)
1319.79	0.039 2 (*0.002 7*)	0.1742 (*0.0053*)	0.429 (*0.023*)	0.803 (*0.013*)	1.242 (*0.022*)

Table 8.4: Simulation results for the self-diffusion coefficient D in $10^{-9}\mathrm{m}^2\mathrm{s}^1$ after correction with Eq. (1). The uncertainty (one standard deviation) is given between parentheses. Uncertainty values in italics were calculated from values for neighboring densities.

8.8. Appendix B: Arrhenius plots

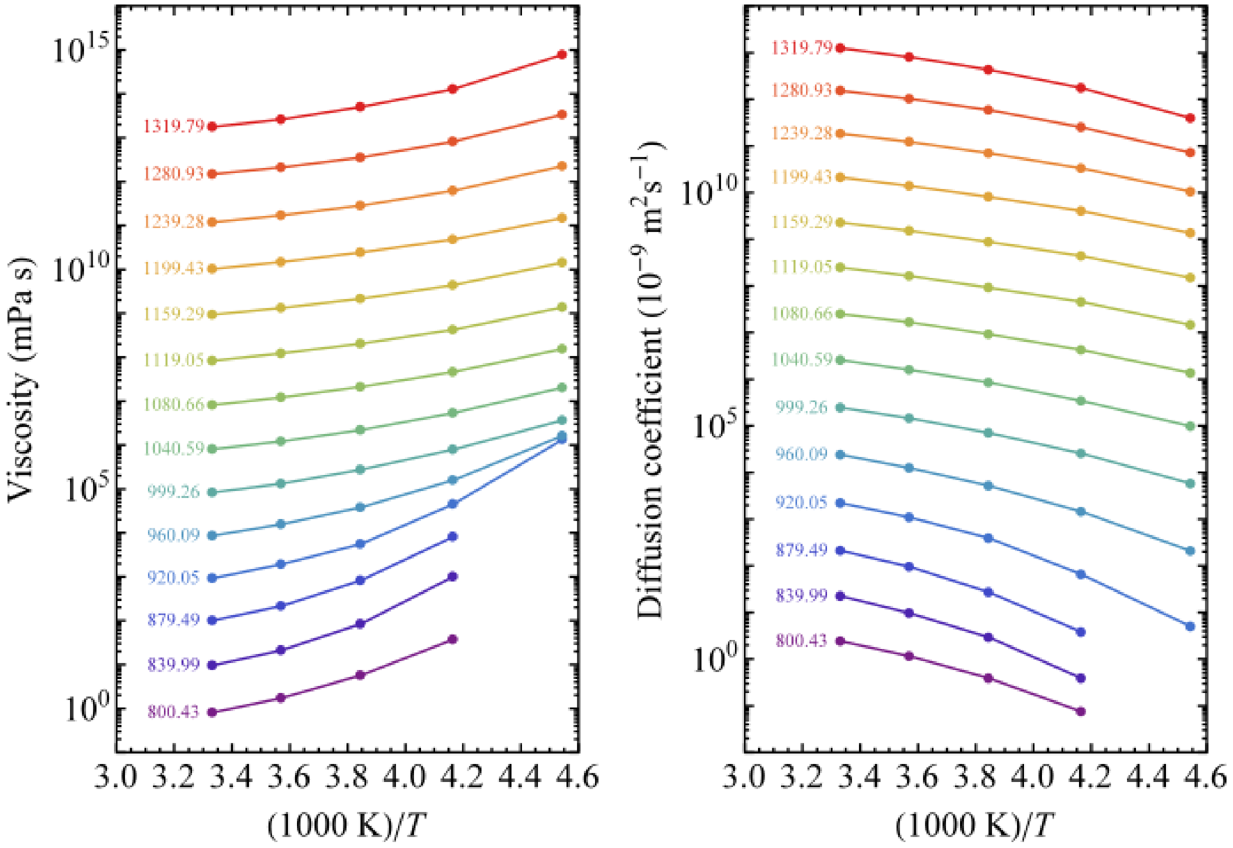

Figure 8.11: Arrhenius plots for shear viscosity (left) and self-diffusion coefficient (right) for a series of isochores, labeled by the density in kg m^{-3}. The data sets have been successively multiplied by 10 for clarity, with lines connecting points to guide the eye.

Bibliography

[1] Paola Gallo, Katrin Amann-Winkel, Charles Austen Angell, Mikhail Alexeevich Anisimov, Frric Caupin, Charusita Chakravarty, Erik Lascaris, Thomas Loerting, Athanassios Zois Panagiotopoulos, John Russo, Jonas Alexander Sellberg, Harry Eugene Stanley, Hajime Tanaka, Carlos Vega, Limei Xu, and Lars Gunnar Moody Pettersson. Water: A tale of two liquids. *Chemical Reviews*, 116(13):7463–7500, 2016.

[2] P. G. Debenedetti. Supercooled and glassy water. 15:R1669–R1726, 2003.

[3] Vincent Holten, CE Bertrand, MA Anisimov, and JV Sengers. Thermodynamics of supercooled water. *The Journal of chemical physics*, 136(9):094507, 2012.

[4] W C Rntgen. *Ann. Phys.*, 258(510), 1884.

[5] E Warburg and J Sachs. *Ann. Phys.*, 258(518), 1884.

[6] Percy Williams Bridgman. The viscosity of liquids ünder pressure. In *Collected Experimental Papers, Volume IV*, pages 1997–2001. Harvard University Press, 2013.

[7] KE Bett and JB Cappi. Effect of pressure on the viscosity of water. *Nature*, 207(4997):620–621, 1965.

[8] Lokendra P Singh, Bruno Issenmann, and Frédéric Caupin. Pressure dependence of viscosity in supercooled water and a unified approach for thermodynamic and dynamic anomalies of water. *Proceedings of the National Academy of Sciences*, 114(17):4312–4317, 2017.

[9] FX Prielmeier, EW Lang, RJ Speedy, and H-D Lüdemann. The pressure dependence of self diffusion in supercooled light and heavy water. *Berichte der Bunsengesellschaft für physikalische Chemie*, 92(10):1111–1117, 1988.

[10] Kenneth R Harris and Paula J Newitt. Self-diffusion of water at low temperatures and high pressure. *Journal of Chemical & Engineering Data*, 42(2):346–348, 1997.

[11] EW Lang and H-D Lüdemann. High pressure o-17 longitudinal relaxation time studies in supercooled h2o and d2o. *Berichte der Bunsengesellschaft für physikalische Chemie*, 85(7):603–611, 1981.

[12] MR Arnold and H-D Lüdemann. The pressure dependence of self-diffusion and spin–lattice relaxation in cold and supercooled h2o and d 2 o. *Physical Chemistry Chemical Physics*, 4(9):1581–1586, 2002.

[13] F. Caupin. Escaping the no man's land: Recent experiments on metastable liquid water. *Journal of Non-Crystalline Solids*, 407:441–448, 2015.

[14] Vincent Holten, Chen Qiu, Emmanuel Guillerm, Max Wilke, Jaroslav Ricka, Martin Frenz, and Frédéric Caupin. Compressibility anomalies in stretched water and their interplay with density anomalies. *The journal of physical chemistry letters*, 8(22):5519–5522, 2017.

[15] P. H. Poole, F. Sciortino, U. Essmann, and H. E. Stanley. Phase behavior of metastable water. *Nature*, 360:324, 1992.

[16] Peter H Poole, Ivan Saika-Voivod, and Francesco Sciortino. Density minimum and liquid–liquid phase transition. *Journal of Physics: Condensed Matter*, 17(43):L431, 2005.

[17] Manish Agarwal, Mohammad Parvez Alam, and Charusita Chakravarty. Thermodynamic, diffusional, and structural anomalies in rigid-body water models. *The Journal of Physical Chemistry B*, 115(21):6935–6945, 2011.

[18] Miguel A. Gonzalez, Chantal Valeriani, Frederic Caupin, and Jose L. F. Abascal. A comprehensive scenario of the thermodynamic anomalies of water using the tip4p/2005 model. *The Journal of Chemical Physics*, 145(5):054505, 2016.

[19] John W Biddle, Rakesh S Singh, Evan M Sparano, Francesco Ricci, Miguel A González, Chantal Valeriani, José LF Abascal, Pablo G Debenedetti, Mikhail A Anisimov, and Frédéric Caupin. Two-structure thermodynamics for the tip4p/2005 model of water covering supercooled and deeply stretched regions. *The Journal of chemical physics*, 146(3):034502, 2017.

[20] Francesco Sciortino, Alfons Geiger, and H Eugene Stanley. Effect of defects on molecular mobility in liquid water. *Nature*, 354(6350):218–221, 1991.

[21] Iosif I Vaisman, Lalith Perera, and Max L Berkowitz. Mobility of stretched water. *The Journal of chemical physics*, 98(12):9859–9862, 1993.

[22] Francis W Starr, Francesco Sciortino, and H Eugene Stanley. Dynamics of simulated water under pressure. *Physical Review E*, 60(6):6757, 1999.

[23] A. Scala, F. W. Starr, E. La Nave, F. Sciortino, and H. E. Stanley. Configurational entropy and diffusivity of supercooled water. *Nature*, 406:166, 2000.

[24] Jeffrey R Errington and Pablo G Debenedetti. Relationship between structural order and the anomalies of liquid water. *Nature*, 409(6818):318–321, 2001.

[25] G Ruocco, M Sampoli, A Torcini, and R Vallauri. Molecular dynamics results for stretched water. *The Journal of chemical physics*, 99(10):8095–8104, 1993.

[26] Paulo A Netz, Francis W Starr, H Eugene Stanley, and Marcia C Barbosa. Static and dynamic properties of stretched water. *The Journal of chemical physics*, 115(1):344–348, 2001.

[27] In-Chul Yeh and Gerhard Hummer. System-size dependence of diffusion coefficients and viscosities from molecular dynamics simulations with periodic boundary conditions. *The Journal of Physical Chemistry B*, 108(40):15873–15879, 2004.

[28] Sami Tazi, Alexandru Boţan, Mathieu Salanne, Virginie Marry, Pierre Turq, and Benjamin Rotenberg. Diffusion coefficient and shear viscosity of rigid water models. *Journal of Physics: Condensed Matter*, 24(28):284117, 2012.

[29] Zane Shi, Pablo G Debenedetti, and Frank H Stillinger. Relaxation processes in liquids: Variations on a theme by stokes and einstein. *The Journal of chemical physics*, 138(12):12A526, 2013.

[30] Emmanuel Guillaud, Samy Merabia, Dominique de Ligny, and Laurent Joly. Decoupling of viscosity and relaxation processes in supercooled water: a molecular dynamics study with the tip4p/2005f model. *Physical Chemistry Chemical Physics*, 19(3):2124–2130, 2017.

[31] Emmanuel Guillaud, Laurent Joly, Dominique De Ligny, and Samy Merabia. Assessment of elastic models in supercooled water: A molecular dynamics study with the tip4p/2005f force field. *The Journal of chemical physics*, 147(1):014504, 2017.

[32] Miguel Angel González and José LF Abascal. The shear viscosity of rigid water models. *The journal of chemical physics*, 132(9):096101, 2010.

[33] Péter T Kiss and András Baranyai. Anomalous properties of water predicted by the bk3 model. *The Journal of Chemical Physics*, 140(15):154505, 2014.

[34] Gabriela Guevara-Carrion, Jadran Vrabec, and Hans Hasse. Prediction of self-diffusion coefficient and shear viscosity of water and its binary mixtures with methanol and ethanol by molecular simulation. *The Journal of chemical physics*, 134(7):074508, 2011.

[35] Takeshi Kawasaki and Kang Kim. Identifying time scales for violation/preservation of stokes-einstein relation in supercooled water. *Science advances*, 3(8):e1700399, 2017.

[36] Debdas Dhabal, Charusita Chakravarty, Valeria Molinero, and Hemant K Kashyap. Comparison of liquid-state anomalies in stillinger-weber models of water, silicon, and germanium. *The Journal of chemical physics*, 145(21):214502, 2016.

[37] Zhonghua Ma, Jicun Li, and Feng Wang. Continuous and discontinuous dynamic crossover in supercooled water in computer simulations. *The journal of physical chemistry letters*, 6(16):3170–3174, 2015.

[38] Mary Vedamuthu, Surjit Singh, and G Wilse Robinson. Properties of liquid water: origin of the density anomalies. *The Journal of Physical Chemistry*, 98(9):2222–2230, 1994.

[39] Chang-Hyun Cho, Jacob Urquidi, and G Wilse Robinson. Molecular-level description of temperature and pressure effects on the viscosity of water. *The Journal of Chemical Physics*, 111(22):10171–10176, 1999.

[40] Chul Hee Cho, Jacob Urquidi, Surjit Singh, Seung C Park, and G Wilse Robinson. Pressure effect on the density of water. *The Journal of Physical Chemistry A*, 106(33):7557–7561, 2002.

[41] Hajime Tanaka. Simple physical model of liquid water. *The Journal of Chemical Physics*, 112(2):799–809, 2000.

[42] Hajime Tanaka. A new scenario of the apparent fragile-to-strong transition in tetrahedral liquids: Water as an example. *Journal of Physics: Condensed Matter*, 15(45):L703, 2003.

[43] Vincent Holten, Jan V Sengers, and Mikhail A Anisimov. Equation of state for supercooled water at pressures up to 400 mpa. *Journal of Physical and Chemical Reference Data*, 43(4):043101, 2014.

[44] Inyong Chang and Hans Sillescu. Heterogeneity at the glass transition: Translational and rotational self-diffusion. *The Journal of Physical Chemistry B*, 101(43):8794–8801, 1997.

[45] Amine Dehaoui, Bruno Issenmann, and Frédéric Caupin. Viscosity of deeply supercooled water and its coupling to molecular diffusion. *Proceedings of the National Academy of Sciences*, 112(39):12020–12025, 2015.

[46] N Galamba. On the hydrogen-bond network and the non-arrhenius transport properties of water. *Journal of Physics: Condensed Matter*, 29(1):015101, 2016.

[47] J. L. F. Abascal and C. Vega. A general purpose model for the condensed phases of water: TIP4P/2005. 123:234505, 2005.

[48] S. Plimpton. Fast parallel algorithms for short-range molecular dynamics. *J. Comput. Phys.*, 117:1, 1995.

[49] R. W. Hockney and J. W. Eastwood. *Computer Simulation Using Particles*, (McGraw-Hill, New York), 1981.

[50] J. P. Ryckaert, G. Ciccotti, and H. J. C. Berendsen. Numerical integration of the cartesian equations of motion of a system with constraints: Molecular dynamics of n-alkanes. 23:327, 1977.

[51] Ting Chen, Berend Smit, and Alexis T Bell. Are pressure fluctuation-based equilibrium methods really worse than nonequilibrium methods for calculating viscosities? *The Journal of chemical physics*, 131(24):246101, 2009.

[52] Jorge Ramírez, Sathish K Sukumaran, Bart Vorselaars, and Alexei E Likhtman. Efficient on the fly calculation of time correlation functions in computer simulations. *The Journal of chemical physics*, 133(15):154103, 2010.

[53] Michael P Allen and Dominic J Tildesley. *Computer simulation of liquids*. Oxford university press, 2017.

[54] International Association for the Properties of Water and Steam No. IAPWS G1215. *Guideline on thermodynamic properties of supercooled water*. 2015.

[55] The value of ν for τ_r is chosen for consistency with the Stokes-Einstein-Debye relation $T\tau_r/\eta = cst_1$, which holds at high temperatures, similar to the Stokes-Einstein relation $D\eta/T = cst_2$[45].

[56] José LF Abascal and Carlos Vega. Widom line and the liquid–liquid critical point for the tip4p/2005 water model. *The Journal of Chemical Physics*, 133(23):234502, 2010.

[57] Tomonari Sumi and Hideo Sekino. Effects of hydrophobic hydration on polymer chains immersed in supercooled water. *RSC advances*, 3(31):12743–12750, 2013.

[58] Takuma Yagasaki, Masakazu Matsumoto, and Hideki Tanaka. Spontaneous liquid-liquid phase separation of water. *Physical Review E*, 89(2):020301, 2014.

[59] Rakesh S Singh, John W Biddle, Pablo G Debenedetti, and Mikhail A Anisimov. Two-state thermodynamics and the possibility of a liquid-liquid phase transition in supercooled tip4p/2005 water. *The Journal of chemical physics*, 144(14):144504, 2016.

[60] SD Overduin and GN Patey. Fluctuations and local ice structure in model supercooled water. *The Journal of chemical physics*, 143(9):094504, 2015.

[61] Philip H Handle and Francesco Sciortino. Potential energy landscape of tip4p/2005 water. *The Journal of chemical physics*, 148(13):134505, 2018.

[62] Wolfgang Wagner, Thomas Riethmann, Rainer Feistel, and Allan H Harvey. New equations for the sublimation pressure and melting pressure of h2o ice ih. *Journal of Physical and Chemical Reference Data*, 40(4):043103, 2011.

[63] Gerold Adam and Julian H Gibbs. On the temperature dependence of cooperative relaxation properties in glass-forming liquids. *The journal of chemical physics*, 43(1):139–146, 1965.

[64] W Götze. The essentials of the mode-coupling theory for glassy dynamics. *Condensed Matter Physics*, 1998.

[65] Thomas Loerting, Violeta Fuentes-Landete, Philip H Handle, Markus Seidl, Katrin Amann-Winkel, Catalin Gainaru, and Roland Böhmer. The glass transition in high-density amorphous ice. *Journal of non-crystalline solids*, 407:423–430, 2015.

[66] JJ Shephard and CG Salzmann. Molecular reorientation dynamics govern the glass transitions of the amorphous ices. *The journal of physical chemistry letters*, 7(12):2281–2285, 2016.

[67] Peter H Poole, Stephen R Becker, Francesco Sciortino, and Francis W Starr. Dynamical behavior near a liquid–liquid phase transition in simulations of supercooled water. *The Journal of Physical Chemistry B*, 115(48):14176–14183, 2011.

[68] Divya Nayar and Charusita Chakravarty. Water and water-like liquids: Relationships between structure, entropy and mobility. *Physical Chemistry Chemical Physics*, 15(34):14162–14177, 2013.

[69] Pradeep Kumar, SV Buldyrev, SR Becker, PH Poole, FW Starr, and HE Stanley. Relation between the widom line and the breakdown of the stokes–einstein relation in supercooled water. *Proceedings of the National Academy of Sciences*, 104(23):9575–9579, 2007.

[70] M Cappelezzo, CA Capellari, SH Pezzin, and LAF Coelho. Stokes-einstein relation for pure simple fluids. *The Journal of chemical physics*, 126(22):224516, 2007.

[71] Robert Zwanzig and Mordechai Bixon. Hydrodynamic theory of the velocity correlation function. *Physical Review A*, 2(5):2005, 1970.

[72] Garrison Sposito. Single-particle motions in liquid water. ii. the hydrodynamic model. *The Journal of Chemical Physics*, 74(12):6943–6949, 1981.

[73] Gilles Tarjus and Daniel Kivelson. Breakdown of the stokes–einstein relation in supercooled liquids. *The Journal of chemical physics*, 103(8):3071–3073, 1995.

[74] MD Ediger and Peter Harrowell. Perspective: Supercooled liquids and glasses. *The Journal of chemical physics*, 137(8):080901, 2012.

[75] Stephen R Becker, Peter H Poole, and Francis W Starr. Fractional stokes-einstein and debye-stokes-einstein relations in a network-forming liquid. *Physical review letters*, 97(5):055901, 2006.

[76] Marco G Mazza, Nicolas Giovambattista, H Eugene Stanley, and Francis W Starr. Connection of translational and rotational dynamical heterogeneities with the breakdown of the stokes-einstein and stokes-einstein-debye relations in water. *Physical Review E*, 76(3):031203, 2007.

Parte IV

Conclusiones

Conclusiones de la Tesis

Al término de este trabajo podemos concluir que se ha abarcado la cinética de la cristalización con énfasis en la nucleación, la cual es la etapa intermedia del proceso que también incluye metaestabilidad del fluido y crecimiento del cristal las cuales ocurren antes y después de la nucleación, respectivamente. Dada la importancia de la termodinámica en el proceso de la nucleación se ha profundizado en el caso de las interfases curvas. Se han estudiado diferentes aspectos de la nucleación de agua, esferas duras y Lennard-Jones. Por otra parte, se ha dedicado un esfuerzo importante a un caso de relevancia como es la formación de hielo donde hemos estudiado no solo la nucleación sino también el crecimiento de hielo y las propiedades de transporte del agua subenfriada. Para llevar a cabo estos trabajos, hemos utilizado la metodología de la simulación molecular acompañada de contexto teórico. A continuación se enumeran las conclusiones principales de esta tesis:

a) La ecuación de Tolman describe adecuadamente la variacion en la tensión interfacial con el radio del núcleo crítico en una interfase sólido-líquido tanto en modelos sencillos (esfera dura y Lennard-Jones) como en el caso del agua (tanto en un modelo realista como es el TIP4P/Ice como en uno más tosco como es el mW). La longitud de Tolman mide la desviación de la tensión interfacial debida a la curvatura respecto de coexistencia y varía poco para un modelo dado en cuanto a lo que nucleación de cristales se refiere.

b) Se ha extendido la técnica de seeding al colectico canónico (NVT). En este colectivo es posible estabilizar una semilla esférica de sólido dentro de un sistema finito. Después demostramos que estos núcleos estables son críticos en el colectivo isotérmico-isobárico (NpT). Por lo tanto, demostramos que los núcleos críticos en el NpT pueden ser termodinámicamente estables en el NVT. También pueden ser metaestables y convertirse en cilindros o interfases planas. Esta técnica permite caracterizar en detalle los núcleos críticos.

c) La longitud de Tolman puede obtenerse ajustando datos de tensión interfacial frente a la curvatura y comparando con la ecuación de Tolman, o bien, midiendo la superficie de tensión y la superficie divisoria de Gibbs y extrapolando su diferencia a coexistencia, es decir, a interfase plana.

d) Los cristales soportan estrés por lo tanto la presión de un núcleo crítico cristalino puede ser menor a la del líquido metaestable que lo rodea. Para hallar la tensión interfacial mediante la ecuación de Young-Laplace uno ha de asumir que la fase externa tiene un carácter macroscópico carente de estrés o defectos y utilizar la igualdad de potenciales químicos para obtener la presión que tendría un cristal macroscópico sin estrés ni defectos a dicho potencial químico. La presión en un sistema donde hay un núcleo crítico es igual a la de la fase externa debido a la condición de equilibrio mecánico. Debido a la interfase, la estructura de un núcleo crítico presenta sutiles diferencias con respecto a la fase macroscópica sin estrés ni defectos que previsiblemente, una vez superada la barrera de energía, terminará formando tras el crecimiento.

e) La termodinámica de interfases curvas permite describir la nucleación en sistemas finitos. En dichos sistemas es posible estabilizar núcleos esféricos/cilíndricos/planos en contacto con líquido metaestable o incluso estabilizar líquido metaestable en lo que se conoce como superestabilización. Bajo ciertas condiciones un núcleo crítico puede perdurar por un tiempo indefinido en un sistema finito pero no cualquier sistema finito permite estabilizar cualquier tamaño de núcleo, solo algunas combinaciones son posibles.

f) La técnica de seeding en el colectivo NVT, la obtención de la presión del núcleo por igualdad de potenciales químicos, la igualdad de presión promedio y externa y la ecuación de Tolman aplican también en fases fluidas para el Lennard-Jones. Gota y burbuja de Lennard-Jones son equivalentes en términos de nucleación pese a que sus densidades y presiones difieran. Sólo una pequeña variación debido a un prefactor cinético las diferencia ligeramente en la tasa de nucleación.

g) La nucleación de hielo a presión negativa es anómala. La tensión interfacial, la barrera de energía libre y la tasa de nucleacion a lo largo de una isoterma presentan un reentrante a presiones negativas. En particular, la tasa de nucleación presenta un máximo y tiende a cero a altas presiones tanto positivas como negativas. El origen está relacionado con el cruce entre las densidades del agua y el hielo y la existencia de un comportamiento reentrante también en la curva de coexistencia. Esto predice también un comportamiento no monotónico en la curva de nucleación homogénea.

h) La velocidad de crecimiento de hielo en función del subenfriamiento presenta un máximo y éste no es un resultado espúreo que resulte de utilizar termostato en la simulación al haberse medido en el colectivo microcanónico (NVE). El calor liberado durante la cristalización se distribuye en el sistema mucho más rápido que lo que el hielo tarda en crecer por lo que no se aprecian gradientes de temperatura.

i) El coeficiente de difusión y la viscosidad del agua subenfriada son anómalos en una determinada región de presiones. Esta anomalía y otras se pueden explicar con un modelo de dos estados del agua. Midiendo ambas variables dinámicas se ha demostrado que a bajas temperaturas la ecuación de Stokes-Einsten pierde validez.